Karlsruher Institut für Technologie

Coherent Two-Qubit Control in Industrial Si/SiGe Spin Qubits

Zur Erlangung des akademischen Grades eines

Doktors der Naturwissenschaften

von der KIT-Fakultät für Physik des
Karlsruher Instituts für Technologie (KIT)

genehmigte
Dissertation

von

M.Sc. Viktor Adam

Tag der mündlichen Prüfung: 18. Juli 2025
1. Referent/Referentin: Prof. Dr. W. Wernsdorfer
2. Referent/Referentin: Prof. Dr. S. Kempf

Abstract

Scalable quantum computing demands qubit systems that combine coherence, control fidelity, and interconnectivity within a reproducible fabrication framework. Silicon spin qubits are particularly attractive due to their compatibility with advanced industrial semiconductor processing. This thesis demonstrates coherent single- and two-qubit operations using Si/SiGe spin qubit devices fabricated by imec (Interuniversity Microelectronics Centre) entirely in an industrial fabrication line, including monolithic integration of cobalt micromagnets for spin control.

Two individual qubits were formed and coherently driven in the MHz range, exhibiting Ramsey coherence times exceeding 1 µs, and Hahn-echo times of up to 79 µs, which are primarily limited by nuclear spin noise from naturally abundant ^{29}Si isotopes. These values confirm robust coherence in an industrial platform, with differences in between both qubits attributed to spatial proximity to decoherence sources. An in-depth qubit control analysis highlights the sensitivity of microwave drive efficiency to gate-defined dot positioning, identifying electrostatic optimization as a practical lever for improved control.

Two-qubit logic was realized by inducing exchange coupling in a double quantum dot, achieving interaction strengths of up to 20 MHz. Conditional resonance shifts under finite coupling confirmed coherent spin-spin interactions and enabled implementation of the conditional rotation (CROT) gate. Coherent two-qubit dynamics were observed in both time and frequency domains, validating functional entangling operations. Future integration of high-speed bias-tee circuitry is proposed to access symmetric operating regimes and enable universal control via fast exchange modulation.

These results validate that industrially fabricated Si-based spin qubits can meet the stringent requirements for coherent multi-qubit operation, supporting silicon spin qubits as a viable architecture for universal quantum computation.

Zusammenfassung

Skalierbare Quanteninformatik erfordert Qubit-Systeme, die Kohärenz, Steuerfidelität und Interkonnektivität innerhalb eines reproduzierbaren Fertigungsrahmens vereinen. Silizium-Spin-Qubits sind besonders attraktiv aufgrund ihrer Kompatibilität mit fortgeschrittener industrieller Halbleiterverarbeitung. Diese Dissertation demonstriert kohärente Einzel- und Zwei-Qubit-Operationen mit Si/SiGe-Spin-Qubit-Einheiten, die von imec (engl. Interuniversity Microelectronics Centre) vollständig in einer industriellen Fertigungslinie hergestellt wurden, einschließlich monolithischer Integration von Kobaltmikromagneten zur Spinsteuerung.

Zwei einzelne Qubits wurden geformt und im MHz-Bereich kohärent angeregt, mit Ramsey-Kohärenzzeiten von über 1 µs und Hahn-Echo-Zeiten von bis zu 79 µs, welche primär durch Kernspinrauschen der natürlich vorkommenden ^{29}Si-Isotope limitiert sind. Diese Werte bestätigen eine robuste Kohärenz in einer industriellen Plattform, wobei Unterschiede zwischen den beiden Qubits auf die räumliche Nähe zu Dekohärenzquellen zurückgeführt werden. Eine eingehende Analyse der Qubitsteuerung hebt die Empfindlichkeit der Mikrowellenanregungseffizienz gegenüber der Quanten-Punkt-Positionierung hervor und identifiziert elektrostatische Optimierung als praxisnahen Ansatz zur Verbesserung der Steuerung.

Zwei-Qubit-Logik wurde durch induzierte Austauschkopplung in einem Doppelpunktsystem realisiert, wobei Kopplungsstärken von bis zu 20 MHz erreicht wurden. Bedingte Resonanzverschiebungen unter endlicher Kopplung bestätigten kohärente Spin-Spin-Wechselwirkungen und ermöglichten die Implementierung des bedingten Rotations-Gatters (CROT). Kohärente Zwei-Qubit-Dynamik wurde sowohl im Zeit- als auch im Frequenzbereich beobachtet, was funktionale verschränkende Operationen validiert. Die zukünftige Integration von Hochgeschwindigkeits-Bias-Tee-Schaltungen wird vorgeschlagen, um das symmetrische Betriebsregime zu erschließen und universelle Steuerung durch schnelle Austauschmodulation zu ermöglichen.

Diese Ergebnisse belegen, dass industriell gefertigte, siliziumbasierte Spin-Qubits die strengen Anforderungen für kohärente Multi-Qubit-Operationen erfüllen können, und unterstützen Silizium-Spin-Qubits als eine vielversprechende Architektur für universelle Quantenberechnung.

Contents

List of Figures

List of Tables

1 Introduction

Semiconductors are the foundation of our modern technological society. The development of integrated circuits and the emergence of Moore's Law [1], which predicted that the number of transistors per unit area would double approximately every two years, enabled the automation of complex calculations and initiated a new technological era. The unprecedented success of microelectronics has been driven by continuous advances in semiconductor manufacturing that expanded the limits of speed, precision, and miniaturization. Today, state-of-the-art chips contain trillions of transistors, feature three-dimensional architectures, and operate at nanometer-scale dimensions [2]. The sustained improvements of microelectronics over the past half century and the modern technological platform for classical computation are both based on silicon complementary metal-oxide semiconductor (CMOS) technology [3]. However, as device features approach atomic dimensions, conventional CMOS scaling encounters fundamental physical and economic challenges [4]. Limitations related to heat dissipation, quantum tunneling, and fabrication precision have prompted growing interest in fundamentally new computing paradigms. A promising alternative is quantum computation, a technology that uses the principles of quantum mechanics to perform certain tasks significantly faster than classical computers [5, 6].

Quantum computers aim to harness key quantum properties, such as superposition and entanglement, to solve problems that are intractable for classical machines [7]. Unlike classical bits, quantum bits or qubits are defined in the ground and excited state of a quantum two-level system and can exist in a coherent superposition of the states $|0\rangle$ and $|1\rangle$. In particular, a register of n interacting qubits can represent 2^n quantum states simultaneously, which offers a path for quantum advantage over classical computers in targeted applications [6]. This underlying concept of quantum advantage is called quantum parallelism [8] and describes the ability of a quantum computer to simultaneously explore all solutions within a large computation space, that grows exponentially with the number of available qubits. It is quantum parallelism that allows quantum algorithms such as Shor's factoring algorithm [9] or quantum simulation of many-body systems [10] to be performed exponentially faster on a quantum computer than on a classical machine. However, solving relevant problems by quantum simulation, such as drug discovery or the solution of the many-particle Schrödinger equation [11], is estimated to require a daunting number of $10^6 - 10^8$ interacting qubits, using currently known quantum algorithms and quantum error correction methods [12, 13]. To realize the advantages of quantum computing in practice, various physical platforms have been explored for qubit implementation, including superconducting circuits[14], trapped ions [15], neutral atoms [16], color centers in diamond [17], molecular spins [18], and semiconductor quantum dots [19].

Among these, semiconductor-based spin qubits in silicon stand out as a particularly promising platform for quantum computation. This technology was proposed by Loss and DiVincenzo in 1998 [20] and relies on using the spin degree of freedom of a single electron as a canonical two-level quantum system. Such spin qubits are realized by isolating electrons in small conductive regions known as quantum dots, which are defined by electrostatic confinement using repulsive potential barriers. The suitability of a qubit platform for quantum information processing is governed by two critical performance metrics, quantum state lifetime and coherence, which are fundamentally dictated by the host material. The lifetime sets how long an excited quantum state remains available for readout, while the coherence time defines how long quantum information can be preserved before it is disrupted by interactions with the environment. Such interactions limit coherence and ultimately lead to the loss of the encoded information in the quantum state. Therefore, long coherence times and stable excited states in comparison to readout and manipulation times are essential for reliable quantum operations. In silicon, the naturally occurring nuclear-spin carrying isotope, ^{29}Si (5% abundance), is the primary source of decoherence, whereas the other dominant isotopes, ^{28}Si (93%) and ^{30}Si (2%) have zero nuclear spin [21]. By enriching qubit devices to nearly pure ^{28}Si, with residual concentrations of less than 800 ppm ^{29}Si, electron spin coherence times exceeding 28 ms have been demonstrated [22]. When combined with quantum state lifetimes on the order of seconds [21, 23, 24] and single-qubit manipulations achievable within 20 ns [21, 25], silicon emerges as one of the most coherent solid-state platforms available for quantum computation. Another compelling reason to pursue silicon-based spin qubits is their seamless compatibility with well-established production lines and mature infrastructure developed over decades for industrial semiconductor manufacturing. Such compatibility enables reproducibility, automation, and the statistical characterization of devices at scale. Recently, industrial fabrication yields have exceeded 99% for functional quantum dot sites [26], enabling wafer-scale testing of device properties and uniformity. A final consideration targets the scalability of quantum computation platforms, where the physical size of a qubit directly impacts the feasibility of integrating a large number of qubits in a small form factor. Silicon spin qubits occupy an area smaller than 0.01 μm^2 [27], allowing very dense integration, potentially over 10^6 qubits in areas less than 5 mm $\times$ 5 mm [28]. This advantage contrasts sharply with the spatial requirements of other platforms like ion traps or superconducting circuits, which require elaborate optical infrastructure or extensive circuitry and therefore occupy orders of magnitude more space [28]. Small physical size is not just a metric of integration density. It also simplifies the design of compact control lines, allows closer proximity of readout and coupling elements, and reduces the thermal load per qubit. These factors contribute directly to the feasibility of scaling up to practical quantum processors.

Recent advances have demonstrated that spin qubits can be industrially fabricated on 300 mm wafers with high uniformity and yield [26], marking significant progress toward manufacturable quantum hardware. However, the realization of quantum processors with millions of qubits will require more than the reproducible fabrication of individual qubits alone. A central requirement for scalable quantum computation is the ability to understand and control multi-qubit interactions. Experimental progress has led to the

demonstration of operational linear qubit arrays with up to twelve spin qubits [29, 30] and two-dimensional 2×2 arrays with tunable coupling [31]. Yet, as systems grow in size, challenges such as maintaining structural uniformity and achieving precise control over inter-qubit coupling become increasingly complex. To address these challenges, future quantum computing architectures are expected to adopt modular designs consisting of locally addressable qubit registers interconnected by long-range couplers. Promising approaches to interconnect qubit registers are actively investigated in form of coherent spin shuttling and superconducting resonators [32, 33]. Furthermore, the co-integration of classical control infrastructure on the envisioned quantum processor chip, such as cryogenic multiplexers and microwave sources, are considered critical for minimizing noise and reducing wiring complexity [27, 28, 34]. The realization of a practical quantum processor therefore requires a co-design approach that integrates high-coherence qubits, modular and densely packed registers, low-noise classical electronics, and robust quantum interconnects. Ultimately, achieving large-scale quantum computation will depend on solving an intertwined set of physical, electrical, and architectural challenges, each of which pushes current technology beyond classical limits.

This thesis addresses two critical challenges in scalable quantum computing: the tunable control of mutual qubit interactions and the demonstration of high-fidelity quantum operations in industrially fabricated spin qubit devices. It presents a comprehensive experimental study of coherent single- and two-qubit control in silicon spin qubit devices fabricated using a 300 mm CMOS-compatible industrial process at the Interuniversity Microelectronics Centre (imec) in Leuven, Belgium [35]. A distinguishing feature of these devices is that the integration of qubit control modules, such as cobalt micromagnets for electron dipole spin resonance (EDSR) control, is fully integrated into the industrial fabrication process, which is unique to date [29, 36]. The first half of this work establishes robust single-qubit operation through electric dipole spin resonance of two independent qubits, demonstrated by Rabi oscillations with frequencies of up to 12 MHz and coherence benchmarks via Ramsey and Hahn-echo measurements, yielding coherence times of up to $T_2^* = 1.1\,\mu s$ and $T_2^{\mathrm{HE}} = 79\,\mu s$, respectively. In the second half, the research focus then advances to the interconnected two-qubit regime and the implementation of exchange-based gate operations. This allows the realization of conditional rotations and characterization of tunable inter-qubit exchange interaction of up to 20 MHz through detuning-dependent exchange spectroscopy. These results validate the feasibility of multi-qubit quantum logic within industrially manufactured Si/SiGe qubits and bridge the gap between laboratory-scale demonstrations and scalable hardware. By experimentally verifying coherent single- and two-qubit control in CMOS-compatible devices, this work paves the way toward large-scale quantum information processing using silicon spin qubits.

This manuscript is structured to follow a logical progression from foundational concepts through single- and two-qubit experiments to the demonstration of conditional gate operations, reflecting the incremental development of control and understanding required to build a multi-qubit silicon quantum processor.

Chapter 2 introduces the underlying physics of spin qubits and describes the formation of zero-dimensional quantum dots in semiconductor heterostructures. It presents the two industrially fabricated device architectures used in this thesis and outlines core qubit device functionalities such as readout and spin manipulation, laying the theoretical groundwork for all experiments in this work.

The experimental infrastructure used to study spin qubit devices is detailed in **Chapter 3**. It introduces the cryogenic measurement setup based on a home-built dilution refrigerator and presents the measurement and manipulation electronics used for coherent qubit control.

In **Chapter 4**, first experimental steps of spin qubit device tuning are presented. It details the formation and calibration of charge sensors and quantum dots in the single-electron regime. It further includes the extraction of key device parameters such as lever arms, tunnel rates, and electron temperature. These results define the operating conditions under which qubits can be reliably initialized and manipulated.

Individual qubit control of a two qubit device is established in **Chapter 5**. It introduces spin-selective readout, maps the qubit resonance frequencies, and applies microwave-driven coherent control to realize Rabi oscillations on both qubits independently. The chapter concludes with a characterization of coherence times using Ramsey and Hahn-echo experiments and discusses differences in performance between the two qubits. These results verify universal quantum control of each qubit and build the foundation for the investigation of spin-spin interactions.

Functional two-qubit operation is approached in **Chapter 6** by realizing readout and manipulation protocols for a coupled spin system and calibrating the voltage space that enables exchange interaction. It then presents the first controlled measurements of exchange splitting and coherence under mutual interaction, confirming the feasibility of two-qubit logic. This chapter lays the experimental groundwork for entangling gate operations and identifies dominant decoherence channels in the coupled regime.

Chapter 7 presents the core results of this thesis by demonstrating applications of two-qubit logic at a fixed exchange interaction. Through precisely timed pulse protocols and a finite exchange interaction, it explores the conditional response of a target qubit to the spin state of a control qubit, enabling spin-selective qubit rotations. These experiments mark the first realization of quantum logic operations within a fully industrially fabricated silicon spin qubit platform.

The final **Chapter 8** embeds key experimental insights in the broader context of academic research and outlines future directions of improvement.

2 From Semiconductors to Spin Qubits

The extraordinary advancement in classical computing technology over recent decades has been largely driven by the semiconductor industry, with silicon serving as its cornerstone. As classical transistor scaling approaches its physical limits, quantum computing has emerged as a fundamentally new approach to tackle classically intractable problems. Among the various quantum computing platforms, spin qubits based on electrons confined in silicon quantum dots combine the unique advantages of quantum mechanics with the scalability of silicon technology. To understand how silicon can support quantum computation, this chapter introduces the physical principles underlying spin qubits, including specific commonly used device platforms. It explains how heterostructure engineering and electrostatic gating allow the formation of controllable quantum dots. Concepts on how spin states are read out and coherently manipulated are introduced based on actual industrially fabricated device architectures. Together, these elements provide a framework for understanding the design and operation of spin-based quantum processors in silicon.

2.1 A quantum bit

At the core of every quantum computer lies the fundamental unit of quantum information: the quantum bit, or qubit. In contrast to classical bits, which can exist in one of the two definite states 0 or 1, a qubit can occupy a coherent superposition of both states simultaneously. Its general state can be written as

$$|\Psi\rangle = a|0\rangle + b|1\rangle\,, \tag{2.1}$$

where a and b are complex probability amplitudes, constrained by the normalization condition $|a|^2 + |b|^2 = 1$. This superposition is a cornerstone of quantum computing, enabling the parallel processing of multiple computational paths within a single operation.

Beyond superposition, qubits gain their unique computational capabilities from entanglement, a quantum correlation that links the states of two or more qubits regardless of their spatial separation. When combined, superposition and entanglement offer a powerful computational advantage over classical systems, but they also impose strict requirements on the physical realization of qubits, demanding precise control and long-lived coherence.

The state of a single qubit can be conveniently visualized on the surface of the Bloch sphere, as shown in Fig. 2.1**a**. This representation maps the qubit state to a point on the

unit sphere in three-dimensional space. In spherical coordinates, the general qubit state is expressed as

$$|\Psi\rangle = \cos(\theta/2)\,|0\rangle + e^{i\phi}\sin(\theta/2)\,|1\rangle\,, \tag{2.2}$$

where θ is the polar angle from the z-axis, and ϕ is the azimuthal angle in the xy-plane. The computational basis states $|0\rangle$ and $|1\rangle$ are located at the north and south poles of the Bloch sphere, respectively, while superposition states lie elsewhere on the sphere. For instance, points on the equator represent equal superpositions such as $(|0\rangle + |1\rangle)/\sqrt{2}$.

The evolution of a qubit under the influence of an external control field, such as an oscillating magnetic field $B^x_{\text{eff}}(t)$ perpendicular to the quantization axis , corresponds to the precession of the qubit state vector along a trajectory on the Bloch sphere. This visualization is essential for understanding quantum gate operations and will be explored in more detail in Sec. 2.7, which discusses the experimental qubit manipulation protocol used in this thesis.

2.2 Loss-DiVincenzo qubits

The seminal proposal of Loss and DiVincenzo envisioned the utilization of confined electron as qubits [20]. For that, a single electron has to be isolated and its spin degeneracy has to be lifted using an external magnetic field. The static magnetic field gives rise to the Zeeman splitting which can be captured by the Zeeman Hamiltonian

$$H_{\text{Z}} = \frac{g\mu_{\text{B}}}{\hbar}\vec{B}\cdot\vec{S}\,, \tag{2.3}$$

where g is the electron Landé g-factor, μ_{B} the Bohr magneton, $\vec{B}$ the static magnetic field and $\vec{S} = \hbar\vec{\sigma}/2$ is the spin vector of the particle with $\vec{\sigma} = (\sigma_x, \sigma_y, \sigma_z)$ being the Pauli matrices. This Hamiltonian can be solved with the time-independent Schrödinger equation and without loss of generality it can be assumed that the static B-field is applied in z-direction. The solution yields the eigenstates of the system to be $\pm\hbar\sigma_z/2$, denoted as spin-down $|\downarrow\rangle$ and spin-up $|\uparrow\rangle$ in the following, and corresponding eigenenergies of

$$E_{\text{Z}} = \pm\frac{1}{2}g\mu_{\text{B}}B_z\,. \tag{2.4}$$

Considering only positive magnetic fields, the lower energetic state $|\downarrow\rangle$ can be associated with the commonly referenced ground state $|0\rangle$ and accordingly $|\uparrow\rangle$ represents the excited state $|1\rangle$.

The implementation of spin qubits in semiconductors relies on the precise confinement of individual electrons in nanoscale structures known as quantum dots. The quantum property of entanglement becomes accessible when extending the system from a single electron in a quantum dot to an array of singly occupied quantum dots, as illustrated in Fig. 2.1**b**. If neighboring dots are spaced closely enough for electron wavefunctions to overlap, the electrons experience an interplay of Coulomb repulsion and the Pauli

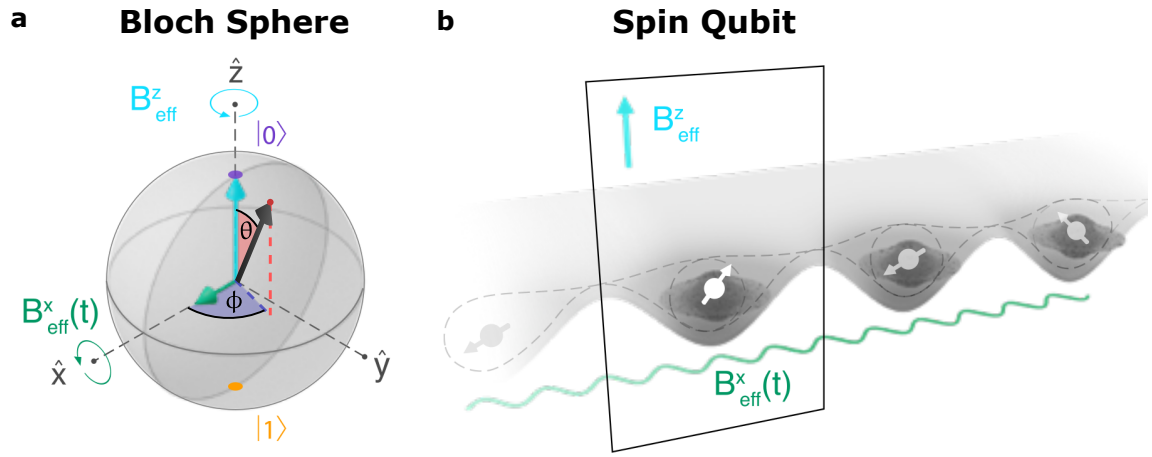

Figure 2.1: a Schematic illustration of spin qubits realized in a linear array of quantum dots. Each dot hosts a single confined electron, with its spin state manipulated by an oscillating transverse magnetic field $B^x_{\text{eff}}(t)$, while a static magnetic field B^z_{eff} defines the quantization axis. **b** Geometric representation of a qubit state on the Bloch sphere. The qubit state $|\Psi\rangle$ (black arrow) corresponds to a point on the unit sphere with polar angle θ and azimuthal angle ϕ. The quantization axis is given by the dominating static $B^{z_{\text{eff}}}$ field (blue arrow). An oscillating magnetic field B^x_{eff} (green arrow) causes coherent rotations of the state vector, enabling universal qubit control. Adapted from Ref. [19].

exclusion principle, giving rise to exchange interaction. This interaction is rooted in the antisymmetry requirement of the total two-electron wavefunction, which includes both spatial and spin components [37, 38]. In the spin-singlet configuration, the antisymmetric spin state allows a symmetric spatial wavefunction, enabling spatial overlap and lowering the system's energy. In contrast, spin-triplet states require spatial antisymmetry, keeping the electrons apart and resulting in higher energy. The energy difference between these states defines the exchange coupling J. This exchange effect between spins i and j is captured by the time-dependent Heisenberg exchange Hamiltonian [19]

$$H_{\text{H}}(t) = J_{i,j}(t)\ \vec{S}_i \cdot \vec{S}_j\,, \tag{2.5}$$

where $J_{i,j}(t)$ is the time-dependent exchange coupling and $\vec{S}_i$ denotes the quantum operator for the spin of the electron at site i. This exchange coupling is tunable by gate voltages and enables coherent two-qubit gate operations between adjacent spins [39, 40]. The experimental realization and tunability of J in this thesis will be discussed in detail in Ch. 6.

2.3 Electron confinement in Si-based qubit devices

Quantum dots in nanoscale semiconductor structures act as artificial atoms with discrete energy levels, that are suitable for quantum information processing. In silicon-based devices, confinement is typically achieved within a two-dimensional electron gas (2DEG), either at the Si/SiO_2 interface in silicon metal-oxide-semiconductor (SiMOS) structures or within a buried quantum well in silicon/silicon-germanium (Si/SiGe) heterostructures.

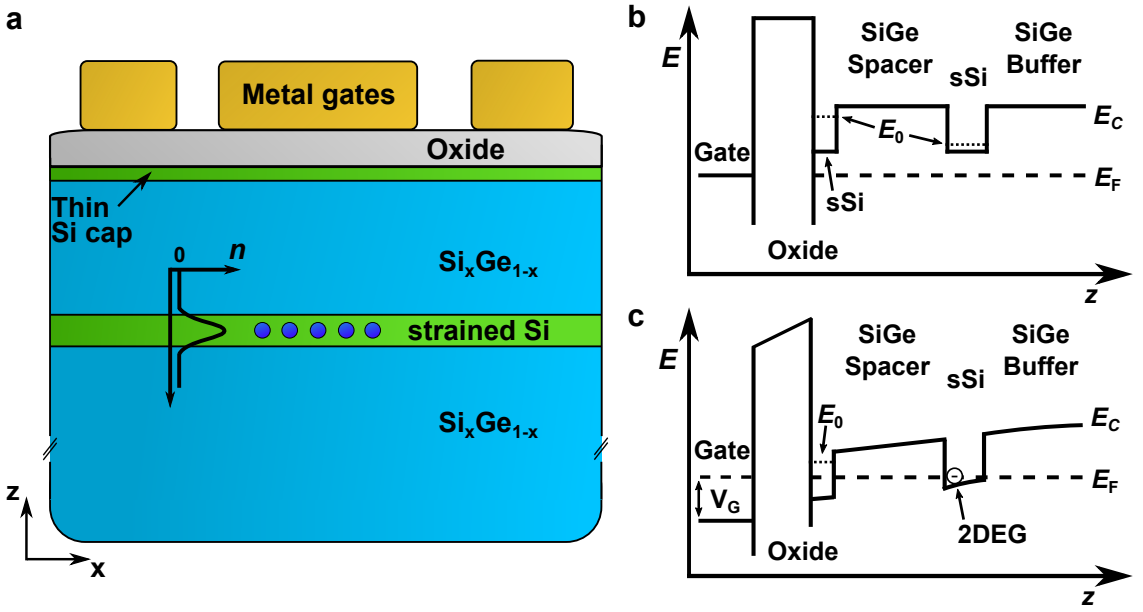

Figure 2.2: Two dimensional electron gas (2DEG) confinement in gate-defined spin qubit architectures. **a** Schematic of a Si/SiGe heterostructure. A Si layer, strained between two SiGe layers, is used as the quantum well, in which a 2DEG can be accumulated by gates deposited on top of the heterostructure. A thin Si cap protects the SiGe layer from oxidation, and an oxide layer insulates the metal gates from the heterostructure. The inset graph illustrates the number of accumulated electrons as a function of the z-coordinate. **b** Conduction band energy E_C in z-direction of the heterostructure. The conduction band edge of the SiGe layers is higher in energy than for pure strained Si (sSi). **c** Conduction band profile under a positive gate voltage V_G. The electrostatic field lowers the band energies, and once the ground state E_0 in the Si quantum well drops below the Fermi level E_F, a 2DEG accumulates. Due to the thinness of the Si cap, its ground state E_0 remains higher than E_F, and no charge accumulation occurs there. Adapted from Ref. [24].

A minimal material stack required for electron confinement consists of a silicon quantum well, a dielectric interface, and surface gate electrodes. This configuration defines the basic SiMOS architecture, where the 2DEG forms directly at the Si/SiO_2 boundary. The more advanced Si/SiGe heterostructure, which is the main focus of this thesis, introduces additional engineering complexity to improve coherence performance. An overview of relevant material stacks used in spin qubit platforms is provided in Fig. 2.4 and discussed further in Sec. 2.4.

Heterostructure of Si/SiGe devices

Two-dimensional confinement of electrons is achieved by electrostatically lowering the conduction band minimum below the Fermi level defined by electric leads. This induces a 2DEG within the quantum well, as illustrated in Fig. 2.2. A schematic cross-section of the Si/SiGe heterostructure is shown in Fig. 2.2**a**. From bottom to top, the epitaxial stack begins with a relaxed Si_xGe_{1-x} buffer layer grown atop a silicon substrate, often using a graded Ge concentration to manage lattice mismatch-induced strain. A thin Si layer (9 nm) is then deposited. Due to the lattice mismatch in between Si and SiGe, the Si layer is tensile

strained, which plays a critical role in lifting valley degeneracy and will be discussed later in this section. In this Si layer, the quantum well will be formed by accumulating a 2DEG gas. Next, a SiGe spacer layer (40 nm) is grown on top, terminated by a thin Si capping layer (2 nm). This cap layer protects the underlying SiGe from oxidation when the gate oxide is deposited. Finally, typically three alternations of gate oxide (SiO_2) and metal gate layers are deposited to conclude the functional buildup of the material stack. The oxide layers electrically insulate the overlapping metal gates from each other and the metal gates are used to electrostatically induce and shape the 2DEG in the quantum well. Not included in the schematic are Ohmic contacts, which are often highly doped regions located outside of the displayed region and serve as source and drain contacts to the quantum well. A corresponding conduction band profile along the vertical (z) direction is shown in Fig. 2.2**b**. A type II band alignment of Si and SiGe occurs due to the strain induced in the silicon layer [41], leading to a lower conduction band energy of the strained Si quantum well compared to the surrounding SiGe barriers. The ground state energy levels E_0 within the two strained Si layers are quantized due to vertical confinement. This implies that the ground state energy of the Si cap at the surface is substantially higher than that of the buried Si quantum well, due to the reduced thickness of the cap layer [3]. In the absence of an applied voltage V_G to the gate, the entire conduction band lies above the Fermi level of source and drain contacts, and the structure remains unpopulated. Upon applying a positive gate voltage V_G, the conduction band is electrostatically pulled downward due to the field effect, as illustrated in Fig. 2.2**c**. Choosing an appropriate gate voltage results in a thin region where the conduction band of the quantum well reaches below the Fermi energy E_F. The well becomes occupied, forming a 2DEG that is confined in the z-direction but free in the xy plane.

By applying suitable voltages to patterned surface gates, the lateral potential landscape can be further shaped to confine the 2DEG into one-dimensional conduction channels, form tunnel barriers, and ultimately establish zero-dimensional quantum dots hosting single electrons. These gate-defined potentials allow the formation of complex qubit architectures based on coupled quantum dots. The actual device layout and specific gate geometries used in this thesis will be introduced in Sec. 2.5.

Lifting the valley degeneracy in silicon

As stated previously, strain in the silicon quantum well is essential for lifting the degeneracy of valley states. This arises from the electronic band structure of silicon, as depicted in Fig. 2.3**a** and **b**. Silicon crystallizes in a diamond face-centered cubic (fcc) structure and is an indirect semiconductor with a band gap of $E_G = 1.17$ eV at 4 K [42]. Its conduction band minimum lies near the X point of the Brillouin zone and is sixfold degenerate along the $\langle 100 \rangle$ directions due to the crystal symmetry. These degenerate minima of the conduction band are known as valley states. This valley degeneracy poses a challenge for spin qubit applications, as electrons occupying different valley states can share the same spin state, thus bypassing the Pauli exclusion principle. To establish an ideal two-level spin qubit system, this degeneracy needs to be lifted beyond the typical energy scales of experimental

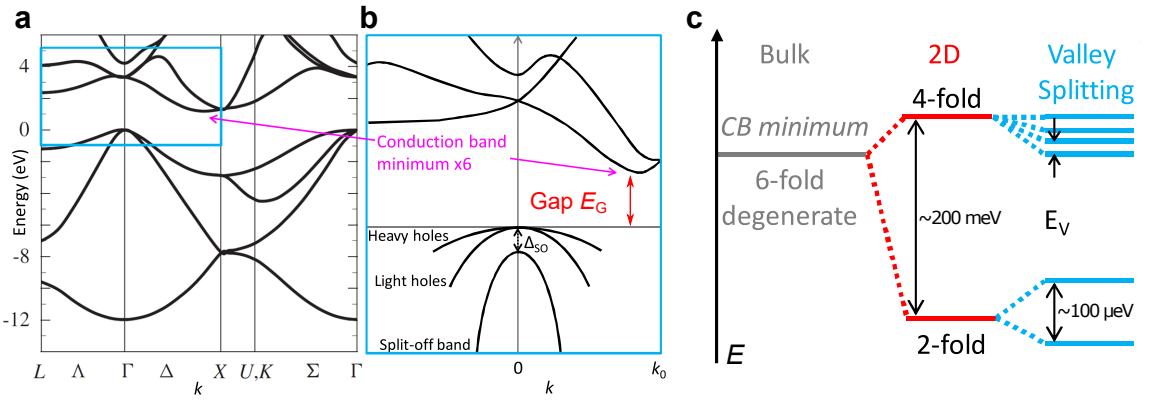

Figure 2.3: a Electronic band structure of bulk silicon, highlighting its indirect bandgap. **b** Enlarged view of the conduction band, showing the six-fold degenerate minima near the X symmetry point of the Brillouin zone, and the indirect bandgap of $E_G = 1.17$ eV at 4 K [42]. **c** Illustration of valley state degeneracy lifting in a strained silicon quantum well. The six-fold degeneracy of the conduction band (CB) in bulk silicon is partially lifted by biaxial tensile strain (2D), which raises the energy of the in-plane ($\pm x$, $\pm y$) valleys and lowers the energy of the out-of-plane ($\pm z$) valleys. Quantum confinement and electric fields further lift the remaining degeneracies in the final step, resulting in a valley splitting E_V. Adapted from Ref. [43].

conditions, including thermal broadening ($k_B T = 13\,\mu$eV at 0.15 K) and Zeeman splitting ($g\mu_B B = 81\,\mu$eV at 0.7 T).

The symmetry of the bulk silicon crystal can be broken through a combination of strain, quantum confinement, and electric fields [43], as illustrated in Fig. 2.3**c**. As mentioned before, strain can be introduced by sandwiching a thin Si layer between SiGe barriers. The mismatch between the lattice constants of Si ($a_{0,\mathrm{Si}} = 5.431$ Å) and Ge ($a_{0,\mathrm{Ge}} = 5.657$ Å) [44] induces tensile strain in the Si layer, which energetically separates the in-plane ($\pm x$ and $\pm y$) and out-of-plane ($\pm z$) valleys by approximately 200 meV [45]. This leaves the two z-valleys as the lowest energy states. The residual twofold degeneracy of the z-valleys is lifted by vertical confinement in the quantum well and by electric fields from gate electrodes [46]. The resulting valley splitting energy E_V typically ranges from 20 μeV to 200 μeV [47, 48], depending sensitively on atomistic details at the Si/SiGe interface. Consequently, the effective valley splitting depends on the exact position of the quantum dot and should be considered in the determination of suitable working points for qubit operation [49, 50].

Although it is generally desirable for the valley splitting energy E_V to exceed the Zeeman energy E_Z, this condition is not always met in practice. If the valley splitting E_V is smaller than the Zeeman energy E_Z, spin qubit operation is still possible, but additional physical effects may influence qubit control. In this regime, the excited spin state of the lowest valley can become nearly degenerate with the ground spin state of the upper valley. This proximity allows for spin-valley mixing via spin-orbit coupling or interface disorder, which couples the spin and valley degrees of freedom. From a practical perspective, this mixing shortens the spin relaxation time, especially near the so-called “hotspot” where the spin and valley levels become degenerate [51]. In summary, operating with $E_V < E_Z$ does not preclude qubit functionality, but introduces additional complexity that can degrade performance unless carefully managed.

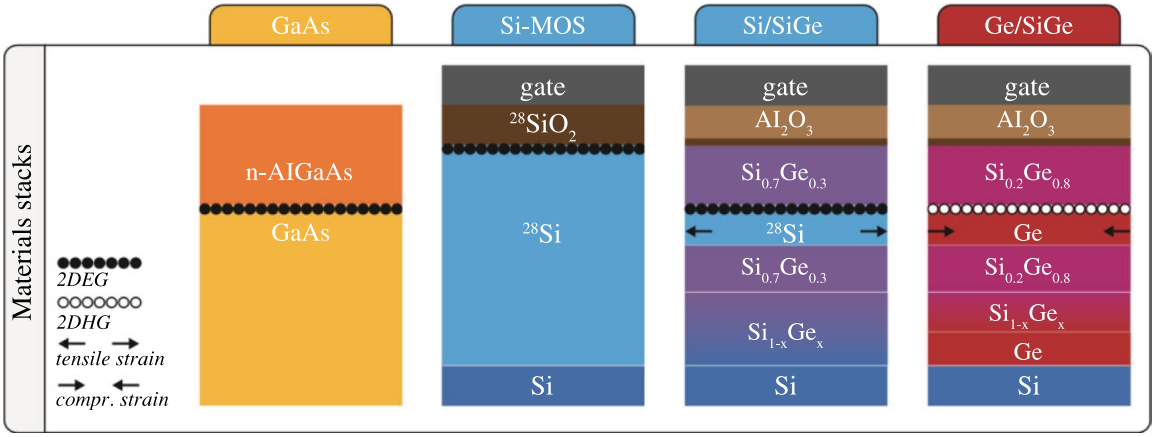

Figure 2.4: Overview of commonly used material stacks for quantum-dot spin qubits, arranged chronologically from left to right based on their development. Each schematic depicts the location of a two-dimensional electron or hole gas (2DEG or 2DHG), shown as a layer of black or white charge carriers, which can be further confined laterally to form qubits. Adapted from Ref. [52].

Given the remarkable degree of control achieved in Si-based quantum-dot devices, including tunable confinement, controllable valley splitting through engineered strain and compatibility with advanced semiconductor manufacturing, silicon emerges as an exceptionally promising platform for realizing scalable, high-fidelity spin-qubit architectures.

2.4 Material platforms for semiconductor spin qubits

Semiconductor spin qubits rely on precisely engineered confinement potentials, formed by combining intrinsic material properties with gate-defined electrostatic fields. A historical overview of the most commonly used semiconductor material stacks for gate-defined spin qubits is provided in Fig. 2.4, and their respective advantages and limitations for spin-qubit implementation are discussed in the following section. This overview follows the comprehensive discussions in Refs. [43, 52, 53].

Historically, gallium-arsenide/aluminium-gallium-arsenide (GaAs/AlGaAs) heterostructures were the first platform to demonstrate gate-defined quantum dots, benefiting from mature epitaxial growth, nearly perfect lattice matching, and exceptionally high electron mobility. Additionally, the low effective electron mass ($m^* = 0.067\, m_e$) allowed for relaxed lithography demands and relatively large quantum dots. Coherent single-spin control in this material system was first demonstrated by Koppens et al. in 2006 [54], following the earlier realization of voltage-controlled two-qubit gates by Petta et al. in 2005 [39]. However, GaAs-based qubits are fundamentally limited by hyperfine interactions with the inherent nuclear spins of all stable isotopes of Ga and As, which induce significant decoherence and ultimately constrain qubit performance.

Motivated by these limitations, research focus shifted to silicon-based structures, primarily due to silicon's naturally abundant nuclear-spin-free isotopes ^{28}Si (92%) and ^{30}Si (3%).

Isotopic enrichment can be utilized to further reduce nuclear spin noise by the ^{29}Si isotope, and thereby greatly improving coherence [21].

Silicon metal-oxide-semiconductor (SiMOS) quantum dots leverage well-established CMOS manufacturing, offering a promising path toward scalability. However, the relatively large electron effective mass in silicon ($m^* = 0.19\, m_e$) necessitates tighter gate pitches, posing increased challenges for device fabrication. Significant milestones include the first demonstration of single-qubit control in an isotopically enriched SiMOS device by Veldhorst et al. in 2014 [22], followed by the realization of two-qubit gates on the same device in 2015 [40]. A key limitation of SiMOS devices arises from the close proximity of the quantum dot to the Si/SiO_2 interface. While the sharp interface supports strong vertical confinement and can lift valley degeneracy up to 0.8 meV [55], it also introduces significant charge noise due to interface traps and defects [56]. This environmental noise remains a dominant factor limiting spin coherence times in these systems [25].

To mitigate the qubit coherence limitations caused by interface disorder in SiMOS devices, silicon/silicon-germanium (Si/SiGe) heterostructures were developed, enabling electron accumulation in a buried quantum well. This buried interface significantly reduces defect densities and scattering sites compared to the Si/SiO_2 interface, leading to enhanced electron mobility and improved qubit coherence. However, challenges remain due to the 4.2% lattice mismatch between Si and Ge, which introduces atomistic disorder at the epitaxial interface and limits the achievable valley splitting to approximately 20 µeV to 200 µeV. However, ongoing efforts aim to improve the heterostructures by incorporating more complex Ge concentration profiles for increased valley splitting [57–59]. Single-electron qubit operation in Si/SiGe was first demonstrated by Kawakami et al. in 2014 [60]. Two-qubit gate implementations in Si/SiGe have been demonstrated in 2018 by Watson et al. [61] and Zajac et al. [62]. The current state-of-the-art is Intel's "Tunnel Falls" device (2024), featuring a 12-qubit Si/SiGe array [29].

More recently, strained germanium/silicon-germanium (Ge/SiGe) heterostructures utilizing hole spins have emerged as a promising platform for scalable quantum computing. Germanium offers a favorable combination of a low hole effective mass ($m^* = 0.05\, m_e$) and compatibility with CMOS technology. Crucially, strong spin-orbit coupling enables all-electric spin control, eliminating the need for additional microwave drive lines or micromagnets. The small effective mass also allows for larger quantum dots, easing nanofabrication constraints compared to silicon-based devices. The inherently low disorder in Ge/SiGe heterostructures, combined with relaxed lithographic requirements, has accelerated progress toward scalable architectures. Within just two years, the field has advanced from single-qubit demonstrations to multi-qubit operations. Hendrickx et al. (2020) [63] demonstrated fast single-hole spin rotations and implemented a two-qubit exchange gate in strained Ge/SiGe heterostructures. Building on this progress, they subsequently realized a 2×2 quantum dot array, the largest two-dimensional spin-qubit architecture reported to date, and demonstrated universal quantum logic with both single- and two-qubit operations [31].

Semiconductor spin qubits offer a clear path toward large-scale, high-density integration, with recent progress showing compatibility with industrial fabrication [29, 64, 65]. As gate

fidelities continue to improve through targeted mitigation of charge and magnetic noise [66–68], no fundamental obstacles remain that would prevent achieving the scalability and yield benchmarks similar to classical CMOS technology.

2.5 Industrially fabricated SiMOS and Si/SiGe qubit devices

Industrial CMOS fabrication is among the most advanced manufacturing techniques worldwide, benefiting from decades of continuous technological innovation. This mature infrastructure enables cost-efficient, high-precision, and reproducible large-scale device production. All devices characterized in this work were fabricated using a 300 mm wafer process line by the Interuniversity Microelectronics Centre (imec) in Leuven, Belgium. Imec's state-of-the-art Class 1000 cleanroom spans 8000 m^2, operates around the clock and is equipped with industry-standard CMOS processing tools [35]. Integrating such industrial fabrication processes into qubit device development offers a promising route to overcome the challenge of scalability in quantum computing [28, 34].

Throughout this thesis, multiple SiMOS and Si/SiGe spin qubit devices have been explored to advance the experimental capabilities of our group, with the overarching goal of realizing two-qubit gate operations. A selection of these devices contributes to the core results presented in this work. An overview of which device is featured in a specific chapter is listed in Tab. 2.1. Although all devices are based on silicon spin qubit platforms and have the same basic operating principles, their measurement order and individual device characteristics are decisive for their appearance in the respective chapters. Unless explicitly noted, all single- and two-qubit experiments were performed on the last device in the list, labeled ^{nat}Si/SiGe D09 Die02. Notably, imec's Si/SiGe devices are, to date, the first spin qubit systems fully realized in a 300 mm industrial semiconductor process, including all fabrication steps from heterostructure growth to the monolithic integration of cobalt micromagnets (CoMM) for spin control. This differentiates the investigated samples from other reported industrially fabricated spin qubit devices, that use post-CMOS processing to integrate CoMMs [26, 29, 36].

Platform	Wafer subdie	Layout	Drive	Primary use in this thesis
^{28}SiMOS	D06 Die07	SD5	ESR	RAP experiments in Sec. 5.4
^{nat}Si/SiGe	D09 Die05	SD15B	EDSR	EDSR-drive optimization in Sec. 5.6.2
^{nat}Si/SiGe	D09 Die02	SD15B	EDSR	All single- and two-qubit measurements

Table 2.1: Reported devices and their appearance in this thesis. A full list of measured imec devices is shown in Tab. A.1 and detailed result protocols are available in group intern notebooks. The different gate layouts are introduced in the following of this section and the different drive mechanisms are explained in Sec. 2.7.

General device structure and functionality

Gate-defined silicon devices employ metallic gates, arranged in a nanometer precise gate layout, to achieve excellent control over the potential landscape in the quantum well.

Applying biases to specific gates allows to shape adjustable tunnel barriers or control the charge occupancy in quantum dots. The gate layout refers to the three-dimensional arrangement of typically three patterned metal gate layers, which enable electrostatic control over the spatial extent of the two-dimensional electron gas (2DEG) in the quantum well.

The SiMOS and Si/SiGe devices examined in this thesis differ not only in their intrinsic material properties (cf. Sec. 2.4) but also in their gate architecture. It is worth noting that the gate layout identifiers (SD5 and SD15B) used throughout this thesis refer to specific subdies on the fabrication wafer, each containing multiple devices with a shared gate design. While the gate layout identifiers do not uniquely define a particular gate geometry in general, they are sufficient to distinguish between the two gate layouts discussed in this work.

Both device types and their respective layouts are shown in Fig. 2.5 and Fig. 2.6. Prior to a discussion of the specific gate designs SD5 (Fig. 2.5**b**) and SD15B (Fig. 2.6**b**), we first outline the general functional roles of the different gate layers to facilitate comparisons across device types. Each gate layout features three metal gate layers. The first layer (brown) is located closest to the quantum well and exerts the strongest electrostatic influence on the conduction band in the quantum well. The effectiveness of this coupling is expressed by the lever arm α in units of eV/V, which is defined as the ratio between the applied gate voltage and the resulting energy shift in the conduction band. Due to that strong influence, this layer primarily hosts screening gates, which are biased below the accumulation threshold to suppress 2DEG formation in undesired regions. As a result, electrons are confined to well-defined one-dimensional channels. The second layer (blue) mainly comprises accumulation gates, which are used to induce mobile electrons in specific regions of the quantum well. These gates are responsible for defining conductive paths and forming quantum dots. The third layer (red), furthest from the quantum well, generally contains barrier gates. Owing to their reduced lever arm, these gates induce only modest energy shifts in the quantum well, yet they are sufficient to locally deplete the electron gas, thereby forming tunnel barriers that modulate inter-dot coupling or tunneling rates to electron reservoirs. Functionally, both gate layouts can be divided into two regions: a charge sensing region, where a single-electron transistor (SET, see Sec. 2.6) is formed, and a qubit region, designed to host one or two quantum dots operating in the single-electron regime.

SiMOS device structure and operation

The SiMOS device layout depicted in Fig. 2.5 illustrates a schematic vertical cross-section of the material stack (panel **a**) along the white dashed line in the top-down scanning electron microscope (SEM) image of the gate layout (panel **b**).

From bottom to top, the material stack of the device comprises a bulk silicon substrate (2 µm thickness) interfaced with a thin (8 nm) thermally grown SiO_2 layer, forming the quantum well at the Si/SiO_2 interface. Phosphorus-implanted regions located far from

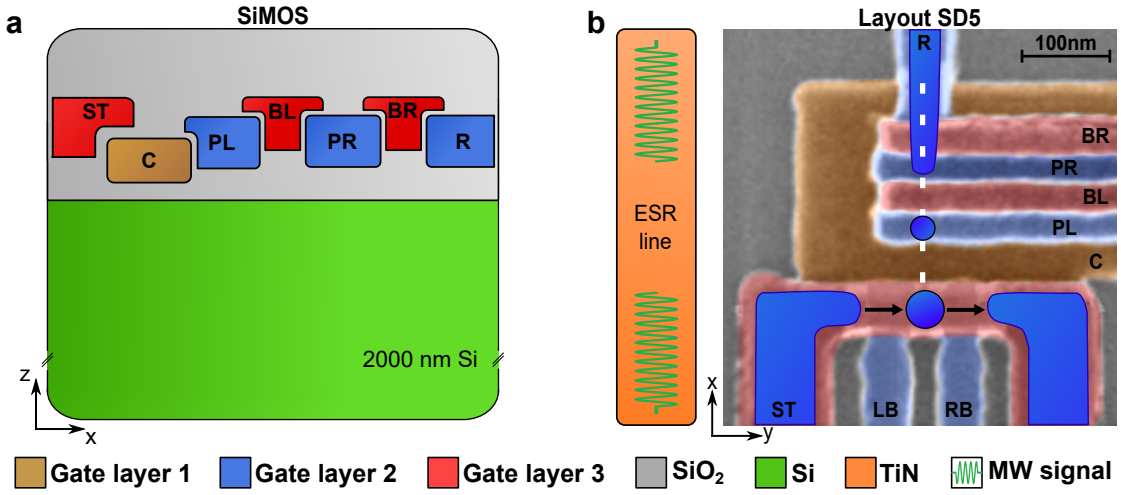

Figure 2.5: a Schematic cross-section of a SiMOS device, showing the Si/SiO_2 interface where the quantum well is formed and three overlapping poly-silicon gate layers. The slice corresponds to the qubit channel marked by a dashed white line in panel **b**. Gate width and proximity to the quantum well qualitatively indicate lever arm hierarchy. The schematic is not to scale. **b** False-colored SEM image of imec's SiMOS gate layout SD5. Dark blue regions indicate areas where electrons are accumulated for single-qubit operation. Black arrows illustrate electron tunneling through the SET formed by gates ST, LB, and RB. A quantum dot is formed under the plunger gate PL, tunnel-coupled by gate BL to an electron reservoir that extends from gate R to gate PR. The titanium-nitride (TiN) ESR line for spin manipulation by microwave (MW) signals is indicated to the left of the gate layout. It is located at a height comparable to the first gate layer and laterally displaced by 300 nm from the qubit site as illustrated.

the qubit area serve as ohmic contacts to electrically access the quantum well. Three overlapping polycrystalline silicon (poly-Si) gate layers (each 20 nm thick), separated by thin insulating SiO_2 (5 nm), provide precise electrostatic control to shape and confine the electron states within the quantum well. An electron spin resonance (ESR, see Sec. 2.7) drive line, consisting of a 100 nm thick titanium-nitride (TiN) layer, is integrated on top of the three gate oxide layers and placed approximately 300 nm laterally displaced from the qubit dot (see panel **b**). Finally, a passivation layer of 200 nm SiO_2 encapsulates the entire structure, with vias etched through this passivation layer establishing electrical contacts to the gates, ohmic regions, and ESR line.

The gate layout, labeled SD5 (Fig. 2.5**b**), is functionally divided into two main regions: a charge sensing region and a qubit region. Conductive regions, marked in dark blue, indicate electron accumulation areas essential for device operation. The charge sensor is realized as a single-electron transistor (SET), defined by accumulation under the SET-top (ST) gate and tunnel barriers created by the left (LB) and right (RB) barrier gates.

The qubit region is primarily controlled by a large C-shaped screening gate (C), biased below the electron accumulation threshold to suppress unwanted conduction paths. Electron reservoirs are formed by accumulating electrons beneath the reservoir gate (R) and extending this reservoir beneath the right plunger gate (PR) and right barrier gate (BR) by positive biasing. A single quantum dot close to the charge sensor is isolated by negatively biasing the left barrier gate (BL) to interrupt conduction. Subsequent tuning of the left

plunger gate (PL) allows to incrementally load electrons into the dot, as evidenced by discrete charge transitions detected by the SET.

For qubit operation, an external static magnetic field $\vec{B}_0$ is applied in-plane to lift the spin-state degeneracy of the electron. A microwave signal applied to the laterally displaced ESR line (aligned along the x-axis) generates an oscillating magnetic field $\vec{B}_1$ oriented perpendicular to the static magnetic field. This perpendicular orientation of static and oscillating fields enables coherent spin rotations on the Bloch sphere, providing precise qubit manipulation capabilities by ESR. A supporting depiction of the spatial relation between the ESR line and the qubit as well as magnetic field directions are provided in Fig. 2.7**a**. Further details of qubit control using ESR are discussed in Sec. 2.7

Si/SiGe device structure and operation

The layered structure of a Si/SiGe two-qubit device is illustrated in Fig. 2.6**a**, alongside a false-colored SEM image of the lateral gate layout in panel **b**. The vertical cross-section in panel **a** corresponds to the dashed white line in panel **b**, highlighting both the material stack and the vertical arrangement of the gates along the qubit channel.

From bottom to top, the heterostructure begins with an 8 µm graded strain-relaxed buffer (not shown), followed by a 1 µm thick unstrained $Si_{0.75}Ge_{0.25}$ layer for dislocation reduction. A 9 nm tensile-strained Si quantum well is grown by chemical vapor deposition (CVD), topped by a 40 nm thick $Si_{0.75}Ge_{0.25}$ spacer layer. Phosphorus implants through this spacer form Ohmic contacts to the buried quantum well. To prevent oxidation of the spacer, a 2 nm Si cap is deposited, followed by an 8 nm thick SiO_2 dielectric layer. The three overlapping gate layers consist of 30 nm TiN in the first layer and 20 nm TiN in the second and third, with 5 nm SiO_2 insulating layers in between. A 250 nm thick c-shaped cobalt micromagnet (CoMM) is deposited on top of the stack to enable electric dipole spin resonance (EDSR, see Sec. 2.7). A final 200 nm thick SiO_2 passivation layer encapsulates the structure, with etched vias connecting the Ohmic contacts, gates, and CoMM.

The lateral gate layout SD15B is shown in the false-colored SEM image in Fig. 2.6**b**. The central screening gate (CC) separates the lower single-electron transistor (SET) channel from the upper qubit channel. Conduction paths are confined by the bottom (CB), central (CC), and top (CT) screening gates. Four Ohmic contacts establish source and drain connections to both channels. The Ohmic contacts overlap with the four accumulation gates (LTA, RTA, LBA, RBA) which induce the electron reservoirs in both channels as indicated by the dark blue regions. The SET is formed in the lower channel by local depletion under LB and RB gates, while a large quantum dot is induced with the ST gate. Similarly, two quantum dots are defined in the upper channel using the interdot barrier (B) and adjacent dot barrier gates (BL, BR). Electrons are loaded and monitored via the SET, which is positioned closer to the right dot, providing asymmetric signal contrast for charge state discrimination of both dots.

Once static confinement is established, the CC gate and CoMM can be used for qubit control. The CC gate doubles as an integrated microwave (MW) line that drives small

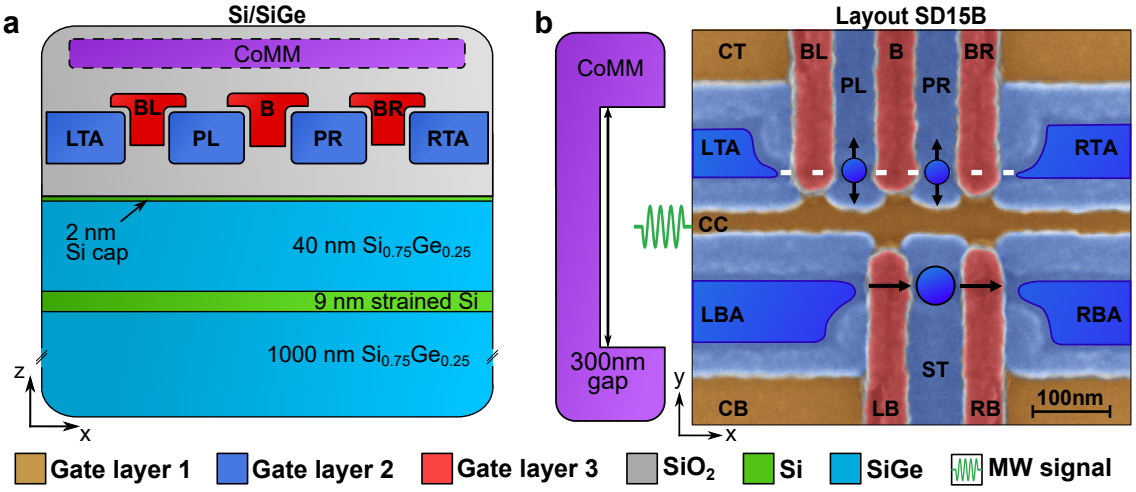

Figure 2.6: **a** Schematic cross-section of a Si/SiGe device showing the strained Si quantum well embedded between relaxed SiGe barriers, capped by a thin Si layer and overlaid with three overlapping TiN gate layers. Gate width and proximity to the quantum well qualitatively indicate lever arm hierarchy. The buried Si quantum well is formed at the interface with the 40 nm SiGe spacer. A c-shaped Co micromagnet (CoMM), located 120 nm above the quantum well, generates the magnetic gradient needed for EDSR. The dashed outline indicates that the CoMM does not intersect the displayed cross-section but is shown to visualize the positioning. The schematic is not to scale. **b** False-colored SEM image of imec's Si/SiGe gate layout SD15B. Dark blue regions mark electron accumulation for two-qubit operation. Blue dots indicate the SET, formed under the ST gate, as well as two quantum dots located under the plunger gates PL and PR. The qubit dots are centered within the 300 nm gap of the CoMM. Black arrows show the SET current path and the microwave-induced lateral motion of the qubit electrons driven via the central screening gate (CC). This oscillatory motion through the magnetic field gradient of the CoMM enables EDSR. The orientation of the CoMM is illustrated to the left of the layout. Adapted from Ref. [24].

spatial displacements of the quantum dots at the MW frequency. These displacements occur in the spatially varying magnetic field gradient created by the CoMM, which is designed such that the qubits reside centered in its 300 nm wide gap. The CoMM is located approximately 120 nm above the plane of the quantum well and subjects each qubit to a distinct local magnetic field which allows to address them individually by their resonance frequency. Prior to qubit operation, the CoMM is polarized with an external magnetic field in y-direction, which leads to a strong out-of-plane (z) magnetic field gradient in the gap. By the oscillating motion of the qubits in this magnetic field gradient they effectively experience an oscillating magnetic field which allows to induce coherent spin rotations via electric dipole spin resonance (EDSR). Further details of qubit control using EDSR are discussed in Sec. 2.7

A previous study by Koch [24] has investigated comparable imec samples with CoMM gaps ranging from 300 nm to 650 nm and concluded that only CoMM with a gap of 300 nm align with simulation results (see Ref. [70]) and allow for the best EDSR drive. Accordingly, only samples with a gap of 300 nm were investigated in this work. The specific CoMM design employed here, shown in Fig. 2.7, is approximately 1.5 µm wide, 4 µm long, and 250 nm thick. Governed by the orientation of the CoMM gap, the external static magnetic field must be applied along the y-direction to ensure perpendicular alignment with the

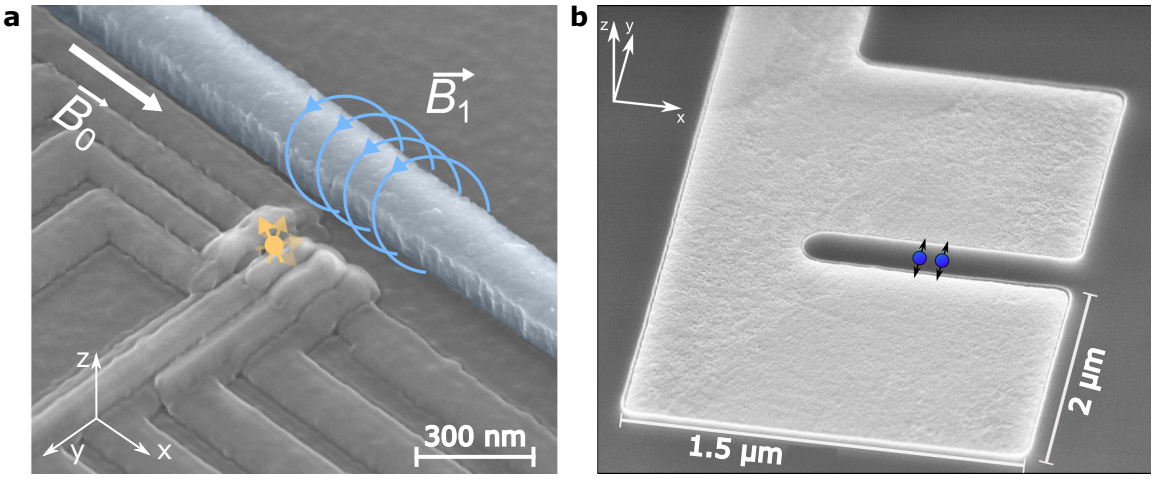

Figure 2.7: a SEM image of the ESR line and gate stack in a SiMOS device. The qubit location is marked with a yellow rotating arrow. A microwave signal through the bright blue ESR line generates an oscillating magnetic field $\vec{B}_1$ (blue loops), which is oriented predominantly in the z-direction at the qubit position. Combined with the in-plane static magnetic field $\vec{B}_0$, this enables coherent spin manipulation via ESR. Adapted from Ref. [69]. **b** SEM image of a cobalt micromagnet (CoMM) with a 300 nm gap used for EDSR control in Si/SiGe devices. The angled view causes apparent shortening in the y-direction. The Co layer is 250 nm thick, encapsulated in SiO_2, and connected to ground via a dedicated contact. Blue dots with black arrows indicate the positions and oscillatory motion of the quantum dots, located approximately 120 nm below the CoMM within the quantum well. Adapted from Ref. [64].

dominant magnetic field gradient, which points in the out-of-plane z-direction within the gap. This perpendicular configuration is essential for efficient qubit manipulation.

2.6 Single-electron transistor as a charge sensor

A single-electron transistor (SET) is a nanoscale charge-sensing device that enables highly sensitive detection of electron tunneling events in adjacent quantum dots. In the context of spin qubit experiments, the SET plays a crucial role in device tuning and qubit readout by transducing changes in quantum dot charge states into a measurable current signal.

Structurally, an SET consists of a quantum dot tunnel-coupled to source and drain leads, and capacitively coupled to nearby electrostatic gates and quantum dots. The devices investigated in this thesis incorporate dedicated charge sensing regions to form an SET in close proximity to the qubit region. The placement of the SET is optimized to ensure strong capacitive coupling to the qubit dots while maintaining independent tunability.

The chemical potential diagram of an SET is illustrated in Fig. 2.8. The central quantum dot is tunnel-coupled to source (S) and drain (D) leads and defined by a top gate (ST) and gate-tunable barriers (LB and RB). The chemical potentials of the leads, μ_S and μ_D, are defined by Ohmic contacts and can be offset by applying a source-drain bias V_{SD}. The discrete charge state potentials of the quantum dot are labeled μ_N with N representing the number of confined electrons in the dot. These states are spaced by the charging energy

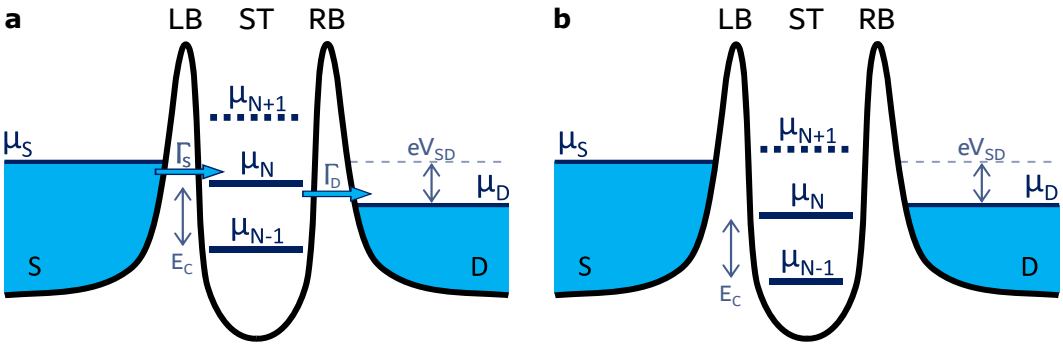

Figure 2.8: Chemical potential diagram of a single-electron transistor (SET). The central quantum dot is defined by gate-tunable barriers (LB and RB) and a top gate (ST), and is tunnel-coupled to source (S) and drain (D) reservoirs. The chemical potentials of source (μ_S) and drain (μ_D) are offset by a source-drain bias V_{SD}, while the discrete energy levels μ_N within the dot are separated by the charging energy E_C. **a** Transport regime: The charge state μ_N lies within the bias window, allowing sequential tunneling from source to drain at rates Γ_S and Γ_D, resulting in a measurable current. **b** Coulomb blockade: All discrete dot levels lie outside the bias window, suppressing electron tunneling and current flow. Based on Ref. [43].

$E_C = e^2/C$, which represents the required energy to add an electron to a quantum dot of self-capacitance C [43].

The so-called Coulomb blockade regime can be achieved if the quantum dot is tuned small enough such that the charging energy exceeds the thermal broadening of both leads, $E_C > 2k_BT$ at given temperature T, and the bias window is smaller than the level spacing in the dot, $eV_{SD} < E_C$ [71]. Under these conditions, electronic transport through the quantum dot is only possible if a charge state level is aligned within the bias window, as displayed in Fig. 2.8**a**. Notably, only one electron from the source can tunnel into the accessible quantum dot level μ_N at a time. Once this electron tunnels to the drain, the level becomes available for the next tunneling event, enabling a measurable current. This sequential single-electron transport defines the operating principle of a single-electron transistor in the Coulomb blockade regime. Figure 2.8**b** depicts a configuration in which no quantum dot level is accessible in the bias window. As a consequence the quantum dot charge remains fixed, and current is suppressed.

Similar to a classical transistor, the conductance of an SET can be modulated between blockade and transmission by tuning the top gate (ST) voltage. Sweeping this voltage results in Coulomb oscillations, a series of conductance peaks as a function of gate voltage as shown in Fig. 2.9**a**. On the flanks of these peaks, the conductance becomes highly sensitive to small changes in the local electrostatic environment. This sensitivity is exploited to detect the charge occupancy of a nearby quantum dot. When an electron enters the dot, its negative charge lowers the local electrostatic potential which causes a detectable change in SET current due to capacitive coupling. In Fig. 2.9**b** the current through the SET is shown as a function of the plunger voltage of a nearby quantum dot. Discrete jumps of the SET current can be observed whenever the plunger voltage exceeds specific values at which electrons occupy the dot. The green and orange markers indicate the current before and after loading an electron, highlighting the high signal-to-noise ratio (SNR) achievable with SET-based charge sensing.

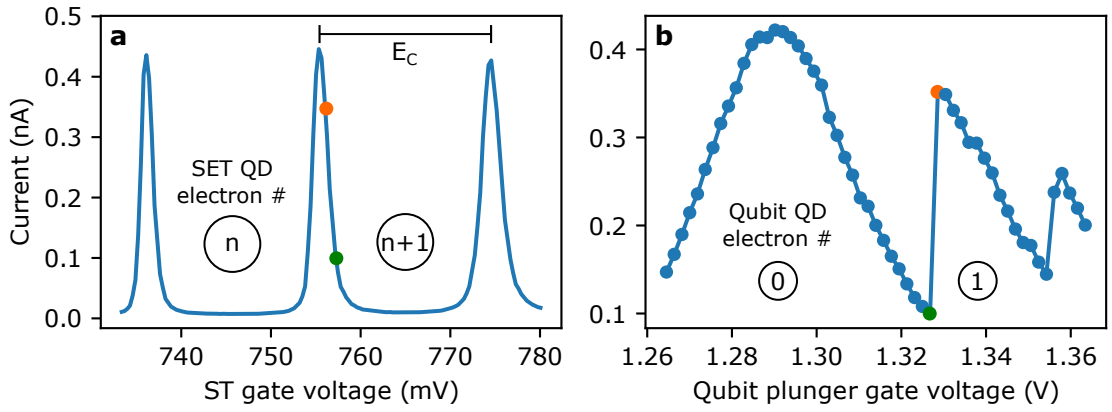

Figure 2.9: Experimentally observed Coulomb oscillations and charge sensing using a single-electron transistor (SET). **a** SET current as a function of the ST gate voltage, showing periodic Coulomb oscillations due to discrete charge states in the SET quantum dot (QD). The green and orange markers indicate SET current levels before and after an electron enters a nearby quantum dot, demonstrating sensitivity to local electrostatic changes. **b** SET current as a function of the plunger gate voltage of an adjacent quantum dot. Due to capacitive cross-coupling of the plunger gate to the SET, the observed current shows a Coulomb oscillation. Discrete jumps in current reflect the iterative loading of electrons into the dot, which affects the electrostatic environment and mimics a negative offset on the ST gate voltage due to the negative charge of electrons.

In practice, the SET is biased at a fixed source-drain voltage and its top gate voltage can be tuned such that it maximizes charge sensitivity and SNR. Although tempting, it is not ideal to maximize the peak SET conductance in order to maximize the charge jump signal. In fact, we have observed that too high SET currents (>1 nA) do adversely impact qubit characteristics such as coherence times or electron temperatures, which can be understood as a result of a local heating and noise caused by the resistive SET current path [72, 73]. Therefore, it is good practice to choose a working point on the left flank of a Coulomb oscillation at which the SET current is minimal during qubit manipulation but provides sufficient current to detect the signal when the electron is unloaded. More details toward experimental practices using the SET are discussed in Ch. 4.

2.7 Coherent spin manipulation

To complete the foundational understanding of spin qubit systems, it is essential to introduce the physical mechanism by which universal quantum control over the spin state of an electron is achieved. While the preceding sections have focused on quantum confinement, initialization, and readout, coherent spin manipulation provides the final ingredient required for universal single-qubit operations.

Universal qubit control

A single electron spin possesses a two-fold spin state degeneracy. This degeneracy is lifted in the presence of an external magnetic field $\vec{B}_{\text{ext}}$ which can be assumed to be oriented in z-direction $\vec{B}_{\text{ext}} = B_z$ without loss of generality. This results in Zeeman splitting between the spin eigenstates $|\downarrow\rangle$ and $|\uparrow\rangle$, with an energy difference

$$\Delta E_{\text{Z}} = g\mu_{\text{B}} B_z \,, \tag{2.6}$$

where $g \approx 2$ is the effective Landé g-factor of electrons in Si [74] and μ_{B} the Bohr magneton. The corresponding Larmor precession frequency of the spin in the static magnetic field defines the resonance condition

$$\omega_0 = \frac{g\mu_{\text{B}} B_z}{\hbar} \,. \tag{2.7}$$

This static magnetic field defines the quantization axis of the spin and allows the representation of the spin eigenstates on the poles of a Bloch sphere.
Spin state transitions can be induced by the introduction of a perpendicular, time-dependent magnetic perturbation field $\vec{B}_1(t) = B_1 \cos(\omega t + \delta)\vec{e}_x$ to the system, where ω denotes the drive frequency, δ represents the initial phase and $\vec{e}_x$ is the unit vector in x-direction. The total Hamiltonian is then given by

$$\begin{aligned} H(t) &= H_0 + H_1(t) && (2.8)\\ &= \frac{1}{2} g\mu_{\text{B}} B_{\text{ext}} \sigma_z + \frac{1}{2} g\mu_{\text{B}} B_1 \cos(\omega t + \delta)\sigma_x && (2.9)\\ &= \frac{g\mu_{\text{B}}}{2} \begin{pmatrix} B_{\text{ext}} & B_1 \cos(\omega t + \delta) \\ B_1 \cos(\omega t + \delta) & -B_{\text{ext}} \end{pmatrix} , && (2.10) \end{aligned}$$

with the respective Pauli matrices σ_x and σ_z. In matrix representation it becomes apparent that the perturbation $B_1(t)$ on the off-diagonal positions couple the two spin eigenstates of the time-independent Hamiltonian H_0. If $\vec{B}_1(t)$ is synchronized to the Larmor frequency ω_0, the perturbation field effectively pushes and pulls the magnetic moment of the spin synchronous to the precession frequency resulting in coherent transitions between $|\downarrow\rangle$ and $|\uparrow\rangle$. In the laboratory frame, the spin precesses around the rotating effective magnetic field, composed of the static external B-field $\vec{B_{\text{ext}}}$ and the oscillating field component $\vec{B_1}$, leading to a spiraling trajectory on the Bloch sphere as depicted in Fig. 2.10**a**.

A more elegant description of the spin dynamics is obtained by transforming to a reference frame rotating at the drive frequency ω. This is achieved via the unitary transformation

$$\left|\tilde{\Psi}(t)\right\rangle = U^{\dagger}(t) \left|\Psi(t)\right\rangle \quad \text{with} \quad U(t) = \exp\left(-\frac{iH_0 t}{\hbar}\right) = \begin{pmatrix} e^{-i\omega t/2} & 0 \\ 0 & e^{i\omega t/2} \end{pmatrix} , \tag{2.11}$$

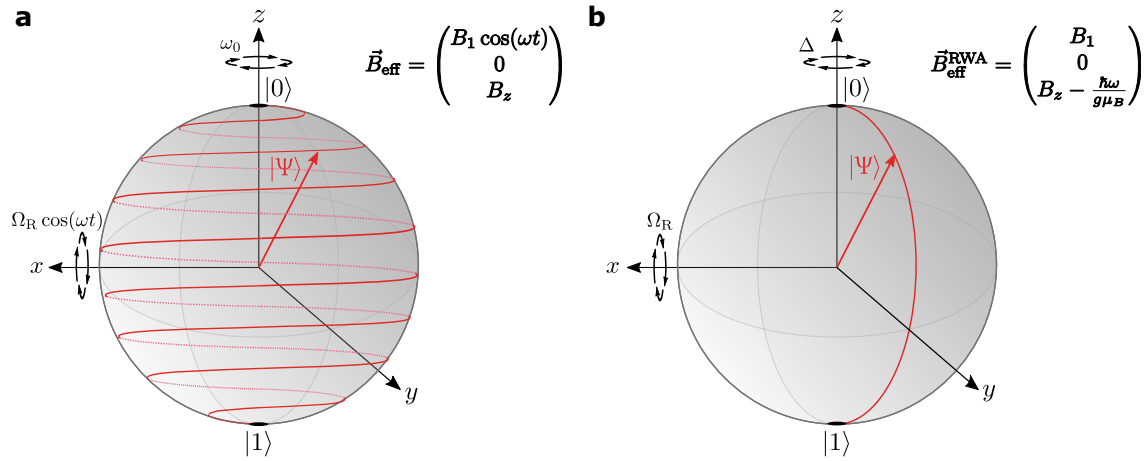

Figure 2.10: Illustration of spin dynamics on the Bloch sphere under resonant transverse driving with frequency $\omega = \omega_0$ and phase $\delta = 0$. The spin is initialized in the ground state $|0\rangle$ at $t = 0$. Effective magnetic field vectors are denoted in the top right of each panel. **a** Spin trajectory in the lab frame. The spin precesses around the total effective magnetic field, which combines the static external field $\vec{B}_{\text{ext}}$ along z with the time-dependent drive field $\vec{B}_1(t)$ along x, leading to a spiraling trajectory on the Bloch sphere. **b** Spin trajectory in the rotating frame, where the effective magnetic field lies along x, because the z-component is canceled at resonant conditions. The spin rotates around the x-axis in a circular motion at the Rabi frequency Ω_R.

where $|\Psi(t)\rangle$ and $\left|\tilde{\Psi}(t)\right\rangle$ represent the qubit state in the lab frame and in the rotating frame, respectively, and $U(t)$ is the unitary transformation operator [75]. Applying this transformation to the time-dependent Schrödinger equation yields

$$
\begin{aligned}
i\hbar\partial_t \left|\tilde{\Psi}(t)\right\rangle &= i\hbar\partial_t \left|U^\dagger(t)\Psi(t)\right\rangle && (2.12)\\
&= \left(i(\partial_t U^\dagger(t))U(t) + U^\dagger(t)H(t)U(t)\right)\left|\tilde{\Psi}(t)\right\rangle && (2.13)\\
&= H_{\text{RWA}}\left|\tilde{\Psi}(t)\right\rangle , && (2.14)
\end{aligned}
$$

from which the transformed Hamiltonian H_{RWA} can be identified. Under the condition $B_1 \ll B_z$, the rotating wave approximation (RWA) allows to neglect rapidly oscillating 2ω terms, yielding the effective Hamiltonian [75]

$$
H_{\text{RWA}} = \frac{\hbar}{2}\Delta\sigma_z + \frac{\hbar}{2}\Omega_R\cos(\delta)\sigma_x + \frac{\hbar}{2}\Omega_R\sin(\delta)\sigma_y = \frac{\hbar}{2}\begin{pmatrix} -\Delta & \Omega_R e^{-i\delta} \\ \Omega_R e^{i\delta} & \Delta \end{pmatrix} . \tag{2.15}
$$

Here, $\Delta = \omega_0 - \omega$ denotes the detuning between the driving and Larmor frequencies, and

$$
\Omega_R = g\mu_B B_1/\hbar \tag{2.16}
$$

is the Rabi frequency, which scales linearly with the driving field amplitude B_1 and characterizes the spin rotation rate between its eigenstates. In the rotating frame, under resonant driving ($\Delta = 0$), the static field B_z is canceled and the spin precesses around an axis in the xy-plane, determined by the phase δ. The resulting Bloch sphere trajectory simplifies to a circular motion around the transformed effective magnetic field vector, as illustrated in

Fig. 2.10**b**. An important observation is that arbitrary rotations on the Bloch sphere can be generated by tuning the frequency ω, amplitude B_1 and phase δ of the driving field $\vec{B}_1$ [75]. Such control forms the basis of universal single-qubit control and will be discussed further alongside experimental measurements in Sec. 5.6.

The probability to observe the spin in the eigenstate $|\uparrow\rangle$ after a manipulation of duration t can be calculated by

$$P_{|\uparrow\rangle}(t) = \left|\langle\uparrow|\tilde{\Psi}(t)\rangle\right|^2 . \tag{2.17}$$

Assuming the qubit is initially in the ground state $\left|\tilde{\Psi}(0)\right\rangle = |\downarrow\rangle$, the probability to find the qubit in the excited state evolves as [76]

$$P_{|\uparrow\rangle}(t) = \frac{\Omega_R^2}{\Omega_{\text{eff}}^2} \sin^2\left(\frac{\Omega_{\text{eff}}}{2}t\right) \quad \text{with} \quad \Omega_{\text{eff}} = \sqrt{\Delta^2 + \Omega_R^2}\,. \tag{2.18}$$

The spin-up probability $P_{|\uparrow\rangle}(t)$ exhibits a periodic evolution, known as Rabi oscillations, and on resonance, perfect spin inversion takes place with the Rabi frequency Ω_R. The Rabi frequency Ω_R is typically attempted to be maximized in order to perform as many qubit manipulations as possible within the limited coherence time of the qubit. Further, the spin-up probability $P_{|\uparrow\rangle}(t)$ is the main observable for qubit experiments in this thesis. Readout is generally performed in the absence of the drive field $\vec{B}_1(t)$ so that the external static field $\vec{B}_{\text{ext}}$ defines the quantization axis for projective spin measurement. Details on how the spin-up probability can be determined experimentally will be provided in Sec. 5.1.

Electron spin resonance (ESR)

Having established that an oscillating magnetic field oriented perpendicular to the spin quantization axis enables coherent spin manipulation, the following discussion addresses the physical realization of such fields in solid-state spin qubit architectures.

The most direct method is electron spin resonance (ESR), where the spin is driven by the oscillating magnetic field associated with a high-frequency current. In this approach, microwave pulses are applied to an on-chip waveguide or transmission line located in close proximity to the qubit. When the drive frequency matches the Larmor frequency ($\omega = \omega_0$), coherent spin transitions are induced. The magnetic field generated by a current-carrying wire is given by the Biot-Savart law. For an ideal infinitely long wire carrying a oscillating current $I(t) = I_0 \sin(\omega t)$, the resulting magnetic field is given by

$$B_{\text{ESR}}(t) = \frac{\mu_0 I_0}{2\pi r} \sin(\omega t)\,, \tag{2.19}$$

where μ_0 is the vacuum magnetic permeability (since Si is non-magnetic) and r is the perpendicular distance from the wire [77]. As seen in Eq. (2.19), the drive field scales linearly with the current amplitude I_0 but is inversely proportional to the distance r. Hence, ESR is particularly suitable for SiMOS structures, where quantum dots are located near

the gate electrodes, enabling strong coupling to the drive line.
However, delivering strong microwave currents at $\sim 20\,\mathrm{GHz}$ close to the qubit presents challenges. At these frequencies, conduction is limited to surface currents due to the skin effect [78], requiring comparatively large drive line structures for impedance matching. Moreover, high currents result in ohmic losses in the drive line causing local heating, which can degrade qubit performance and has to be prevented.

Nevertheless, ESR has been successfully implemented across various device architectures. On-chip ESR lines have demonstrated Rabi frequencies as high as 10 MHz in GaAs [54], though more typical values are around 1 MHz in SiMOS devices [22, 79–81]. The SiMOS devices studied in this thesis are operated with ESR, and the integration of the drive line near the qubits is shown in Fig. 2.7**a**.

Electric dipole spin resonance (EDSR)

In Si/SiGe heterostructures, quantum dots are located in a buried quantum well tens of nanometers beneath the gate layers, resulting in weak coupling to transmission lines. To overcome this limitation, electric dipole spin resonance (EDSR) enables spin manipulation via oscillating electric fields applied to gate electrodes.

In EDSR, a microwave voltage $V_1(t) = V_1 \sin(\omega t)$ is applied to a confinement gate, inducing periodic displacement of the quantum dot's center with the frequency ω. Golovach et al. [82] have derived that such a periodic displacement can drive spin transitions by exploiting the spin-orbit coupling of the electron. However, the spin-orbit coupling is weak in highly confined quantum dots in Si [19], which renders intrinsic EDSR impractical. Artificially enhanced spin-orbit coupling can be achieved by moving a spin along a transverse magnetic field gradient, commonly introduced in spin qubit devices using an on-chip micromagnet. A periodic displacement in the presence of such a field gradient translates into an effective oscillating magnetic field that drives spin transitions.

Assuming that the oscillating electric field $E_1(t) = V_1(t)/d$, with the distance d of the gate to the quantum dot, displaces the electron in y-direction, the resultant oscillating magnetic field can be derived as

$$B_{\mathrm{EDSR}}(t) = \frac{e l_{\mathrm{orb}}^2}{E_{\mathrm{orb}}} \frac{V_1(t)}{d} \frac{\partial B_\perp}{\partial y}\,, \tag{2.20}$$

with the orbital splitting E_{orb} of the quantum dot, the orbital length scale l_{orb} and the transverse magnetic field gradient $\partial B_\perp / \partial y$ of the micromagnet [19, 83]. An effective EDSR drive field can be expressed as

$$B_{\mathrm{EDSR}}(t) = \frac{\partial B_{\perp,\mathrm{eff}}}{\partial y} y_0 \sin(\omega t)\,, \tag{2.21}$$

by absorbing all system constants into $B_{\perp,\mathrm{eff}}$ and expressing the drive field as a function of the actual displacement

$$y(t) = -\frac{e E_1(t)}{m^* \omega_{\mathrm{conf}}^2} = y_0 \sin(\omega t)\,, \tag{2.22}$$

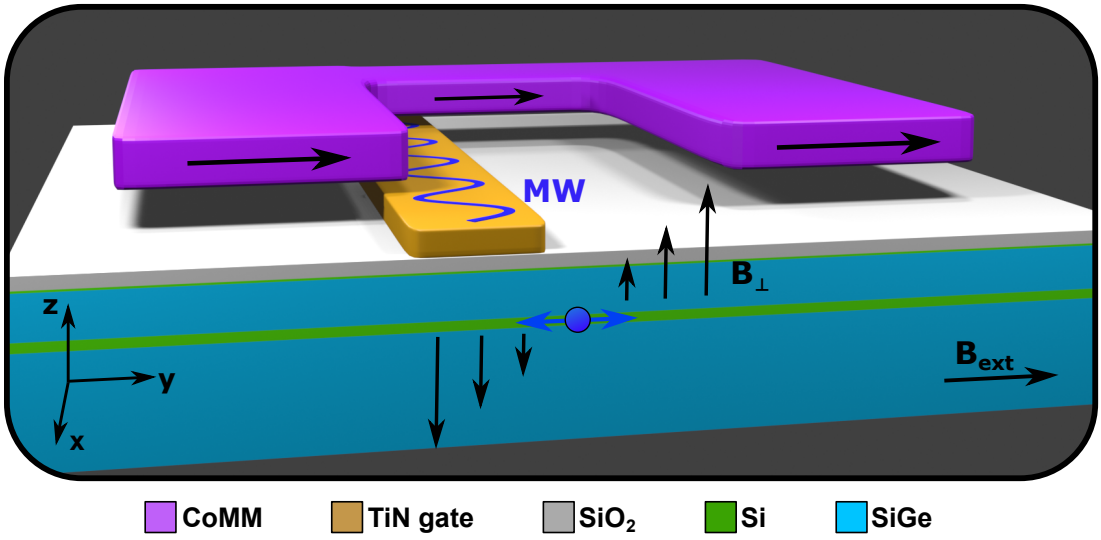

Figure 2.11: Illustration of the electric dipole spin resonance (EDSR) principle, based on the specific gate layout SD15B of the Si/SiGe devices in this thesis. An external magnetic field B_{ext} applied along the y-axis magnetizes the cobalt micromagnet (CoMM) in the same direction. The qubit quantum dot is formed in the silicon quantum well, approximately 120 nm below the center of the 300 nm gap in the CoMM. The micromagnet generates an inhomogeneous magnetic field $B_{\perp}$ within the plane of the Si quantum well. The CC gate is pulsed with a microwave (MW) signal, causing spatial oscillations of the quantum dot in the inhomogeneous magnetic field. The perpendicular component of the field gradient effectively creates a driving amplitude at the same frequency as the microwave signal applied to the CC gate. When this is in resonance with the electron's Larmor frequency, a spin transition can be induced. Adapted from Ref. [24]

with m^* denoting the effective mass of the electron and $\hbar\omega_{\text{conf}}$ being the confinement energy of the quantum dot [19]. As can be seen in Eq. (2.21), the amplitude of $B_{\text{EDSR}}(t)$ depends linearly on the displacement amplitude y_0, given by the microwave voltage amplitude, and the effective magnetic field gradient $\partial B_{\perp,\text{eff}}/\partial y$, governed by the design of the micromagnet.

The principle of EDSR is illustrated in Fig. 2.11 based on the Si/SiGe device architecture used in this thesis. The external static magnetic field applied along the y-direction defines the quantization axis of the electron spin and magnetizes the C-shaped cobalt micromagnet (CoMM). The qubit is formed beneath the micromagnet's gap, experiencing an inhomogeneous magnetic field. A microwave pulse applied to the central confinement gate (CC) causes the quantum dot to oscillate within this field, resulting in an effective oscillating magnetic field $B_{\perp}(t)$ that can induce spin transitions when resonant with the Larmor frequency.

EDSR was initially demonstrated in GaAs devices, where strong intrinsic spin-orbit coupling enabled Rabi frequencies up to 4.7 MHz [84]. In silicon, where intrinsic spin-orbit coupling is eight times weaker [19], comparable manipulation speeds have been achieved by incorporating micromagnets that generate strong transverse magnetic field gradients [85]. Optimized micromagnet designs have demonstrated gradients up to 1.6 mT/nm [86], enabling Rabi frequencies as high as 35 MHz with typical quantum dot displacements

on the order of 1 nm [25, 87]. In addition to enhancing drive strength, micromagnets enable frequency-selective qubit addressing via engineered longitudinal field gradients. Asymmetric geometries can yield resonance frequency splittings between adjacent qubits of up to 2.5 GHz [88], addressing a key scalability challenge in ESR-based systems.
However, micromagnets also introduce sensitivity to charge noise due to spatial magnetic field variations, limiting qubit coherence times [25]. The micromagnet integration further complicates fabrication, as ferromagnetic materials like cobalt require careful handling to avoid contamination. Notably, imec has implemented the monolithic integration of cobalt micromagnets within its industrial 300 mm-wafer process line [64]. The micromagnet geometry of the SiGe samples in this work was optimized in simulations to maximize the coupling strength, while minimizing the spin dephasing caused by the micromagnet field gradient [70].

In conclusion, both ESR and EDSR enable coherent spin manipulation by generating an oscillating magnetic field transverse to a static Zeeman field. When driven at the Larmor frequency, the spin undergoes Rabi oscillations, forming the basis for quantum gates. Precise control over the drive amplitude, duration, and phase allows for arbitrary single-qubit rotations, completing the fundamental toolbox for silicon spin qubits.

3 Experimental Setup

This chapter provides an overview of all necessary constituents to perform quantum experiments on semiconducting qubit devices. It starts with a description the custom-built He^3/He^4-dilution refrigerator and the cryogenic setup inside. The chapter further provides details on the printed circuit board (PCB) which hosts the sample and allows to connect it electrically. Next, the electronic setup is presented including the cabling and filtering of electrical lines followed by details on measurement and manipulation electronics. The chapter concludes with a brief discussion on IQ mixing and its application in this thesis.

3.1 Dilution refrigerator

Cryogenic temperatures are essential for resolving low-energy quantum phenomena that would otherwise be masked by thermal excitations. For example, the Zeeman energy splitting of an electron with $g = 2$ in an external magnetic field of 0.75 T is given by $\Delta E_Z = g\mu_B B \approx 87\,\mu\text{eV}$, which corresponds to a thermal energy of $k_B T$ at approximately 1 K. This highlights the need for sub-Kelvin operating temperatures to ensure reliable qubit initialization, manipulation, and single-shot readout.

To achieve such conditions, ^{3}He/^{4}He dilution refrigerators are employed, as they provide continuous cooling from room temperature down to the millikelvin range. These devices utilize the endothermic process of diluting liquid ^{3}He into liquid ^{4}He, which occurs even at 0 K. By evaporating ^{3}He from this mixture and returning it to the mixing chamber, the refrigerator can be operated continuously. A detailed account of the dilution refrigeration process is provided in [89].

The experiments in this thesis were conducted using a Sionludi refrigerator comparable to the now commercially available Qinu XL cryostats [90]. The name “Sionludi” is derived from a phonetic inversion of the word "dilution," reflecting the design’s unconventional orientation of temperature stages. This system features an inverted configuration of thermal stages with the mK-plate on top of the arrangement, differing from conventional dilution refrigerators. With compact dimensions of approximately 42 cm in diameter and 50 cm in height, the system allows convenient experimental access and integration of supporting hardware. A major innovation of the Sionludi cryostat design is the fast injection line, which enables direct precooling of the mixing chamber via 4 K cold mixture circulation and leads to significantly reduced cooldown times. Typical performance metrics of the system include a base temperature of 30 mK, a cooling power of up to 300 µW at 100 mK, and a cooldown duration of 9 h until base temperature. Full warm-up of the system

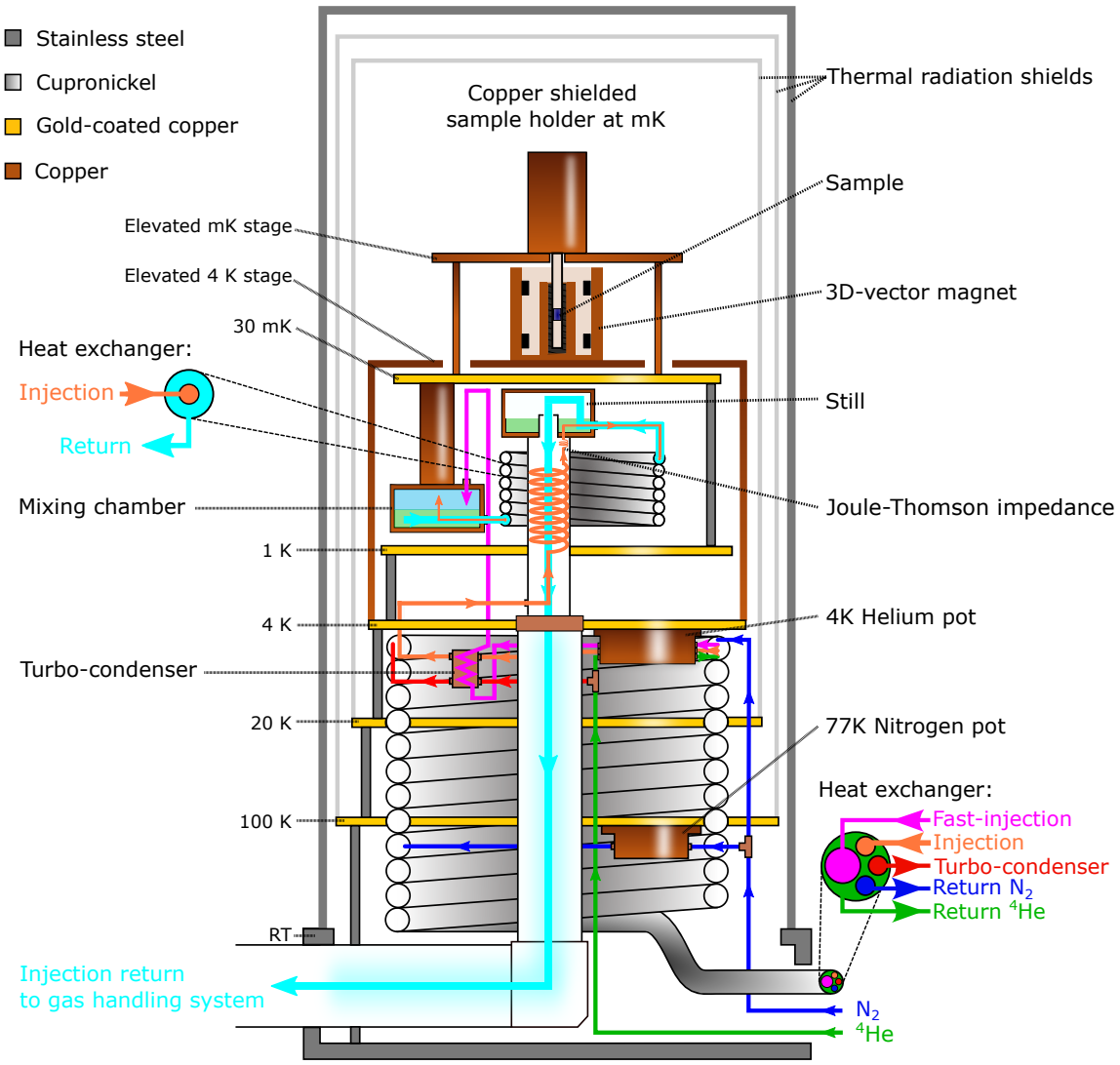

Figure 3.1: Schematic representation of the Sionludi dilution refrigerator nicknamed “Obelix”. Distinct features of Obelix are the additional liquid N_2 lines, the elevated 4 K stage that hosts the superconducting 3D-vector magnet, and the elevated mK stage that is compatible with a fast-exchangeable sample holder.

to room temperature can be achieved within 2 h by introducing ^{4}He exchange gas into the isolation vacuum and heating of the outer-most shield. A detailed technical discussion of these custom-built Sionludi cryostats is presented in [91].

The customized dilution refrigerator used in this work, named "Obelix", is illustrated in Fig. 3.1 and incorporates several unique design features. The cryostat can be divided into two functional units, each with an independent cooling cycle. The precooling unit, located below the 4 K stage, is responsible for cooling the 4 K, 20 K and 100 K temperature stages down to operational temperatures. This is achieved by supplying liquid helium to the 4 K pot and distributing the cooling power through a counter-flow heat exchanger, where the returning gaseous ^{4}He cools the injected ^{3}He/^{4}He mixture to approximately 4 K. The precooled mixture then passes through the turbo-condenser, where it is further cooled

to approximately 3 K, and is subsequently liquefied in the Joule-Thomson stage before entering the dilution unit above the 1 K plate. In normal operation the precooled mixture is injected into the mixing chamber and distilled ^{3}He is continuously evacuated from the still by pumping and subsequently resupplied to the circulation loop. It shall be emphasized that the ^{3}He/^{4}He circuit is fully independent from the ^{4}He precooling circuit.
When the precooling cycle is operated with liquid ^{4}He from a 100 l helium can, Obelix consumes 19 l/day in normal cryogenic operation, requiring the replacement of the helium can every 4 to 5days. The first unique design element of Obelix is the liquid nitrogen supply line connected to the 4 K and 100 K stages. The total enthalpy difference between 1 l liquid N_2 at melting temperature and the same molar volume in gaseous form at room temperature is about 1.8 times larger than the same enthalpy difference of helium. In practical terms, every liter of supplied liquid nitrogen provides the same cooling capacity as 1.8 l of liquid helium. Consequently, by supporting the precooling unit with liquid nitrogen, the helium consumption of Obelix can be significantly reduced to about 13 l/day, extending the can exchange interval to 6 days. The nitrogen supply to the 4 K stage is only effective during the cool down of the cryostat and will automatically shut down as soon as the 4 K stage drops below the melting temperature of nitrogen at 77 K and the liquid nitrogen freezes solid in the upper branch.

A second distinct feature of Obelix is the elevated 4 K stage positioned above the mK-stage. This design facilitates the integration of a superconducting 3D vector magnet directly into the experimental space, while taking advantage of the higher cooling power in the range of 10 W available at the 4 K stage. Thermalization of the superconducting coils at the 4 K stage is significantly more efficient than at the mK-stage, resulting in faster overall cooldown times. Moreover, the increased cooling capacity enables higher magnetic field ramping rates, as it can more effectively dissipate the heat generated by eddy currents during rapid field changes, and accelerates the reestablishment of operational temperatures after a magnet quench.

The last distinguishing feature is the elevated mK-stage that was developed to use in combination with a fast-exchangeable shielded sample holder, named the "Quickswap" system. As the name suggests, this system allows a PCB-mounted sample to be exchanged within minutes. Electrical connections to the cryostat wiring are achieved via SMP (sub miniature push-on) and split-PCI (peripheral component interconnect) connectors that plug into corresponding sockets at the elevated mK stage, while mechanical stability is ensured by three 4 mm banana plugs fitting into dedicated hollow bars. This Quickswap system permits sample preparation in parallel to cryostat operation, minimizing downtime during sample exchange.

Photographs of the experimental setup above the mK stage and the Quickswap sample holder are provided in Fig. 3.2. The image in panel **a** displays the experimental volume where the elevated 4 K plate (3) carries the 3D vector magnet (5) in the center and the corresponding thermal anchor for superconducting current supply lines (4). Below, the mK stage (1) and attached DC line filter boxes (2) can be seen. The elevated mK plate (7) on the top houses the Quickswap system (8) which is installed upside-down. The cold finger of the sample holder, containing the mounted sample, is inserted into a copper tube which

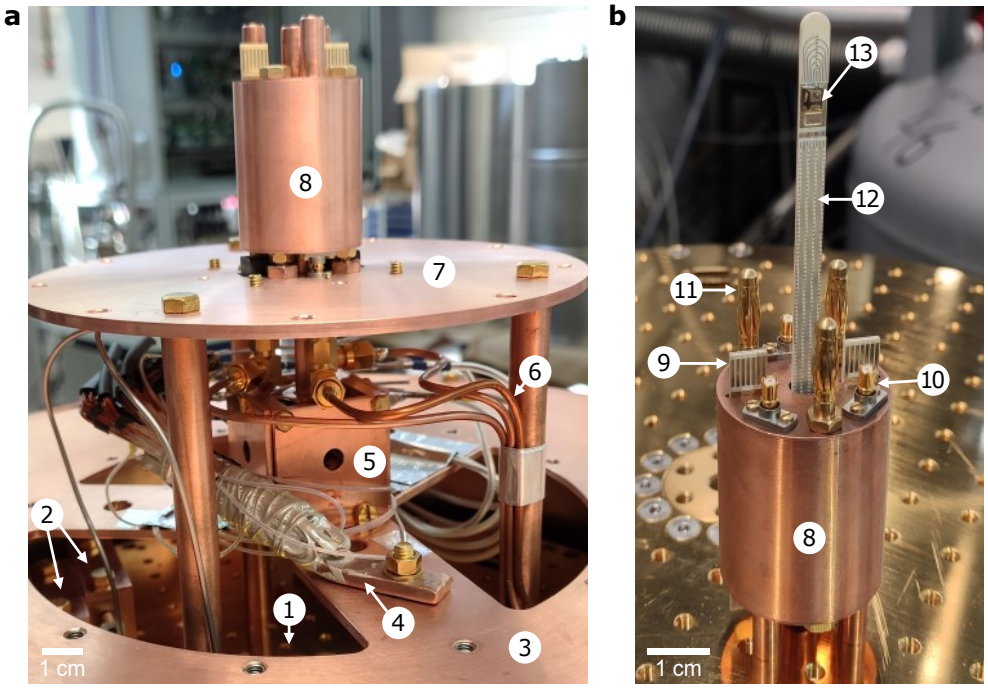

Figure 3.2: a Photograph of the experimental volume above the mK stage. 1: mK state, 2: First DC line filtering stage at mK, 3: Elevated 4 K stage, 4: Thermal anchor for superconductor current supply lines for the vector magnet, 5: Superconducting 3D vector magnet, 6: Coaxial copper cables for three RF lines, 7: Elevated mK stage, 8: Copper radiation shield of the Quickswap system. **b** Detailed view of the Quickswap sample holder. 8: Copper radiation shield for the second DC line filtering stage inside, 9: Double-sided split-PCI connectors for 24 DC lines, 10: Three SMP connectors for RF lines, 11: Banana plugs for mechanical stability, 12: Cold finger of sample PCB, 13: Sample space.

extends below the elevated mK stage into the central bore of the vector magnet assembly, such that the sample is located at the center of the magnet assembly. The Quickswap sample holder is shown in detail in Fig. 3.2**b**. Its copper radiation shield (8) encloses the internal second-stage DC line filters integrated into the sample PCB, which will be detailed in Sec. 3.2. Electrical connections are interfaced via double-sided split-PCI connectors (9) for 24 DC lines and three SMP connectors (10) for RF lines, with mechanical support provided by three banana plugs (11). The cold finger (12) of the sample PCB routes all electrical connections toward bonding pads surrounding the sample space (13) where the glued sample is located.

3.2 Printed circuit board for sample interfacing

The printed circuit board (PCB) used for interfacing the sample with the cryogenic setup was designed by Tino Cubaynes and is shown in Fig. 3.3**a**. The PCB provides 24 DC lines and 3 RF lines. Dedicated pads are integrated into the PCB layout to allow the installation of onboard RC filters for the DC lines. A detailed schematic of the surface mount devices (SMD) that comprise the second-stage DC line filters and the capacitances installed in

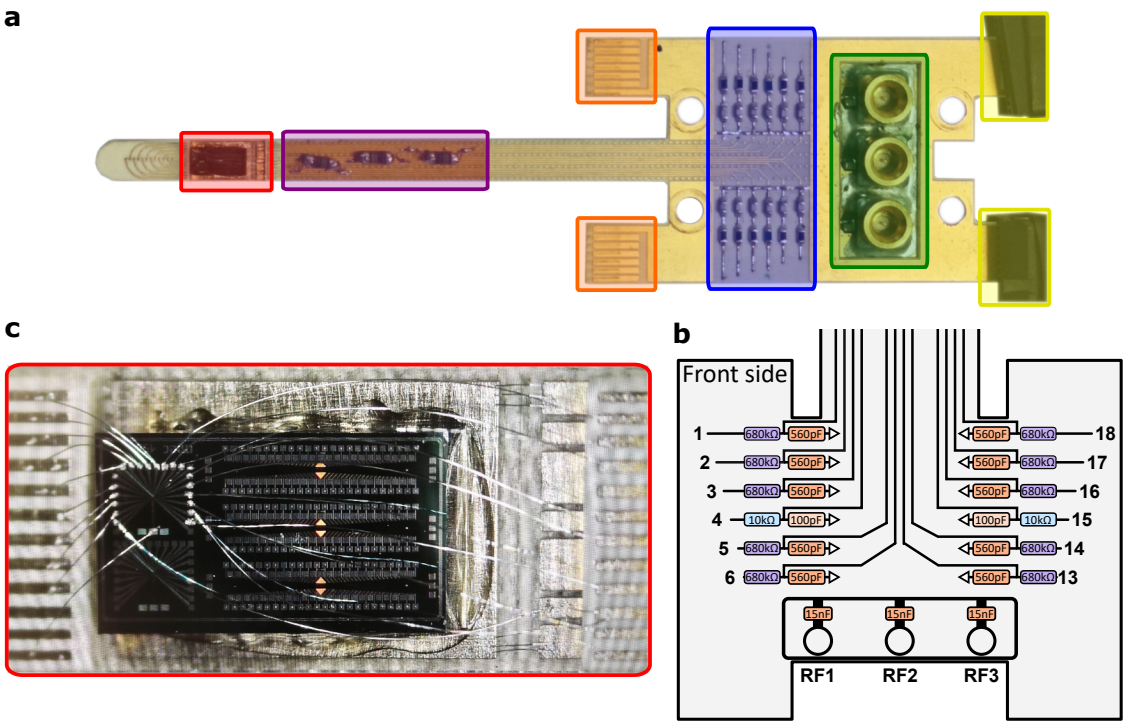

Figure 3.3: a Photograph of the sample PCB with color-coded highlights. The sample space, where the chip is glued and wire-bonded to adjacent RF and DC line ends, is marked in red. The purple region features optional MELF resistors, installed in series with selected DC lines to serve as bias-tee components. The second-stage RC filtering of the DC lines is marked in blue. Orange and yellow highlight the PCI connectors at both ends used to interface the DC lines with internal cryostat wiring. The yellow region additionally shows black connectors that short-circuit all DC lines to common ground when a sample is mounted, preventing electrostatic charge buildup. Green highlights the SMP connectors used to attach external RF lines to the co-planar wave guides on the PCB. **b** Schematic of the surface-mounted components composing the second-stage DC filtering on the front side of the PCB. The same filtering is found on the back side, for the remaining twelve DC lines. **c** Close-up photograph of the 12 mm × 6 mm sample area, showing a glued and wire-bonded Si/SiGe device connected to surrounding RF and DC lines.

series with the RF inner conductor is depicted in Fig. 3.3**b**. The exact filter configuration and cut-off frequencies of the DC lines will be discussed in Sec. 3.3.

Electrical connectivity to the DC lines is established via two sets of split-PCI connectors, featured on both the top and bottom of the PCB. This dual-connector design enables galvanic grounding of the DC lines during installation or exchange, minimizing the risk of sample damage due to electrostatic discharge. The RF lines are connected through SMP connectors and routed to the sample region via three individual coplanar waveguides, designed to support frequencies up to 20 GHz. The sample is positioned at the end of an extended cold finger, ensuring its placement at the center of a 3D vector magnet. It is mounted onto a 12 mm × 6 mm gold-coated copper plate, which can serve either as a back gate or as a ground plane, depending on the experimental requirements. Electrical contact between the sample and the surrounding PCB lines is established via wire bonds to both DC and RF bonding pads encircling the sample area, as shown in Fig. 3.3**c**. Optional resistive bias-tees can be added by soldering a capacitor in series of the inner conductor of

an RF line and a resistor in series with the corresponding DC line. Close to the sample, the RF and DC lines are joined by wire bonds to complete the bias-tee configuration. As shown in Fig. 3.3**a**, bias-tees are installed on all three RF lines to be used with DC lines 6,9 and 16. The prepared bias-tees consist of 15 nF SMD capacitors and 10 MΩ metal electrode leadless face (MELF) resistors. However, no bias-tees have been employed in this thesis.

A peculiar property of this PCB is the presence of parasitic capacitive coupling between the RF and DC lines, with the coupling strength strongly dependent on their distance. The most pronounced couplings occur between RF1 and DC6, and between RF3 and DC13. This phenomenon, validated across multiple PCBs and samples [24], can be used to an advantage. Specifically, we utilize the coupling between RF3 and DC13 by connecting DC13 to the CC gate in the SD15B gate layout. This allows the RF signal to be capacitively coupled into the gate without a direct wire bond from RF3, thereby galvanically isolating the RF line from the sample. This isolation substantially reduces sample heating during microwave manipulation, which we attribute to the elimination of direct thermal contact between the sample and the last RF attenuator at the millikelvin stage, a known source of elevated electron temperature. Consequently, significantly higher microwave powers can be applied via the capacitive path, enabling faster qubit manipulation without thermal limitations. This parasitic coupling, which we fondly named the "Ghost line" in recognition of its beneficial impact, has since been routinely used to improve qubit control performance.

3.3 Cabling and filtering

The dilution cryostat is equipped with 48 DC lines and 6 RF lines. Each DC line consists of superconducting NbTi filaments embedded in a constantan matrix with a total wire diameter of 100 µm. The DC lines are bundled in groups of 12, embedded in Apiezon grease, and routed through a CuNi capillary with an outer diameter of 1.7 mm. The Apiezon grease prevents insulation damage by reducing friction during assembly and may also enhance thermalization between the wires and the CuNi capillary. The capillary is later galvanically connected to ground, providing electromagnetic shielding and mechanical stabilization.

The DC lines are filtered at millikelvin temperatures by two-stage RC low-pass filters, achieving combined cutoff frequencies of 250 Hz for static voltage gates ("slow" lines) and 60 kHz for DC lines used in current measurements and plunger gate control ("fast" lines). The source and drain contacts, as well as the two qubit plunger gates, are connected to fast DC lines to enable shorter signal rise times and fast plunger pulsing. Each line is also equipped with an LFCN-80+ SMD band-pass filter, providing additional mid-frequency filtering between 225 MHz and 4500 MHz. A schematic of the filter configurations and the passive components used is shown Fig. 3.4**a** and **c**. The LFCN-80+ and the first RC filter stage are soldered onto a dedicated filter PCB, enclosed in a copper housing and thermally anchored to the 30 mK stage. The second-stage RC filters are soldered directly onto the sample PCB, as illustrated in Fig. 3.3**a**.

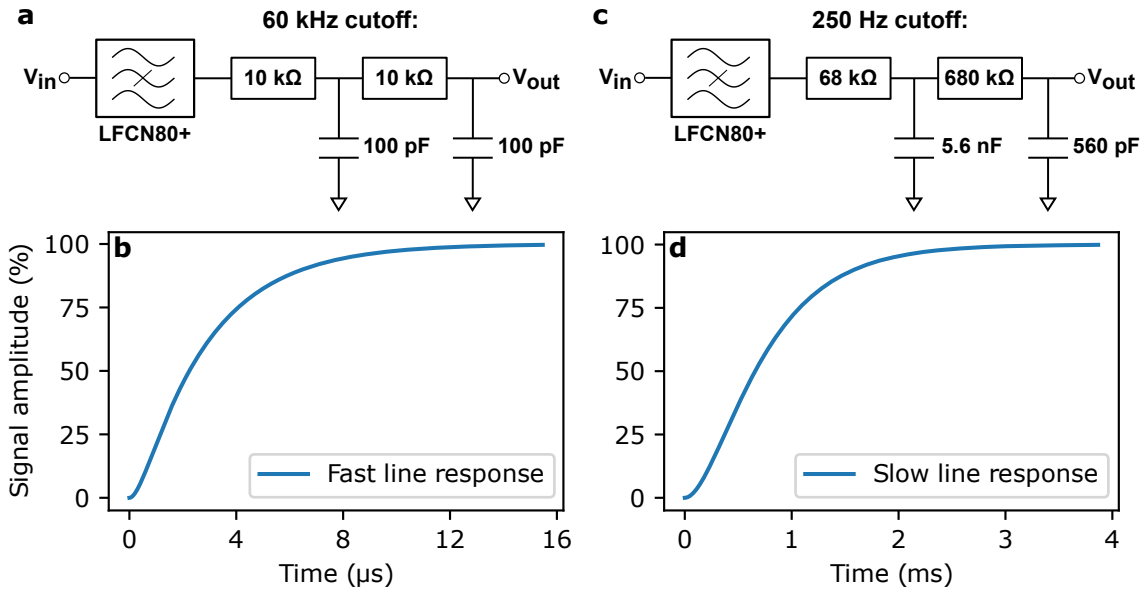

Figure 3.4: DC filter configurations and signal rise times. Each DC line is filtered at mK temperatures using a combination of LFCN-80+ SMD bandpass filters, first-stage RC filters mounted in a copper box at the lower mK stage, and second-stage RC filters located on the sample PCB. **a** Schematic of the fast DC line filter configuration with a cutoff frequency of 60 kHz, used for plunger gate pulsing and current readout. **b** Simulated response of a fast line to a rectangular voltage pulse, with a rise time of 7.6 µs. **c** Schematic of the slow DC line filter configuration with a cutoff frequency of 250 Hz, used for static gates. **d** Simulated response of a slow line to a rectangular voltage pulse with a rise time of 1.8 ms.

The signal rise time is critical for time-resolved experiments. As shown in Fig. 3.4**b** and **d**, slow and fast lines respond in different time scales to a rectangular voltage pulse. The characteristic rise times are $\tau = 1.8$ ms for slow lines and $\tau = 7.6$ µs for fast lines. To achieve 99% of the final signal amplitude, a wait time of approximately 10τ is required. Knowledge of the response time is particularly important for two-qubit operations described in Ch. 6.

A total of six RF lines are installed in the cryostat to route microwave signals to the sample. Each RF line is composed of three CuNi coaxial cables: one running from room temperature to the 4 K stage, another from the 4 K to the 1 K stage, and a third from the 1 K stage to the 30 mK stage. A final copper coaxial cable connects the first 30 mK stage to the elevated mK stage. The total attenuation of the three RF transmission lines, measured from the outer SMA connector at the cryostat access window to the SMP feedthrough adapters at the elevated mK stage, is shown in Fig. 3.5 for frequencies up to 20 GHz. Additional RF attenuators of 3 dB, 6 dB, and 10 dB are installed at the 4 K, 1 K, and 30 mK stages, respectively, to reduce noise.

In this work, only RF line 3 was used for qubit manipulation. It is capacitively coupled to DC line 13, which is connected to the central screening gate (CC) of the Si/SiGe sample, as explained in Sec. 3.2. By considering an operating frequency of 19.5 GHz, the actual microwave power arriving at the sample can be estimated by accounting for approximately −28.5 dB of line attenuation and an additional −19 dB due to installed attenuators. The total input power reduction, including the IQ mixer conversion loss, is quantified in Sec. 3.5.

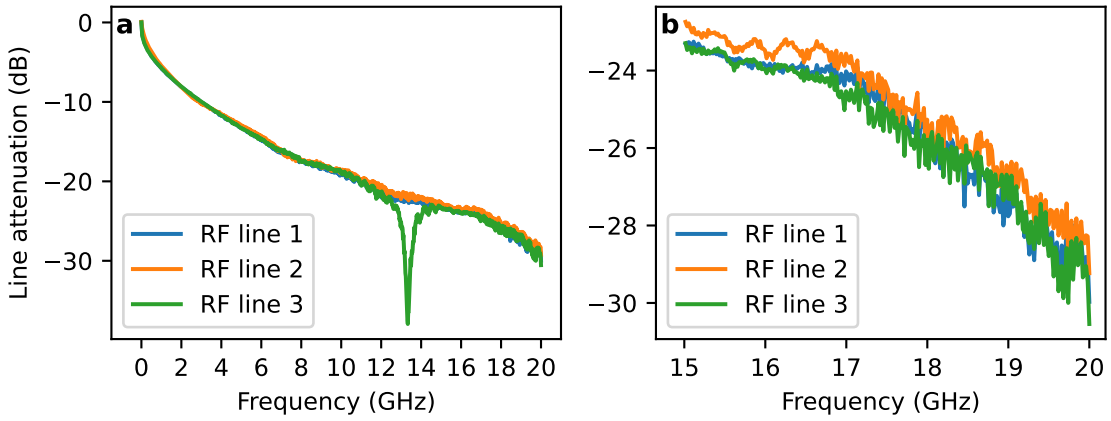

Figure 3.5: Measured attenuation of three commonly used RF lines at room temperature, taken from the external SMA connector at the cryostat access window to the SMP connector at the elevated mK stage. **a** Full frequency range from 10 kHz to 20 GHz. **b** Zoom into the relevant region for qubit operation from 15 GHz to 20 GHz.

3.4 Cryogenic wiring and measurement hardware

A schematic overview of the employed measurement setup for qubit experiments is provided in Fig. 3.6, detailing both the cryogenic wiring and the room-temperature electronics. All DC lines inside the cryostat are routed through an external breakout box and controlled by an Adwin Pro II real-time control system (Jaeger Messtechnik), featuring a voltage resolution of 300 µV. Source-drain currents are converted into voltage signals at room temperature using SP983c current-voltage (IV) converters (Basel Precision Instruments), and subsequently digitized by analogue input modules of the Adwin Pro II with a sampling rate of up to 4 MHz. For the standard amplification setting of 10^9 V/A used in this thesis, the IV converter bandwidth is specified as 1.6 kHz.

Fast voltage pulses for qubit manipulation are generated by a HDAWG arbitrary waveform generator (Zurich Instruments), providing four output channels with a sampling rate of 2.4 GHz. Microwave control of the qubits is performed using an SMW200A vector signal generator (Rohde & Schwarz), which delivers up to 24 dBm output power at frequencies up to 20 GHz. The SMW200A is equipped with an integrated IQ mixer, whose in-phase (I) and quadrature (Q) channels are controlled by two HDAWG outputs. A discussion of IQ mixing and its role in qubit control is provided in Sec. 3.5. All measurement instruments are automated via a laboratory computer running the Python-based *spin-excite* software suite developed by Ferrero [92].

Inside the cryostat, DC wiring is carefully filtered and thermally anchored at various temperature stages. As indicated by the orange and red markers in Fig. 3.6, thermal anchoring is realized using silver epoxy below 3.72 K to avoid the loss of thermal conductivity associated with the superconducting transition of tin. For clarity, only three RF lines and one DC capillary containing 12 DC lines are shown in Fig. 3.6, although the full setup includes four DC capillaries and six RF lines. Each RF line is routed through multiple attenuation

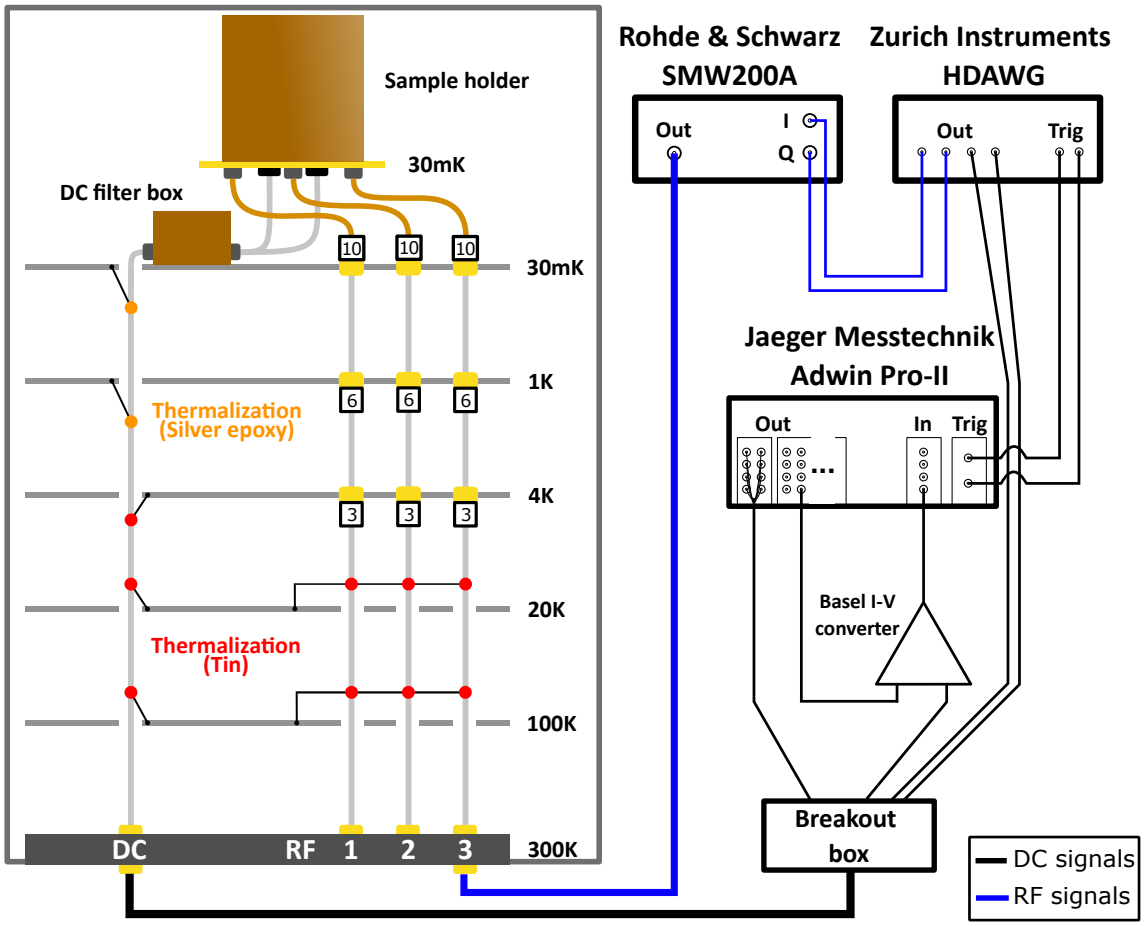

Figure 3.6: Schematic of the employed measurement setup for qubit experiments. On the left, the cryostat is represented with built-in DC and RF lines. The small black-framed boxes represent attenuators, the number inside indicating the attenuation in dB. The orange/red dots represent thermalization of the cables with either silver-epoxy or tin. Silver-epoxy is used for temperatures below 3.72 K, where tin becomes superconducting and drastically less thermally conductive. Only one DC capillary and three RF lines are shown for clarity, but the cryostat is equipped with four such DC capillaries and six RF lines. On the right, the measurement electronics and their interconnections are detailed.

stages at different thermalization points, ensuring both efficient cooling and suppression of high-frequency noise entering the sample environment. This integrated setup enables coherent control of quantum devices while maintaining low-noise and thermally optimized experimental conditions.

3.5 IQ mixing for coherent qubit control

In-phase and quadrature (IQ) mixing played a central role in coherent qubit control presented in this thesis. It enabled precise manipulation of amplitude, frequency, and phase of microwave pulses during the pulse duration, which is beneficial for single-qubit

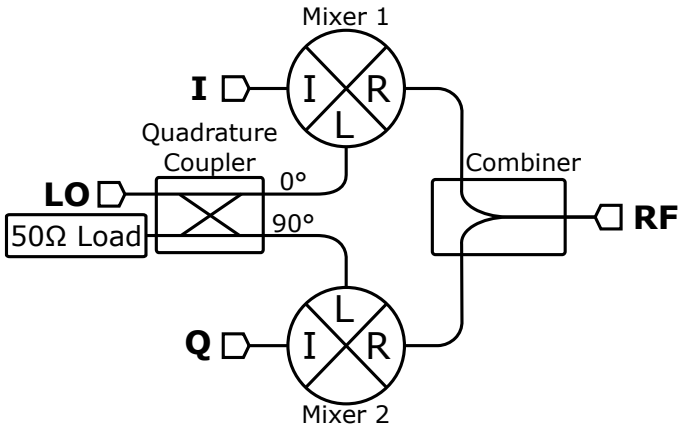

Figure 3.7: Schematic of an IQ mixer consisting of a quadrature hybrid coupler, two matched RF mixers, and an in-phase combiner. The local oscillator (LO) signal at frequency ω_{LO}, is split into two equal-amplitude signals with a 90° phase difference and supplied to the two mixers. By controlling the relative phase of AWG signals at frequency ω_{AWG} supplied to the I and Q inputs, the mixer enables either single- or double-sideband modulation at frequencies $\omega_{\mathrm{LO}} \pm \omega_{\mathrm{AWG}}$. Adapted from [93].

operation but essential for the implementation of two-qubit gates. The following section builds on the comprehensive discussion on IQ mixers in [93].

An IQ mixer is a four-port device comprising two matched mixers, a quadrature (90°) hybrid coupler, and an in-phase combiner. As depicted in Fig. 3.7, the local oscillator (LO) signal, $\cos(\omega_{\mathrm{LO}}t)$, is split into two equal-amplitude signals with a 90° phase difference: $\cos(\omega_{\mathrm{LO}}t)$ and $-\sin(\omega_{\mathrm{LO}}t)$. These signals feed two separate mixers, each receiving baseband inputs labeled I (in-phase) and Q (quadrature-phase) from two channels of the AWG. After mixing, the outputs of these mixers are combined by the in-phase combiner, resulting in the final RF output signal. Assuming an IQ mixer as an perfect frequency multiplier, the resulting RF output can be mathematically expressed as

$$V_{\mathrm{RF}}(t) = I(t) \cdot \cos(\omega_{\mathrm{LO}}t) - Q(t) \cdot \sin(\omega_{\mathrm{LO}}t)\,, \tag{3.1}$$

using the I and Q channel input signals $I(t)$ and $Q(t)$, respectively.

Single- and double-sideband signals

The advantage of IQ mixing lies in its flexibility to generate either single- or double-sideband signals by controlling the relative phase of I and Q input signals. Consider first the case where only the I input is active: $I(t) = \cos(\omega_{\mathrm{AWG}}t)$, and $Q(t) = 0$. Using the trigonometric identity $\cos(x)\cdot\cos(y) = \frac{1}{2}\left[\cos(x-y) + \cos(x+y)\right]$, the output becomes

$$\begin{aligned} V_{\mathrm{RF}}(t) &= \cos(\omega_{\mathrm{AWG}}t) \cdot \cos(\omega_{\mathrm{LO}}t) && (3.2)\\ &= \frac{1}{2}\left[\cos\left((\omega_{\mathrm{LO}} + \omega_{\mathrm{AWG}})\,t\right) + \cos\left((\omega_{\mathrm{LO}} - \omega_{\mathrm{AWG}})t\right)\right]\,. && (3.3) \end{aligned}$$

The resulting signal contains two equal-amplitude sidebands at frequencies $\omega_{\mathrm{LO}} \pm \omega_{\mathrm{AWG}}$, corresponding to standard double-sideband mixing.

In contrast, applying a -90° phase-shifted signal to the Q input, such that $I(t) = \cos(\omega_{\mathrm{AWG}} t)$ and $Q(t) = \sin(\omega_{\mathrm{AWG}} t)$, results in

$$V_{\mathrm{RF}}(t) = \cos(\omega_{\mathrm{AWG}} t) \cdot \cos(\omega_{\mathrm{LO}} t) - \sin(\omega_{\mathrm{AWG}} t) \cdot \sin(\omega_{\mathrm{LO}} t) \tag{3.4}$$

$$= \cos\left((\omega_{\mathrm{LO}} - \omega_{\mathrm{AWG}})\, t\right) \,. \tag{3.5}$$

In this configuration, known as single-sideband (SSB) mixing, one of the sidebands is eliminated by precise cancellation, as the 90°-shifts in LO and baseband signals create a total 180° phase difference. As calculated, a phase shift of -90° results in SSB frequency down-conversion and yields a single frequency at $\omega_{\mathrm{LO}} - \omega_{\mathrm{AWG}}$.

A key advantage of IQ mixers is their ability to rapidly switch between upper and lower sidebands by adjusting the relative phase between the in-phase (I) and quadrature (Q) signals. At the AWG sample rate of 2.4 GHz, this sideband selection can be controlled on a sub-nanosecond timescale. Specifically, reversing the sign of the quadrature signal $Q(t)$ allows to switch between the upper and lower single sideband

$$V_{\mathrm{RF}}(t) = \cos\left((\omega_{\mathrm{LO}} \pm \omega_{\mathrm{AWG}})t\right) \,. \tag{3.6}$$

The choice of phase difference (±90°) between the I and Q inputs directly determines which sideband is suppressed and which remains. This technique is essential for two-qubit operations, allowing rapid frequency switching during pulse sequences without altering the LO frequency itself.

Output amplitude control in single-sideband mixing

In SSB mixing, the amplitude of the resulting RF signal is determined by the combined influence of the LO amplitude and the amplitudes of the I and Q baseband inputs. The RF output power P_{RF} of an ideal mixer scales as

$$P_{\mathrm{RF}} \propto A_{\mathrm{LO}}^2 \cdot A_{\mathrm{AWG}}^2 \,, \tag{3.7}$$

where A_{LO} is the LO signal amplitude and A_{AWG} denotes the common amplitude of the I and Q modulation signals. This relationship allows dynamic power tuning either through the LO or baseband inputs, enabling per-qubit adjustment of drive strength during a pulse sequence.

Experimental characterization

An experimental validation of SSB mixing performance is presented in Fig. 3.8**a**. In this measurement, a Rohde & Schwarz microwave generator provides an 18 GHz LO signal at a nominal power of 6 dBm. This signal is mixed with 150 MHz modulation signals from the AWG of 1 V amplitude and a relative I-Q phase shift of -90°. The RF output from the

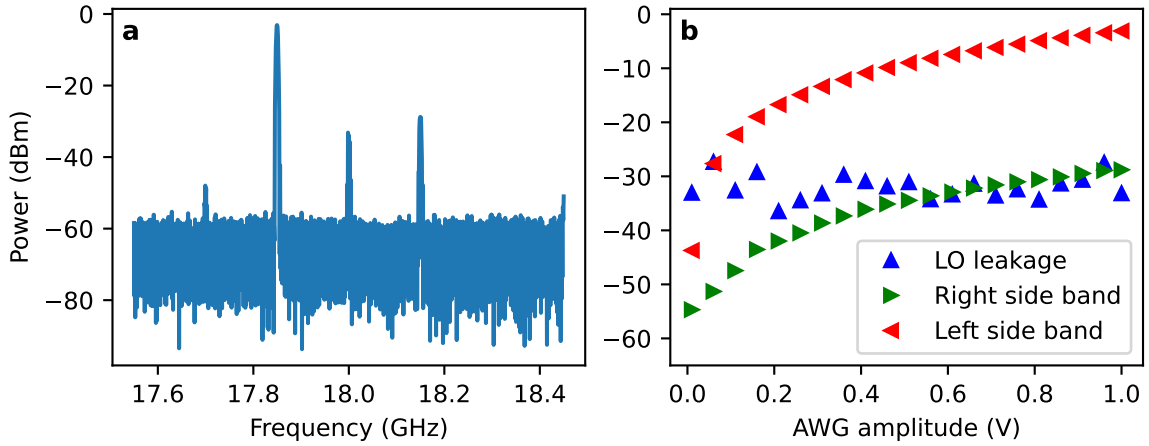

Figure 3.8: Measured output of IQ mixing using a 6 dBm LO signal at 18 GHz and a 150 MHz modulation signal applied to the IQ channels with a -90° phase shift. **a** Frequency spectrum at 1 V AWG amplitude showing the enhanced single-sideband at $f_{LO} - f_{AWG} = 17.85$ GHz along with LO leakage at $f_{LO} = 18$ GHz, the suppressed upper sideband at $f_{LO} + f_{AWG} = 18.15$ GHz and a residual peak from higher-order mixing at $f_{LO} - 2f_{AWG} = 17.7$ GHz. **b** Dependence of the signal power on the modulation amplitude from the AWG for the three main peaks. The both sidebands show a monotonic increase in output power, confirming the quadratic dependence on IQ amplitude, while the LO leakage remains nearly constant.

internal IQ mixer is fed directly into a Keysight N9010B signal analyzer to obtain the shown frequency spectrum with four distinct peaks. The dominant peak at $f_{LO} - f_{AWG}$ is the enhanced sideband used for qubit manipulation, and reaches a measured power of −3 dBm. This indicates a mixer conversion loss of approximately 9 dB under given conditions, which has to be taken into account when converting the LO power to an actual microwave power at the sample. The LO leakage peak at f_{LO} is attenuated by more than 30 dB relative to the enhanced sideband, while the suppressed upper sideband at $f_{LO} + f_{AWG}$ is attenuated by approximately 25 dB. The weakest feature at $f_{LO} - 2f_{AWG}$ arises from higher-order mixing effects and is attenuated by more than 40 dB, making it negligible in practice.

Additional peaks in the output spectrum arise from practical limitations of the IQ mixer, which deviates from the behavior of an ideal frequency multiplier. However, these spurious components are strongly suppressed, and the mixer effectively isolates the intended single sideband. The degree of suppression at undesired frequencies and particularly suppression of the LO leakage is a critical indicator of IQ mixer performance. While sideband signals are pulsed and time-limited, LO leakage is continuous and can cause constant microwave exposure to the sample. Even off-resonant signals can contribute to dielectric losses and heating which degrades qubit coherence and gate fidelity. Effective LO suppression, as demonstrated here, is therefore essential to minimize thermal load and optimize qubit control.

In quantum experiments, achieving fast qubit operations within limited coherence times requires maximizing RF drive strength. However, increasing power typically raises LO leakage and associated thermal effects. A practical approach to balance these competing requirements is to use the AWG modulation amplitude as a tunable control. This method

permits nanosecond-scale power modulation during a microwave burst, bypassing the latency associated with direct LO control. The measured dependence of RF output power on the AWG amplitude is shown in Fig. 3.8**b**. The main peak power scales quadratically with AWG amplitude, while the LO leakage remains unaffected. This feature enables an increase of up to 9 dB in drive power by using 1 V IQ modulation compared to the nominal 0.35 V input specified by the manufacturer. While further gains may be achievable up to the ±2 V damage threshold of the IQ mixer inputs, this was not pursued due to the associated risk. Unless explicitly stated, all qubit manipulations were performed using an IQ modulation amplitude of 1 V. Based on this configuration, the total microwave power attenuation from the internal LO source to the sample at 18 GHz is estimated to be 54 dB, comprising 9 dB of IQ mixer conversion loss, 26 dB attenuation along the RF3 line (cf. Fig. 3.5), and additional 19 dB RF attenuators (cf. Fig. 3.6) within the cryostat.

In summary, IQ mixers are valuable tools to generate and modulate microwave signals with high temporal resolution and tunability. Their versatility is particularly advantageous in spin qubit experiments, where precise control over microwave power, frequency, and phase is essential for robust single- and two-qubit gate operations, as will be detailed in Sec. 5.7 and Ch. 6.

4 Device Tuning and Characterization

Establishing a functional set of static gate voltages, the so called working point, is a crucial step in operating gate-defined semiconductor qubit devices. While finding a working point is merely a prerequisite for performing quantum operations, this task can be particularly challenging due to unpredictable but strong influence of individual defect state occupation or charge traps in the quantum dot environment. Therefore, device tuning and working point optimization are among the most important and time-consuming tasks in experimental work. Successful tuning requires a thorough understanding of the device under test as well as constant awareness to sample-specific behavior.

This chapter outlines how a specific gate layout of a semiconducting qubit device can be put to operation. While the methodic approach and systematic formation of functional units are universally applicable, the chapter focuses on Si/SiGe samples by imec with gate layout SD15B, representing the main device architecture in this work. A systematic tuning protocol for spin qubit devices without prior knowledge of characteristic numbers has been developed in our working group and is documented in the thesis of Koch [24]. The following sections provide a supplementary protocol with heuristic adjustments based on prior tuning experience, as is often the case in practice. This mixed strategy is designed to reduce tuning time by leveraging prior knowledge, while accepting increased complexity and the need for careful validation if sample-specific deviations from expected behavior arise. The chapter concludes with the extraction of key device characteristics that can be measured without an external B-field.

4.1 2D electron gas accumulation in the quantum well

The heterostructure and gate layout of the Si/SiGe devices investigated in this thesis have been introduced in Sec. 2.5. As described there, the device features three gate layers with specific purposes. The lowest gate layer contains screening gates dedicated to restrict the 2D electron gas (2DEG) to defined one-dimensional conduction channels. The second layer hosts accumulation gates that are purposed to accumulate mobile charge carriers in the conduction band of the Si quantum well. The third layer comprises barrier gates, which are used later in the tuning procedure to define quantum dots via the formation of tunnel barriers. The SD15B layout supports two conduction channels: a lower channel for the single-electron transistor (SET) and an upper channel for the spin qubits. For brevity, the set of barrier and plunger gates in the upper channel is referred to as "finger gates" due to their appearance.

To establish a stable working point in the Si/SiGe devices of this thesis, several best-practice guidelines should be followed. Most importantly, high voltages on large accumulation gates above the empirical threshold of ∼1 V have to be avoided, as they can induce tunneling into or accumulation of electrons within the Si cap. Occupation of charge traps in the Si cap can be responsible for increased charge noise [94] and degraded operating point stability, often necessitating frequent retuning. Once populated, these traps can only be cleared by large energy inputs, typically requiring a warm-up of the sample to temperatures above 200 K as investigated in the course of the study in Ref. [94]. Second, source-drain currents through the semiconducting channels should be kept below 10 nA at all times to minimize the risk of device damage from strong local heating. Finally, the voltage difference between adjacent gates should remain below 3.5 V to prevent breakdown of the thin SiO_2 insulation layer. The tuning strategy presented here is tailored to reach the working point without excessively overshooting functional gate voltages, especially on the accumulation gates (LTA, RTA, LBA, RBA), as lower operating voltages are believed to be associated with more stable device behavior.

Device tuning at cryogenic temperatures begins with the accumulation of a 2DEG in the silicon quantum well to form conductive paths between the device and its external leads. The goal is to establish two one-dimensional conduction channels: one in the SET channel and one in the qubit channel, as illustrated by the dark blue regions in Fig. 4.1**a**. Source-drain conductance in both channels is monitored using current-voltage (IV) converters, with a 1 mV bias voltage applied. The digitized IV converter output is monitored continuously while sweeping gate voltages.

The first step is to define dedicated conduction channels by tuning the screening gates to ∼ 300 mV below the typical accumulation voltage at which conduction sets in in the semiconductor. In practice, all gates are ramped simultaneously to 300 mV to fulfill this condition. The next step is to accumulate a mobile electron gas in the desired conduction channels. A success is marked by the onset of a current of exceeding 100 pA in the SET channel. In practice, the screening gates (CB, CC, CT) remain at 300 mV, while all residual gates are gradually increased to 700 mV or until the current threshold is reached. Typically, the SET channel will accumulate first due to the larger gate pitch between the CB and CC gates compared to the CC and CT gates of the upper channel. Figure 4.1**b** shows such an experimentally obtained current onset in the SET channel at an accumulation voltage of 0.61 V. Once accumulation is observed, the conduction channel can be solidified by increasing the lower accumulation gates (LBA, RBA) by 30 mV. If the SET current exceeds 3 nA at any point during the tuning procedure, it should be reduced to below 1 nA by decreasing the barrier gate voltages (LB, RB), to minimize the risk of damaging the device.

With conduction in the SET channel established, attention shifts to the qubit channel. Since the narrow finger gates are prone to limit conduction in the upper channel, the plunger gates (PL, PR) are positively offset by ∼300 mV and barrier gates (BL, B, BR) by ∼500 mV, based on their expected field effect on the quantum well. This preemptive measure helps identify the lowest accumulation gate voltages (LTA, RTA) required to establish a conductive path in the upper channel, while minimizing risks to device stability

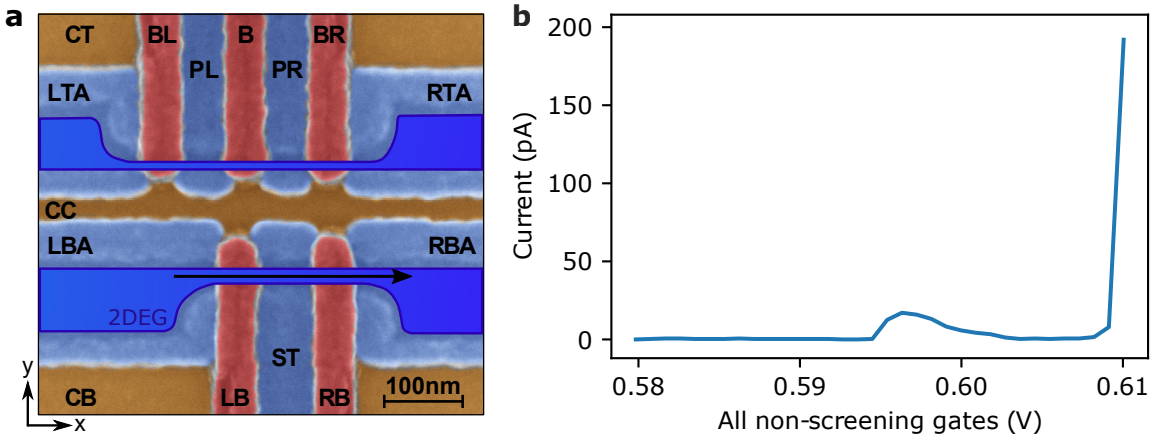

Figure 4.1: a False colored SEM image of the Si/SiGe device gate structure. Dark blue regions indicate accumulated 2DEG areas and established one-dimensional conduction channels after the first tuning stage. **b** First current onset in the SET channel at an accumulation voltage of 0.61 V. The small preceding peak likely resembles a weak Coulomb oscillation and indicates that the conduction channel is limited by the barrier gates. The voltage ramping of all non-screening gates is halted automatically once the measured current exceeds 100 pA at 1 mV bias.

associated with overbiasing the large accumulation gates. The narrow finger gates can be increased well beyond 1 V without stability concerns, as their small cross-sectional area renders significant tunneling into the Si cap unlikely. The tuning procedure continues by simultaneously increasing all upper accumulation gate and offset finger gate voltages until either the accumulation gates reach 1 V or a current of 20 pA is observed in the upper channel. This low current threshold is sufficient to verify that the upper channel is operational, however, the final working point will require significantly lower finger gate voltages since the quantum dots are intended to operate in single electron occupation rather than in full transmission. If no current is observed up to 1 V at the accumulation gates, the upper screening gate (CT) may be increased up to about 550 mV to facilitate accumulation in the upper channel, while preventing the formation of a conductive channel underneath the CT. As a last resort, the central screening gate voltage (CC) can also be raised to assist accumulation. If no consistent current is observed despite these efforts, a thermal cycle may be required to redistribute obstructive charge traps, after which the tuning procedure should be restarted using the conventional method outlined in Ref. [24].

Once current is observed, it is helpful to confirm that the conduction path lies beneath the finger gates. This is done by sweeping down each individual finger gate voltage and checking whether the conduction channel can be pinched off or at least significantly influenced. The pinch-off voltages provide insight into lever arms and help identify device asymmetries or malfunctioning gates. If the current is unaffected by changes on the finger gates, a leakage path between the SET and qubit channels may exist. In such a case, lowering the central screening gate (CC) typically restores proper channel isolation. With both channels successfully accumulated and controllable via the intended gates, the device has reached the first goal in the tuning process.

4.2 Quantum dot formation and charge sensing

The next goal of the tuning procedure is to establish an SET in the form of a quantum dot in the lower channel to create a proximal charge sensor. Once a sensitive SET is formed, it can be used to detect discrete charge changes in the charge state of the quantum dots formed in the upper channel, allowing to tune them into the single-electron regime.

Since all gates in the device layout influence the potential landscape in the quantum well, it is beneficial to decrease all upper barrier gate voltages (BL, B, BR) to their individual pinch-off voltages or by a generic value of 500 mV in order to reduce the number of SET tuning iterations.

A quantum dot in the lower channel is formed by first identifying the individual pinch-off voltages of the barrier gates (LB, RB) and then setting them to these voltages. Subsequently, the current through the lower channel is reestablished by increasing the SET top gate voltage (ST) until a current of ~500 pA is observed. By continuing to iteratively suppress the conduction with the BL and BR barrier gates and reestablishing it with the ST gate, the SET regime is obtained when Coulomb oscillations are observed in the source-drain current, as depicted in Fig. 4.2**b**. Upon reaching this signature the accumulated 2DEG region should now be distributed as visualized in Fig. 4.2**a**.

To ensure balanced coupling between the SET and both source and drain reservoirs, a two-dimensional sweep of LB and RB is performed while recording the SET current. The sweep spans ~200 mV and should encompass the individual pinch-off voltages of both barrier gates. The resulting graph, depicted in Fig. 4.2**c**, displays Coulomb oscillations in the barrier-barrier gate space due to cross-capacitive coupling of the barrier gates onto the SET quantum dot levels. A good SET working point (WP) is located at the center of a well-isolated oscillation, where the tunnel barriers provide symmetric coupling to source and drain, as indicated by the green marker. The quality of the chosen working point can be assessed by measuring the SET current as a function of the ST gate voltage, as shown in Fig. 4.2**d**. An ideal SET for qubit readout features well-separated, symmetric and sharp Coulomb peaks with low off-peak conductance. The current-voltage response of Coulomb oscillations is used to transduce small electrostatic changes in the SET's environment into a measurable current signal. While any point on the slope of a Coulomb peak can be used for charge sensing, the highest sensitivity is achieved at the steepest part of the oscillation flank. However, for practical charge sensing, broader Coulomb peaks with finite off-peak conductance are often preferred, as they provide sensitivity across a wider range of electrostatic conditions. As introduced in Sec. 2.6, the shape of Coulomb oscillations strongly depends on the applied source-drain bias. In Fig. 4.2**d**, the bias is optimized for charge sensing and features a large sensitive gate voltage range, defined as the region where the current derivative is nonzero.

In the next step of the tuning protocol, the formed SET is employed as a charge sensor to monitor electron occupation events in the two adjacent quantum dots. A good starting point is already established by setting the barrier gates in the upper channel to their respective pinch-off voltages. The search for discrete charge jumps is performed by

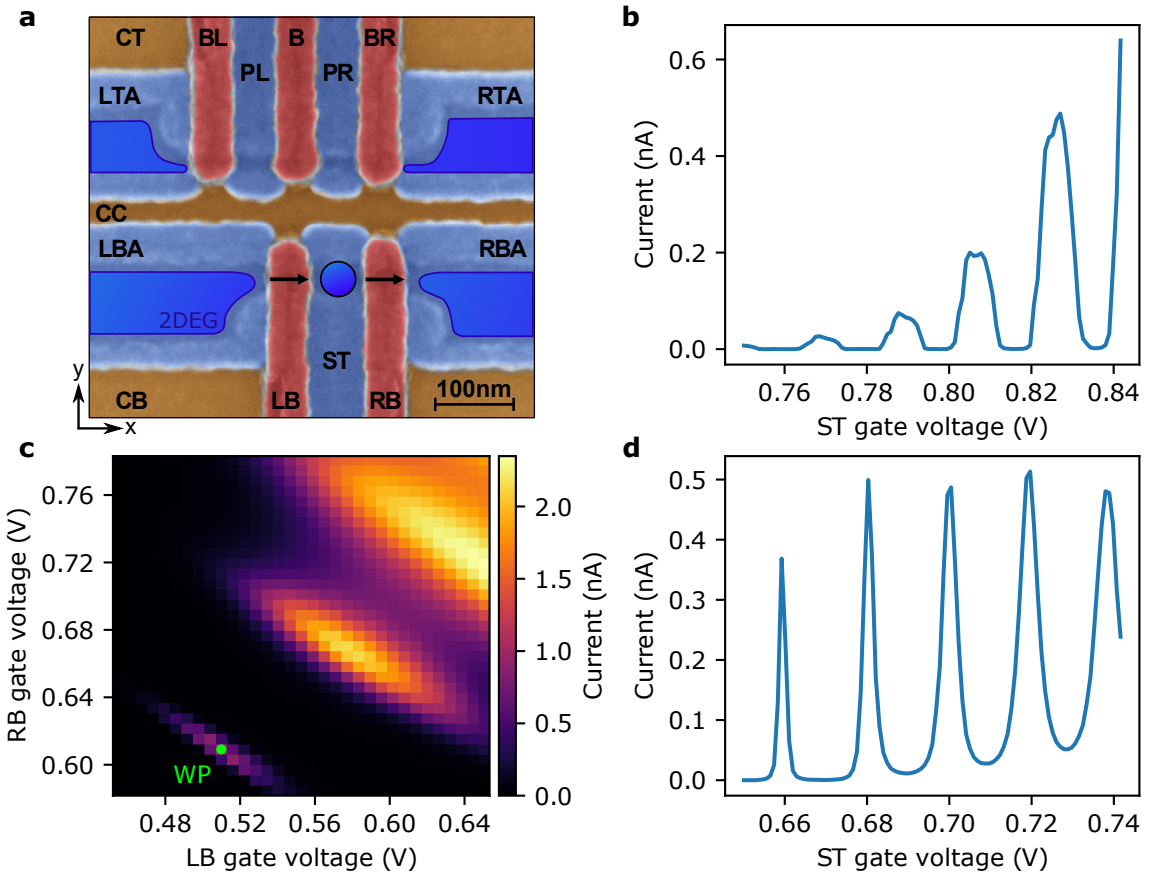

Figure 4.2: **a** False colored SEM image of the Si/SiGe device gate structure. Dark blue regions indicate the 2DEG areas accumulated during this tuning stage. The SET quantum dot is formed underneath the ST gate, with the arrows indicating a source-drain current through the dot. **b** Source-drain current as a function of the ST gate voltage, showing the first appearance of Coulomb oscillations and confirming successful SET formation. **c** SET current as a function of both barrier gate voltages (LB, RB). The observed Coulomb oscillations arise from capacitive cross-coupling of the barrier gates to the SET dot. The current increases with higher barrier gate voltages due to enhanced electron tunneling through the energetically lowered potential barriers. A suitable SET working point (WP) on an isolated Coulomb oscillation is marked by the green dot. **d** Refined Coulomb oscillations after tuning the source-drain bias to optimize the SET for charge sensing. The broad peaks and finite off-peak conductance ensure sensitivity to electrostatic changes over a wide voltage range.

monitoring the SET current while sweeping both quantum dot plunger voltages (PL, PR) across a large range (e.g. 0.6 V to 1.8 V). It is useful to monitor the conductance of the upper channel during the sweep, as a continuous current above the current detection limit of 1.2 pA indicates that the barrier gate voltages are too high to achieve the desired single-electron regime with a ~1 kHz reservoir coupling. Normally, the plunger-plunger gate sweep is repeated for progressively increased barrier gate voltages until discrete charge transitions are observed as sharp changes in the SET signal. Such transitions manifest as parallel lines in the plunger-plunger gate map, with periodic spacing that reflects the sequential addition of electrons to the quantum dots. Ideally, these features should appear as horizontal and vertical lines, indicating independent charging of the left and right dot, respectively. In practice, a finite capacitive cross-coupling of the plunger

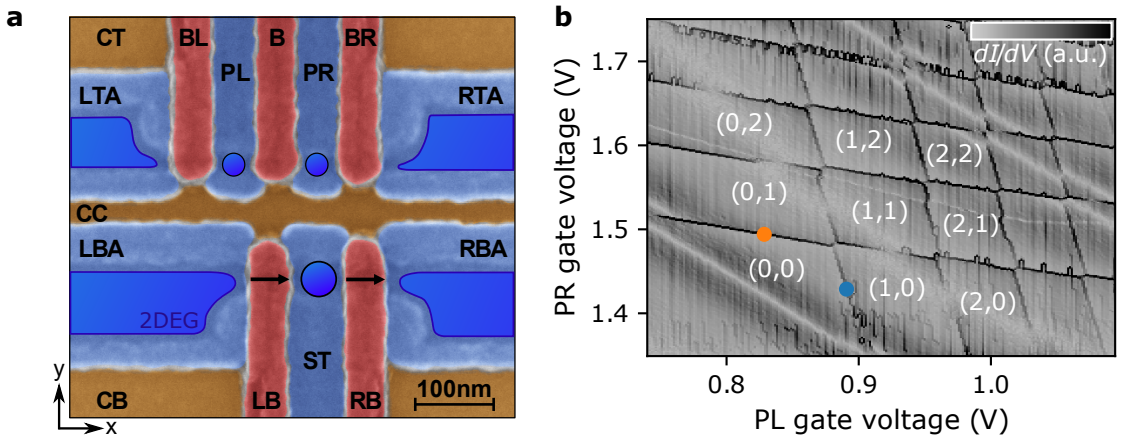

Figure 4.3: a False-colored SEM image of the device gate structure. Dark blue regions indicate areas of accumulated 2DEG and the dots indicate the position of the SET underneath the ST gate and two quantum dots, later used as qubits, under the plunger gates PL and PR. The 2DEG regions under the LTA and RTA gates serve as electron reservoirs for the quantum dots. **b** Derivative of the SET current as a function of the plunger gate voltages (PL, PR). Every straight dark line indicates the tunneling of an additional electron into one of the dots. This double-dot charge stability diagram shows the (0,0) charge state in the bottom left up to the (4,4) state in the top right. The faint white line traversing the graph corresponds to the (un)occupation of a defect state. The blue and orange dots mark single-qubit operation points of the left and right quantum dot, respectively.

gates leads to a slight tilt of the charge transition lines. Further information on charge stability diagrams of double-dot systems are provided in Refs. [53, 95].

Three distinct scenarios can be encountered during this tuning step. First, if charge jumps are absent or appear only along one axis, it is likely that the dots are not sufficiently confined. In this case, decreasing the voltages applied to barrier gates adjacent to the unresponsive dot can induce a stronger confinement. Second, if diagonal lines dominate the map, a single, merged dot has likely formed. This can be resolved by reducing the interdot barrier gate voltage (B) until the dots are separated. The third scenario, and the desired outcome, is the appearance of two sets of nearly orthogonal lines, indicating successful formation of a double-dot system with independent charge control. Once this regime is reached, the individual electron occupancy of each dot can be counted by identifying the plunger gate voltage at which the first charge transition occurs. The resulting 2DEG and dot positions after successful quantum dot formation are visualized in Fig. 4.3**a** and the corresponding charge stability diagram is presented in Fig. 4.3**b**. Here, the derivative of the SET signal is shown to enhance visibility of abrupt changes in current. The diagram reveals up to four charge transitions in each gate direction, with the associated charge configurations labeled as (n,m), where n and m denote the number of electrons in the left and right dot, respectively. A continuous background gradient arises from Coulomb oscillations of the SET, reflecting the capacitive coupling between the plunger gates and the SET dot. A faint white line traversing the diagram, oriented rather horizontally, likely corresponds to a localized charge defect that couples predominantly to the right plunger gate. Such defects can be shifted outside the operating region by identifying gates with strong capacitive influence and adjusting them accordingly. In the present case, increasing

the top screening gate voltage (CT) removed the perturbing state from the (1,1) charge configuration region, which was relevant for two-qubit operations.

With these steps completed, both quantum dots are formed in the single-electron regime and are independently addressable via their respective plunger gates. The SET is tuned to a sensitive regime, enabling the detection of discrete charge transitions. This configuration establishes a well-defined working point for the final device tuning step: the calibration of tunnel couplings, which is addressed in the following section.

4.3 Signal-to-noise ratio and reservoir coupling adjustments

In practice, the first obtained charge diagram rarely appears as presented in Fig. 4.3**b**, as the tunnel coupling of the quantum dots to electron reservoirs, has to be adjusted to the kHz regime in order to match the bandwidth of the measurement electronics.

In this final tuning stage, the source-drain bias across the quantum dot channel is set to zero to ensure stability and avoid perturbations from direct transport, as the system now solely relies on charge sensing. The 2DEGs underneath the accumulation gates (LTA, RTA) are kept accumulated as they continue to serve as electron reservoirs for the quantum dots. The tuning proceeds by approaching a working point near the first electron transition of either quantum dot. In this thesis, single-qubit working points were typically chosen at a detuning of ~50 mV from the $(0,1) - (0,0) - (0,1)$ charge state degeneracy point to investigate isolated qubits in an effective single-dot regime. The corresponding working points for the left and right quantum dots are indicated by the blue and orange markers in Fig. 4.3**b**.

Readout in spin qubit experiments exploits energy-selective tunneling between a quantum dot and its adjacent electron reservoir. The principle relies on aligning the dot's ground state below the reservoir's chemical potential such that only electrons in the ground state remain confined. Excited-state electrons, on the other hand, may tunnel out, allowing the detection of spin-dependent energy levels. Consequently, optimizing the signal-to-noise ratio (SNR) of this charge transition is essential for robust single-shot readout. The SNR is typically defined as

$$\mathrm{SNR} = \frac{|A_\mathrm{H} - A_\mathrm{L}|}{\sigma_\mathrm{H} + \sigma_\mathrm{L}}, \tag{4.1}$$

where A_H and A_L represent the high and low current levels of the SET, and σ_H, σ_L denote their respective standard deviations. This ratio quantifies the high and low current level separation relative to their noise broadening. Enhancing the SNR can be achieved either by increasing the signal amplitude $|A_\mathrm{H} - A_\mathrm{L}|$ or by minimizing the noise sensitivity at the high and low signal amplitudes.

The peak signal amplitude is directly related to the maximum conductance of the SET, which can be enhanced by decreasing its barrier gate voltages to increase tunnel rates, or by raising the source-drain bias. However, this approach has proven to be not optimal in practice, because SET currents exceeding 1 nA have been observed to degrade qubit

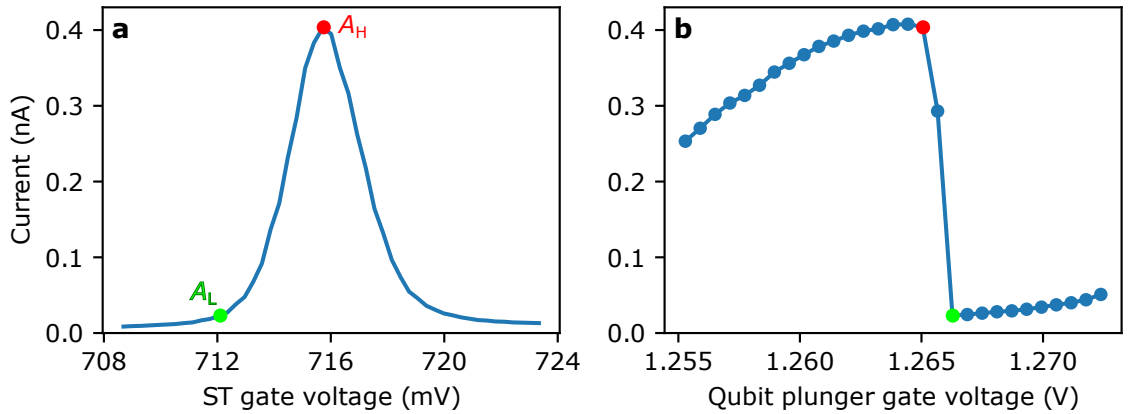

Figure 4.4: a SET current as a function of the SET top gate (ST) voltage, showing a Coulomb oscillation optimized for qubit readout. The peak current is 0.4 nA at a source-drain bias of 10 µV. The red and green markers indicate the high and low current levels corresponding to the high SNR-charge transition in the right panel. **b** SET current as a function of the plunger gate voltage of the dot under test. A charge transition of the right qubit of sample ^{nat}Si/SiGe D09 Die02 is shown with a signal visibility of 0.38 nA. The charge transition causes an SET working point offset from the red to the green marker in panel **a**. The solid line connects the data points and serves as guide for the eye.

coherence, likely due to local heating and charge noise arising from current through the resistive SET path [72, 73]. As a compromise, peak SET currents were limited to approximately 0.5 nA throughout this work. An alternative strategy to improve SNR is to tune the SET such that the high and low signal levels lie at noise-insensitive regions of a Coulomb oscillation, in particular, the peak and the trough between peaks. An example of an optimized high-SNR charge transition for the right dot of sample ^{nat}Si/SiGe D09 Die02 (panel **b**), along with the corresponding Coulomb oscillation (panel **a**), is shown in Fig. 4.4.

Achieving this optimal condition requires aligning the half-width of a Coulomb oscillation with the electrostatic shift caused by a single electron tunneling into or out of the dot. The sharpness of a Coulomb oscillation can be tuned by reducing the SET barrier gate voltages and source-drain bias while maintaining the peak current by increasing the SET top gate voltage. However, the relative spatial positioning of the SET and quantum dots plays a significant role in the observable shift and determines how well this alignment can be achieved. While adjusting the top and bottom screening gate voltages (CT, CB) can bring the SET and dots closer in y-direction (cf. Fig. 4.3), such changes may affect other aspects of the device's performance. Moreover, optimal conditions cannot be achieved for both dots simultaneously, due to the differing distances of the left and right dot from the SET. While this asymmetric design limits the achievable SNR for one of the dots, it also allows to natively discriminate between tunneling events of the left and right dot. In the case of multiple quantum dots, the tuning guideline is to prioritize that the SET current is noise-insensitive and low when an electron is loaded, since qubit manipulation occurs in this regime and local heating or charge noise caused by a high SET current could impact the qubit control fidelity.

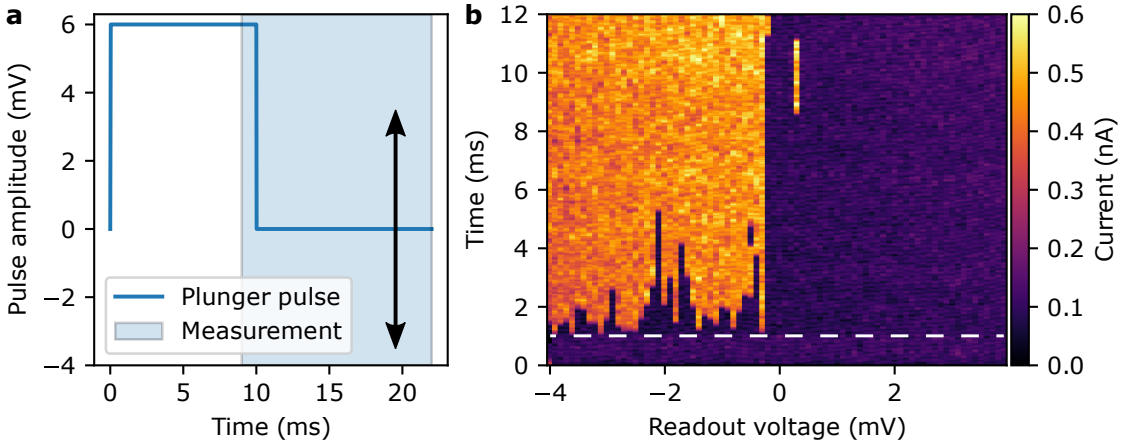

Figure 4.5: a Plunger gate pulse sequence used to assess the reservoir coupling of a quantum dot. The static plunger gate voltage is defined as the reference at 0 mV and is tuned to a charge transition prior to the measurement. The pulse consists of a loading stage, during which a 6 mV rectangular voltage pulse is applied for 10 ms to load an electron into the dot, followed by a readout stage where the voltage is returned to a variable value near the charge transition. For each readout voltage in a range of −4 mV to 4 mV (indicated by the arrow), the SET current is recorded for 12 ms during the blue-shaded measurement window to resolve tunneling events. **b** Time-resolved SET current traces as a function of readout voltage. The dashed white line at 1 ms indicates the transition from the loading to the readout stage. Single-shot readout allows the resolution of individual tunneling events. Consistent with Fig. 4.4, a high SET current corresponds to an empty dot, whereas a low current indicates the presence of a loaded electron. For negative readout voltages, tunneling events typically occur within the first ms after the end of the loading stage, consistent with the desired reservoir coupling in the kHz regime.

With reliable charge sensing established, the final step is to match the tunnel coupling of each dot to the reservoir with the bandwidth of the measurement electronics. As described in Sec. 3.4, the measurement setup is optimized for DC current measurements with a bandwidth of 1.6 kHz determined by the IV converter operating at the 10^9 V/A gain setting. Accordingly, the reservoir coupling rate should also lie in the kHz range to enable high-fidelity readout. The coupling rate is measured using a pulsed gate voltage manipulation illustrated in Fig. 4.5**a**. A square pulse is applied to the plunger gate of the dot under test, beginning with a deep loading pulse of 6 mV for 10 ms, followed by a return to a readout voltage near the charge transition. The SET is biased for maximum SNR and the static plunger gate voltage is positioned at the transition point. For each tested readout voltage in the range from −4 mV to 4 mV, the SET current is recorded during a fixed time window (blue shaded area) to resolve individual tunneling events. The resulting time-resolved current traces are shown in Fig. 4.5**b**. For readout voltages below 0 mV, electrons remain trapped, leading to a high SET signal. For voltages above 0 mV, the electron tunnels out, producing a lower signal. The average tunnel rate to the reservoir can be estimated by the typical time scale by which the electron tunnels out of the dot for negative readout voltages. As presented in the pulse form graph in panel **a**, data is recorded 1 ms before pulsing to the readout voltage, therefore all data until the dashed white line in Fig. 4.5**b** correspond to the loading stage. The desired regime is one in which individual tunneling events are resolved and occur, on average, within the first millisecond after the dashed

white line, as shown in Fig. 4.5**b**. This timing ensures that the tunneling dynamics are well-matched to the acquisition bandwidth. While the reservoir coupling rate could be determined quantitatively using a lock-in measurement technique, this is generally not necessary, as the readout fidelity can be experimentally optimized later-on using qubit measurements.

The coupling rate for each dot is tuned by adjusting the outer barrier gate voltage (BL or BR) until the target tunneling timescale is achieved. Once this calibration is complete for all operational dots, a full set of gate voltages compatible with qubit operation has been identified. The exact working point of each qubit in the system may require minor adjustments over time, but at this point the device tuning is accomplished and the qubits are ready for coherent spin control.

4.4 Plunger gate lever arms

Before proceeding with coherent spin measurements, it is helpful to extract key device characteristics, such as the individual lever arms of each quantum dot's plunger gate and the thermal broadening of the corresponding electron reservoirs.

The lever arm α of a gate electrode quantifies the electrostatic coupling between the applied gate voltage and the energy level of a quantum dot. It defines the conversion factor between a change in gate voltage and the resulting energy shift of the dot's electrochemical potential. Accurate calibration of α is essential for expressing experimental voltage scales in physically meaningful energy units, enabling consistent interpretation of spectroscopic features such as Zeeman splittings, valley splittings, and interdot exchange interactions.

Experimentally, the lever arm α can be determined by using the Fermi level shift of a biased reservoir as a known energy reference. In this method, a finite bias voltage V_B is applied to the electron reservoir connected to a quantum dot, causing the reservoir's Fermi level to shift by the energy eV_B. By scanning the quantum dot's plunger gate voltage V_P and monitoring the charge transition, i.e. the alignment of the dot's energy level with the reservoir's Fermi level, the gate voltage shift, that is needed to compensate for the energy offset, is revealed. The lever arm is then given by

$$\alpha = \frac{\Delta E}{\Delta V_\mathrm{P}} = \frac{e\Delta V_\mathrm{B}}{\Delta V_\mathrm{P}}\,. \tag{4.2}$$

This method was applied to the left and right quantum dot of the $^{\mathrm{nat}}$Si/SiGe D09 Die02 device. As shown in Fig. 4.6, a linear dependence of the electron transition condition and the applied reservoir bias is clearly observed. The inverse slopes yield lever arms of $\alpha_\mathrm{L} = (0.123 \pm 0.001)$ eV/V and $\alpha_\mathrm{R} = (0.108 \pm 0.001)$ eV/V for the left and right plunger gates, respectively. The error bars reflect the statistical uncertainty of the linear fits. For completeness, the same measurements were conducted at the $(1,1)-(1,0)$ and $(1,1)-(0,1)$ charge transitions relevant to the two-qubit configuration in Ch. 6, resulting in similar values of $\alpha_\mathrm{L} = (120 \pm 1)$ meV/V and $\alpha_\mathrm{R} = (109 \pm 1)$ meV/V. This confirms the consistency

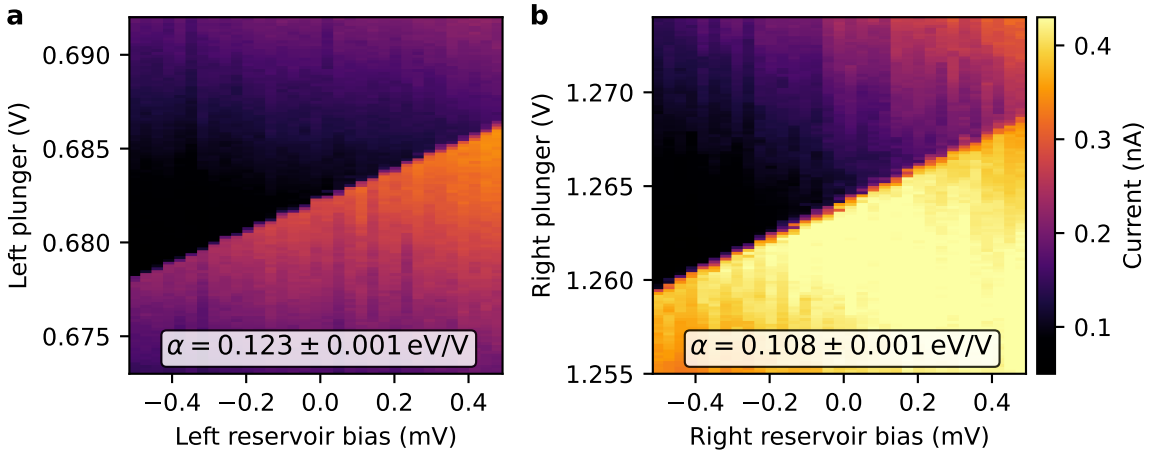

Figure 4.6: Plunger gate voltage scans as a function of applied reservoir bias for **a** the left and **b** the right quantum dot, shown with a shared color scale that represents the SET current. In each vertical trace, the point of contrast change indicates a charge transition, enabled by the alignment of the dot's energy level with the reservoir's Fermi level, which is linearly shifted by the applied reservoir bias. The inverse slope of these transition lines yields the lever arms noted in each panel. Exact transition voltages were identified by locating the maxima of the numerical derivative of the SET current with respect to the plunger gate voltage.

of the lever arms across different operating regimes. Nevertheless, the accurate lever arm values of each operating regime were taken into account in all subsequent analyses.

Potential systematic errors in this extraction method include lifetime broadening of the electron transition at high tunneling rates and thermal broadening of the reservoir's Fermi level at finite temperatures. However, these effects are negligible under the measurement conditions used, as discussed in the following section.

4.5 Electron reservoir temperature

The electron reservoirs, kept at zero bias during qubit operation, play a critical role in charge sensing and spin readout. Specifically, their electron temperature defines the thermal broadening of the reservoir's Fermi level, which sets the energy resolution limit for charge-based measurements. Accurate knowledge of this broadening is essential to evaluate its impact on qubit readout fidelity and to ensure that relevant energy splittings exceed the thermal energy scale.

Charge sensing of the quantum dot's transition width provides a means to estimate the electron temperature of the coupled reservoir. The thermally broadened Fermi level of the reservoir defines an energy window within which electron tunneling becomes energetically allowed. As the quantum dot level moves through this window, its average occupancy changes according to the Fermi-Dirac distribution. This occupancy variation can be probed capacitively by monitoring the tunneling current through the nearby SET. To ensure that the transition width is governed by temperature, the experiment is performed in the regime

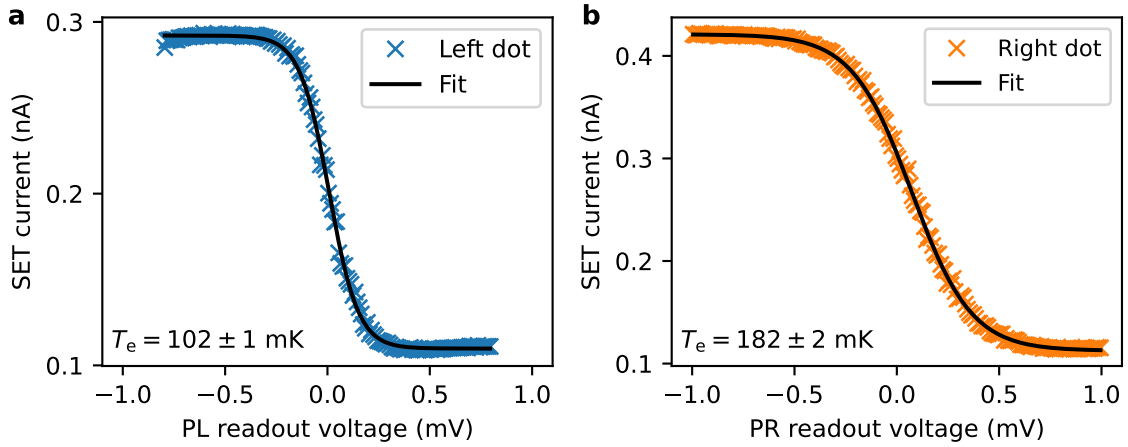

Figure 4.7: Electron temperature characterization of **a** the left and **b** the right electron reservoirs, based on the thermally broadened first electron transition of the respective dot. Each SET current value represents a 2 s time-averaged signal, corresponding to the mean dot occupancy, as a function of the readout voltage relative to the charge transition threshold (0 mV). The transitions are fitted using the Fermi-Dirac distribution in Eq. (4.3), yielding the denoted electron temperatures. The error bars of the fit values reflect both the statistical uncertainty of the fit and the propagated uncertainty from the lever arm calibration.

$h\Gamma \ll k_B T_e$, where the tunneling rate Γ to the reservoir is small compared to the thermal energy $k_B T_e$. This suppresses lifetime broadening and ensures thermal effects dominate the lineshape [96]. However, since the presence of charge noise can also lead to a broadening of the observed transition width, the extracted electron temperature should be regarded as an upper bound estimate.

Experimentally, the broadening of the first electron transition of each dot is probed by pulsing the plunger gate voltage across the transition and recording the SET current for 20 ms at each intermediate gate voltage. This is repeated 100 times and averaged, yielding a total acquisition time of 2 s per gate voltage. The observed transitions widths are fitted using the Fermi-Dirac distribution [96]

$$I_{\mathrm{SET}} = \frac{I_{\mathrm{A}}}{\exp\left(\frac{\alpha \cdot (V - V_0)}{k_B T_e}\right) + 1} + I_{\mathrm{C}}\,, \tag{4.3}$$

where I_{A} and I_{C} are fit parameters dependent on the SET working point, V_0 is the gate voltage at the center of the transition, α the plunger gate lever arm determined in Sec. 4.4, and the electron temperature $\mathrm{T_e}$.

The extracted transition widths and fitted curves are shown in Fig. 4.7. The electron temperatures are found to be $T_{\mathrm{e,L}} = (102 \pm 1)$ mK and $T_{\mathrm{e,R}} = (182 \pm 2)$ mK for the left and right dot, corresponding to thermal energies of (8.7 ± 0.1) µeV and (15.6 ± 0.2) µeV, respectively. The error bars reflect both the statistical uncertainty from the fit and the uncertainty in the lever arm calibration. The same analysis was performed at the two-qubit regime near the $(1,1) - (1,0)$ and $(1,1) - (0,1)$ charge transitions, yielding slightly lower temperature of (98 ± 1) mK and (160 ± 2) mK for the left and right dot, respectively. Across

different working points, the electron temperatures remained consistent, though the right reservoir consistently showed nearly double the temperature of the left. This discrepancy may suggest a systematic error. A potential issue may stem from the residual connection of an IV converter to the right reservoir, which could have introduced additional noise despite being nominally inactive and DC-filtered at 250 Hz. The more plausible explanation is related to local heating and noise caused by the resistive SET, which is situated closer to the right dot [72, 73]. However, further investigation is required to identify the origin of this asymmetry.

In summary, the extracted thermal energies are well below the typical Zeeman splitting of 80 μeV associated with qubit frequencies around 19 GHz, confirming that the experimental setup is sufficiently cold and well-suited for reliable spin qubit experiments.

5 Single–Qubit Control

Reliable control of individual spin qubits is a fundamental prerequisite for any scalable quantum computing architecture. Establishing such control requires not only precise manipulation of the qubit state but also accurate readout and spectral characterization to ensure high-fidelity gate operations. This chapter begins by implementing spin-selective readout via energy-selective tunneling, enabling single-shot detection of the spin state through charge sensing. With this capability in place, the qubit resonance frequency is determined using two complementary spectroscopic methods: rapid adiabatic passage (RAP) and single-tone spectroscopy. RAP is further explored and validated using the ^{28}SiMOS D06 Die07 sample, where its effectiveness for robust resonance identification and spin inversion is experimentally confirmed. The focus then shifts back to the primary device of this thesis, the ^{nat}Si/SiGe D09 Die02 sample, in which coherent single-qubit control of both qubits is demonstrated through Rabi oscillations, Ramsey fringes, and Hahn-echo measurements. These experiments yield quantitative coherence metrics, including dephasing and echo times, and mark the achievement of universal single-qubit control in an industrially fabricated silicon platform.

5.1 Spin selective readout and blip analysis

With the application of an external B-field, the confined single electrons in the quantum dots can be finally regarded as qubits due to lifting the degeneracy of the spin states and forming a two-level system for quantum operation. While applying an external B-field appears conceptually simple, this important step introduces two new challenges. First, the magnetic field must be precisely known and tunable to ensure a Zeeman splitting significantly larger than the thermal broadening of the electron reservoirs. This guarantees resolvable spin states and enables the choice of spin resonance frequencies within accessible experimental ranges, while optimizing spin relaxation rates and frequency-dependent microwave transmission. Second, a spin-selective readout mechanism must be established to evaluate the qubit state, despite the fact that the SET sensor is only charge sensitive. While calibration of the external B-field and determination of well-suited values will be addressed throughout the following sections, this section introduces the spin readout protocol which builds the foundation for all subsequent qubit experiments.

Spin-selective readout

A fundamental requirement for spin qubit operation is the ability to determine the spin state of a confined electron. This can be accomplished via energy-selective spin-to-charge conversion, commonly referred to as the Elzerman readout technique [97]. This method utilizes the Zeeman energy difference between spin-up ($|\uparrow\rangle$) and spin-down ($|\downarrow\rangle$) states in conjunction with a controlled gate voltage pulse sequence to convert spin information into a charge signal that can be detected by the SET. As mentioned in Sec. 4.5, the Zeeman energy $E_Z = g\mu_B B_{ext}$ must exceed the thermal broadening $k_B T_e$ of the reservoir to ensure distinguishable spin-states. Given the previously measured electron reservoir temperatures of below 200 mK (cf. Sec. 4.5), an external field of at least 300 mT, corresponding to a Larmor frequency of 8.4 GHz, is sufficient to achieve a Zeeman splitting that exceeds the thermal reservoir broadening by a factor of two.

The illustration of the Elzerman readout protocol in Fig. 5.1 is composed of the conceptual working principle (**a**), the corresponding plunger gate pulse sequence (**b**), and a typical sensor response (**c**). Panel **a** schematically depicts the alignment between the reservoir's Fermi level (E_F) and the Zeeman-split spin states of a single electron confined in a quantum dot. In these illustrations, the quantum dot is tunnel-coupled to the electron reservoir via a finite-height barrier (thin black line) and terminated on the other side by an infinite-height barrier (thick black line). To avoid confusion, it is important to note that the two energy levels in the dot represent the spin-up and spin-down states of a single electron, respectively, of which only one state can be occupied. The charging energy required to load a second electron is orders of magnitude larger than the Zeeman energy scale.

The Elzerman protocol proceeds through four sequential stages to initialize and determine the spin state of a single electron in a quantum dot via control of the plunger gate voltage (see Fig. 5.1**b**):

Emptying stage The plunger gate voltage V_P is pulsed well below the charge transition threshold so that both spin states lie above E_F, preventing electron occupation in the dot.

Loading stage The plunger voltage V_P is raised such that both energy states of the dot are below the reservoir level. In this regime, either a spin-up or spin-down electron from the reservoir can tunnel into the dot. After loading, the system can be allowed to evolve for a waiting time t_{wait}, during which spin relaxation processes may occur.

Readout stage For the readout duration t_{read}, the plunger voltage is adjusted such that only the spin-up energy level lies above E_F, while the spin-down state remains below. If the electron is in the spin-up state, it can tunnel out to the reservoir and the dot is subsequently reoccupied by a spin-down electron. If the electron is already in the spin-down state, it remains in the dot and no tunneling occurs. This conditional tunneling event is the essence of spin-to-charge conversion.

Reset stage After the readout phase, the dot is always occupied by a spin-down electron. In the final step, this electron can be unloaded to restore the initial conditions and prepare for the next cycle. In practice, the spin-down electron is often retained in the dot and directly used as a deterministically initialized spin state for subsequent coherent manipulation.

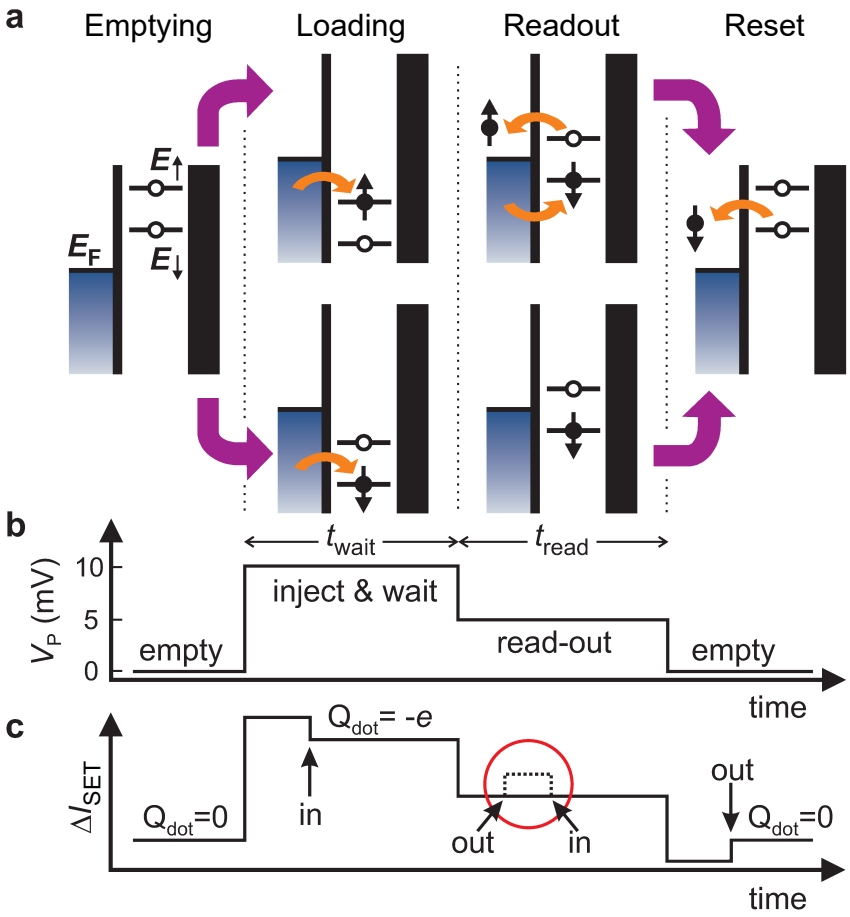

Figure 5.1: Schematic illustration of spin-selective readout using the Elzerman protocol. Adapted from Ref. [97]. **a** Energy diagrams showing the relative alignment between the quantum dot spin states and the reservoir's Fermi level E_F during each stage of the pulse sequence. A static magnetic field splits the spin-up ($E_\uparrow$) and spin-down ($E_\downarrow$) states via the Zeeman effect. The readout protocol consists of four sequential stages: *Emptying stage*: Both spin states are pulsed above E_F, and the dot is unoccupied. *Loading stage*: Both spin states are pulsed below E_F, allowing an electron with either spin to tunnel into the dot. Optionally, the system can be allowed to evolve for a waiting time t_{wait} to probe spin relaxation processes. *Readout stage*: For the readout duration t_{read}, the dot levels are positioned such that $E_\uparrow > E_F > E_\downarrow$. In this configuration, a loaded spin-up electron tunnels out and is replaced by a spin-down electron, while a loaded spin-down electron remains trapped. *Reset stage*: The dot is emptied again and the sequence can be repeated. **b** Time-resolved plunger gate pulse sequence that implements the four stages of the Elzerman readout protocol. **c** Characteristic time-resolved SET current response to both the gate voltage pulses and the charge dynamics in the quantum dot. The red circle highlights a transient "blip" during the readout stage, which is the unique signature of a spin-up state leaving the dot and being replaced by a spin-down electron. In the absence of a blip, the electron is identified as spin-down.

The characteristic SET current response shown in Fig. 5.1**c** reflects both the applied plunger gate voltage pulses and the resulting charge dynamics in the quantum dot. Since the SET is sensitive to local electrostatic changes, its current responds not only to electron tunneling events in the nearby dot but also to changes of the plunger gate voltage. As such, the larger steps in the sensor current follow the plunger gate voltage, shown in Fig. 5.1**b**, due to cross-capacitive coupling of the plunger gate with the energy levels of the SET.

Additionally, the charge state of the dot, denoted by Q_{dot}, leads to a persistent shift in the sensor current in the loading phase, and likewise in the final emptying stage. The time-scale after which the dot is (un)occupied is governed by the barrier-defined tunneling rate. During the readout stage, a spin-up electron will tunnel out and subsequently be replaced by a spin-down electron. This sequence creates a brief rise in the sensor current due to the electron leaving the dot, followed by a return to the baseline as the quantum dot is reoccupied. This transient feature in the SET current is known as "blip". The onset and duration of this blip are primarily determined by the tunnel coupling to the reservoir, which needs to be adjusted to match the bandwidth of the measurement system (see Sec. 4.3). In contrast, if no blip is detected, the electron is inferred to be in the spin-down state throughout the readout window. The red circle in panel **c** highlights this distinctive blip, which is the unique signature of a spin-up state.

This spin-selective readout method enables single-shot spin detection and relies on precise gate voltage control to ensure the correct alignment between the qubit energy levels and the reservoir. The identification of an appropriate readout voltage for this alignment will be addressed in the following section.

Spin tail with finite external B-field

The readout voltage range in which spin-selective readout can be performed is defined by the Zeeman energy splitting of the spin states. An experimental signature of this Zeeman splitting can be observed in probing the first electron transition of the dot, similar to the tunnel rate measurement in Fig. 4.5, but in the presence of a finite magnetic field and with prior initialization of spin-up electrons in the quantum dot. Under such conditions, the electron transition exhibits an additional feature, the so-called "spin tail", arising from the extended energy window created by the Zeeman-split spin states, within which tunneling between the dot and the reservoir can occur.

The initialization of the qubit in the excited spin-up state can be performed via two methods, of which the respective plunger pulse forms are depicted in Fig. 5.2**a**. The zero-voltage reference of these pulse forms corresponds approximately to the charge transition point, that marks the plunger gate voltage at which an electron can occupy the dot, as explained in Sec. 4.3. The first method, labeled "Elzerman init." in Fig. 5.2**a**, utilizes the plunger gate pulse sequence presented in the Elzerman protocol and can be performed at the early stages of device operation without knowledge about qubit control parameters. As discussed in Sec. 5.1, this approach relies on loading the dot with either a spin-up or spin-down electron from the reservoir with equal probability. The second method, labeled "Coherent init.", can only be performed after observing Rabi oscillations (cf. Sec. 5.6) of the qubit and is briefly mentioned here since it allows a clearer representation of the spin tail. A detailed description of this pulse sequence is presented in Sec. 5.3, together with the first instance of coherent qubit manipulation. In the coherent initialization method, a spin-down electron is deterministically loaded into the dot and subsequently excited by a microwave burst, which coherently rotates the spin into the spin-up state with up to perfect fidelity.

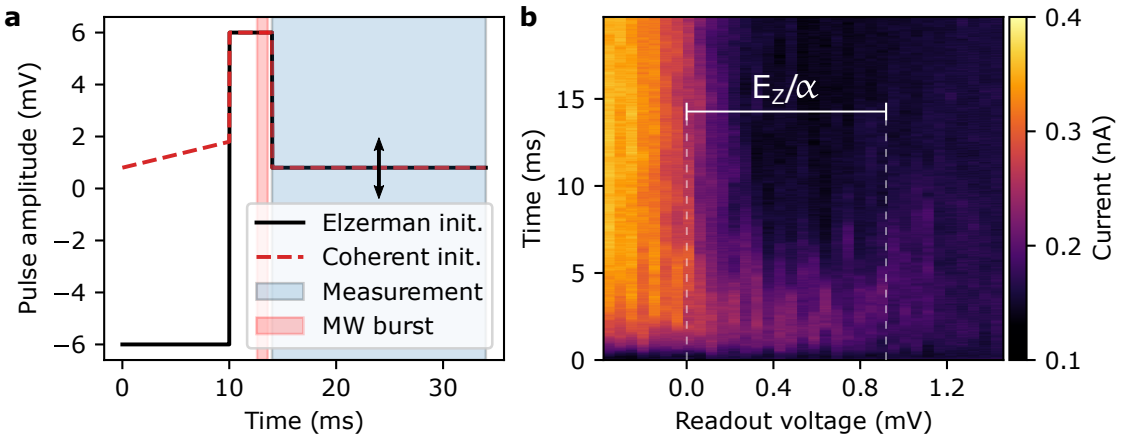

Figure 5.2: a Initialization and measurement pulse sequences for probing spin-dependent tunneling. The black trace ("Elzerman init.") represents spin-up initialization using the standard Elzerman protocol, where spin-up and spin-down electrons tunnel into the dot with equal probability. The red trace ("Coherent init.") performs deterministic loading of a spin-down electron, followed by a resonant microwave (MW) burst that coherently rotates the spin into the spin-up state. The final readout voltage is stepped across the charge transition (indicated by the black arrow) to probe spin-dependent tunneling within the blue-shaded measurement window, during which the SET current is recorded. **b** Time-resolved SET current as a function of readout voltage following coherent spin-up initialization of the left dot at 19.6 GHz. Each readout voltage point is averaged over 100 single-shot traces. The voltage region between the dashed lines reveals an extended spin tail where only spin-up electrons can tunnel out of the dot and generate transient sensor responses (blips). The width of this window corresponds to the Zeeman energy divided by the lever arm, E_Z/α, and enables estimation of the Zeeman splitting and the optimal range for spin-selective readout.

After initialization of the qubit using either method prior the readout stage, the qubit is probed by stepping the readout voltage across the charge transition and recording the SET current at each step for 20 ms. At each voltage point, 100 single-shot time traces are averaged to extract statistically meaningful behavior. The resulting data, obtained using the coherent initialization method to enhance visibility, is shown in Fig. 5.2**b**. The transition in between permanent absence of an electron in the dot (high SET current) to permanent occupation of the dot (low current) can be observed close to 0 mV readout voltage. This transition represents the alignment of the spin-down state of the qubit with the reservoir's Fermi level. The spin tail appears as an extended region from approximately 0 mV to 0.9 mV, in which only the spin-up energy level is above the reservoir level. In this voltage window, spin-up electrons will tunnel out of the dot and be replaced by spin-down electrons, producing a transient blip. The fading of the spin tail at approximately 0.9 mV marks the alignment of the spin-up state of the qubit with the reservoir level. For any higher plunger gate voltages, both spin states are energetically lower than the reservoir's Fermi level, and the dot remains occupied.

As indicated in the graph, the width of the spin tail directly corresponds to the Zeeman energy divided by the plunger gate lever arm, E_Z/α. However, thermal broadening of the reservoir blurs the sharp boundaries of the spin tail such that the Zeeman energy can only be estimated. Nevertheless, this measurement allows the selection of appropriate readout voltages for spin-selective readout by choosing a value within the spin tail region. The

exact choice of the readout voltage involves a trade-off between maximizing blip signal visibility and minimizing the rate of thermal background events. This can be understood by assuming a positive readout voltage close to 0 mV. In this regime, the dot occupation is unstable as thermal excitations allow the continuous transition of spin-down electrons in between dot and reservoir, causing blip-like tunneling events. On the other hand, at a higher readout voltage of 0.9 mV, the spin-up state is aligned with the reservoir such that only half of all Fermi-distributed reservoir states are accessible to the spin-up electron. This leads to a slower tunneling rate and an increased risk of the blip event occurring after the duration of the measurement window. Such slowing of the tunneling rate can be observed in Fig. 5.2**b** by noticing the upward trend of the average blip onset times beyond the second dashed line marking the Zeeman energy. Consequently, an optimal readout voltage is located about half the reservoir broadening below the end of the spin tail, as this maintains optimal tunneling conditions for spin-up electrons while minimizing thermally induced events.

Blip evaluation

Spin-selective readout is routinely employed in qubit experiments by repeatedly executing the same pulse sequence and evaluating the average number of detected blips. This approach enables extraction of the spin-up fraction resulting from a particular qubit manipulation, thereby allowing inference of the qubit's superposition state through repeated projective measurements. This section introduces the automated analysis of blips in raw data, which is used throughout this thesis to extract spin-up fractions of single-electron qubits.

In the simplest case, Elzerman initialization can be used to statistically load either a spin-up or spin-down electron into the dot with equal probability. Given the selection of a suitable readout voltage, spin-up electrons are identified during the readout phase by a characteristic transient blip, whereas spin-down electrons do not produce a signal. This differentiation is illustrated in Fig. 5.3**a** at the example of two representative single-shot readout traces.

Unlike classical bits, qubits can exist in superposition states of the form $a\,|\uparrow\rangle + b\,|\downarrow\rangle$, and a single projective measurement only yields one of the eigenstates. Consequently, repeated measurements are required to determine the probability amplitudes, which are reflected by the measured spin-up fraction. Fig. 5.3**b** shows a projective measurement comprising 100 single-shot readouts. Each vertical line corresponds to a 20 ms readout trace, with blips (high current) indicating spin-up events. A total of 57% of the traces exhibit blips, of which 50% can be attributed to perfect Elzerman initialization and the excess 7% may result from limited statistics or false-positive thermal events. Notably, most blips occur within the first 5 ms of the measurement window. This is comprehensive, as the tunneling rate to the reservoir was previously tuned close to 1 kHz, corresponding to a characteristic tunneling time of $T_{\mathrm{QD}} \sim 1$ ms, and the temporal probability distribution of a tunneling event is distributed as $\rho_{\mathrm{QD}}(t) \propto \exp(t/T_{\mathrm{QD}})$ [98, 99]. In contrast, thermally induced tunneling events can occur at any time and are randomly distributed throughout

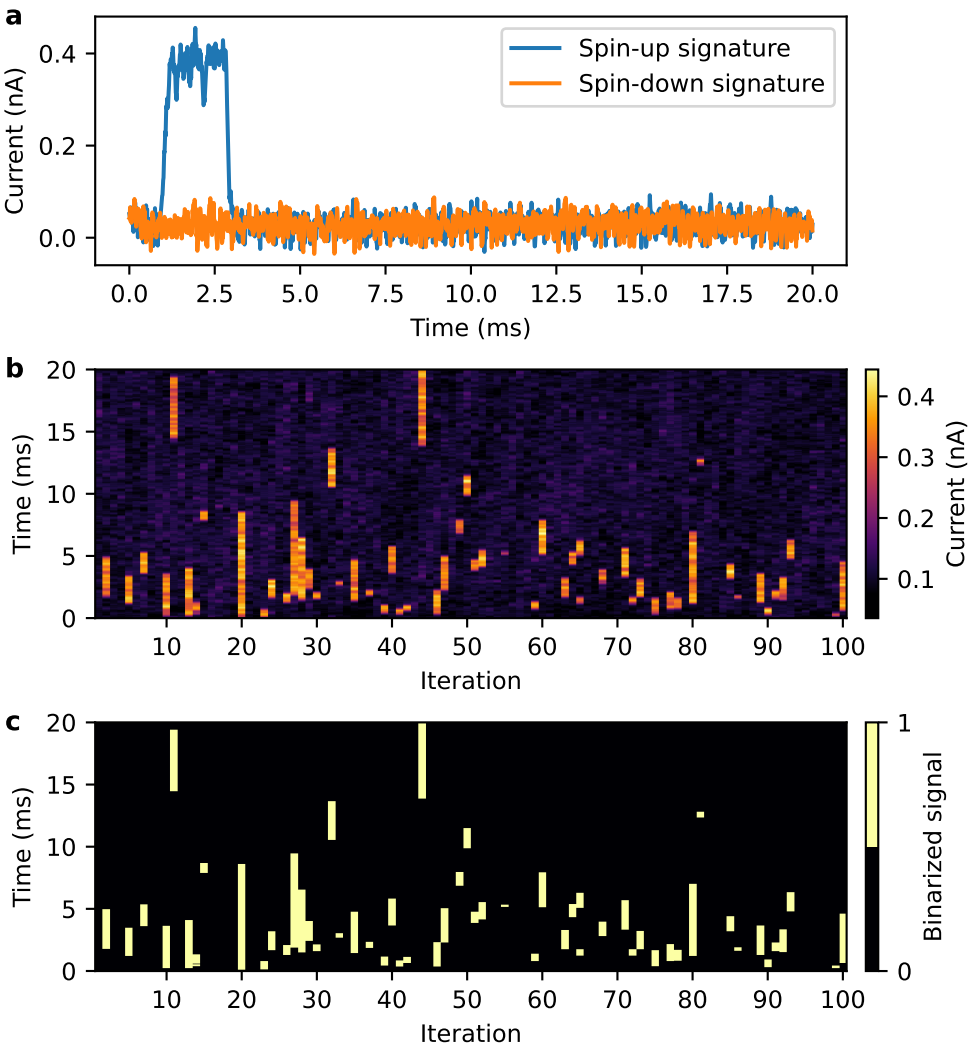

Figure 5.3: Exemplary qubit state evaluation using spin-selective readout and automated blip binarization. **a** Representative single-shot current traces showing the characteristic SET response during the readout phase for spin-up (blue) and spin-down (orange) discrimination. A transient increase in current, called blip, indicates a spin-up tunneling event. **b** Raw data from a projective qubit state measurement comprising 100 repetitions of single-shot readout. Each vertical line represents a 20 ms readout trace. Bright vertical segments correspond to blips. Most blips occur within the first 5 ms, consistent with the tuned reservoir tunneling rate of 1 kHz. **c** Binarized representation of the measurement in panel **b** using threshold binarization. Each bright region marks a detected spin-up trace, yielding a spin-up fraction of 57%. Such automated blip analysis enables efficient extraction of spin-up fractions from large datasets, which are used to infer the superposition state of the qubit.

the readout window. The presence of such events becomes apparent in the raw data as particularly late blips. Importantly, thermal tunneling can only increase the total blip count, as it enables spin-down electrons to leave the dot as well. Consequently, while such events introduce a false-positive offset, they do not interfere with genuine spin-up detection.

To enable efficient evaluation of large datasets, the identification of blip events is automated via digital post-processing. An example of the resulting binarized data is shown in Fig. 5.3**c**, where spin-up events are isolated to extract the spin-up fraction. The difficulty of such blip binarization scales inversely with available SNR, as it becomes challenging to evaluate blip events at SNR < 1, where the noise on the high and low current levels exceeds the signal amplitude. In this work, two methods of signal binarization have been employed, being threshold binarization and total variation binarization (TVB). In the threshold binarization, each current trace is first smoothed and normalized, then compared to a user-defined threshold. Each point that exceeds the threshold is assigned a digital one and the full trace containing this point is counted as a spin-up detection. This method, detailed in Ref. [24], is straightforward to implement, but prone to yield false-positive counts if the SNR is low or the threshold is inappropriate, as any noise excursion exceeding the threshold will be interpreted as a blip. The TVB method is more robust to noise, as all current traces of the measurement are histogramized and fitted with a bimodal Gaussian model to automatically determine an optimal threshold value. Additionally, a cost-function is implemented that prevents short noise fluctuations in the current traversing the threshold value to be detected as individual blips. The minimum duration for a signal to qualify as a valid event is the only user-defined parameter in this method, which has been developed as part of the thesis of Gläser [99]. The TVB algorithm is computationally more expensive but yields a more accurate blip count, as it can detect multiple blips in a single trace and also returns accurate blip onset and duration timings that can be used for further analysis and applications.

In the present work, all measurements were performed at high-SNR operating points, as established in Sec. 4.3. Under these conditions, both binarization techniques yield equivalent results, and were used interchangeably without further distinction. With the implementation of spin-selective readout and robust data processing techniques, the essential prerequisites for single-qubit experiments are fulfilled. Thus, the focus of the subsequent sections shifts to first single-qubit control experiments.

5.2 Frequency spectroscopy techniques

Active spin manipulation relies on precise knowledge of the Larmor frequency of the qubit. The determination of the resonance condition is a non-trivial task, as the effective magnetic field at the qubit site depends on individual properties of the hand-wound magnetic coils and the micrometer sized cobalt magnet on the sample. While the magnetic field can be estimated from design parameters, realistic conditions can introduce deviations from simulation results in the GHz range, in which the qubit resonance with a typical linewidth of below 1 MHz needs to be located.

The technique of rapid adiabatic passage (RAP) involves sweeping the detuning of a driven two-level system across resonance slowly enough that the system adiabatically follows its instantaneous eigenstate. When the adiabatic condition is satisfied, RAP enables high-fidelity spin inversion, as long as the resonance frequency lies within the sweep range.

This makes RAP a powerful tool for efficiently locating the qubit resonance, as the sweep range can initially be set broad and then progressively narrowed to the few-MHz scale. Once the frequency range is narrowed down, single-tone spectroscopy can be employed in a final step to finely resolve the qubit's resonance frequency and extract its transition linewidth.

5.2.1 Rapid adiabatic passage

Originally developed in the context of nuclear magnetic resonance (NMR) [100], RAP has found widespread application in spin qubit platforms [101–104]. The theoretical underpinning of RAP is closely related to the Landau-Zener theory [105], which describes the transition probabilities between eigenstates in a two-level system subjected to a time-dependent energy splitting. The starting point for describing the working principle of RAP is the same microwave-driven Hamiltonian derived earlier in Sec. 2.7, with the key modification that the drive frequency becomes explicitly time-dependent due to a linear frequency sweep, commonly referred to as a chirp. In the rotating frame under the rotating wave approximation (RWA), the now time-dependent Hamiltonian reads

$$H_{\mathrm{RWA}}(t) = \frac{\hbar}{2}\begin{pmatrix} -\Delta(t) & \Omega_{\mathrm{R}} \\ \Omega_{\mathrm{R}} & \Delta(t) \end{pmatrix}, \tag{5.1}$$

where Ω_{R} is the Rabi frequency, and $\Delta(t) = \omega_0 - \omega(t)$ is the instantaneous detuning between the qubit's resonance frequency ω_0 and the time-dependent microwave drive frequency $\omega(t) = \omega(0) - t\dot{\omega}$ with constant chirp rate $\dot{\omega}$. The instantaneous eigenenergies of the system

$$E_{\pm}(t) = \pm\frac{\hbar}{2}\sqrt{\Delta^2(t) + \Omega_{\mathrm{R}}^2}, \tag{5.2}$$

exhibit a characteristic avoided level crossing at resonance ($\Delta = 0$) with a minimum energy gap of $\hbar\Omega_{\mathrm{R}}$, as visualized in Fig. 5.4**a**.

According to the Landau-Zener theory, if the system is initially in its ground state far from resonance and the detuning is swept linearly through the avoided crossing, the probability to adiabatically stay in the instantaneous ground state is given by [102, 106]

$$P_{|g\rangle,\mathrm{LZ}} = 1 - \exp\left(-\frac{\pi\Omega_{\mathrm{R}}^2}{2\dot{\omega}}\right) = 1 - \exp\left(-\frac{\pi^2 f_{\mathrm{Rabi}}^2}{\dot{f}}\right), \tag{5.3}$$

where the second equality is expressed in terms of experimentally accessible linear frequency units (Hz instead of rad/s), using the Rabi frequency $f_{\mathrm{Rabi}} = \Omega_{\mathrm{R}}/2\pi$ and the constant frequency chirp rate $\dot{f}$ in Hz/s. This equation shows that the probability of adiabatically remaining in the ground state increases with the square of the Rabi frequency and decreases with the chirp rate. Therefore, the adiabatic condition is given by $\dot{f} \ll f_{\mathrm{Rabi}}^2$. At the same time, the total manipulation time must remain shorter than the spin relaxation time T_1 (see Sec. 5.5) to prevent loss of the spin state before readout. These two opposing requirements define the "rapid" and "adiabatic" attributes of RAP.

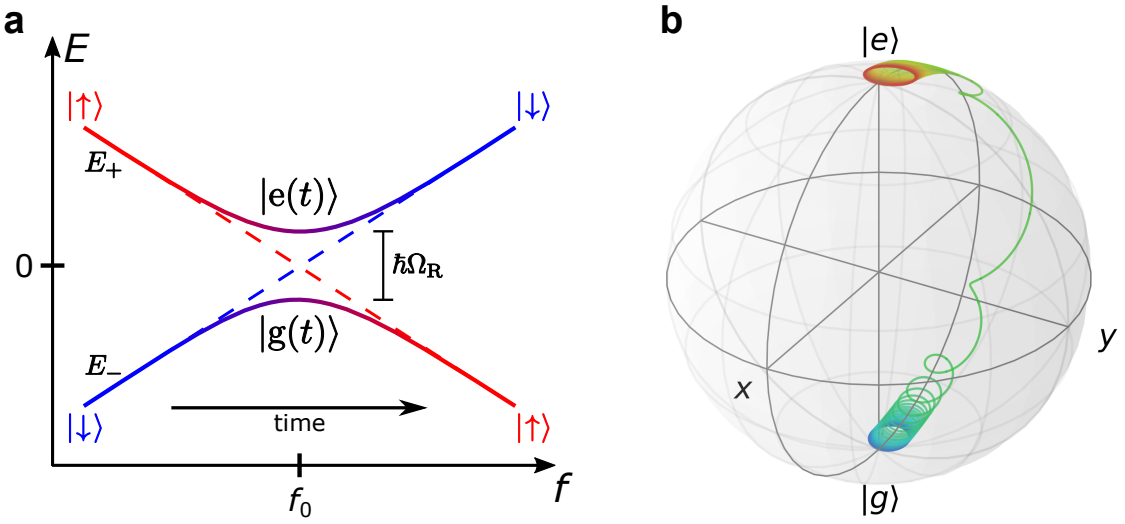

Figure 5.4: Schematic illustration of rapid adiabatic passage (RAP). **a** Energy diagram of a two-level spin system over drive frequency. The avoided level crossing at resonance $f = f_0$ represents the systems Rabi frequency $\hbar\Omega_R$. Spin inversion of an initial pure state at large detuning can be achieved by chirping adiabatically across the resonance frequency. The color gradient of the eigenenergy branches $E_\pm$ illustrates the mixing of pure spin states during time-evolution of the instantaneous eigenstates $|g(t)\rangle$ and $|e(t)\rangle$. Inspired from Refs. [101, 105, 107] **b** Spin trajectory on the Bloch sphere during RAP under the rotating wave approximation. In the process of adiabatically chirping the drive frequency across the resonance frequency, the effective magnetic field gets inverted and the spin vector follows the instantaneous eigenstate leading to a spin inversion. The emphasized wobble in this trajectory reflects the nutation of the spin around the time-varying effective magnetic field. Reprinted from Ref. [102].

In the absence of coupling or for large detuning, the eigenstates of the system correspond to the pure spin states, $|\downarrow\rangle$ and $|\uparrow\rangle$. Once coupled via an adiabatically chirped transverse drive, the instantaneous eigenstates can be expressed as time-dependent superpositions of the pure spin states states [107]

$$|g(t)\rangle = \cos\left(\frac{\theta(t)}{2}\right)|\downarrow\rangle + e^{i\phi}\sin\left(\frac{\theta(t)}{2}\right)|\uparrow\rangle\,, \tag{5.4}$$

$$|e(t)\rangle = \sin\left(\frac{\theta(t)}{2}\right)|\downarrow\rangle - e^{i\phi}\cos\left(\frac{\theta(t)}{2}\right)|\uparrow\rangle\,, \tag{5.5}$$

where ϕ is the initial phase of the microwave drive and the mixing angle

$$\theta(t) = \arctan\left(\frac{\Omega_R}{\Delta(t)}\right), \tag{5.6}$$

describes the angle between the effective magnetic field and the quantization axis in the rotating frame. The representation of the instantaneous eigenstates emphasizes that, as the detuning $\Delta(t)$ is adiabatically swept from $-\infty$ to $+\infty$, the system evolves from an assumed initial state $|\downarrow\rangle$ at $t = 0$, through an equal superposition of spin states at resonance ($\Delta = 0$), to the pure excited state $|\uparrow\rangle$. This adiabatic evolution along the instantaneous eigenstates is color-coded in the energy level diagram in Fig. 5.4**a**.

On the Bloch sphere, this evolution is governed by the mixing angle $\theta(t)$, which defines the azimuthal orientation of the spin vector with respect to the quantization axis. The spin thereby traces a continuous trajectory from the south pole to the north pole, as visualized in Fig. 5.4**b**. The emphasized wobble in this trajectory reflects the nutation of the spin around the time-varying effective magnetic field. As the chirped microwave frequency approaches the resonance condition, the transverse component of the effective field increases and causes the spin to spiral with growing azimuthal phase. Such gradual build-up of transverse drive strength leads to a transient precessional motion that follows the adiabatically evolving eigenstate [103].

In essence, the RAP protocol inverts the direction of the effective magnetic field in the rotating frame over the course of the chirp. If the sweep is performed sufficiently slow to satisfy the adiabatic condition, the spin vector follows the effective magnetic field and assumes the opposite pure spin state when projected onto the quantization axis in the absence of drive.

5.2.2 Single-tone spectroscopy

To complement the frequency spectroscopy technique of RAP, a more conventional approach to probe the qubit resonance is single-tone spectroscopy. In this method, the qubit is subjected to a microwave burst of fixed frequency and pulse duration. When the drive frequency ω matches the qubit's Larmor frequency ω_0, Rabi oscillations are excited between the spin eigenstates, which manifest as an oscillatory population transfer as discussed in Sec. 2.7.

However, real qubit systems deviate from the idealized case of a perfectly static resonance condition. Several mechanisms lead to temporal fluctuations of the effective magnetic field at the qubit site. These include current noise in the magnetic field coils, slow drifts in gate voltages altering the qubit confinement potential, and stochastic nuclear spin flips from the ^{29}Si isotopes in natural silicon, described by Overhauser field noise [108, 109]. Any magnetic field noise contributes to effective detuning $\Delta(t)$ in the qubit Hamiltonian, resulting in time-dependent fluctuations of the z-component of the effective magnetic field in the rotating frame. As a consequence, the coherent spin trajectory on the Bloch sphere becomes distorted, and over time, the qubit loses phase coherence. The characteristic timescale at which this dephasing occurs is denoted by the T_2 time, and for Rabi experiments, a specific coherence time $T_{2,\mathrm{Rabi}}$ is defined. This timescale quantifies the decay of Rabi oscillations under continuous driving, capturing the decoherence induced by detuning noise around the Rabi frequency [110].

The resulting spin-up probability under continuous resonant driving, including commonly assumed exponential decoherence [111], is described by

$$P_{|\uparrow\rangle}(t) = \frac{\Omega_\mathrm{R}^2}{\Omega_\mathrm{eff}^2} \sin^2\left(\frac{\Omega_\mathrm{eff}}{2}t\right) \exp\left(-\frac{t}{T_{2,\mathrm{Rabi}}}\right), \quad \text{with} \quad \Omega_\mathrm{eff} = \sqrt{\Delta^2 + \Omega_\mathrm{R}^2}\,. \tag{5.7}$$

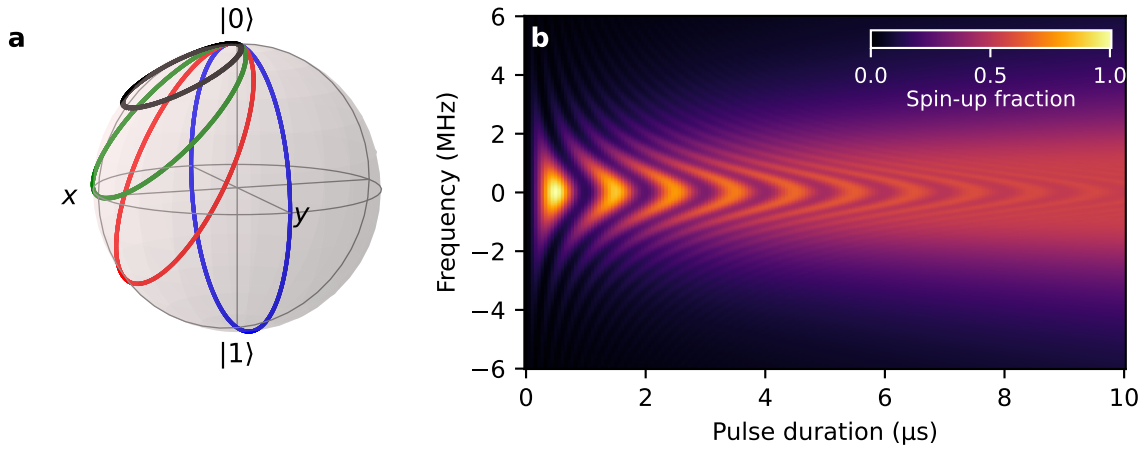

Figure 5.5: Single-tone qubit drive and the effects of detuning and decoherence. **a** Bloch sphere trajectories of a qubit under continuous single-tone drive for different detuning conditions, excluding decoherence. At resonant drive ($\Delta = 0$, blue), the spin vector undergoes full Rabi oscillations about a rotation axis in the equatorial plane. For increasing detuning ($\Delta_{\text{red}} < \Delta_{\text{green}}$), the effective magnetic field in the rotating frame tilts toward the z-axis, which leads to an increase of the oscillation frequency Ω_{eff} and a reduction of the oscillation amplitude according to $\Omega_{\text{R}}^2/\Omega_{\text{eff}}^2$. In the far-detuned regime (black), the rotation axis converges toward the quantization axis and effectively suppresses population transfer. **b** Simulated single-tone spectroscopy map showing the spin-up probability as a function of pulse length and drive detuning, calculated using the QuTiP python package. The frequency axis is offset by the qubit's Larmor frequency ω_0 and the simulation parameters of the Rabi frequency and decoherence time are chosen $f_{\text{Rabi}} = 1\,\text{MHz}$ and $T_{2,\text{Rabi}} = 3\,\mu\text{s}$, respectively. The resulting detuning-dependent Rabi oscillations resemble a "Chevron" pattern and visualize the influence of detuning and decoherence on coherent qubit control. As pulse duration increases, decoherence leads to loss of contrast and saturation of the spin-up probability at half the initial oscillation amplitude.

Here, Ω_{R} denotes the Rabi frequency, Δ is the static detuning from resonance, and Ω_{eff} is the effective Rabi frequency accounting for the energy difference between the spin states under detuned driving, which is visible in Fig. 5.4**a** as a detuning-dependent energy gap. The exponential envelope models the loss of phase coherence due to noise components near the drive frequency, and is generally sufficient for fitting experimental data. However, more detailed theoretical treatments suggest that non-exponential decay forms, such as Gaussian or power-law behaviors, can provide more accurate descriptions in the presence of certain noise spectra [112, 113].

The effect of frequency detuning and decoherence on single-tone qubit driving is illustrated in Fig. 5.5. Panel **a** shows the evolution of the qubit state on the Bloch sphere under different detuning conditions, where the population transfer is governed by the amplitude term $\Omega_{\text{R}}^2/\Omega_{\text{eff}}^2$ in Eq. (5.7) excluding decoherence effects. Under resonant driving ($\Delta = 0$) the spin undergoes coherent Rabi oscillations about an axis in the equatorial plane, resulting in full population transfer between the eigenstates $|0\rangle$ and $|1\rangle$ (blue trajectory). As the detuning increases, the rotation axis tilts towards the z-axis, and the spin precesses around this new axis with reduced amplitude and higher effective frequency Ω_{eff} (green and red trajectories). In the far-detuned limit, the trajectory becomes confined near the initial state, resulting in weak population oscillation (black trajectory). Panel **b** presents a

simulated spectroscopy map of the spin-up probability as a function of single-tone pulse duration and drive detuning near the qubit's Larmor frequency ω_0. The resulting characteristic "Chevron" pattern reflects both the detuning-dependent oscillation dynamics and exponential dephasing modeled in Eq. (5.7). As the pulse duration increases beyond the decoherence time $T_{2,\mathrm{Rabi}} = 3\,\mu\mathrm{s}$ in this simulation, dephasing leads to a significant reduction of oscillation contrast, demonstrating the impact of $T_{2,\mathrm{Rabi}}$ in long-time qubit control. Importantly, even when the qubit's phase is fully decohered, the spin-up fraction approaches half of the initial oscillation amplitude, as is observable for long pulse durations in the simulation. In practice, single-tone spectroscopy is used to resolve the qubit resonance, to enable the subsequent determination of the Rabi frequency or the $T_{2,\mathrm{Rabi}}$ coherence time of the system. However, successful single-tone spectroscopy requires two prerequisites: a sufficiently strong microwave drive and an approximate knowledge of the resonance frequency. Both prerequisites are established through the prior usage of RAP, as it allows to identify a frequency range in which the qubit resonance is located and a suitable single-tone drive power can be achieved by increasing the microwave power used for RAP by about 10 dBm. Furthermore, the yet unknown coherence time can be exploited to make sure that a measurable qubit signal is obtained by performing the single-tone spectroscopy for a pulse duration much longer than $T_{2,\mathrm{Rabi}}$ in comparable spin qubit systems. Usually $T_{2,\mathrm{Rabi}}$ is found to be in the range of several µs in natural silicon devices [21], thus by driving the qubit for more than 10 µs, the resonance can be visualized by probing the fully decohered signal from the qubit, which can yield up to 0.5 spin-up fraction with resonant drive.

In conclusion, RAP and single-tone spectroscopy are complementary techniques to determine the resonance frequency of a qubit system. RAP offers broadband, high-fidelity spin inversion and can be used to coarsely locate the resonance frequency range, which then guides the parameter window for finely resolved single-tone measurements. As further discussed in Sec. 5.3, both techniques jointly enable efficient identification of the qubit resonance condition and facilitate subsequent magnetic field calibration and qubit parameter extraction.

5.3 Determination of the qubit resonance frequency

This section presents the experimental implementation of qubit resonance frequency determination of the $^{\mathrm{nat}}$Si/SiGe D09 Die02 sample using a combined approach of rapid adiabatic passage (RAP) and single-tone spectroscopy. These measurements represent some of the earliest results obtained during device commissioning and are critical for enabling coherent qubit control. Once a suitable spin-selective readout working point has been established, the next objective is to determine the resonance frequency for a given applied magnetic field. This, in turn, allows extraction of the coil calibration factor that converts the applied coil current to an accurately calibrated magnetic field at the qubit site.

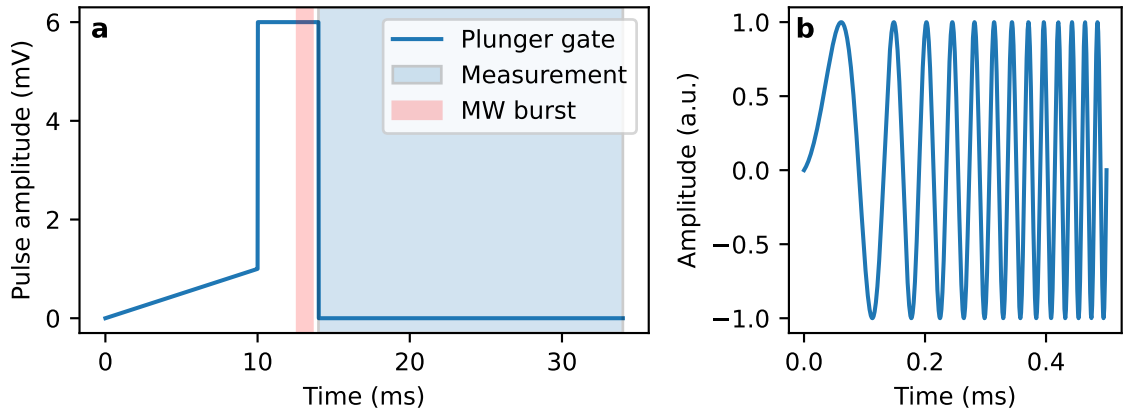

Figure 5.6: a Modified Elzerman-type plunger gate pulse used for spin-down initialization, spin manipulation, and spin-selective readout. The gradual voltage ramp during the loading stage minimizes thermal tunneling errors and improves initialization fidelity. The blue trace shows the voltage pulses applied to the plunger gate, the red shaded region marks the microwave (MW) burst used for qubit control, and the light blue region indicates the measurement window during which the SET current is recorded. **b** Schematic of a frequency-chirped waveform used for RAP. The illustrated chirp represents the in-phase (I) channel generated by an AWG. A quadrature (Q) channel with a ±90° phase shift is simultaneously applied for single-sideband (SSB) modulation via IQ mixing. The chirp duration and chirp range are optimized for illustrative clarity and are significantly greater in the actual experiment.

Plunger pulse form for single-qubit manipulation

To probe the qubit response to a microwave drive, a deterministic spin state must first be initialized, from which spin excitations can be reliably detected via spin-selective readout. The voltage pulse sequence applied to the qubit's plunger gate is shown in Fig. 5.6**a** and fulfills the tasks of loading an electron into the $|\downarrow\rangle$ state, pulsing the quantum dot deep below the reservoir for coherent manipulation, and returning to readout voltage for spin-selective readout. The blue trace depicts the plunger gate voltage, the red shaded region marks the timing and duration of the microwave burst, and the light blue window indicates the readout window, during which the SET current is recorded. This pulse sequence was employed for all single-qubit manipulations presented throughout this chapter.

The presented pulse is a modified version of the Elzerman protocol and incorporates a sloped loading stage, which starts at the readout voltage, and is designed to improve spin-down initialization fidelity and enhance robustness against electrostatic fluctuations. This approach is inspired by the ramped readout technique in Ref. [114], where a time-dependent voltage sweep during readout was utilized to perform spin state discrimination by analyzing the timing of blip events. In the context of spin initialization, sudden plunging from the readout voltage into the manipulation region has a finite probability to take place when the quantum dot is temporarily unoccupied due to thermally induced tunneling events. If the dot is empty at that moment, an excited spin-up electron could be loaded unintentionally, degrading initialization fidelity. By starting at the readout voltage, where only the spin-down energy state is below the reservoir, and gradually lowering the dot levels below the reservoir level, the thermal excitation probability is reduced to near zero

before the manipulation phase begins. Consequently, the sloped initialization method ensures deterministic preparation of a spin-down electron in the dot.

The microwave manipulation waveform used in RAP, shown schematically in Fig. 5.6**b**, represents a frequency chirp, which is an AC signal whose frequency increases linearly with time. In this work, linear chirps are characterized by a chirp rate $\dot{f} = \Delta f / \Delta t$, where Δf is the chirp range over which the frequency is modulated in the chirp duration Δt.

Experimental RAP and single-tone spectroscopy

Chirped pulses for RAP are generated using two output channels of an arbitrary waveform generator (AWG), which supply the in-phase (I) and quadrature (Q) signals to an IQ mixer with a relative phase shift of ±90°. The IQ mixer combines these signals with a local oscillator (LO) tone from a vector microwave source to produce single-sideband (SSB) modulation centered around the LO frequency in the GHz range (see Sec. 3.5). Broad-band RAP spectroscopy is performed by incrementally stepping the LO frequency while keeping the chirp parameters fixed, until the qubit resonance can be identified. As a practical guideline, the LO step size should be no greater than one-third of the chirp bandwidth Δf, which ensures that at least three neighboring chirp windows overlap the resonance frequency and produce measurable spin inversion, when the resonance lies within the chirp range.

The result of a RAP-based resonance search across a 0.6 GHz range is shown in Fig. 5.7**a**. For the initial scan (blue trace), a chirp with a modulation depth of 30 MHz (spanning 100 MHz to 130 MHz) and a chirp duration of 0.9 ms was applied using an external microwave power of −1 dBm and an AWG amplitude of 1 V. A distinct plateau consisting of three adjacent frequency points with elevated spin-up fraction near 19.6 GHz reveals the approximate qubit resonance. In the absence of a clear signature, suitable values for drive power and chirp rate can be determined empirically by incrementally increasing the drive power and decreasing the chirp rate over successive scans. Conveniently, wide chirp bandwidths can be used to minimize the number of parameter iterations needed to identify the resonance. In this setup, chirps ranges up to 300 MHz have been used successfully, limited primarily by the maximum AWG sampling rate and the requirement of at least eight samples per oscillation period at the highest frequency to preserve waveform integrity.

Once a coarse frequency range of interest is identified, a second RAP scan can be performed with finer resolution. The green trace in Fig. 5.7**a** and **b** shows a RAP sweep with a narrower 3 MHz chirp and an accordingly scaled chirp duration of 90 µs, centered at the previously identified resonance region. This refinement localizes the resonance to within a few MHz. In the final step, single-tone spectroscopy was used to resolve the resonance frequency with sub-MHz accuracy. The red trace in Fig. 5.7**b** shows a single-tone scan over the refined region using a 10 µs microwave burst and 0.2 MHz frequency steps. The spin-up fraction peaks at 50%, as expected for fully decohered Rabi oscillations under long pulse durations as discussed in Sec. 5.2.2. Additionally, the resonance peak can be fit using a Lorentzian lineshape [115] to extract the center frequency precisely.

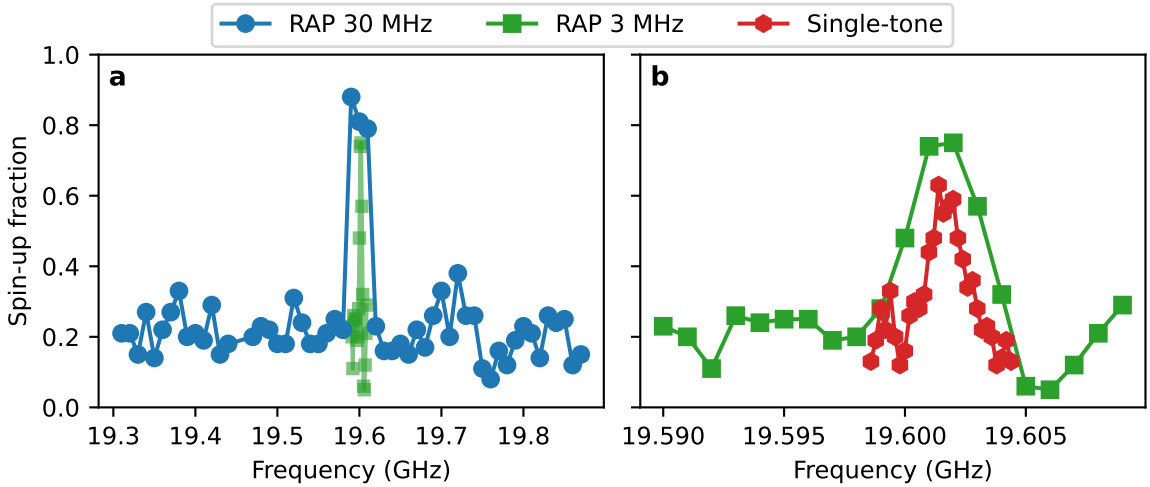

Figure 5.7: Identification of the left qubit resonance frequency of sample ^{nat}Si/SiGe D09 Die02 using RAP and single-tone spectroscopy. Each data point represents the average of 100 single-shot readouts, and solid lines are guides to the eye. **a** RAP spectroscopy performed by stepping the microwave frequency across a 0.6 GHz interval using −1 dBm external microwave power and 1 V AWG amplitude. The initial coarse sweep (blue trace) used a chirp bandwidth of 30 MHz and a duration of 0.9 ms. The appearance of three adjacent frequency points with elevated spin-up fraction identifies a frequency region containing the qubit resonance. A refined scan (green trace) centered around this region used a narrower 3 MHz chirp range and reduced chirp duration of 90 µs. **b** Low-range frequency scans using RAP and single-tone spectroscopy. The green trace represents the narrow-band RAP spectroscopy from panel **a** and further confines the resonance frequency to a ~4 MHz range of elevated spin-up fractions. The red trace shows a single-tone spectroscopy measurement with a 10 µs drive pulse, stepped in 0.2 MHz intervals. The resulting signal resolves a peak with Lorentzian lineshape centered at the qubit resonance frequency. Together, these techniques allow efficient coarse-to-fine localization of the qubit resonance, without requiring prior knowledge of qubit-specific parameters.

As soon as the qubit resonance frequency is determined, qubit-specific parameters such as optimal microwave power, Rabi frequency and π-pulse durations can be determined, as will be discussed in Sec. 5.6. This process is then repeated for each qubit on a chip to enable multi-qubit control. To illustrate the final outcome of the resonance search procedure, Fig. 5.8**a** and **b** show high-resolution single-tone spectroscopy data for the left and right qubit of sample ^{nat}Si/SiGe D09 Die02, respectively. In both cases, microwave pulse durations were chosen to match a π-rotation, yielding Lorentzian line shapes with improved visibility. The solid lines represent Lorentzian fits, yielding resonance frequencies of $f_{0,\mathrm{L}} = 19.593$ GHz and $f_{0,\mathrm{R}} = 19.863$ GHz for the left and right qubit, respectively. Notably, the left and right qubit resonances show a frequency difference of 270 MHz which originates from the magnetic field gradient created by the integrated cobalt micromagnet (CoMM) that allows to specifically target each qubit by their individual frequency to perform qubit operations, which will become relevant for two-qubit interaction, as discussed further in Sec. 6.1.

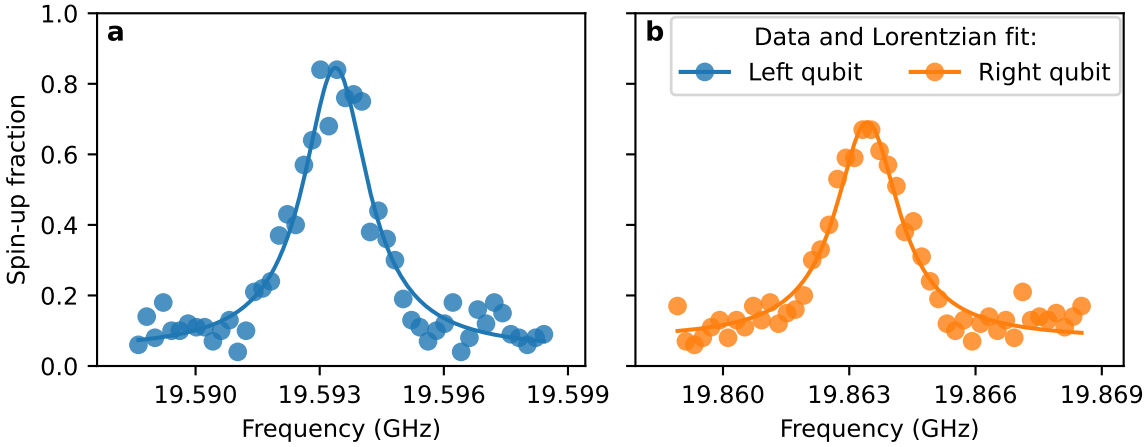

Figure 5.8: Single-tone spectroscopy of both qubits of sample ^{nat}Si/SiGe D09 Die02 using drive pulses with calibrated π-pulse durations. The experiments were performed with 18 dBm external microwave power and AWG amplitudes of 0.4 V for the left qubit and 1 V for the right qubit. Each data point averages 100 single-shot readouts. Solid lines represent Lorentzian fits to the data. **a** Spin-up fraction of the left qubit as a function of microwave frequency, showing a resonance centered at $f_{0,\mathrm{L}} = 19.593$ GHz. **b** Analogous measurement for the right qubit, yielding a resonance frequency of $f_{0,\mathrm{R}} = 19.863$ GHz. The observed frequency separation of 270 MHz between the two qubits originates from the magnetic field gradient of the cobalt micromagnet integrated in the device.

Magnetic field setup and cobalt micromagnet calibration

Accurate control and calibration of the magnetic field experienced by spin qubits are critical for frequency-selective qubit addressing and the interpretation of magnetospectroscopy measurements. The total effective magnetic field B_{tot} at the qubit site determines its resonance frequency ω_0 through the Zeeman relation

$$\hbar\omega_0 = g\mu_{\mathrm{B}}B_{\mathrm{tot}} = g\mu_{\mathrm{B}}(\kappa_{\mathrm{coil}}I_{\mathrm{coil}} + B_{\mathrm{CoMM}}), \tag{5.8}$$

where $g \approx 2$ is the Landé factor for electrons in silicon [74] and μ_{B} is the Bohr magneton. In the second equality, B_{tot} is expressed in terms of separate contributions of the superconducting vector magnet, which is represented by the coil calibration factor κ_{coil} in T/A times the applied current I_{coil}, and the on-chip cobalt micromagnet (CoMM), whose magnetization generates a field offset B_{CoMM}.

To extract both parameters experimentally, the resonance frequencies of the left and right qubit of sample ^{nat}Si/SiGe D09 Die02 were measured over a range of coil currents using the combined RAP and single-tone spectroscopy procedure described in Sec. 5.3. Accurate determination of the CoMM's magnetic offset requires consistent magnetization due to the hysteresis of ferromagnetic materials. To ensure consistent magnetization, the external field was always ramped to its maximum value of about 1 T in between each measurement point to guarantee full saturation in the applied field direction. Prior work on nominally identical devices confirm that the micromagnet reaches magnetic saturation at fields above 0.2 T [24]. The resulting data of the calibration measurement, plotted in Fig. 5.9, were fit with a linear model for each qubit. The extracted coil calibration factors

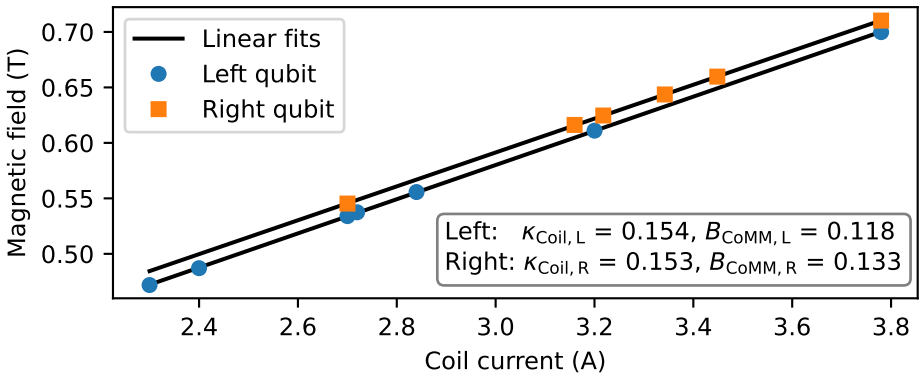

Figure 5.9: Effective magnetic field calibration using the resonance frequencies of the left and right qubit as a function of applied coil current. Data points are obtained using RAP and single-tone spectroscopy and each point averages 100 single-shot readouts. Linear fits (black lines) yield nearly identical coil calibration factors of 0.154 T/A and 0.153 T/A for the left and right qubit, respectively. The extracted cobalt micromagnet (CoMM) field offsets are 0.118 T for the left and 0.133 T for the right qubit, resulting in a magnetic field difference of 15 mT at zero external field.

$\kappa_{\mathrm{coil,L}} = 0.154\,\mathrm{T/A}$ and $\kappa_{\mathrm{coil,R}} = 0.153\,\mathrm{T/A}$ demonstrate good agreement across both qubits. The slight discrepancy is likely due to limited statistics, as the qubits are spaced by less than 100 nm and field inhomogeneities from the external coil are assumed to be negligible on that scale. The extracted CoMM offsets are $c_{\mathrm{CoMM,L}} = 0.118\,\mathrm{T}$ and $c_{\mathrm{CoMM,R}} = 0.133\,\mathrm{T}$, corresponding to a magnetic field difference of 15 mT at zero external field. This difference stems from the spatial magnetic field gradient engineered into the CoMM design to enable individual qubit addressability and plays an important role in enabling two-qubit operation in this device.

Using this magnetic field calibration, qubit control can be optimized by deterministically targeting specific resonance frequency ranges. This enables, for example, the selection of operating points with favorable RF-line transmission characteristics or operation far from the valley splitting to avoid regions of enhanced energy relaxation. During extended cool-downs, a helium vessel replacement of the cryostat requires powering down the magnetic field coils. To reliably restore the magnetic field state afterward, the coils were first ramped to the maximum field to re-saturate the cobalt micromagnet (CoMM), and then returned to the desired setpoint. Without further stabilization, this procedure can lead to resonance frequency shifts on the order of 10 MHz. To enhance reproducibility, a damped oscillatory ramp protocol was employed: the target current was overshot by about 10% and then approached using a damped sinusoidal trajectory. This approach consistently restored the qubit resonance frequency to within 1 MHz of its original value. The resulting protocol allowed to reuse the calibration of both the external magnetic field and the micromagnet offset across experimental sessions.

5.4 Applications and limitations of the rapid adiabatic passage method

Rapid adiabatic passage (RAP) is a widely used and valued technique for spin manipulation in semiconductor qubits, enabling high-fidelity state inversion even at low drive power and noisy environments [101–104]. As outlined in the theoretical framework of Sec. 5.2.1, RAP enables up to ideal spin inversion fidelities without requiring precise resonance conditions, making it especially attractive for systems with inhomogeneous broadening or fluctuating environments. This section presents experimental demonstrations and limitations of RAP-based spin inversion in a silicon spin qubit. All measurements were performed a single-qubit on the ^{28}SiMOS D06 Die07 device with the SD5 gate layout (cf. Sec. 2.5) and employing ESR-based qubit control (cf. Sec. 2.7). The experiments were carried out using a cryogenic setup that is comparable to the one used throughout this thesis (for details see Ref. [116]), and represent early device and setup characterization results. This particular SiMOS device exhibited significant magnetic noise fluctuations that rendered coherent manipulations unstable and required frequent retuning. However, the excellent signal-to-noise ratio of this sample enabled detailed investigation of RAP performance under realistic experimental conditions.

5.4.1 Quantifying spin inversion fidelity

Building on its successful application for coarse qubit resonance identification, an important question is how closely RAP can approach ideal spin inversion fidelity under realistic experimental conditions. While adiabatic frequency sweeps theoretically enable near-perfect inversion, system-specific interactions beyond the ideal Landau-Zener model and control imperfections may limit the experimentally achievable fidelity. To investigate this, spin inversion by RAP is systematically analyzed by testing different chirp rates $\dot{f}$ while stepping the microwave drive frequency over a ±10 MHz range around the qubit resonance. Each RAP manipulation is performed with a fixed chirp range $\Delta f = 10\,\mathrm{MHz}$, while the chirp duration Δt is varied to tune the adiabaticity parameter $f_{\mathrm{Rabi}}^2/\dot{f}$. All experiments begin with deterministic spin-down qubit initialization at a suitable spin-selective readout working point.

The results of a subset of all tested chirp durations are shown in Fig. 5.10**a**. Each trace corresponds to a different chirp duration, with plateau-like regions of elevated spin-up fraction emerging for LO frequencies within ±5 MHz of the resonance. The width of these plateaus closely matches the chirp range, confirming that RAP reliably inverts the spin when the resonance lies within the swept frequency band. The sharp edges of the plateaus indicate that the frequency range that needs to be chirped over the resonance for full spin inversion is narrower than the measurement resolution of 0.5 MHz. Importantly, longer chirp durations yield higher plateau amplitudes, consistent with increased adiabaticity and reduced Landau-Zener transition probabilities.

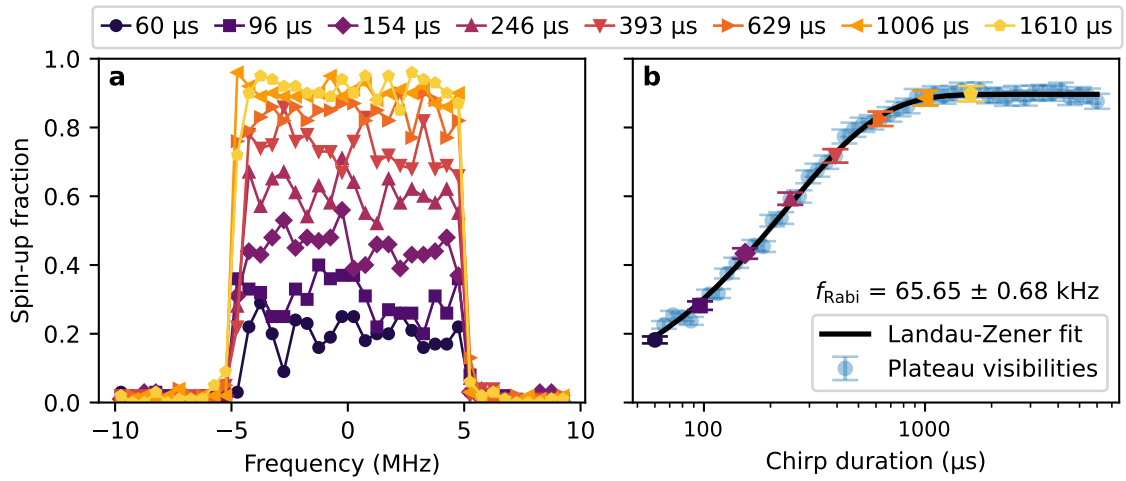

Figure 5.10: Characterization of spin inversion fidelity using RAP on the ^{28}SiMOS D06 Die07 device. The measurements were performed at an external microwave power of −2 dBm on a comparable cryogenic setup (see Ref. [116] for details). **a** Spin-up fraction resulting from RAP as a function of microwave frequency, offset by the qubit's resonance frequency $f_0 = 18.5\,\mathrm{GHz}$. Each colored trace corresponds to a fixed chirp duration, using a constant chirp range of $\Delta f = 10\,\mathrm{MHz}$. The formation of plateaus in the spin-up fraction confirms successful spin inversion whenever the resonance frequency lies within the chirped frequency band. Longer chirp durations yield higher plateau amplitudes, consistent with improved adiabaticity and reduced Landau-Zener transition probabilities. Each point represents the average of 100 single-shot readouts and solid lines serve as guide for the eye. **b** Extracted spin-up visibilities as a function of chirp duration on a logarithmic scale. The visibility is defined as the difference between the average spin-up fraction within and outside the plateau region. The data are fitted using the Landau-Zener model in Eq. (5.9), yielding a Rabi frequency of $f_{\mathrm{Rabi}} = (65.65 \pm 0.68)\,\mathrm{kHz}$. Colored points correspond to the traces in panel **a**, and error bars represent the propagated standard deviation of each visibility estimate. These results confirm the high fidelity and robustness of RAP and establish its utility for extracting qubit parameters and assessing SPAM errors.

To quantify spin inversion fidelity, the RAP visibility is defined as the difference between the average spin-up fraction within the plateau and that of off-resonant background regions. The extracted visibilities are plotted in Fig. 5.10**b** as a function of chirp duration. Each point represents a full RAP scan, with error bars indicating the standard deviation across plateau and background averages. As expected, the visibility increases with chirp duration and saturates around 90%, suggesting a maximum achievable fidelity limited by state preparation and measurement errors (SPAM, [117]) rather than RAP itself.

To model the experimental trend, the data are fitted with the Landau-Zener transition probability subtracted from unity, yielding

$$P_{|g\rangle,\mathrm{LZ}} = A\left(1 - \exp\left(-\frac{\pi^2 f_{\mathrm{Rabi}}^2}{\dot{f}}\right)\right), \tag{5.9}$$

where A accounts for the SPAM-limited visibility ceiling, and $\dot{f} = \Delta f/\Delta t$ is the chirp rate. Using this fit, the effective Rabi frequency is extracted as $f_{\mathrm{Rabi}} = (65.65 \pm 0.68)\,\mathrm{kHz}$, in good agreement with independently determined Rabi frequencies under coherent drive (see Sec. 5.6). This confirms that RAP can also be employed as a tool to estimate Rabi frequencies

in systems where coherent oscillations are obscured by noise. Further discussion on this application is provided in Sec. 5.4.3.

Interestingly, the saturation of visibility beyond a chirp duration of 1006 µs suggests that a threshold condition for adiabaticity is reached. Using the extracted Rabi frequency, this threshold corresponds to $f_{\mathrm{Rabi}}^2/\dot{f} > 0.4$, providing a useful experimental benchmark for the adiabatic regime.

In conclusion, these measurements demonstrate that RAP enables high-fidelity spin inversion under realistic experimental conditions, closely approaching theoretical limits. The remaining deviations from perfect inversion are likely due to state preparation and measurement (SPAM) errors, arising from the control protocol or readout configuration rather than limitations of the RAP method itself. This makes RAP not only a robust and efficient technique for reliable qubit control, but also a valuable tool for quantifying and reducing SPAM errors. Its inherent insensitivity to precise resonance conditions and its high visibility make RAP an effective strategy for efficient resonance frequency determination and benchmarking the fidelity of control and readout schemes.

5.4.2 Frequency-dependent RF-line transmission

Beyond its utility for resonance identification, RAP provides a sensitive tool for probing the frequency-dependent transmission properties of the microwave lines in a given experimental setup. This is particularly valuable for identifying optimal frequency windows for qubit operation and diagnosing unwanted dissipation effects.

The results in Fig. 5.11**a** show RAP measurements as a function of applied magnetic coil currents in which the resonance frequency of a spin qubit was determined across a range of 6 GHz to 20 GHz. The RAP protocol was performed at a fixed external microwave power of 13 dBm, using a chirp range of 10 MHz, a chirp duration of 105 µs, and a frequency resolution of 3 MHz. For each probed microwave frequency, the magnetic field (via the coil current) was swept to identify the resonance condition, thereby enabling calibration of the coil's field conversion factor. The RAP parameters were chosen to induce a spin-up fraction of approximately 40% at a nominal qubit resonance frequency of 18.5 GHz. This value corresponds to operation on the slope of the Landau-Zener curve (see Fig. 5.10**b**), rendering the resulting spin-up signal highly sensitive to the Rabi frequency and thus to any frequency-dependent variations in the transmission efficiency of the RF lines.

The measurement results depicted in Fig. 5.11**a** reveal pronounced variations in the spin-up fraction as a function of microwave frequency, affecting both the plateau amplitude and off-resonant background. Although the measurement was automated and the qubit working point was not re-optimized for each field setting, the reservoir level was consistently aligned between the two spin states. This ensures reliable readout fidelity over a broad Zeeman energy range and allows the observed variations to be reasonably attributed to RF-line transmission characteristics.

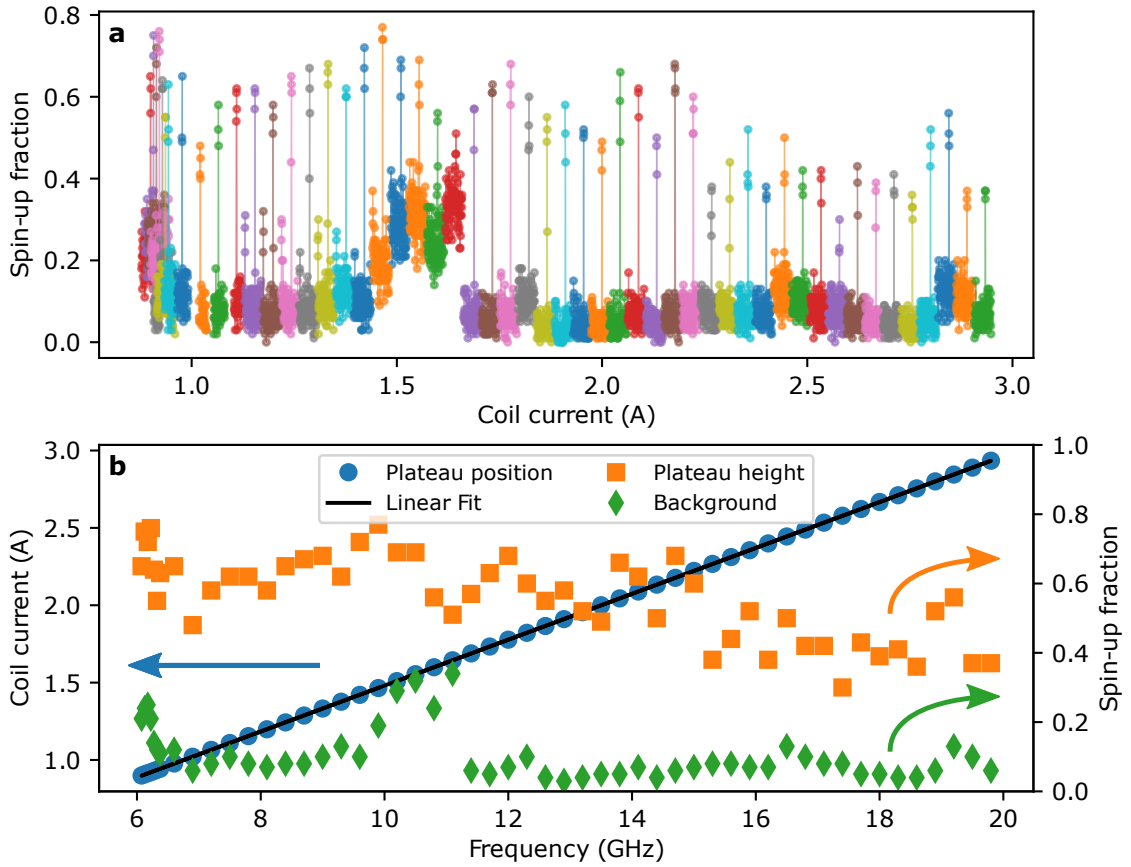

Figure 5.11: Calibration of magnetic field setup and RF-line characterization using RAP across a frequency range of 6 GHz to 20 GHz on the ^{28}SiMOS D06 Die07 device. Measurements were conducted with 13 dBm external microwave power, a chirp range of 10 MHz, chirp duration of 105 µs, and frequency resolution of 3 MHz. **a** RAP-induced spin-up fractions as a function of applied coil current for each microwave frequency. Each trace represents one RAP sweep over magnetic field at a fixed frequency. Variations in plateau height and background levels reflect frequency-dependent RF-line transmission and drive efficiency. The chosen RAP parameters provide sensitivity to Rabi frequency fluctuations, allowing this data to highlight optimal transmission windows. Each point averages 100 single-shot readouts. **b** Extracted RAP peak positions (blue circles) plotted as coil current versus microwave frequency. A linear fit (black line) through the origin yields a coil calibration factor of $\kappa_{\text{coil}} = 0.241$ T/A. Orange squares denote maximum spin-up fractions, while green diamonds indicate off-resonant background levels. The results identify frequency bands with optimal signal-to-noise performance (e.g., 14 GHz and 19 GHz), as well as regions with elevated dissipation (e.g., 10.5 GHz), providing valuable feedback for selecting robust qubit control frequencies.

In Fig. 5.11**b**, the extracted resonance positions (blue points) exhibit a linear dependence on coil current, consistent with the expected Zeeman relation. A linear fit through the origin yields a coil calibration factor of $\kappa_{\text{coil}} = 0.241\,\text{T}\,\text{A}^{-1}$. The orange and green markers display the peak RAP signal amplitude and background counts, respectively, highlighting the impact of frequency-dependent RF transmission on the effective spin inversion fidelity. In particular, a notable increase in background signal around 10.5 GHz suggests significant microwave-induced heating or dissipation, making this range suboptimal for qubit operation. Conversely, frequency windows near 14 GHz and 19 GHz exhibit enhanced RAP

signal and reduced background, indicating favorable signal transmission and low noise operation regimes ideal for high-fidelity qubit control.

These observations underscore RAP's utility not only for qubit initialization and resonance mapping, but also as a diagnostic tool for identifying suitable operating frequencies and optimizing control hardware for spin qubit platforms.

5.4.3 Rabi frequency estimation and fidelity limits in chirped spin inversion

Beyond its primary role in enabling robust spin initialization, RAP also serves as a valuable diagnostic technique for estimating the Rabi frequency as a function of applied microwave power, particularly in regimes where conventional coherent control is limited by noise. To investigate this application, a series of RAP visibility measurements was performed following the protocol described in Sec. 5.4.1. All measurements were conducted at a fixed qubit resonance frequency of 18.5 GHz, using a constant chirp range of 10 MHz, while systematically varying the chirp duration and external microwave power. The resulting spin-up fractions are shown in Fig. 5.12**a**, with each trace corresponding to a distinct drive power. Error bars indicate the propagated uncertainties from the visibility extraction.

For low microwave powers, the data follow the expected Landau-Zener trend, where increasing chirp duration leads to higher visibility due to improved adiabaticity. However, for higher powers and longer chirp durations, a reduction in spin-up fraction is observed after initial saturation. This deviation signals the emergence of drive-induced dissipation (DID), a non-negligible loss mechanism in strongly driven systems [103]. DID originates from enhanced coupling between the driven qubit and its electromagnetic environment. As the qubit is swept through resonance under strong drive, transitions between instantaneous eigenstates can couple resonantly to high-frequency environmental modes, such as charge noise or electromagnetic fluctuations. Unlike quasi-static dephasing, which primarily limits coherence in idle states, DID induces energy relaxation during the drive itself. This dissipation becomes increasingly effective with larger drive amplitudes and longer interaction durations, scaling with the strength of the Rabi frequency and the spectral density of environmental noise near the instantaneous energy splitting. To model this effect, the Landau-Zener formula is extended with a phenomenological term accounting for DID [103]:

$$\begin{aligned} P_{|g\rangle,\mathrm{DID}} =& \frac{A}{2}\left(1-\exp\left(-\frac{\pi^2 f_{\mathrm{Rabi}}^2}{\dot{f}}\right)\right) \\ & \times\left[1+\exp\left(-f_{\mathrm{Rabi}}^2\tau_c\Delta t\right)\tanh\left(\frac{\dot{f}}{2\pi f_{\mathrm{Rabi}}}\left(\Delta t-\frac{\Delta f}{\dot{f}}\right)\right)\right], \end{aligned} \tag{5.10}$$

where τ_c describes the signal decay rate, f_{Rabi} is the Rabi frequency, $\dot{f}$ is the chirp rate, and Δt is the chirp duration. This model captures both the adiabatic nature of RAP and the observed decay at high power and long chirp durations.

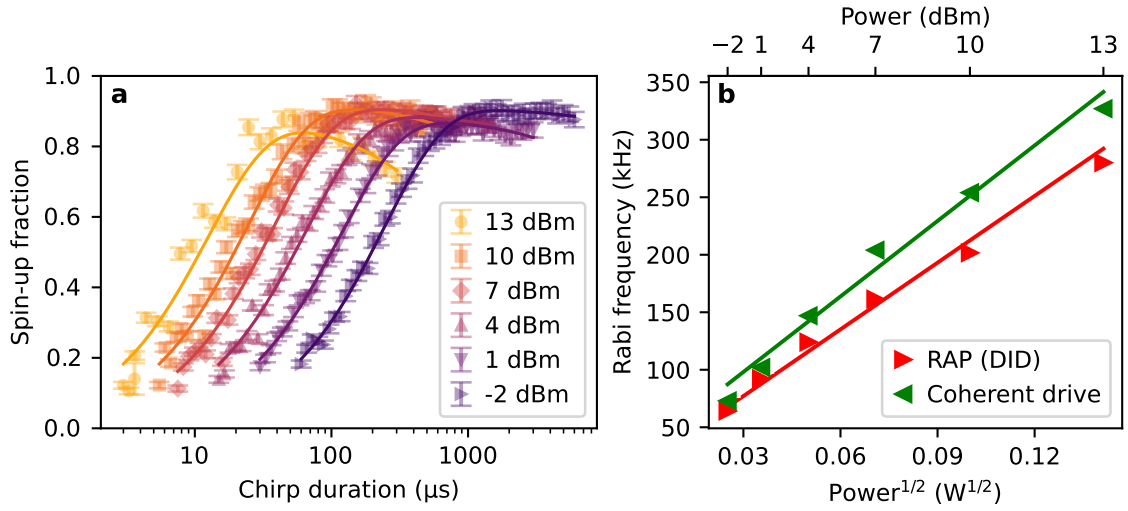

Figure 5.12: Characterization of power-dependent spin inversion fidelity and Rabi frequency estimation using RAP on the ^{28}SiMOS D06 Die07 device. **a** Spin-up visibilities as a function of chirp duration obtained using RAP for different external microwave powers at a fixed qubit resonance frequency of 18.5 GHz. All traces use a constant chirp range of $\Delta f = 10$ MHz. The saturation and subsequent decline in visibility at high powers reflect the onset of DID for strong driving conditions and long pulse durations. Solid lines are fits using the DID-extended Landau-Zener model of Eq. (5.10), which captures both the adiabatic transition probability and the decay in fidelity due to environmental coupling. Error bars represent propagated uncertainties from visibility extraction. **b** Extracted Rabi frequencies (red) from panel **a** plotted as a function of the square root of the applied microwave power. For reference, independently obtained Rabi frequencies from coherent manipulation (green) are shown for comparison. Linear fits (solid lines) confirm a linear scaling of Rabi frequencies with drive amplitude and validate the method of Rabi frequency estimation using RAP.

Fits of the DID-extended Landau-Zener model (Eq. (5.10)), shown as solid lines in Fig. 5.12**a**, accurately capture the observed data and allow reliable extraction of the Rabi frequency f_{Rabi} for each microwave power setting. The extracted values are plotted in Fig. 5.12**b** as a function of the square root of the applied microwave power, revealing a clear linear dependence consistent with the expected scaling from Eq. (2.19). For comparison, independently determined Rabi frequencies obtained from coherent oscillation experiments (see Sec. 5.6) are included as green points. These values are systematically higher than those derived via RAP, a discrepancy that may arise from transient detuning effects or resonance frequency drift caused by magnetic field fluctuations over the extended acquisition times required to resolve slow oscillations in the kilohertz regime. Such fluctuations, which also impaired the stability of coherent control, likely contribute to the enhanced dissipation observed in the chirped protocol.

In conclusion, RAP offers a reliable and experimentally validated approach for estimating Rabi frequencies in the presence of environmental noise and drive-induced dissipation. Its intrinsic resilience to detuning and its dependence on the instantaneous energy gap render it particularly suitable for operation in regimes where coherent control is unstable or infeasible. By extending the Landau-Zener model to incorporate dissipation effects, the observed spin inversion fidelities can be accurately described even under strong driving. Importantly, high-fidelity spin inversion using RAP remains effective without

requiring precise resonance alignment, relying instead on a sufficiently broad frequency chirp to encompass the qubit transition. These characteristics establish RAP as a robust and versatile technique for qubit initialization and characterization in realistic and noise-affected experimental environments.

5.5 Spin relaxation time and valley splitting estimation

The energy relaxation time T_1 quantifies the lifetime of an excited quantum state before it decays into the ground state. In the context of spin qubit operation, T_1 sets an upper bound for coherent qubit control, involving state preparation, manipulation, and readout. A sufficiently long T_1 ensures that the qubit remains in its prepared state during the manipulation sequence and that spin relaxation does not obscure readout fidelity. Understanding and measuring T_1 is therefore central to assessing qubit performance and benchmarking device quality.

To measure T_1, the spin qubit is first initialized in its excited state $|\uparrow\rangle$, followed by a variable wait time t, and then read out via spin-to-charge conversion. The probability of detecting the spin-up state decays exponentially with wait time and can be modeled as [97]

$$P_{|\uparrow\rangle}(t) = A \cdot \exp\left(-\frac{t}{T_1}\right) + c\,, \tag{5.11}$$

where A denotes the initial amplitude governed by state preparation and readout fidelities, and the offset c captures thermal events in the readout window which occurrence strongly depends on the selected readout voltage. Since thermal events are evenly distributed over time, they will shift the baseline of the measurement but do not affect the exponential decay profile.

The spin relaxation time experiment on the left qubit of sample $^{\text{nat}}$Si/SiGe D09 Die02 utilized the plunger pulse sequence scheme described in Sec. 5.3 and was performed with spin-up initialization using RAP for robust state preparation. Fig. 5.13**a** shows a representative measurement of the exponential decay of spin-up probability over wait time on a logarithmic scale, yielding $T_1 = (227 \pm 17)\,\text{ms}$. While the displayed data have been recorded using the left qubit at an exemplary magnetic field of $B = 504\,\text{mT}$, similar results have been obtained for the right qubit. Such T_1 times are consistent with previously reported values in natural silicon, typically ranging from tens of milliseconds to seconds [21]. Although cobalt micromagnets (CoMMs) can reduce T_1 via magnetic field noise [23], the measured value here remains sufficiently long for reliable qubit operation, where a single-shot measurement takes about 20 ms. The inset in Fig. 5.13**a** illustrates the interleaved short/long wait time sequence in which the T_1 measurement has been performed. The interleaved sequence serves as an experimental stability check, since well-separated signal levels forming a continuous "ribbon" indicate minimal working point drift and reliable spin-up fraction acquisition, while large fluctuations or distortion from the ribbon shape challenge the validity of the measurement.

However, T_1 is not a fixed quantity and can vary substantially across different qubit working points. It is sensitive to electron temperature, magnetic field strength, and electrostatic confinement, all of which may shift due to gate voltage tuning.

Valley splitting

The lifting of valley state degeneracy in Si-based qubit device architectures was introduced in Sec. 2.3. The influence of the first excited valley state becomes particularly relevant in the context of spin relaxation times. Spin relaxation in silicon quantum dots is predominantly driven by the interplay of spin-orbit coupling and spin-valley mixing, mediated by phonon and Johnson noise [51]. In the regime of low temperatures and high magnetic fields, which is relevant for the device under investigation, the dominant spin relaxation mechanism is phonon-assisted spin-valley relaxation [48]. At intermediate magnetic fields, the relaxation rate $1/T_1$ increases sharply near magnetic fields where the Zeeman energy E_Z matches the valley splitting energy E_V as has been experimentally demonstrated in literature [23, 48, 51, 64]. The valley splitting E_V quantifies the energy difference between the two lowest conduction band valleys in a silicon quantum dot. When the Zeeman energy $E_Z = g\mu_B B$ approaches E_V, the spin-up state of the lower valley hybridizes with the spin-down state of the upper valley, forming an avoided level crossing. This spin-valley anti-crossing opens a strong spin relaxation channel, by permitting phonon-induced spin-flip transitions due to spin-orbit coupling induced state hybridization that strongly mixes the valley and spin degrees of freedom [55]. Therefore, it is important to assess the valley splitting in Si-based qubit systems to avoid operation at magnetic fields were the Zeeman splitting is close to the valley splitting in order to establish suitably long T_1 times for qubit operation.

A schematic Zeeman diagram in Fig. 5.13**b** illustrates the spin-valley anti-crossing and the evolution of ground-state energies across different charge occupancies of a quantum dot, denoted as (n). The four branches represent the energy evolution of the $|\downarrow\rangle$ and $|\uparrow\rangle$ states in the ground and first excited orbital states as a function of magnetic field. Although the energy spacing between these levels is generally governed by the singlet-triplet splitting E_{ST}, in strongly confined Si-based qubit systems the lower and upper pairs of branches can be associated with the ground and excited valley states, respectively, which are separated by the valley splitting E_V [118, 119]. In a real quantum dot, this energy evolution can be experimentally accessed by tracking the magnetic-field dependence of charge transition voltages for increasing electron occupations. In particular, E_V can be extracted by measuring the $(1) - (2)$ charge transition as a function of magnetic field and identifying the field B_{ST} at which the transition slope changes sign.

Experimental tracking of the $(1) - (2)$ charge transitions for the left and right dot of device ^{nat}Si/SiGe D09 Die02 device as a function of magnetic field are presented in Fig. 5.13**c** and **d**, respectively. In both measurements, the charge transition was probed via the remote plunger gate of the opposite dot, instead of the dedicated plunger gate of the probed quantum dot, to intentionally reduce the lever arm and hence improve the energy resolution. The color scale in the plots represents the differential SET conductance, with the charge transition voltage identified at the point of maximum derivative. To facilitate

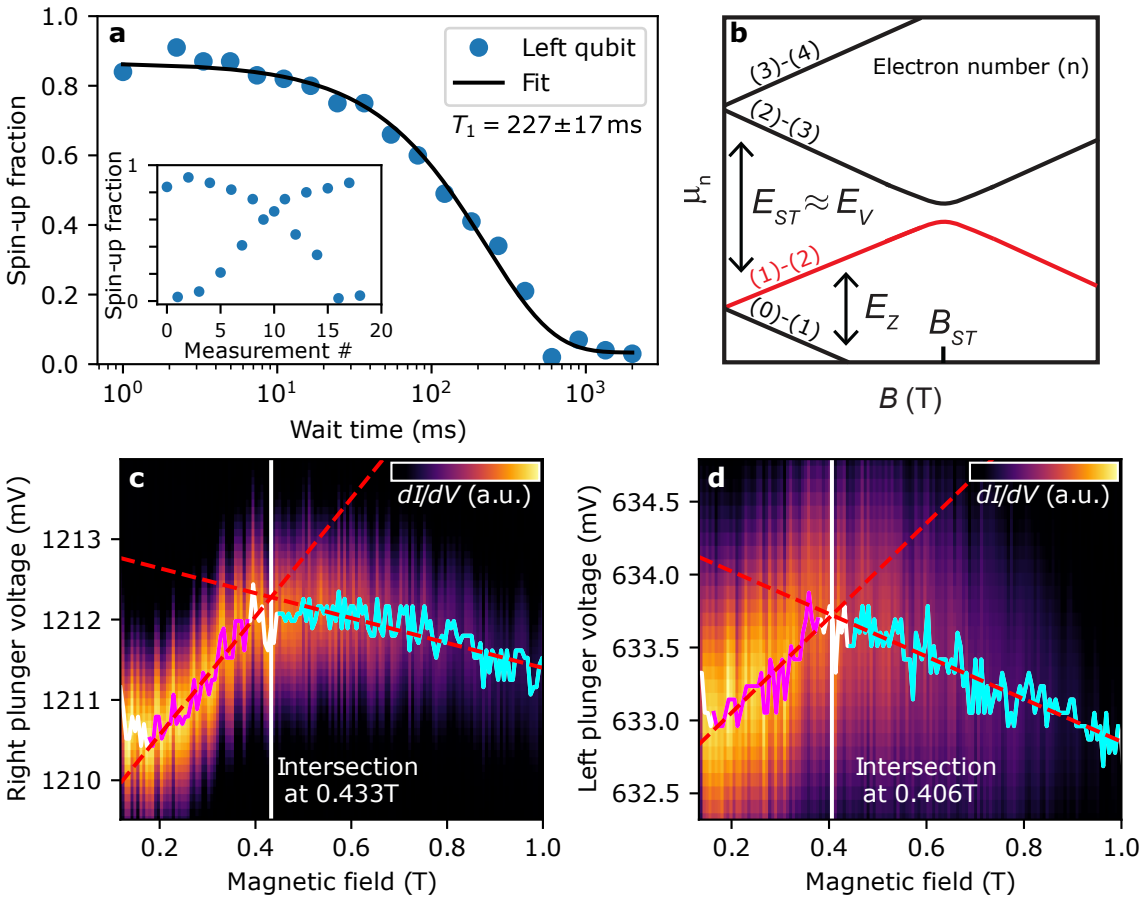

Figure 5.13: Spin relaxation and valley splitting characterizations of the ^{nat}Si/SiGe D09 Die02 device. **a** Spin-up probability as a function of wait time after RAP-based spin-up initialization of the left qubit at a magnetic field of 504 mT. Each data point represents the average of 100 single-shot readouts. The data follow an exponential decay, yielding a relaxation time of $T_1 = (227 \pm 17)$ ms, indicating long-lived spin states suitable for qubit control. The inset shows an interleaved sequence of short and long wait times, used to confirm experimental stability by verifying consistent spin-up fraction contrast over time. **b** Zeeman diagram representing the conceptual energy evolution of spin states in the two lowest valley levels of a silicon quantum dot. The red line can be traced by measuring the $(1) - (2)$ charge transition and it undergoes a characteristic slope inversion when the Zeeman energy E_Z matches the valley splitting E_V at the spin-valley anti-crossing. This signature enables extraction of E_V from magnetospectroscopy measurements. Adapted from Ref. [58]. **c** Valley splitting determination for the left quantum dot, measured from high to low magnetic fields to ensure reproducible CoMM magnetization. The smoothed differential SET current is shown as a function of right plunger voltage and magnetic field while tracking the $(1) - (2)$ charge transition. The right plunger gate was used to achieve a higher energy resolution of the left dot's charge transition due to weak cross-capacitive coupling. The charge transition of each vertical trace is extracted as the point of maximal derivative (white line), and linear fits (dashed red lines) are applied to segments before (pink) and after the slope inversion (cyan). Their intersection at $B_{ST,L} = 0.433$ T yields a valley splitting of $E_{V,L} = 50$ µeV. **d** Analogous measurement for the right dot using the left plunger gate. The transition exhibits a kink at $B_{ST,R} = 0.406$ T, corresponding to a valley splitting of $E_{V,R} = 47$ µeV. Both valley splittings are well below the typical operational field of 700 mT with corresponding Zeeman splitting of $E_Z = 81$ µeV.

interpretation, the maxima of each vertical line derivative were traced with a white line and subsequently linear fits (dashed red lines) were applied to pink and cyan colored segments

to extract the B_{ST} value at their intersection. The $(1) - (2)$ charge transition voltages of both quantum dots change linearly with magnetic field, and the slopes exhibit a sign change at $B_{ST,L} = 0.433\,\mathrm{T}$ and $B_{ST,R} = 0.406\,\mathrm{T}$, corresponding to valley splitting energies of $E_{V,L} = 50\,\mu\mathrm{eV}$ and $E_{V,R} = 47\,\mu\mathrm{eV}$ for the left and right quantum dot, respectively.

The obtained valley splitting energies are significantly smaller than the Zeeman splitting of $E_Z = 81\,\mu\mathrm{eV}$ at the chosen operational magnetic field of $B = 700\,\mathrm{mT}$, which effectively suppresses spin-valley relaxation. However, this same condition permits partial thermal occupation of excited valley states, thereby enabling valley-related effects to affect qubit control. The most prominent observed valley-related signature is the appearance of a second resonance peak in single-tone spectroscopy using pulse durations (>20 µs) which originates from a finite thermal population of the valley state during qubit initialization that can be excited coherently at a characteristic resonance frequency. The evolution of this signature is resolved as a function of the interdot barrier tuning and further discussed in Sec. 6.2.1. In practice, valley-related effects were limited to long pulse operations in this device and did not interfere with typical qubit gate timescales (~1 µs). In confined quantum systems, the pronunciation of valley effects is strongly dependent on local disorder of the interface quality at the qubit site. This renders the energy relaxation time and valley splitting energy of a Si-based spin qubit very sensitive to the exact working point as impressively demonstrated in Ref. [50]. However, the valley splitting shown here was obtained for the final set of working point voltages compatible with two-qubit operation, although significantly higher valley splittings have been observed during early tuning stages (see Sec. A.2 in the appendix). The optimization of the working point for larger valley splittings in conjunction with establishing operational two-qubit conditions have not been pursued within this thesis, but might be a fruitful approach for further improving control fidelity and reducing valley-induced artifacts in future experiments.

The results presented in this section give reference values for spin relaxation rates and valley splitting of the studied SiGe sample. The presented T_1 time of 227 ms represents the order of magnitude of spin relaxation times for most working points of both qubits and is sufficient for robust qubit control. The reported valley splitting energies of both dots at a working point compatible with two-qubit operation are well below the operated magnetic field values and necessitate the consideration of valley-related effects in data interpretation.

5.6 Coherent spin manipulation

Coherent manipulation of individual spin states represents the central requirement for operation of spin-based quantum information processors. The experimental realization of such control builds upon previously discussed efforts ranging from quantum dot formation and reservoir coupling optimization to resonance frequency determination. Having established robust qubit initialization and readout conditions, this section presents coherent quantum state control for both qubits in the ^{nat}Si/SiGe D09 Die02 device, which is a major milestone in the functional validation of the Si/SiGe platform studied in this work.

5.6.1 Rabi oscillations

The continuous spin state population transfer induced by a resonant microwave drive, known as Rabi oscillations, enables the preparation of arbitrary spin superposition states by precisely timed rotations on the Bloch sphere. Such calibrated manipulation pulses, called qubit gates, comprise the fundamental building blocks of quantum computation. Following the theoretical framework introduced in Sec. 2.7, a spin qubit subjected to a transverse oscillating field $B_1(t) = B_1 \cos(\omega t + \phi)$ will undergo deterministic evolution on the Bloch sphere about an equatorial rotation axis. The polar angle of the rotation axis is defined by the phase ϕ of the drive field. In particular, a drive field with $\phi = 0$ rotates the spin vector about the x-axis and a manipulation with $\phi = \pi/2$ corresponds to a rotation about the y-axis. The blue trajectory in Fig. 5.14**a** conceptually illustrates the controlled evolution of the qubit state vector under resonant driving with $\phi = 0$ and the black arrows indicate that specific pulse durations correspond to targeted locations on the Bloch sphere.

Rabi oscillations can be probed experimentally by stepping the pulse duration of the microwave manipulation and observing the resulting spin-up fraction after each duration. In Fig. 5.14**b**, an exemplary AWG output of fixed pulse duration is shown, generating I and Q signals with a $\pm 90^\circ$ phase shift to select either the upper or lower IQ mixer sideband (cf. Sec. 3.5), to target one of the two qubit frequencies determined as described in Sec. 5.3. With knowledge of the resonance frequencies of $f_{0,\mathrm{L}} = 19.6\,\mathrm{GHz}$ for the left and $f_{0,\mathrm{R}} = 19.87\,\mathrm{GHz}$ for the right qubit, microwave bursts of variable duration were applied to probe the time-dependent evolution of each single-qubit at an intermediate external microwave power of 18 dBm. AWG modulation amplitudes were set at 0.4 V (left qubit) and 1.0 V (right qubit) to achieve comparable driving conditions, facilitating subsequent comparative analysis of coherence and performance metrics.

The results of both experiments are presented in Fig. 5.14**c** and **d** for the left and right qubit, respectively. Both qubits exhibit clear oscillatory behavior of the spin-up population, whereas the left qubit displays a maximum spin-up fraction of 90% that indicates better manipulation and readout fidelity than for the right qubit that features a maximum spin-up fraction of 74%. This difference correlates with the observation of a larger reservoir broadening for the right qubit (see Sec. 4.5). As a consequence, the readout voltage must be set close to the alignment of the dot's spin-up state with the reservoir's Fermi level to effectively suppress the thermal background offset. However, this setting can also affect the coupling between the dot and the reservoir, potentially reducing the tunnel rate and degrading the readout fidelity. The fit function to extract the Rabi frequency f_{Rabi} and coherence time constant $T_{2,\mathrm{Rabi}}$ of the spin population transfer is derived from Eq. (5.7) by applying the trigonometric identity $2\sin^2(\omega t/2) = (1 - \cos(\omega t))$ and using A to express the signal amplitude and c to capture the thermal background events

$$P_{|\uparrow\rangle}(t) = A\cos\left(2\pi f_{\mathrm{Rabi}} t\right)\exp\left(-\frac{t}{T_{2,\mathrm{Rabi}}}\right) + c\,. \tag{5.12}$$

This fit yields Rabi oscillation frequencies of $f_{\mathrm{Rabi,L}} = 1.43\,\mathrm{MHz}$ and $f_{\mathrm{Rabi,R}} = 1.50\,\mathrm{MHz}$ with negligible fit uncertainties and coherence times of $T_{2,\mathrm{Rabi,L}} = (6.17 \pm 0.88)\,\mu\mathrm{s}$ and

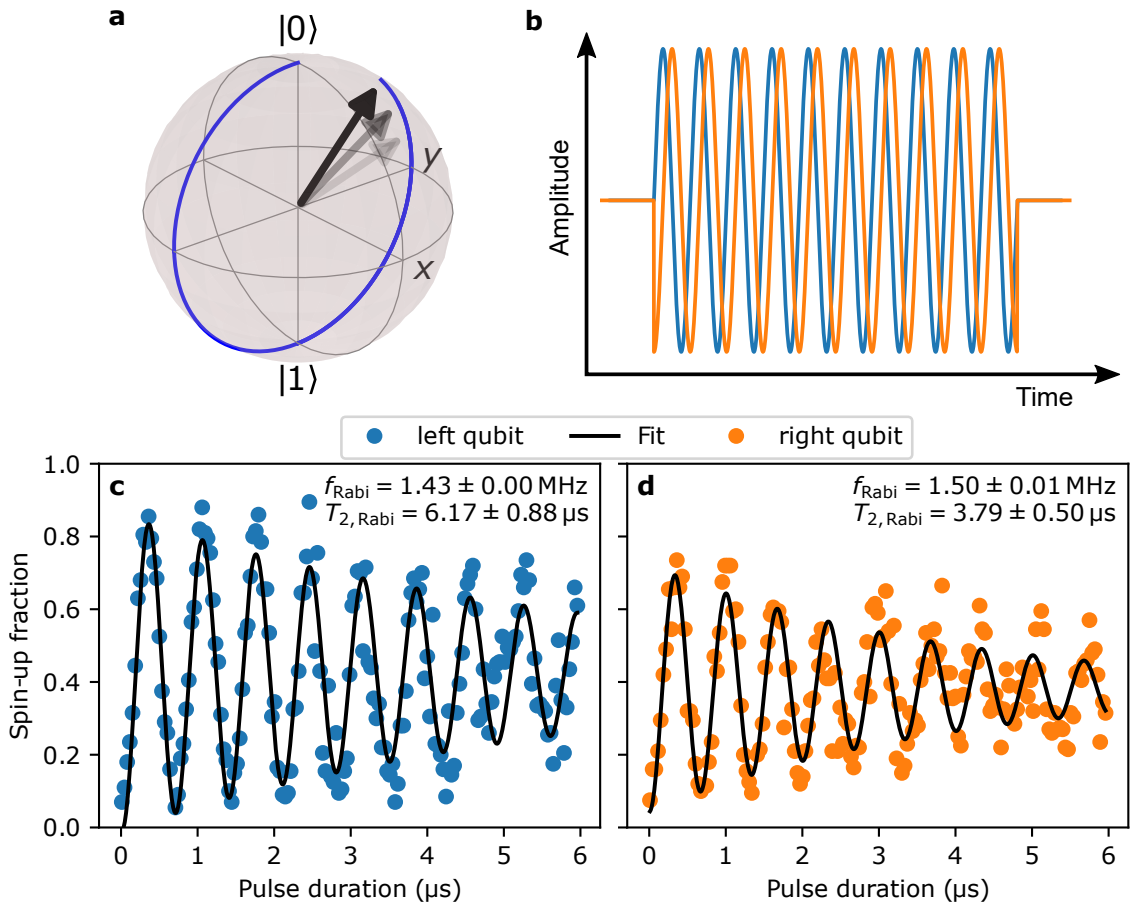

Figure 5.14: Coherent single-qubit control via Rabi oscillations. **a** Conceptual Bloch sphere representation of a qubit undergoing coherent rotations under resonant microwave drive with a phase of $\phi = 0$. The trajectory (blue) illustrates Rabi oscillations about the x-axis, with black arrows highlighting selected superposition states accessible by timed manipulation. **b** Example output of two 90° phase shifted AWG signals used to control the qubit manipulation by IQ mixing. The left and right qubit are addressed by single-sideband mixing and the duration of the microwave manipulation is controlled by the duration of the AWG pulse. **c,d** Experimentally observed Rabi oscillations for the left and right qubit of device $^{\mathrm{nat}}$Si/SiGe D09 Die02, respectively, at resonance frequencies of 19.60 GHz (left) and 19.87 GHz (right). The measurements were conducted using 18 dBm external microwave power and AWG modulation amplitudes of 0.4 V (left) and 1.0 V (right) to establish comparable drive conditions. Both qubits display pronounced coherent oscillations as a function of pulse duration. The black lines represent a fit with Eq. (5.12) and yield the Rabi frequencies and decay constants stated in the panels, with standard deviations derived from statistical fit uncertainties. Each data point averages 100 single-shot readouts.

$T_{2,\mathrm{Rabi,R}} = (3.79 \pm 0.05)$ µs, for the left and right qubit, respectively. The Rabi frequencies of both qubits are adjusted to about 1.5 MHz by choice of the AWG modulation amplitudes (see Sec. 3.5), which is the maximum Rabi frequency with decent coherence time that could be achieved for the right qubit at two-qubit operation compatible gate voltage settings. Furthermore, the right qubit exhibits a reduced spin coherence time in comparison with the left qubit, which indicates a more noisy local environment. However, spin coherence times of both qubits will be discussed conclusively in Sec. 5.7.3.

While sustained coherent oscillations are not necessary for quantum computing, since any target state on the Bloch sphere can be reached with a single π-rotation about an appropriate axis, the Rabi coherence time $T_{2,\mathrm{Rabi}}$ remains a valuable metric for quantifying the performance of driven qubit systems. A common figure of merit is the quality factor (Q-factor), defined as $Q = T_{2,\mathrm{Rabi}}/t_\pi$, where $t_\pi = 1/(2f_{\mathrm{Rabi}})$ is the duration of a π-pulse [87]. This ratio indicates how many π-rotations can be executed before coherence is lost and offers an estimate of the maximum number of gates possible within the system's coherence window. Here, the extracted f_{Rabi} and $T_{2,\mathrm{Rabi}}$ values correspond to Q-factors of 18 and 11 for the left and right qubit, respectively. These operating points were chosen as a compromise to support stable control of both qubits under a shared two-qubit-compatible configuration. For comparison, Q-factors up to 92 have been achieved in a nominally identical SiGe device from the same wafer by optimizing for single-qubit performance alone [24].

5.6.2 EDSR-drive optimization

Achieving coherent qubit control, as demonstrated by clear Rabi oscillations, marks the transition from fundamental device characterization toward practical quantum computation. While Rabi oscillations enable fundamental quantum gate operations, the frequency of these oscillations directly determines the potential "clock speed" of quantum logic gates. Consequently, identifying optimal parameters that maximize Rabi frequencies while minimizing microwave-induced heating and environmental decoherence becomes critically important for high-performance qubit operations and scalable quantum computing architectures.

The electric dipole spin resonance (EDSR) mechanism, introduced in Sec. 2.7, relies on translating oscillating electric fields into effective magnetic fields via displacement of the electron in a static magnetic gradient, provided by the integrated cobalt micromagnet (CoMM). As expressed by Eq. (2.21) and Eq. (2.22), the Rabi frequency in EDSR scales linearly with both the perpendicular magnetic field gradient $\partial B_\perp/\partial y$ and the driven electron displacement amplitude y_0, the latter determined primarily by the effective microwave amplitude V_1 at the quantum dot site. The magnetic field gradient is a design parameter of the CoMM which has been optimized for qubit control [70] and cannot be influenced in-situ. However, the effective microwave amplitude at the qubit site is directly dependent on the applied microwave power and also the electron displacement can be influenced by shaping the confinement potential of the qubit [120], or increasing the microwave gate lever arm by moving the dot closer to the drive line. Identifying and characterizing these parameters thus constitutes a central aspect of qubit drive optimization. Representative studies of EDSR-drive optimization are depicted in Fig. 5.15, obtained from two nominally identical SiGe devices fabricated on the same wafer. Panels **a** and **b** contain data from the central $^{\mathrm{nat}}$Si/SiGe D09 Die02 device extensively studied in this thesis, while panel **c** showcases complementary data from the $^{\mathrm{nat}}$Si/SiGe D09 Die05 device featured in Ref. [64].

To systematically investigate the microwave amplitude dependence, Rabi oscillations were measured for external microwave powers ranging from 15 dBm to 24 dBm using a fixed

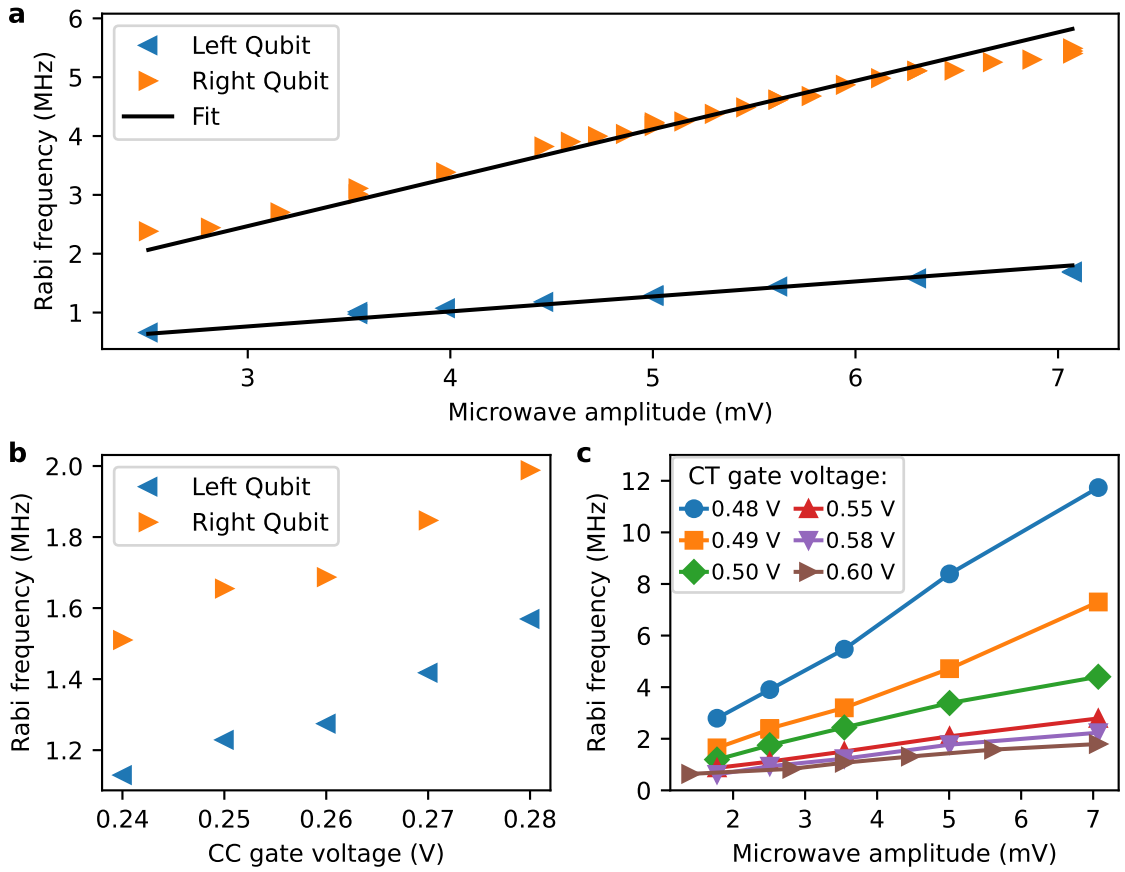

Figure 5.15: Optimization of EDSR-drive parameters for spin qubit manipulation. **a** Observed Rabi frequencies of the left (blue) and right (orange) qubit of device ^{nat}Si/SiGe D09 Die02 as a function of the effective microwave amplitude after accounting for an estimated inline attenuation of 54 dBm. A linear dependence is observed up to amplitudes of approximately 6.25 mV, beyond which saturation becomes particularly apparent for the right qubit. The solid lines represent linear fits through the origin, confirming the expected linear scaling of the Rabi frequency with drive amplitude in the non-saturated regime. **b** Rabi frequency of device ^{nat}Si/SiGe D09 Die02 as a function of the central confinement gate voltage (CC), which also serves as the EDSR drive gate. Increasing (attractive) CC gate voltages enhance the Rabi frequency of both qubits, attributed to reduced lateral separation between the drive gate and the dot, increasing the effective microwave amplitude. **c** Rabi frequency of the left qubit in the ^{nat}Si/SiGe D09 Die05 device as a function of microwave amplitude for different top screening gate (CT) gate voltages. More negative (repulsive) CT voltages yield higher Rabi frequencies, again consistent with reduced dot-drive gate separation. Each data point is averaged over 100 single-shot readouts.

AWG modulation amplitude of 1 V at resonance frequencies of 18.15 GHz and 18.50 GHz for the left and right qubit respectively. Extracted Rabi frequencies from these measurements, plotted as a function of microwave amplitude after accounting for an estimated inline attenuation of 54 dBm (see Sec. 3.5), are shown in Fig. 5.15**a**. Consistent with theoretical expectations (Eq. (2.21)), the Rabi frequency increases linearly with microwave amplitude up to approximately 6.25 mV, as emphasized by the close agreement between the data and linear fits through the origin shown as black lines. Beyond this value, saturation of the Rabi frequency becomes apparent in the right qubit data and is also observed,

though less pronounced, in the left qubit. Such saturation behavior is widely reported in spin-qubit literature [25, 64, 87, 121] and commonly attributed to nonlinearities in the confinement potential of the quantum dot at large electron displacements or to heating effects and nonlinear dielectric losses in microwave delivery. In this case, non-linear losses in the microwave setup are likely contributing to the observed Rabi frequency saturation. This is evidenced by the left qubit showing signs of saturation despite lower drive amplitudes, assuming similar magnetic field gradients at both qubit sites. Moreover, similar saturation behavior has been observed in other SiGe devices at comparable drive powers, suggesting the effect may not be device-specific. By reducing attenuation in the RF lines and extending the accessible drive power range, an ongoing study aims to differentiate whether the saturation is related to operating the microwave electronics at output power limits or to losses in passive components. A notable observation from Fig. 5.15**a** is the significantly slower oscillation frequency of the left qubit compared to the right qubit at identical microwave powers, contrasting the findings at higher resonance frequencies near 19.5 GHz (see Fig. 5.14**c,d**). This unexpected discrepancy emphasizes a considerable frequency-dependent power transmission variability of the microwave lines. Although the operating regime near 19.5 GHz was empirically determined as optimal for coherent two-qubit operation, a full characterization of microwave transmission over frequency by measurement of Rabi frequencies remains to be conducted and may help identify optimal qubit frequencies for future benchmarking experiments.

Beyond adjusting the microwave amplitude, the effect of the confinement potential on achievable Rabi frequencies can be assessed by varying the voltages on the screening gates CC and CT, which define the dot confinement along the direction of microwave-induced displacement (see Fig. 2.6). Data from varying the central confinement (CC) gate, which doubles as the EDSR drive gate, are displayed in Fig. 5.15**b**. These measurements, taken at resonance frequencies of 14.95 GHz (left qubit) and 15.27 GHz (right qubit) and 3.5 mV microwave amplitude, reveal a noticeable increase in Rabi frequencies with more positive (attractive) CC gate voltages. A complementary measurement on the nominally identical $^{\text{nat}}$Si/SiGe D09 Die05 device in Fig. 5.15**c**, presents the Rabi frequency as a function of microwave amplitude for different CT gate voltages, measured on the left qubit at a resonance frequency of 18.5 GHz. Interestingly, the data indicate highest Rabi frequencies achieved at the lowest (most repulsive) CT gate voltages. Taken together, the results of Fig. 5.15**b** and **c** strongly suggest that increased Rabi frequencies primarily result from enhanced microwave gate lever arms, achieved by moving the quantum dot closer to the CC drive line. While increasing the voltage on the CC and CT gates might also soften the confinement potential of the quantum dot, this effect can be ruled out as the primary source of enhanced Rabi frequencies, since it would uniformly increase electron displacement amplitudes for increasing gate voltage, independent of the gate involved.

Notably, Rabi frequencies of up to 12 MHz (Fig. 5.15**c**) and up to 5.5 MHz (Fig. 5.15**a**) were achieved, marking exceptionally high values compared to other industrially fabricated Si-based spin qubit devices [26, 29]. However, the highest Rabi frequencies were associated with decreased device stability due to marginal confinement or vanishing coherence times. Empirically, coherence times under strong driving scale inversely with microwave amplitude as $T_{2,\text{Rabi}} \propto A_{\text{MW}}^{-4}$, as demonstrated by Ref. [87]. Optimal performance can

be obtained by maximizing the Q-factor to balance drive strength and coherence for benchmarking measurements.

Conclusion

The results presented in this section establish coherent single-qubit control of both qubits on the ^{nat}Si/SiGe D09 Die02 sample, demonstrated through tunable Rabi oscillations with sufficient signal amplitude and coherence for reliable quantum gate operations. This achievement provides a solid foundation for the two-qubit control experiments discussed in Sec. 6.1. To ensure consistent and robust control across both qubits during two-qubit operation, a stable CT gate voltage of 0.28 V and an intermediate microwave power of 18 dBm were selected. These settings enabled the results shown in Fig. 5.14**c** and **d**.

5.7 Spin coherence times

The demonstration of coherent Rabi oscillations confirms the basic ability to manipulate qubit states. However, for practical quantum computing, it is equally important to preserve qubit coherence in the absence of continuous control. Ramsey and Hahn-echo coherence times define how long a quantum state retains its phase information in the idle state and set the limits for reliable quantum information storage and processing. Ramsey interferometry measures the intrinsic dephasing time T_2^*, while the Hahn-echo sequence suppresses low-frequency noise to extract the echo coherence time T_2^{HE}. Results from these measurements are key benchmarks of device performance and give insight into the dominant noise sources affecting the qubit. All data presented in this section were obtained exclusively using the ^{nat}Si/SiGe D09 Die02 device.

5.7.1 Ramsey experiment

Ramsey interferometry is a widely used technique in quantum information science, originally proposed by Norman Ramsey and based on foundational concepts developed by Isidor Rabi [122]. In a Ramsey experiment, the free induction decay of a qubit is measured, which captures the impact of low-frequency noise on the qubit's phase coherence during idle periods. This measurement establishes an upper bound on the duration over which coherent qubit control can be maintained in the absence of active error mitigation.

The Ramsey pulse sequence, illustrated in Fig. 5.16**a**, consists of an initial $\pi/2$-pulse to place the qubit state into a coherent superposition on the equatorial plane of the Bloch sphere, followed by a variable idle time τ, and finally a second in-phase $\pi/2$-pulse. As depicted in Fig. 5.16**b**, the first $\pi/2$-pulse rotates the spin from the ground state $|0\rangle$ by 90° about the x-axis, preparing it in a coherent superposition. During the subsequent idle time τ, the qubit accumulates phase noise due to fluctuations in the resonance frequency, arising primarily from low-frequency magnetic and electric field variations in the environment.

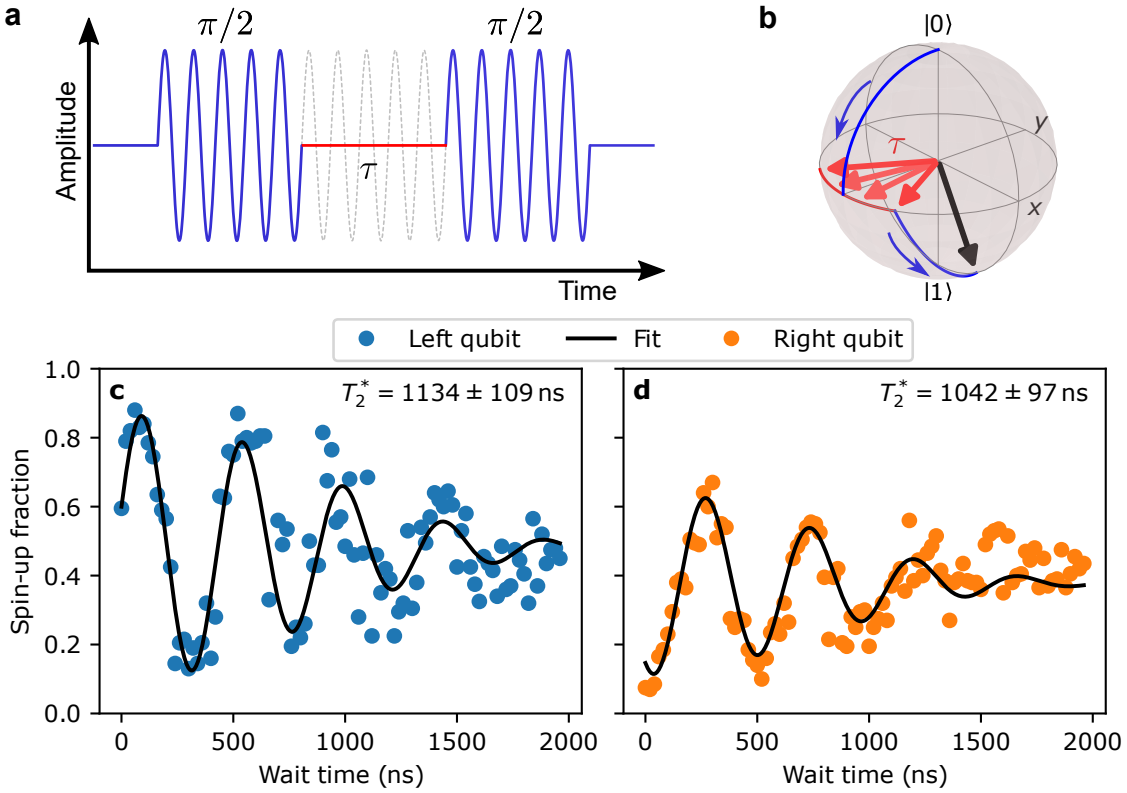

Figure 5.16: Ramsey coherence measurements in single-qubit operation. **a** Ramsey pulse sequence used to probe qubit phase coherence. It consists of two in-phase $\pi/2$-pulses separated by a variable idle time τ, during which the qubit evolves freely and accumulates phase noise. **b** Bloch sphere illustration of the Ramsey protocol. The initial $\pi/2$-pulse rotates the spin vector from the ground state to the equator. During the free evolution interval τ, quasi-static noise causes the spin to acquire a random phase (red trajectory). The final $\pi/2$-pulse projects the spin vector onto the quantization axis to probe the accumulated phase. **c,d** Measured spin-up fraction after a Ramsey sequence for both qubits as a function of wait time τ. The measurements were conducted at resonance frequencies of 19.60 GHz (left) and 19.87 GHz (right) using 18 dBm external microwave power and AWG modulation amplitudes of 0.4 V (left) and 1.0 V (right). The microwave drive was detuned by 2 MHz from the qubit resonance frequency to induce predictable oscillations. The decaying envelope reveals spin dephasing due to low-frequency nuclear spin fluctuations. Black lines represent fits using Eq. (5.13), yielding coherence times of $T_2^* = (1134 \pm 109)$ ns for the left and $T_2^* = (1042 \pm 97)$ ns for the right qubit. Each data point averages 100 single-shot readouts.

These fluctuations cause random rotations of the qubit state about the z-axis, gradually obscuring the initially defined phase relationship and leading to decoherence, as visualized by the red trajectory on the Bloch sphere. The final in-phase $\pi/2$-pulse ideally completes a full π-rotation when $\tau = 0$, transferring the qubit from $|0\rangle$ to $|1\rangle$. However, for finite waiting times τ, accumulated random phases cause the final state to deviate significantly from the ideal, eventually resulting in an average spin-up fraction of 50% once phase information is entirely lost.

Performing the Ramsey experiment with a known detuning Δ by intentionally offsetting the microwave drive frequency from the qubit's Larmor frequency ω_0, is particularly advantageous. In this detuned configuration, the phase of the microwave drive evolves relative to the qubit as $\Delta t = (\omega - \omega_0)t$, causing the final spin projection to oscillate at

the detuning frequency. These oscillations provide a sensitive and predictable signal, allowing both accurate fitting of the decaying Ramsey envelope and precise determination of the qubit resonance frequency. Deviations from the expected oscillation period can be used to fine-tune the resonance condition, making this method superior to the resonant Ramsey experiment, where unintended low-frequency detuning can distort the envelope and compromise the extraction of the intrinsic coherence time T_2^*.

Experimentally measured Ramsey oscillations with an applied detuning of 2 MHz for both the left and right qubit are shown in Fig. 5.16**c** and **d**. With quasi-static noise being the main source of decoherence, these oscillations exhibit Gaussian rather than exponential decay envelopes, as widely established in spin-qubit literature [123, 124]. Consequently, the experimental data were fitted with a Gaussian-damped oscillation of the form

$$P_{|\uparrow\rangle}(t) = A\cos(\Delta t + \phi)\exp\left(-\left(t/T_2^*\right)^2\right) + c\,, \tag{5.13}$$

where A denotes the oscillation amplitude, Δ represents the true frequency detuning from resonance, ϕ captures the initial phase offset due to detuned drive, and c accounts for thermally induced background events.

Extracted spin dephasing times yield $T_2^* = (1.13 \pm 0.11)$ µs for the left qubit and $T_2^* = (1.04 \pm 0.10)$ µs for the right qubit. These values align well with previously reported spin coherence times for natural silicon quantum dot devices [21] and provide a useful reference for evaluating the qubits' sensitivity to intrinsic noise under idle conditions. However, Ramsey sequences are inherently sensitive to low-frequency noise and environmental drifts. To further disentangle dynamic and static contributions to decoherence, complementary Hahn-echo measurements will be presented in the following section. A comparative discussion of both qubits' coherence characteristics will be subsequently detailed in Sec. 5.7.3.

5.7.2 Hahn-Echo experiment

While the Ramsey experiment provides essential insight into intrinsic spin coherence and sensitivity to low-frequency noise, practical quantum computing requires strategies to mitigate such dephasing. A widely used approach to counteract the detrimental effects of slow environmental fluctuations is the Hahn-echo pulse sequence, first demonstrated by Erwin Hahn in the context of nuclear magnetic resonance experiments [125]. By incorporating a refocusing pulse within the idle evolution period, the Hahn-echo technique effectively reverses the influence of low-frequency noise and provides an extended qubit coherence time, denoted T_2^{HE}.

The pulse sequence used for the Hahn-echo experiment is schematically illustrated in Fig. 5.17**a**. It begins with an initial $\pi/2$-pulse, rotating the qubit state onto the equator of the Bloch sphere to establish a coherent superposition that is sensitive to dephasing. Subsequently, the qubit state evolves freely for a duration $\tau/2$, accumulating a phase shift due to environmental fluctuations. Following this idle interval, an in-phase refocusing π-pulse is applied, flipping the qubit state across the equator of the Bloch sphere. The

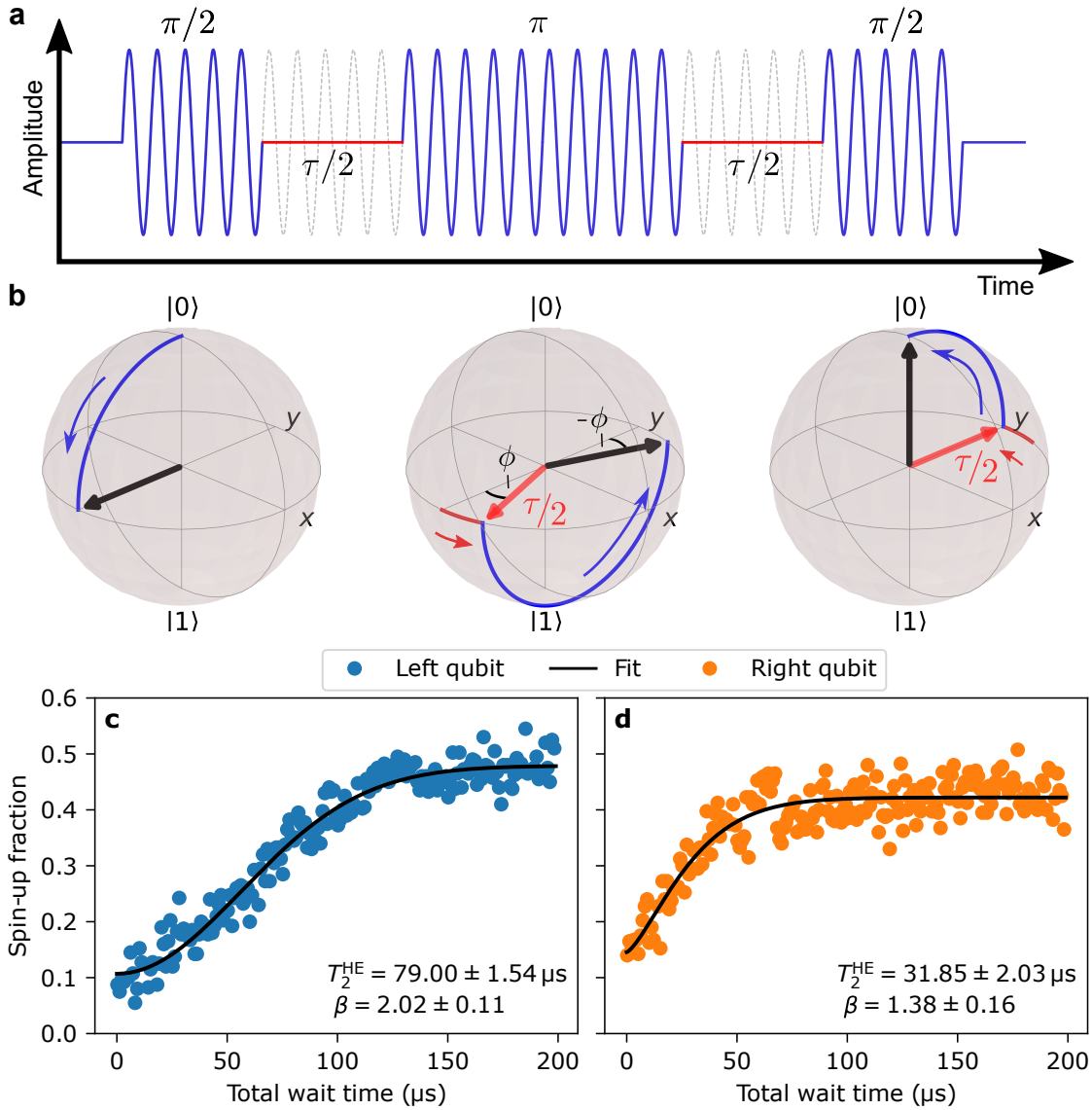

Figure 5.17: Hahn-echo coherence measurements of both qubits in single-qubit operation. **a** Pulse diagram of the Hahn-echo sequence, consisting of a $\pi/2$-pulse, an idle evolution time $\tau/2$, a refocusing π-pulse, followed by another $\tau/2$ idle period and a final in-phase $\pi/2$-pulse. This pulse sequence reverses phase accumulation caused by low-frequency fluctuations. **b** Bloch sphere illustrations of the spin evolution during the Hahn-echo sequence, aligned with the manipulation pulses in panel **a**. First, the qubit is initialized in a coherent superposition by the first $\pi/2$-pulse (left sphere). Then, the spin vector accumulates a exemplary phase ϕ during the first idle period (center sphere), which is inverted to $-\phi$ by the intermediate π-pulse. After the second $\tau/2$ evolution (right sphere), the spin vector ideally refocuses and is projected onto the quantization axis for readout with the final $\pi/2$-pulse. **c,d** Measured spin-up fraction as a function of total wait time τ for the left and right qubit, respectively. Qubit transitions were driven at resonance frequencies of 19.6 GHz (left) and 19.87 GHz (right), using an external microwave power of 18 dBm and AWG amplitudes of 0.4 V and 1.0 V. The black lines represent fits to the stretched exponential function in Eq. (5.14), yielding Hahn-echo coherence times of $T_{2,\mathrm{L}}^{\mathrm{HE}} = (79.00 \pm 1.54)\,\mu\mathrm{s}$ and $T_{2,\mathrm{R}}^{\mathrm{HE}} = (31.85 \pm 2.03)\,\mu\mathrm{s}$, and exponents of $\beta_{\mathrm{L}} = 2.02 \pm 0.11$ and $\beta_{\mathrm{R}} = 1.38 \pm 0.16$, indicating different noise environments of the two qubits. Each point averages 100 single-shot readouts.

state then evolves again during a second interval $\tau/2$ under similar noise conditions. The final in-phase $\pi/2$ pulse completes a full 2π rotation when the waiting time $\tau = 0$. For finite τ, however, accumulated random phases lead the final state to deviate increasingly from the ideal, ultimately resulting in an average spin-up fraction of 50% once phase coherence is lost. The refocusing pulse is a central element of the Hahn-echo sequence, since it effectively reverses noise-induced phase shifts accumulated during the first interval. Specifically, for noise frequencies significantly lower than $1/\tau$, the refocusing pulse inverts the sign of the accumulated phase midway through the total idle duration, allowing the spin vector to realign to its initial coherent state. This process is termed spin-echo or refocusing. Conversely, for noise frequencies significantly higher than $1/\tau$, the rapid fluctuations average out within each individual interval, minimizing net phase accumulation. It is predominantly noise at frequencies on the order of $1/\tau$ that contributes noticeably to the final decoherence.

The action of the Hahn-echo pulse sequence on the qubit state vector is depicted on the Bloch spheres in Fig. 5.17**b**. Initially, the $\pi/2$-pulse places the qubit into a coherent superposition, aligned along the equatorial plane. During the first evolution interval ($\tau/2$), environmental noise introduces a rotation of the qubit state around the z-axis, resulting in a phase shift ϕ. The intermediate π-pulse precisely flips this state across the equator, effectively transforming the accumulated phase shift ϕ into a negative shift $-\phi$. As the qubit evolves during the second interval ($\tau/2$), the subsequent environmental noise similarly affects the qubit state. Crucially, due to the reversed sign of the accumulated phase, this second interval compensates for the initial dephasing and significantly mitigates low-frequency noise effects. The sequence concludes with a final in-phase $\pi/2$-pulse, projecting the qubit state back onto the measurement axis and allowing to measure the degree of remaining coherence accurately. Because of the selective cancellation of quasi-static and slowly varying noise components, the spin-echo sequence provides enhanced coherence protection compared to a Ramsey experiment.

The experimentally observed spin-up fractions following the Hahn-echo pulse sequence, recorded for increasing total waiting times τ, are presented in Fig. 5.17**c** (left qubit) and **d** (right qubit). These data are well-modeled by a phenomenological stretched exponential decay function [123]

$$P_{|\uparrow\rangle}(t) = A \exp\left(-(t/T_2^{\mathrm{HE}})^{\beta}\right) + c\,, \tag{5.14}$$

where A describes the signal amplitude, β the stretching exponent indicative of the noise frequency distribution, and c accounts for thermal background events. Fitting the experimental data yields the Hahn-echo coherence time of $T_{2,\mathrm{L}}^{\mathrm{HE}} = (79.00 \pm 1.54)\,\mu\mathrm{s}$ with a stretching exponent $\beta_{\mathrm{L}} = 2.02 \pm 0.11$ for the left qubit, and $T_{2,\mathrm{R}}^{\mathrm{HE}} = (31.85 \pm 2.03)\,\mu\mathrm{s}$ with $\beta_{\mathrm{R}} = 1.38 \pm 0.16$ for the right qubit. The Hahn-echo coherence times are significantly longer than the Ramsey-measured coherence times, demonstrating the effectiveness of the Hahn-echo sequence and the dominance of low-frequency noise in the qubit system. A detailed comparative discussion of these Hahn-echo measurements and their implications, particularly concerning the differences observed between both qubits and their noise environments, will be presented in the following coherence analysis section.

5.7.3 Discussion and comparison of spin coherence times

To conclude the detailed characterization of single-qubit control and coherence properties, a comparative analysis is conducted between the two qubits hosted within the same ^{nat}Si/SiGe D09 Die02 device. This direct comparison offers valuable insight into the environmental and operational factors that constrain device performance and coherence. Throughout this discussion, the left qubit, which consistently exhibits superior coherence characteristics, will serve as the reference standard. For clarity, all experimentally extracted single-qubit metrics are summarized in Tab. 5.1.

Parameter	**Left Qubit**	**Right Qubit**
Maximum visibility (%)	90	74
Rabi frequency f_{Rabi} (MHz)	1.43	1.50
Rabi coherence time $T_{2,\text{Rabi}}$ (µs)	6.17 ± 0.88	3.79 ± 0.50
Ramsey coherence time T_2^* (µs)	1.13 ± 0.11	1.04 ± 0.10
Hahn-echo coherence time T_2^{HE} (µs)	79.00 ± 1.54	31.85 ± 2.03
Hahn-echo exponent β	2.02 ± 0.11	1.38 ± 0.16

Table 5.1: Single-qubit performance metrics measured at an external microwave power of 18 dBm, with AWG modulation amplitudes of 0.4 V and 1 V for the left and right qubit, respectively. The displayed standard deviations represent statistical fit uncertainties.

Contextualizing the measured spin dephasing times, the Rabi coherence time is strongly dependent on the drive amplitude and therefore difficult to compare directly with values reported in literature. However, optimized Rabi coherence times on the order of 10 ms are regularly reported in natural silicon systems [21, 64, 87]. The obtained Ramsey coherence times of $T_2^* \approx 1$ ms are consistent with reported values for natural silicon-based spin qubit devices [21, 29, 87, 126]. The underlying noise is typically attributed to low-frequency fluctuations arising from thermal nuclear spin dynamics of naturally abundant ^{29}Si isotopes in the local qubit environment [43, 127]. Similarly, the Hahn-echo coherence times of $T_{2,L}^{\text{HE}} = 79$ µs and $T_{2,R}^{\text{HE}} = 32$ µs compare well with previously reported values ranging from a few microseconds up to 73 µs [21, 126]. In the Hahn-echo experiment, the left qubit exhibits a Gaussian decay envelope with exponent $\beta \approx 2$, indicating decoherence primarily driven by a $1/f$ noise spectrum arising from low-frequency nuclear spin and charge noise within the device [53, 112, 126]. In contrast, the right qubit shows a sub-Gaussian decay exponent ($\beta = 1.38$), suggesting dominant contributions from localized fluctuators [128, 129]. This behavior is typical for a noise environment dominated by a small number of strongly coupled charge defects. Supporting this interpretation, charge stability diagrams (see Fig. 4.3**b**) reveal a parasitic horizontal charge transition line, indicative of a defect strongly coupled to the right plunger gate. Although the defect was tuned to be energetically distant from the relevant $(0,1)$, $(1,0)$ and $(1,1)$ charge configurations for this thesis using the upper screening gate, residual capacitive interactions may have persisted. Even in the absence of direct tunneling events, slow fluctuations in the defect's charge occupancy or local potential can modulate the qubit's electrostatic environment, thereby degrading its coherence. The absolute difference of the T_2^* and T_2^{HE} value of each qubit highlights the

frequency-dependent nature of the dominant decoherence channels and reveals that noise amplitudes increase at lower frequencies.

In a direct comparison at the selected working point, the right qubit displays qualitatively similar behavior across all experiments but with lower visibility and shorter absolute coherence times $T_{2,\mathrm{Rabi}}$ and T_2^{HE}. The observed difference in visibility is consistent with transition broadening identified in electron temperature measurements (cf. Sec. 4.5). The right qubit shows greater reservoir broadening, requiring the readout voltage to be set close to the spin-up state alignment with the reservoir's Fermi level. While this maintains a comparably low thermal background as for the left qubit, the reduced visibility can be a consequence of this setting. In particular, spin-up electrons may tunnel at a modified rate, resulting in a lower fraction being detected within the readout time. A likely contributor to the reduced coherence of the right qubit is its position relative to the interdot barrier and micromagnet, which may enhance sensitivity to electric field fluctuations and magnetic field gradients. This increased susceptibility manifests experimentally by its elevated Stark shift parameter $\lambda_{\mathrm{S,R}}$ in following investigations of two-qubit operation (see Fig. 6.11). Another relevant factor is the device's asymmetric layout, which places the right qubit closer to the SET. The SET's positively biased top gate may perturb the local confinement potential through electrostatic attraction. Additionally, the SET itself can act as a noise source due to its continuous tunnel current. Although coherence measurements were performed over a range of SET currents, no definitive correlation was observed, leaving its influence inconclusive but still potentially relevant. Taken together, these considerations suggest that the right qubit's reduced coherence arises from a combination of geometric asymmetry and coupling to a nearby charge defect. However, the similarity of T_2^* values between the two qubits supports the interpretation that quasi-static dephasing is primarily driven by uniformly distributed ^{29}Si nuclear spins in the natural silicon substrate. This behavior aligns with expectations of decoherence caused by Overhauser field fluctuations [127], which affect both qubits equally. Thus, while device geometry and local defects introduce additional decoherence channels, reducing the abundance of nuclear spin in the substrate emerges as a universally significant factor for coherence enhancement. This insight is reinforced by literature demonstrating orders-of-magnitude improvement in coherence times upon isotopic enrichment with nuclear spin-free ^{28}Si [21].

In summary, the established single-qubit control and detailed coherence metrics presented in this chapter form a robust foundation for advancing toward two-qubit gate operations. Comparative coherence analysis clearly identifies nuclear spin noise and localized charge fluctuations as key limiting factors. Future studies on device generations utilizing isotopically enriched silicon substrates are expected to mitigate the dominant nuclear-spin-induced decoherence and enable substantial improvements in both intrinsic qubit coherence and operational fidelities, marking an important step toward practical quantum computing implementations.

6 Spin–Spin Interaction

The implementation of two-qubit gates marks a pivotal step toward the realization of universal quantum computation. While single-qubit control is essential for preparing and rotating quantum states, the ability to entangle two qubits enables the full spectrum of quantum algorithms and error correction [130]. In semiconductor quantum dot systems, the most natural and widely used mechanism for qubit-qubit coupling is the exchange interaction, which arises from wavefunction overlap and Coulomb repulsion between neighboring electrons [131]. All measurements presented in this section were obtained exclusively using the ^{nat}Si/SiGe D09 Die02 device (see Sec. 2.5).

6.1 Spin interaction in the two-qubit regime

The conceptual foundation for exchange-based two-qubit gates is the Heisenberg interaction between two electron spins confined in adjacent quantum dots. When the electrons are close enough for their wavefunctions to overlap, an exchange interaction arises from the Pauli exclusion principle, which requires the total two-electron wavefunction, encompassing spin and spatial components, to be antisymmetric [37, 38]. In the spin-singlet state, the antisymmetric spin component allows a symmetric spatial wavefunction, enabling electrons to occupy the same region and lowering their energy. Conversely, spin-triplet states require an antisymmetric spatial wavefunction, keeping the electrons spatially separated and raising their energy. The resulting energy difference defines the exchange coupling J. In double quantum dot systems, charge configurations are typically denoted as (n, m), with n and m indicating the number of electrons in the left and right dot, respectively. The exchange interaction becomes particularly significant near interdot charge transitions, such as $(1, 1) - (2, 0)$, where electrons can partially delocalize between the dots. The seminal proposal by Loss and DiVincenzo [20] established that such a coupling can be harnessed to implement two-qubit gates. The Hamiltonian for such a two electron system is given by

$$H = hf_1 S_z^1 + hf_2 S_z^2 + hJ(\vec{S}^1 \cdot \vec{S}^2 - 1/4)\,, \tag{6.1}$$

where h is Planck's constant, f_i are the Larmor precession frequencies of each qubit, J is the exchange coupling and $\vec{S}^i$ represent the spin operators of both electrons. This Hamiltonian is adapted from [132] by substituting the Zeeman terms by hf, assuming the external magnetic field to be oriented along the z-axis, and definition of the exchange energy as

hJ where J represents the strength of the coupling as a linear frequency in Hz. The first two terms describe the Zeeman energies of both individual spins in an external magnetic field. The last term corresponds to the Heisenberg Hamiltonian of coupled spins where the interplay of interdot tunneling rate and Coulomb repulsion is combined in the exchange energy hJ and the dot product $\vec{S}^1 \cdot \vec{S}^2$ reflects the coupling between spins. In the remainder of this thesis, all frequencies are expressed in regular, not angular, units (Hz), and all energy terms appear as hf. This choice facilitates direct comparison with experimentally measured quantities, where resonance frequencies and exchange couplings are typically reported in Hz.

Eigenstates and coupling regimes

When $J = 0$, the two spins are uncoupled, and the eigenstates are simply product spin states (such as $|\uparrow\downarrow\rangle$) and the four eigenenergies are the sum of the individual Zeeman energies. In the presence of exchange, the situation becomes more nuanced. Depending on the relative magnitude of J compared to the Zeeman frequency difference $|f_1 - f_2|$, the Hamiltonian can be analyzed in two limits [133]:

- **Weak coupling** ($J \ll |f_1 - f_2|$): In this case, the exchange term causes a small perturbative shift in the energies of antiparallel states. The basis $\{|\uparrow\uparrow\rangle, |\uparrow\downarrow\rangle, |\downarrow\uparrow\rangle, |\downarrow\downarrow\rangle\}$ remains a good approximation for the eigenstates. The exchange interaction lowers the energy of the antiparallel states by $hJ/2$, as they contain a singlet component.
- **Strong coupling** ($J \gg |f_1 - f_2|$): Here, the Hamiltonian is more naturally expressed in the singlet-triplet basis $\{|T_+\rangle, |T_0\rangle, |T_-\rangle, |S\rangle\}$, where only the singlet state $|S\rangle$ is energetically shifted by $-hJ$, while the triplet states remain unaffected.

A detailed derivation of the eigenenergies can be found in Sec. A.3 of the appendix and the eigenstates and eigenenergies in both limits are summarized in Tab. 6.1.

$J \ll \lvert f_1 - f_2 \rvert$			$J \gg \lvert f_1 - f_2 \rvert$		
Eigenstate		**Eigenenergy**	**Eigenstate**		**Eigenenergy**
$\lvert\uparrow\uparrow\rangle$ =	$\lvert T_+\rangle$	$\frac{h}{2}(f_1 + f_2)$	$\lvert T_+\rangle$ =	$\lvert\uparrow\uparrow\rangle$	$\frac{h}{2}(f_1 + f_2)$
$\lvert\downarrow\uparrow\rangle$ =	$\frac{\lvert T_0\rangle - \lvert S\rangle}{\sqrt{2}}$	$\frac{h}{2}(f_2 - f_1) - \frac{hJ}{2}$	$\lvert T_0\rangle$ =	$\frac{\lvert\downarrow\uparrow\rangle + \lvert\uparrow\downarrow\rangle}{\sqrt{2}}$	0
$\lvert\uparrow\downarrow\rangle$ =	$\frac{\lvert T_0\rangle + \lvert S\rangle}{\sqrt{2}}$	$\frac{h}{2}(f_1 - f_2) - \frac{hJ}{2}$	$\lvert S\rangle$ =	$\frac{\lvert\downarrow\uparrow\rangle - \lvert\uparrow\downarrow\rangle}{\sqrt{2}}$	$-hJ$
$\lvert\downarrow\downarrow\rangle$ =	$\lvert T_-\rangle$	$-\frac{h}{2}(f_1 + f_2)$	$\lvert T_-\rangle$ =	$\lvert\downarrow\downarrow\rangle$	$-\frac{h}{2}(f_1 + f_2)$

Table 6.1: Eigenstates and eigenenergies of the two-qubit Hamiltonian (Eq. (6.1)) in the case of weak and strong exchange interaction. The derivation of the eigenenergies can be found in Sec. A.3 of the appendix.

Exchange interaction in semiconductor spin qubits

In experimental devices, the exchange interaction is not fixed, but rather depends on the gate-defined potential landscape. Most notably, it is a function of the detuning parameter ε, which represents the energy difference between the two quantum dots. By tuning ε with gate voltages, one can shift the system toward the $(2,0)$ charge state, enhancing wavefunction overlap and thereby increasing J. In this thesis, we consider only the gate space where each dot maximally contains two electrons. Assuming a strong Coulomb interaction, as is typical in strongly confined single-electron double-dot potentials, and a well separated valley-degree of freedom, we are allowed to only consider the lowest five energy states. Under these conditions the Hamiltonian in Eq. (6.1) can be written in the basis $\{|\uparrow\uparrow\rangle, |\uparrow\downarrow\rangle, |\downarrow\uparrow\rangle, |\downarrow\downarrow\rangle, S(0,2)\}$ as follows [133]

$$H = \begin{pmatrix} \overline{E}_z & 0 & 0 & 0 & 0 \\ 0 & \Delta E_z/2 & 0 & 0 & t_0 \\ 0 & 0 & -\Delta E_z/2 & 0 & -t_0 \\ 0 & 0 & 0 & -\overline{E}_z & 0 \\ 0 & t_0 & -t_0 & 0 & U-\varepsilon \end{pmatrix}, \tag{6.2}$$

where $\overline{E}_z$ is the average and ΔE_z the difference in Zeeman energy of the two dots, t_0 is the interdot tunnel coupling which quantifies the wavefunction overlap, ε is the detuning or relative alignment of the energy ground states of both quantum dots and the on-site Coulomb interaction U is the charging energy cost of moving both electrons onto the same dot.

The energy structure of Eq. (6.2) is shown in Fig. 6.1**a** as a function of detuning energy ε. As the detuning approaches the charge transition $\varepsilon \to U$, the exchange interaction increases, leading to observable shifting of the energy levels. The four distinct spin-flip transition frequencies associated with conditional qubit operations are labeled f_1 to f_4 and are detectable in two-qubit spectroscopy (cf. Sec. 6.3). To aid physical intuition, Fig. 6.1**b** presents a schematic of how the detuning energy ε affects the alignment of the double quantum dot potential. This illustration introduces the scaled detuning parameter ε', which is defined as $\varepsilon' = \varepsilon/U$. In this convention, $\varepsilon' = 0$ corresponds to the symmetric $(1,1)$ charge configuration, while $\varepsilon' = \pm 1$ marks the charge transitions, where both electrons occupy the same dot. This concept is translated into experimental gate space in Fig. 6.1**c**, which shows an exemplary charge stability diagram. The red line highlights the scaled detuning axis ε', connecting the $(0,2)-(1,1)$ and $(1,1)-(2,0)$ transitions and the red points label the characteristic detuning values $\varepsilon' = 0, \pm 1$.

Effective exchange coupling strength

Using perturbation theory and assuming conditions near the charge transition, $|U-\varepsilon| \ll t_0$, one can eliminate the energetically distant charge state $|S(0,2)\rangle$ and associated off-diagonal

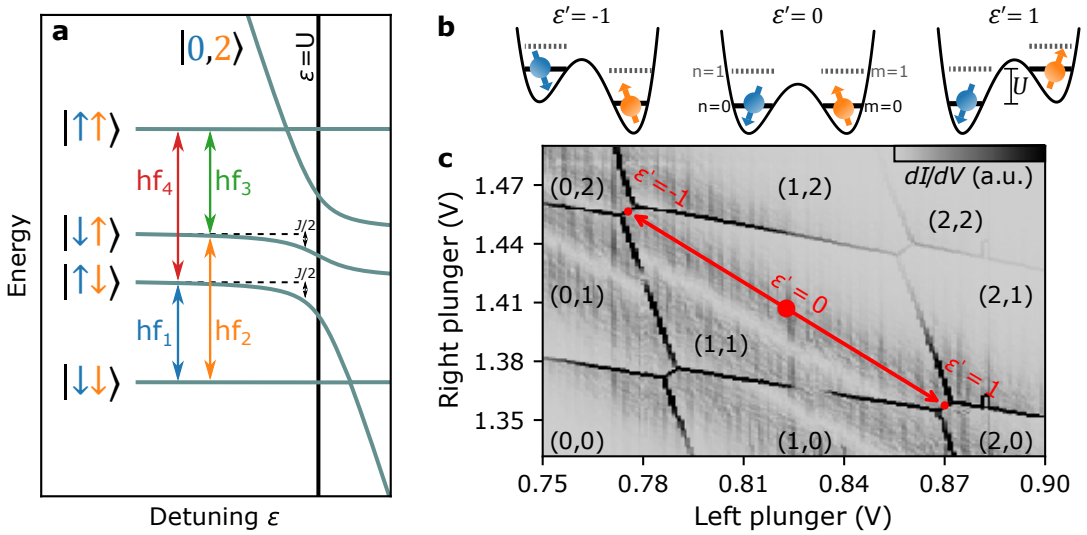

Figure 6.1: Energy structure and detuning axis of a two-qubit system. **a** Eigenenergies of the full two-qubit Hamiltonian from Eq. (6.2) as a function of detuning energy ε. The eigenstates represent the spin state of the left (blue) and right (orange) qubit, respectively. In the regime $\varepsilon < U$, the system satisfies $J \ll |f_1 - f_2|$, and the eigenstates evolve as described in Tab. 6.1. Four distinct transition frequencies f_1 to f_4 arise depending on the initial eigenstate, all of which are experimentally accessible. Inspired by Ref. [40]. **b** Schematic representation of the double quantum dot potential tilted by the detuning parameter ε, illustrating the charge redistribution between the two wells. The scaled detuning $\varepsilon' = \varepsilon/U$ is defined such that $\varepsilon' = 0$ corresponds to balanced wells, while $\varepsilon' = \pm 1$ represents the limits where both electrons prefer to occupy one dot. The central configuration reflects the (n, m) charge notation, where n (m) indicates the number of electrons in the left (right) dot. **c** Exemplary charge stability diagram at an interdot barrier gate voltage of $V_{\mathrm{IB}} = 0.85\,\mathrm{V}$. Dark lines indicate charge transitions, and the corresponding charge configurations (n, m) are labeled in each region. The red line denotes the scaled detuning axis ε', spanning from the $(0, 2) - (1, 1)$ transition (defined as $\varepsilon' = -1$), through the symmetric $(1, 1)$ point ($\varepsilon' = 0$), to the $(1, 1) - (2, 0)$ transition ($\varepsilon' = +1$).

terms in the Hamiltonian. Thus, the effective low-energy Hamiltonian is simplified to a spin-exchange form in the basis $\{|\uparrow\uparrow\rangle, |\uparrow\downarrow\rangle, |\downarrow\uparrow\rangle, |\downarrow\downarrow\rangle\}$ [133]

$$H = \begin{pmatrix} \overline{E}_z & 0 & 0 & 0 \\ 0 & \Delta E_z/2 - J/2 & J/2 & 0 \\ 0 & J/2 & -\Delta E_z/2 - J/2 & 0 \\ 0 & 0 & 0 & -\overline{E}_z \end{pmatrix}, \tag{6.3}$$

emphasizing exchange interaction terms and absorbing the detuning and Coulomb interaction into

$$J = \frac{t_0^2}{U - \varepsilon - \Delta E_z/2} + \frac{t_0^2}{U + \varepsilon - \Delta E_z/2}. \tag{6.4}$$

Gaining control over J is the key to perform two-qubit gates between the electron spins. The expression in Eq. (6.4) illustrates that J can be controlled either by dynamically pulsing the detuning ε or the tunnel coupling t_0. The first method can be realized by standard gate control of the qubits and has been successfully demonstrated in Refs. [40, 61]. This method is straightforward to implement but has the downside that electrical gate noise

can directly modulate J through the detuning and adversely impact the two-qubit gate performance [134, 135]. The second method modulates the interdot tunnel coupling t_0 by pulsing the inter-dot barrier gate to control the exchange energy. This necessitates the implementation of compensation pulses on the plunger gates but allows to operate at the so-called symmetry point $\varepsilon' = 0$, where $\partial J/\partial \varepsilon = 0$ and J is therefore first-order insensitive to detuning noise [135]. This method has also been successfully demonstrated in literature by [62, 79]. In this thesis, the experimental setup includes four AWG channels capable of pulsed control. However, two channels are dedicated to IQ-mixer control for microwave driving, leaving only two channels for direct qubit manipulation. As a result, only the first method of controlling J via detuning by pulsing the plunger gate voltages was feasible in the present setup.

Phenomenological model and experimental fitting

Although, the analytical expression of the exchange parameter $J(\varepsilon)$ in Eq. (6.4) is physically insightful, it contains multiple correlated parameters (U, t_0, ΔE_z) which complicates experimental fitting. A more tractable approach is motivated by a phenomenological assumption: the dependence of the interdot tunnel coupling t_0 on detuning reflects the increasing overlap of the electron wavefunctions as they tunnel through a finite-height potential barrier. This motivates the commonly used Ansatz that t_0, and by extension J, depends exponentially on detuning ε [62, 136]. A simplified exponential model of $J(\varepsilon)$ preserves the essential physics while facilitating robust fitting of experimental data [123]:

$$J(\varepsilon_u) \approx J_0 \exp\left(-\frac{\varepsilon_u}{\varepsilon_0}\right), \tag{6.5}$$

where the detuning axis is offset as $\varepsilon_u := U - \varepsilon$ such that J_0 is the exchange coupling at $\varepsilon_u = 0$ and ε_0 is the characteristic detuning scale over which J decays.

To further align the two-qubit Hamiltonian model with experimental data, it is common to incorporate a Stark shift correction, which accounts for additional energy shifts arising from electrostatic gate voltage changes [22, 137]. In practice, this correction factor can also absorb other effects that are related to changes of the confinement potential such as spin-orbit coupling, magnetic field gradients, or other perturbations not captured in the simplified Hubbard-like model [133]. The Stark shift $\Delta E_S(\varepsilon)$ is typically approximated as linear function for small variations around an operational point

$$\Delta E_S(\varepsilon_u) \approx \lambda_S \varepsilon_u, \tag{6.6}$$

where λ_S is the Stark shift coefficient. Combining these two effects, the measured qubit transition frequency f_i as a function of the detuning parameter ε can be expressed through the combined fit function

$$f_{res}(\varepsilon_u) = f_0 + \lambda_S \varepsilon_u \pm \frac{J_0}{2} \exp\left(-\frac{\varepsilon_u}{\varepsilon_0}\right), \tag{6.7}$$

where f_0 encapsulates the qubit's intrinsic transition frequency and constant offsets. This fit function can be applied to all four experimentally obtained resonance curves in the weak coupling regime, because the $\pm J(\varepsilon)$ term respects whether a transition is measured from the $|\downarrow\downarrow\rangle$ (- sign) or toward the $|\uparrow\uparrow\rangle$ state (+ sign). The parameters f_i, $\lambda_{\mathrm{S,L}}$, $\lambda_{\mathrm{S,R}}$ and J_0 can then be extracted from experimental data by optimizing the same parameter set to describe all curves simultaneously, enabling consistent extraction of device properties and precise calibration of the two-qubit control regime in semiconductor spin qubits.

6.2 Two-qubit working point

Among all experimental procedures presented in this thesis, the demonstration of coherent qubit-qubit interaction imposes the highest level of complexity and the most stringent requirements on the device itself. The main requirements can be summarized in three key points. First, each qubit must demonstrate high individual quantum quality, characterized by spectral isolation, and sustained coherence during single-qubit operations, even in the presence of a second confined electron. Second, the micromagnet must generate a strong magnetic field gradient across the double dot. A significant difference in the absolute field values at the positions of the two qubits is essential to achieve well-separated resonance frequencies and enable individual addressability without crosstalk. Finally, the interdot tunnel coupling must be well adjustable via the barrier gate separating the two dots. This tunability is critical to raise the inter-dot tunnel coupling t_0 high enough to achieve measurable exchange interaction. In the devices used in this work, the barrier gate is located in the third gate layer (c.f Sec. 2.5), which results in a relatively weak electrostatic lever arm and thus limits the range of tunable coupling. A key advantage of the Si/SiGe sample layout SD15B is that the 18 gates allow for a high degree of tunability of the device. However, when combined with external control parameters, such as the applied magnetic field, microwave drive power, and specific characteristics of the experimental setup, including RF line transmission, electronic noise, filtering and attenuation, the parameter space becomes exceptionally large and could not be conclusively optimized for the challenge of performing two-qubit operations with maximum fidelity. Instead, a targeted optimization loop was performed to identify and refine the parameters most critical for improving qubit performance in the two-qubit regime in order to pioneer the control of two coupled spin qubits within our group. The two most influential tuning knobs were found to be the precise shape of the initialization and readout pulse and the voltage applied to the interdot barrier gate. These parameters will be discussed in detail in the following subsections.

6.2.1 Interdot barrier potential

In the context of the two-qubit Hamiltonian, Eq. (6.4) reveals that the exchange interaction J scales quadratically with the interdot tunneling rate t_0. Therefore, a necessary precondition for measuring exchange coupling in a real system is to operate in a regime where t_0 is

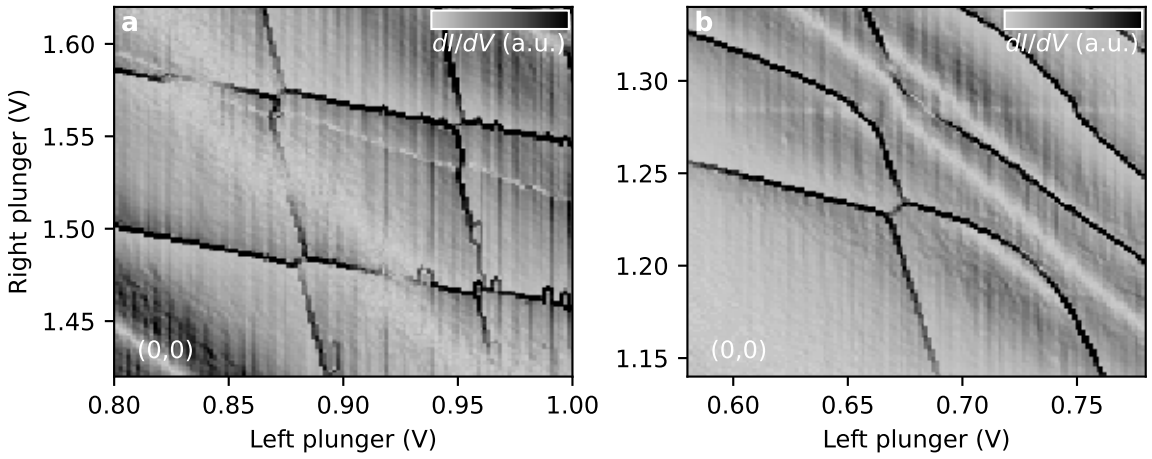

Figure 6.2: Derivative of the charge stability diagram of **a** 0.2 V and **b** 1.7 V interdot barrier voltage. Both graphs show a $0.2\,\mathrm{V} \times 0.2\,\mathrm{V}$ window of the left and right plunger gate voltage starting from the $(0, 0)$ charge state. The continuous color gradients in the background are Coulomb oscillations of the SET, whereas the dark lines indicate charge transitions. The faint white lines show a spurious defect state being (un)occupied.

sufficiently large. This can be achieved by lowering the potential energy of the interdot barrier, which brings the two electron wavefunctions spatially closer and increases their overlap, thereby enhancing tunnel coupling. As a first step toward entering a regime of strong qubit-qubit interaction, the interdot barrier gate voltage was increased from 0.28 V, the value used during single-qubit characterization, to 1.7 V, at which point the two quantum dots effectively merge into a single-dot confinement potential. The impact of this tuning is illustrated in Fig. 6.2. The charge stability diagram in Fig. 6.2**a** shows evenly spaced, linear charge transition lines with a characteristic spacing of approximately 70 mV for both dots, indicative of a well-defined double-dot configuration. In contrast, Fig. 6.2**b** reveals significant curvature in the charge transition lines beyond the first electron occupation, which bend toward parallel trajectories. Additionally, the disappearance of the charge transitions between the $(2, 0) - (1, 1)$ and $(1, 1) - (0, 2)$ configurations clearly marks the crossover from a double-dot to a single-dot regime. Since the $(1, 1)$ charge region becomes ill-defined under these conditions, the interdot barrier voltage should remain below 1.7 V to maintain a usable two-qubit configuration.

A systematic approach to identify a suitable interdot barrier voltage for demonstrating exchange interaction between two neighboring electrons is through frequency spectroscopy. In this method, the interdot barrier is varied while tracking shifts in the resonance frequencies of both qubits. The result of such a measurement is shown in Fig. 6.3, recorded under zero detuning ($\varepsilon' = 0$) using a long 50 µs excitation pulse and a reservoir tunneling rate of approximately 1 kHz for each qubit. Panels **a** and **b** display raw EDSR spectra of the right and left qubit, respectively, as a function of interdot barrier voltage. The corresponding extracted peak positions are shown in panels **c** and **d**. Both qubits exhibit a secondary resonance branch at higher frequency, which is likely associated with resonant driving of electrons occupying the first excited valley state. This observation can be explained by thermal effects. During the initialization stage, a fraction of electrons may occupy the upper valley due to thermal broadening of the reservoir distribution

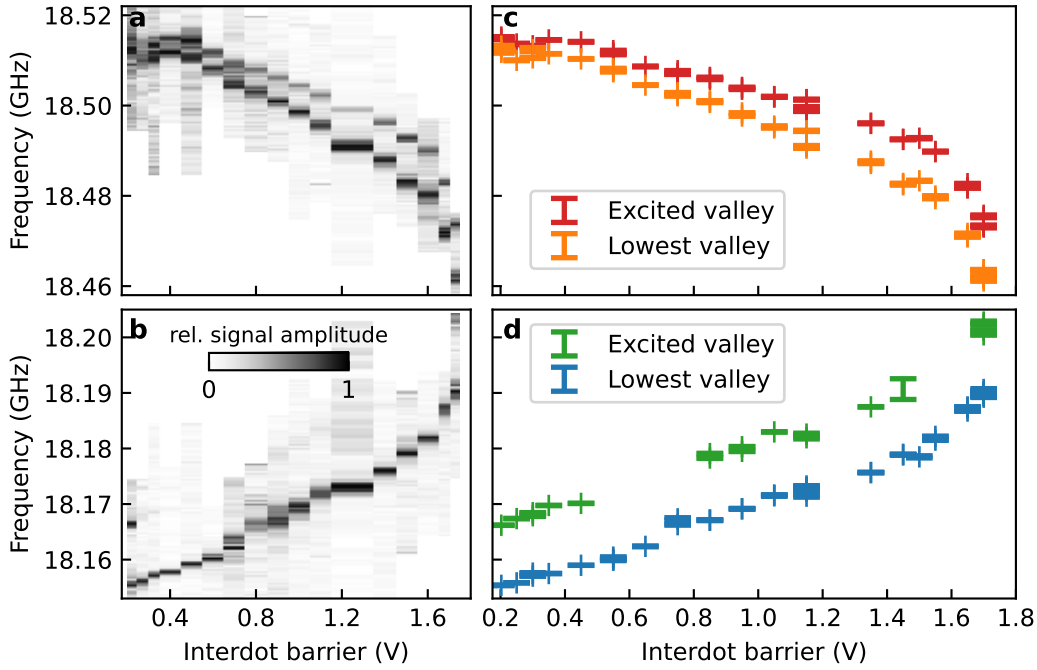

Figure 6.3: Resonance frequencies over the interdot barrier voltage. **a**,**b** Exemplary frequency measurement data with a 50 µs excitation pulse for each barrier voltage. Panel **a** shows the frequency range in which the right qubit is resonant, whereas panel **b** shows the frequency range for the left qubit. Both graphs display the relative signal amplitude per trace, as indicated by the color bar. Each pixel averages 100 single-shot readouts. **c**,**d** Lorentzian fitted resonance peak positions of both appearing peaks per qubit. The second peak is attributed to resonant transitions of thermally populated valley spin states with a slightly different g-factor. The error bars represent the fitting uncertainty on the peak position.

or equilibration processes, depending on whether the valley relaxation time is shorter than the delay between injection and manipulation. The ratio of the peak amplitudes reflects this fractional occupation [60]. For the left qubit a estimate of the valley splitting yields $E_V \approx 580\,\mathrm{mK} \cdot k_B$ (cf. Sec. 5.5) which is several times higher than both electron temperatures (cf. Sec. 4.5). While thermal injection into the excited valley should be suppressed under these conditions, it cannot be fully excluded. The higher resonance frequency of the excited valley state may be attributed to a difference in g-factor between valley states [138], which appeared to depend linearly on the interdot barrier voltage. This dependence could originate either from direct modulation of valley splitting by the out-of-plane electric field [55], or from a renormalization of the g-factor due to effective magnetic field gradients and spin-orbital mixing induced by the micromagnet [60]. A detailed investigation of this effect has not been performed in the scope of this thesis.

Increasing the interdot barrier voltage corresponds to lowering the interdot potential barrier in energy space. This causes the resonance frequencies of both qubits to converge, as the increased barrier voltage pulls the electrons toward the center of the double-dot system, where the magnetic field gradient is reduced. Ultimately, they can merge to one

quantum dot with charge occupation of two and experience the exact same magnetic field. Obviously, this limit is not desirable for two-qubit operation since the two electrons form a singlet state and are no longer individually addressable. However, entering this regime serves as an upper bound for the interdot barrier voltage and provides a reference point for when strong qubit-qubit interaction is reached.
Ideally, a second effect can be observed as the barrier is lowered and the tunnel coupling t_0 increases. If the double dot is initialized in $|\downarrow\downarrow\rangle$, both qubits' resonance frequencies should exhibit the onset of simultaneous drift to lower frequencies. This shift arises from the onset of exchange interaction at the operated detuning point, which leads to a frequency shift of $-J/2$ for both qubits, as summarized in Tab. 6.1 and has been demonstrated in Ref. [80]. In the present sample, it was not possible to reach a regime where exchange interaction becomes spectroscopically visible at zero detuning. The primary limitation was a significant degradation in the readout and initialization fidelity of the right qubit above 1.6 V, which coincides with the region of accelerated frequency convergence in Fig. 6.3**c**. This behavior is likely due to spatial displacement of the right qubit's orbital toward the interdot region and away from its electron reservoir. Although the reservoir coupling was maintained at approximately 1 kHz using thermal broadening features in the data, spin-up events displayed excessive timing jitter and required substantially longer readout windows for reliable signal discrimination. This increased the number of background events and ultimately reduced readout fidelity above 1.6 V. To balance the need for strong exchange coupling with stable readout, an interdot barrier voltage of 1.55 V was selected for all subsequent experiments.

A successful enhancement of the interdot tunnel coupling can be inferred from a detailed analysis of the $(1,1)-(2,0)$ charge transition in the charge stability diagram measured at an interdot barrier voltage of 1.55 V. The schematic in Fig. 6.4**a**, illustrates how the curvature and anti-crossing behavior of this transition are governed by the interdot tunnel coupling t_0 and the Coulomb energy U', both of which are key parameters influencing the exchange interaction J. It shall be clarified, that the Coulomb energy U' connects the charge states $(0,1)$ and $(1,2)$ and refers to the energy cost of adding an additional electron to both dots at maximum detuning $\varepsilon = U$. This energy serves as a lower bound to estimate the order of magnitude of the interdot Coulomb energy U, which measures the energy that is required to load an additional electron to one dot at $\varepsilon = 0$. Experimental data at $\varepsilon = U$ with a similar construction as in panel **a** is shown in Fig. 6.4**b**. Due to the limited resolution of the measurement and the sensitivity of linear fits to the selected range, the extracted values should be considered approximate. Using estimated lever arms for the left and right plunger gates, the Coulomb energy is found to be $U' \approx 1.9$ meV, and the energy splitting at the anti-crossing provides an upper bound of $t_0 < 60$ GHz. Both values are in good agreement with results reported for similar Si/SiGe double quantum dot systems. Tunnel couplings in the range of GHz and interdot Coulomb energies on the order of meV have been shown in comparable devices [40, 79]. The extracted parameters confirm that the device is operating in a regime suitable for observing exchange interactions in a two-qubit system.

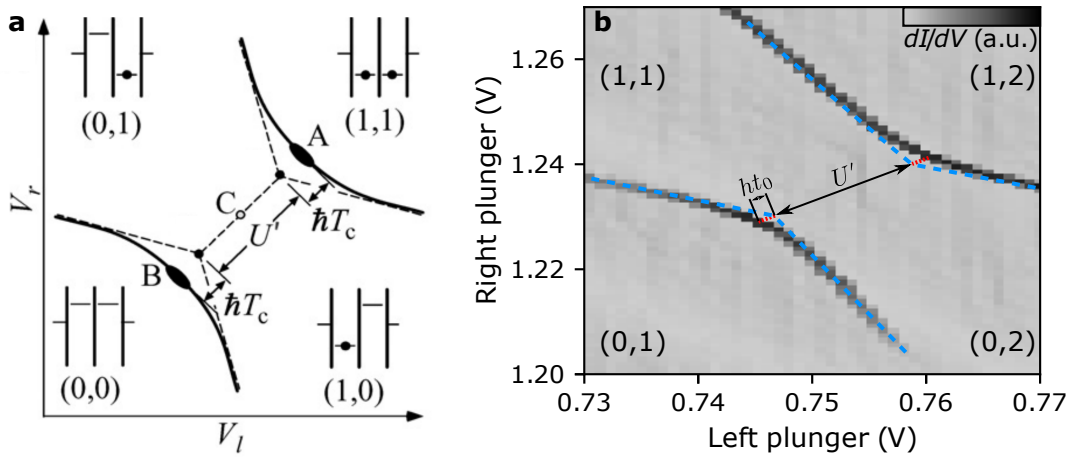

Figure 6.4: Characteristics of exchange interaction in the charge stability diagram. **a** Schematic illustration of the interplay between Coulomb energy U' at maximum detuning and tunnel coupling t_0 (denoted as T_c in this figure). The anti-crossing behavior at the triple points reflects coherent tunneling between charge states and highlights the energetic landscape of the double quantum dot system. Adapted from Ref. [139]. **b** Experimental close-up of the $(1,1) - (0,2)$ charge transition at an interdot barrier voltage of 1.55 V. Blue dashed lines are linear fits to the charge transition branches far from the anti-crossing. Their extrapolated intersection allows to approximate the location of the bare crossing point. From this construction, the Coulomb energy is estimated as $U' = 1.9$ meV, while the minimum splitting between the charge branches gives an upper bound on the tunnel coupling of $t_0 < 60$ GHz. The red dashed line extends from the intersection point to the measured transition lines, and the vertical separation between these lines corresponds to the energy scale ht_0.

6.2.2 Two-qubit working point and pulse sequence

Working point considerations

The transition from single-qubit to two-qubit operation is achieved in two stages. First, the charge configuration must be changed from a single-electron occupation to a multi-electron (n, m) state, where both n and m are odd and non-zero. This condition ensures that each dot hosts an unpaired electron allowing for spin-spin interaction with the neighboring dot. In this work, the configuration $(1, 1)$ was chosen as the basis for two-qubit operation. The corresponding charge stability diagram of the Si/SiGe device is shown in Fig. 6.5**a**, along with the adjacent charge states labeled in white.

Establishing a well-defined double quantum dot from the single-dot regime requires substantial adjustments to the confinement gate voltages. These modifications ensure proper tunnel coupling of each dot to its respective electron reservoir, optimize the electrostatic confinement for electric-dipole spin resonance (EDSR) addressability, and maintain strong sensitivity of the asymmetrically placed charge sensor to both qubits. Additional care must be taken to avoid interaction with defect states and to control the spatial proximity of each qubit to the microwave drive line (cf. Sec. 5.6.2). While the device's 18 tunable gates offer excellent flexibility for satisfying these requirements, the necessary tuning is time-consuming due to cross-capacitance effects. Each gate adjustment typically necessitates iterative compensation on adjacent gates.

Two-dimensional control of the plunger gates is essential for full two-qubit manipulation, as both dots must be initialized, manipulated, and read out in a coordinated sequence. The detuning parameter ε, representing the relative energy difference between the dots, is implemented by moving along a calibrated detuning axis in the charge stability diagram. All key operating points in the pulse sequence are defined within this diagram and approached via a reproducible vector-based path construction using a set of purple reference markers in Fig. 6.5**a**.

Initialization and readout positions for each qubit are indicated in yellow and are located 10 mV from the triple point connecting the $(1, 0)$, $(0, 1)$, and $(1, 1)$ charge states. The scaled detuning axis $\varepsilon' = \varepsilon/U$ is marked in red and defined to pass through the midpoint of the charge transitions between the $(1, 1)$ and $(2, 0)$ or $(0, 2)$ state. In absolute terms, a scaled detuning of $\varepsilon' = 1$ corresponds to a combined plunger voltage shift of 57.3 mV. Using the previously determined lever arms of $\alpha_\mathrm{L} = 0.120\,\mathrm{eV/V}$ for the left and $\alpha_\mathrm{R} = 0.109\,\mathrm{eV/V}$ for the right plunger (cf. Sec. 4.4), this yields a total detuning energy of approximately 6.57 meV. It should be noted that the asymmetry in the charge-state anticrossings near $\varepsilon' = \pm 1$ likely causes a slight underestimation of the extracted value for the charging energy U. Although this does not impact the present analysis, it could be accounted for in a more refined construction of the detuning axis in future work.

Pulse sequence overview

The plunger pulse sequence used to initialize and measure two qubits in a double quantum dot is illustrated in Fig. 6.5**b**. Each measurement cycle begins with the deterministic initialization of both qubits into the ground state $|\downarrow\downarrow\rangle$. The plunger gate voltages are then pulsed along the detuning axis to a specified operating point, where the strength of the qubit-qubit exchange interaction can be tuned. At this position, coherent qubit control is performed via microwave bursts. Following manipulation, the system is returned to a designated readout point, where the spin state of one qubit is measured. To capture the response of both qubits to the same manipulation, the full procedure is then repeated with identical parameters, ending in the readout of the other qubit.

Initialization The plunger manipulation sequence begins with a single electron loaded at the yellow "Init" point (see Fig. 6.5**a**), corresponding to step I in Fig. 6.5**b**. This point lies directly at the charge transition between the $(0, 1)$ and $(1, 0)$ state, which has been identified as one of three T_1 relaxation hotspots in the vicinity of this transition, as reported in [61]. The remaining two hotspots have been attributed to spin-orbit mixing [140] and spin-valley-orbit mixing [55], both of which can be enhanced by interface disorder in the quantum well. In these regions, phonon-mediated spin relaxation is enabled through spin-orbit coupling, which hybridizes valley states and allows inter-valley transitions of excited spins followed by rapid valley relaxation, facilitating efficient relaxation into the spin-down ground state. T_1 relaxation times as short as 220 ns have been reported at the $(0, 1) - (1, 0)$ transition [61], emphasizing the effectiveness of these hotspots for spin initialization. Although the precise T_1 relaxation time at the "Init" point was not characterized in this

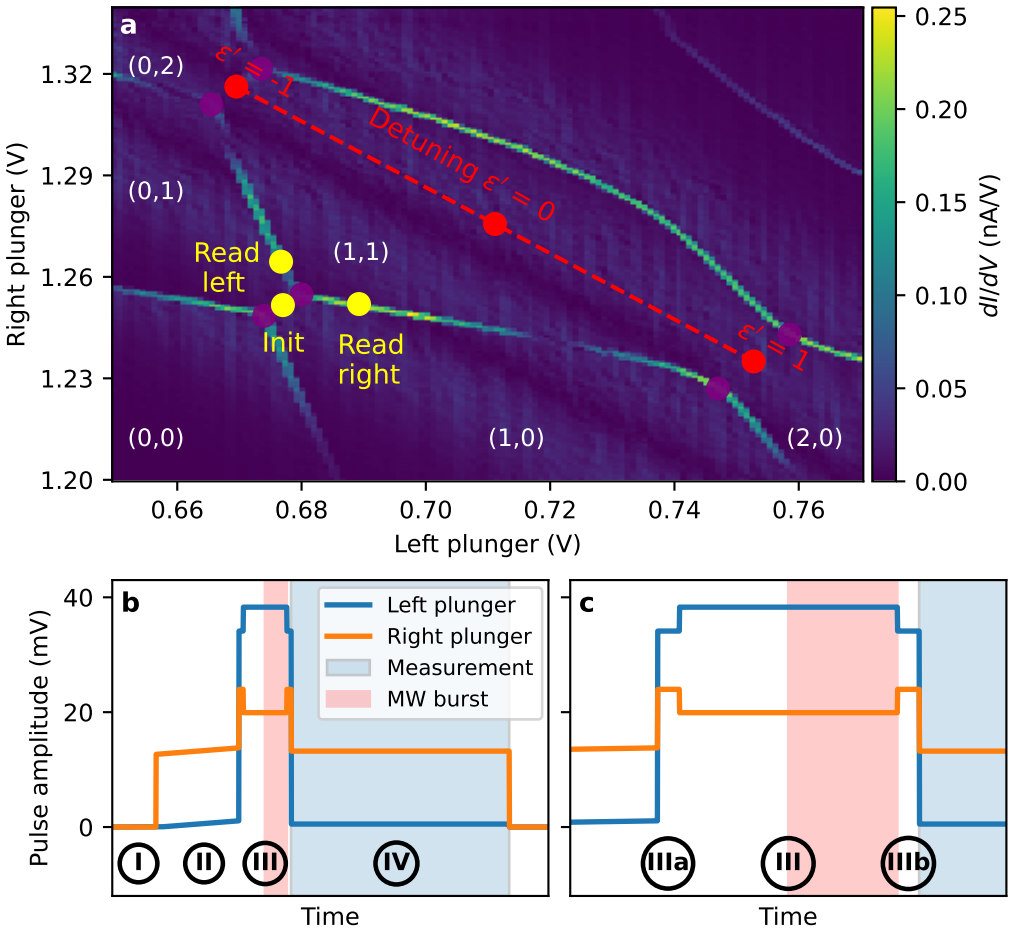

Figure 6.5: **a** Charge stability diagram showing the differential sensor signal dI/dV at an interdot barrier voltage of 1.55 V. Charge configurations are labeled as (n, m), where n and m denote the electron occupations in the left and right dot, respectively. Purple markers at characteristic points of the diagram are used for vectored construction of all functional positions. The red markers define the scaled detuning axis ε', as introduced in Fig. 6.1. The initialization/readout position of each qubit is indicated in yellow. **b** Pulse sequence applied to the left and right plunger gates during two-qubit experiments. The measurement window indicates the interval during which the charge sensor signal is recorded. Roman numerals label the functional sections. I: initialization of the first qubit at the "Init" point; II: loading and initialization of the second qubit at the "Read left" point; III: coherent manipulation at the desired detuning (e.g. $\varepsilon' = 0.5$) via microwave (MW) excitation; IV: spin-selective readout of one qubit at the "Read left" point. The same sequence is repeated for the other qubit immediately after, with initialization and readout performed at the alternate point ("Read right"). By that, both qubit's response to an identical microwave manipulation can be obtained. **c** Expanded view of stage III, showing the timing of the microwave burst. The qubit is first pulsed to $\varepsilon' = 0$ (IIIa), then held at the target detuning for the duration of the burst (III), and finally returned to $\varepsilon' = 0$ (IIIb). This procedure ensures a consistent approach to the working point by following a common voltage trajectory along the detuning axis, independent of the absolute detuning value. A delay of 100 µs precedes the burst to allow the 60 kHz low-pass filters on the plunger lines to settle. All durations in **b** and **c** are schematic and not to scale.

work, a conservative initialization time of 5 ms was employed throughout all experiments. This duration was verified experimentally to be sufficient for reliable preparation of the spin-down ground state.

Following this, the second electron is loaded at the "Read left" position (step II), corresponding to the $(0,1) - (1,1)$ charge transition. Spin-selective loading is achieved in analogy with the single-qubit initialization protocol introduced in Sec. 5.3. The plunger voltages are slowly ramped across the transition to preferentially capture a spin-down electron. By that, the energy of the quantum dot is gradually lowered below the Fermi level of the reservoir until the probability of a thermal excitation becomes negligible. Here, the loading and initialization ramp was chosen to be 10 ms because of the reservoir coupling of approximately 1 kHz. At the end of this initialization protocol the two-qubit system is initialized in $|\downarrow\downarrow\rangle$.

Manipulation The temporal resolution of detuning control in this experiment is fundamentally limited by the 60 kHz low-pass filters in the plunger gate lines (see Sec. 3.3). These filters introduce an exponential voltage settling behavior, requiring approximately 100 µs to reach steady state following a step voltage change. To accommodate this, a minimum delay of 100 µs was inserted between arrival at the target detuning point and the start of any microwave burst, ensuring that the system has reached its intended operating condition.

In addition, the time-dependent voltage trajectory toward a given detuning value varies significantly depending on its absolute position within the detuning axis. To guarantee a consistent and reproducible approach across all detuning values, auxiliary pulses (labeled IIIa and IIIb in Fig. 6.5**c**) are applied immediately before and after the manipulation pulse (III). These pre- and post-pulses bring the system to the symmetry point $\varepsilon' = 0$, effectively guiding all detuning trajectories through a common intermediate state. This standardization minimizes variations in transient voltage behavior caused by gate cross-capacitance or different trajectories in gate space, and proves particularly beneficial for coherence measurements and detuning-dependent gate calibration.

After reaching the target detuning point, the system is held at this position for the duration of the microwave burst, which is tuned on the nanosecond scale to implement the desired Rabi rotation. In this way, both the timing and spatial voltage trajectory of the manipulation are consistently defined for all detuning points, enabling reliable detuning-dependent qubit operation across the entire accessible range.

Readout In the final stage (IV), the system is pulsed back to the "Read left" point to determine the quantum state of the first qubit via spin-selective tunneling to the reservoir (see Sec. 5.1).

The entire sequence of initialization, manipulation, and readout is then repeated immediately, with the only difference that the "Read right" point is used for both initialization and readout. This approach enables sequential access to the spin states of both qubits,

providing valuable insight into their mutual interaction and the influence of the control sequence. Direct observation of both qubit responses facilitates a more complete interpretation of two-qubit dynamics and represents an important diagnostic tool for optimizing gate operations. In contrast to most studies on two-qubit systems, which typically read out one qubit after manipulation, only a few works to date have implemented dual-qubit readout protocols [61, 62, 141].

6.2.3 Verification of qubit control at zero detuning

The previously described adjustments to the interdot barrier and the careful engineering of the initialization and readout pulse sequence were essential for enabling reliable operation of both qubits in the $(1, 1)$ charge state. With this configuration, it was possible to perform systematic characterization of single-qubit gates in the two-qubit regime at $\varepsilon' = 0$, and to benchmark their performance. The purpose of this section is not only to assess the coherence of qubits, but also to validate the functionality of the newly developed two-qubit pulse scheme. This includes demonstrating reliable initialization, accurate detuning control, and robust readout for each qubit.

Long term stability

As a first benchmark of system stability, a long-term frequency-resolved Rabi measurement was conducted over a continuous duration of 35 h. This measurement was performed on the left qubit at a scaled detuning of $\varepsilon' = 0$ and the results are displayed in Fig. 6.6. The qubit was driven using a combination of 18 dBm external microwave power and a 1 V AWG amplitude, resulting in a Rabi frequency of $f_{\mathrm{Rabi}} = 3.65\,\mathrm{MHz}$. The measurement in Fig. 6.6**a** displays the characteristic interference pattern commonly referred to as a Chevron pattern due to its symmetric structure around the resonance frequency (see Sec. 5.2.2). For reference, a numerically simulated Chevron pattern using the experimentally extracted f_{Rabi} and Rabi decay time $T_{2,\mathrm{Rabi}} = 5.5\,\mu\mathrm{s}$ is shown in the inset. The black dashed line in panel **a** indicates the location of peak positions within the Chevron interference pattern, corresponding to the drive frequencies that maximize spin-up population as a function of pulse duration. These peaks are extracted along vertical cuts through the data and represented in panel **b** to provide a direct measure of the effective qubit resonance frequency over time. A slow drift in the resonance frequency is visible, amounting to approximately 2 MHz across the 35-hour data acquisition.

This gradual shift of the resonance frequency observed in Fig. 6.6**a** and **b** is most likely attributable to a slow drift of the electrostatic working point, caused by quasi-static charge noise in the surrounding environment. Such fluctuations are a well-known source of instability in gate-defined quantum dots and can ultimately limit qubit coherence times [25, 129]. A second potential contributor could be changes in the polarization of the cobalt micromagnet. However, previous studies have shown that the CoMM remains fully saturated for external magnetic fields above 300 mT [64], which was satisfied in this

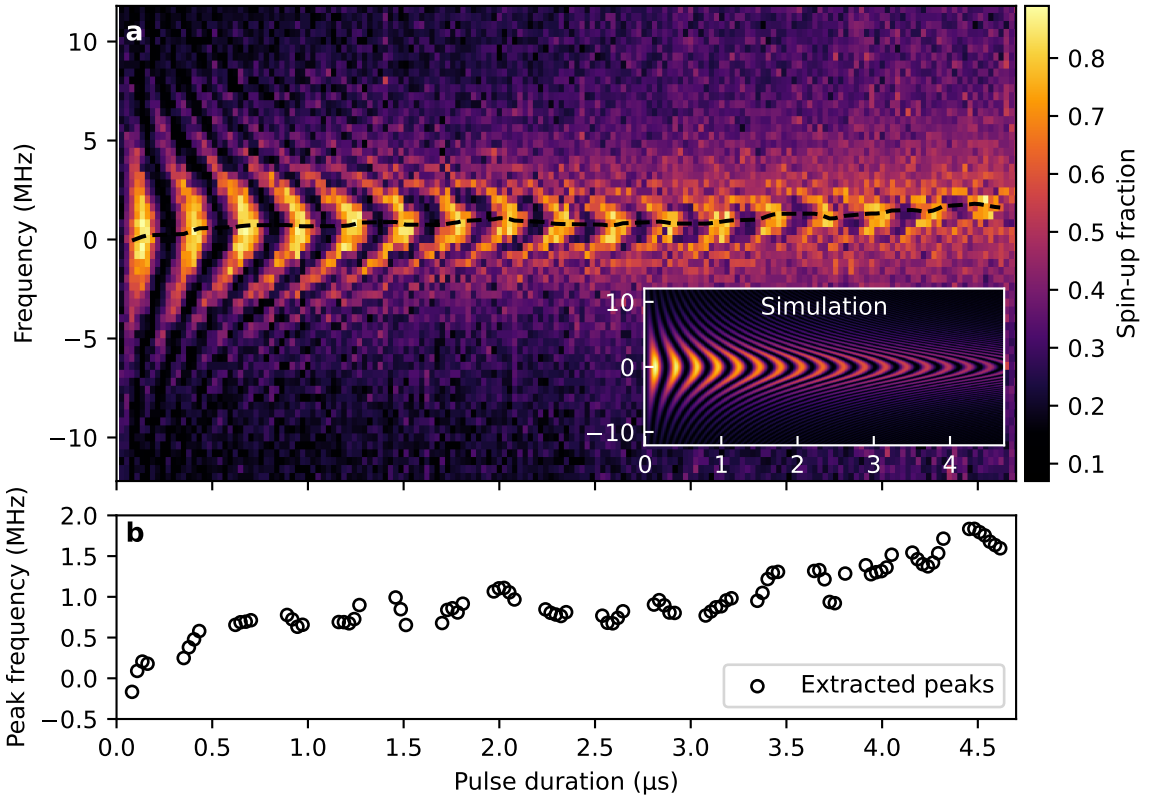

Figure 6.6: Long-term stability of the two-qubit working point at charge configuration $(1, 1)$ and scaled detuning $\varepsilon' = 0$. The frequency axis in all panels is offset by the qubit's resonance frequency of 19.598 GHz. **a** Chevron pattern of the left qubit measured at 18 dBm drive power and 1 V AWG amplitude, showing Rabi oscillations with $f_{\text{Rabi}} = 3.65$ MHz recorded continuously over a period of 35 h. The dashed black line is a guide to the eye based on the extracted peak positions in panel b, highlighting the drift of the central resonance. The inset shows a simulated ideal Chevron pattern using the same Rabi frequency and a coherence time $T_{\text{Rabi}} = 5.5$ µs, as extracted from the experimental data. Each data point is averaged over 100 single-shot readouts. **b** Extracted peak positions from vertical slices of the Chevron pattern. The results indicate a slow resonance frequency drift of approximately 2 MHz over 35 hours, demonstrating stable operation at the working point.

experiment at 19.6 GHz. A final consideration involves current stability of the current sources of the superconducting magnet, which can induce small fluctuations in the static magnetic field. These fluctuations occur on a 100 MHz timescale, as specified by the manufacturer, and are negligible in this context since they either average out over the comparatively long pulse durations or are effectively suppressed by the large inductance and capacitance of the coil circuit. Moreover, an increase in background signal is observed for extended pulse durations, evident as a rising baseline in the spin-up fraction of the measured data in comparison with the inset. This is attributed to dissipation from extended microwave bursts, which result in increased local heating and a higher probability of thermally activated tunneling events during the readout phase.

Despite these minor effects, the observed frequency drift remains below the linewidth of the qubit resonance and is negligible on the timescale of standard single-qubit operations, which generally require only a few π-pulses and complete within less than an hour. This

result highlights the remarkable long-term stability of both the experimental setup and the natural Si/SiGe quantum device, even in the presence of an idle second electron within the double dot configuration.

Single-qubit rotations

The results of Rabi, Ramsey, and Hahn-echo experiments (see Secs. 5.6 and 5.7 for details) performed on both qubits in the $(1, 1)$ charge configuration at a detuning of $\varepsilon' = 0$ are presented in Fig. 6.7. Due to the design of the plunger pulse sequence, both qubits are subjected sequentially to the same microwave burst, allowing a direct comparison of their response under identical conditions. In each panel, the data from the driven (target) qubit is shown in solid colors, while the simultaneously recorded spin-up probability of the idle (control) qubit is plotted as semi-transparent points. At zero detuning, where the exchange interaction is negligible, the off-resonant qubit is expected to remain unaffected by the microwave drive. However, a finite and nearly constant spin-up probability is observed in the idle qubit across all measurements. This adjustable offset originates from thermal background events, which are indistinguishable from genuine spin-up tunneling events in the raw readout signal. As a result, they produce a systematic positive offset in the measured spin-up fraction across all experiments (see Sec. 5.1).

All experiments shown in Fig. 6.7 were conducted using an external microwave power of 18 dBm, with AWG modulation amplitudes of 0.4 V for the left qubit and 1 V for the right qubit. In consideration of all known losses in the microwave setup this corresponds to about −52 dBm and −44 dBm for the left and right qubit at the sample (see Sec. 3.5). The reduced microwave amplitude for the left qubit was selected to match the Rabi frequency of the right qubit, thereby ensuring comparable drive conditions for both. This calibration resulted in a Rabi frequency of $f_{\mathrm{Rabi}} = 1.38$ MHz for the left qubit (Fig. 6.7**a**) and $f_{\mathrm{Rabi}} = 1.37$ MHz for the right qubit (Fig. 6.7**b**), achieved by resonant driving at 19.60 GHz (left) and 19.88 GHz (right). The fit uncertainties on the Rabi frequencies are below 6 kHz and are therefore omitted. The left qubit displays a visibility of 86% without significant decay over the measured 6 µs, while the right qubit shows reduced visibility of 55% and a Rabi decay time of approximately 5 µs. The visibility is defined as the difference between the peak spin-up probability and the thermal background offset. In practice, the maximum achievable visibility is limited by the interplay between the Zeeman energy splitting and the thermal broadening of the reservoir's Fermi distribution. This results in a high sensitivity to the precise alignment between the reservoir level and the spin-dependent energy levels of the qubit during the readout stage. The higher visibility observed in the left qubit is consistent with its reduced transition broadening compared to the right qubit, as previously discussed in Sec. 4.5. However, it should be emphasized that these experiments were not optimized for maximum visibility. Instead, the primary objective was to characterize the coherence properties of both qubits at zero detuning as a prerequisite for subsequent two-qubit gate implementation.

Based on the extracted Rabi frequencies, calibrated π and $\pi/2$ pulses were used to perform Ramsey (cf. Sec. 5.7.1) and Hahn-Echo (cf. Sec. 5.7.2) measurements. Ramsey experiments

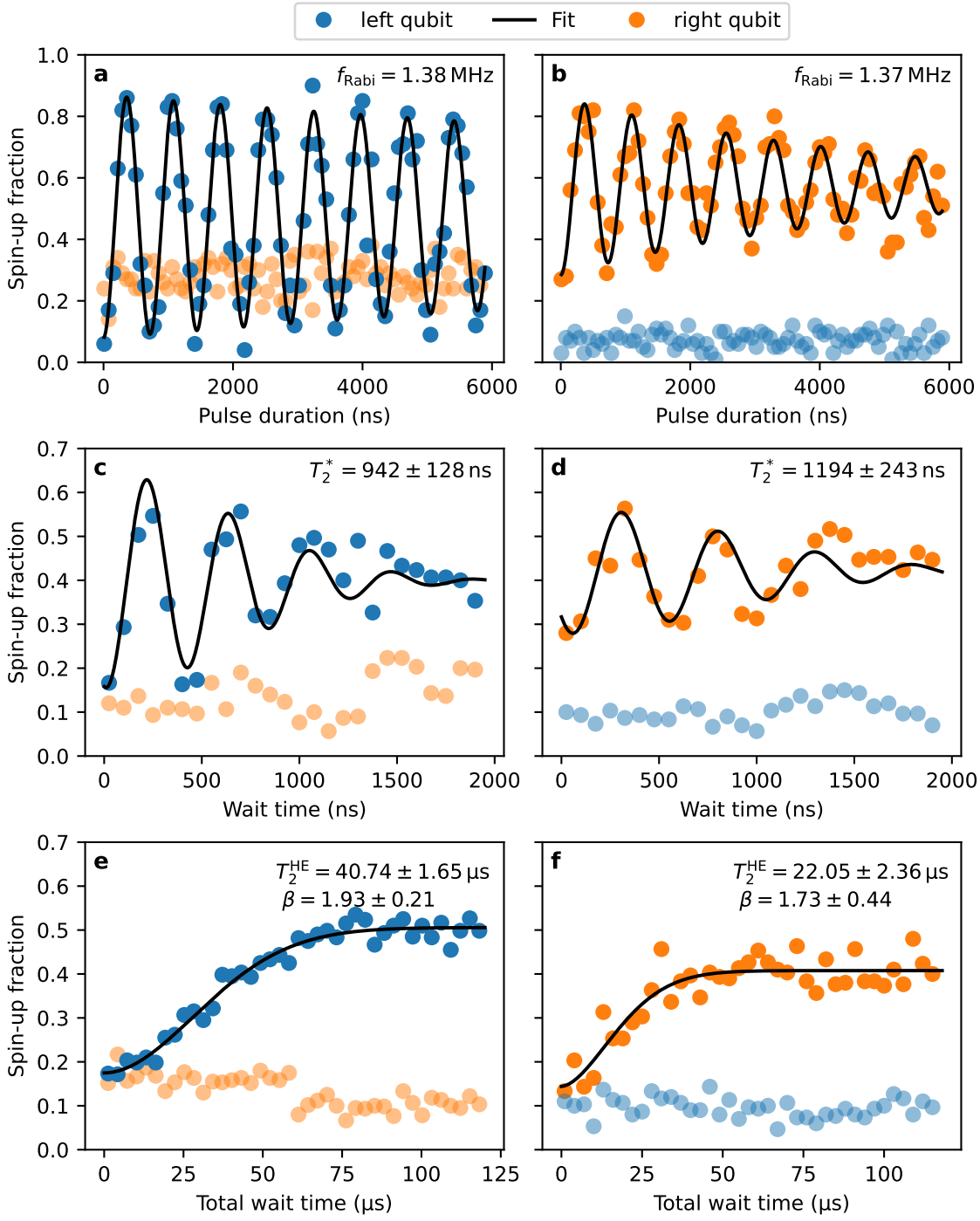

Figure 6.7: Single qubit operations in the $(1, 1)$ charge state at zero detuning. Plain colors indicate the manipulated qubit, while opaque colors show the off-resonant qubit under the same manipulation. All experiments were performed at 18 dBm external microwave power with AWG modulation amplitudes of 0.4 V and 1 V for the left and right qubit manipulation, respectively. Errors indicate statistical fit uncertainties. Panels **a** and **b** display Rabi oscillations at 19.60 GHz (left) and 19.88 GHz (right), fitted with Eq. (5.12). Each point is the result of 100 single shot readouts. Panels **c** and **d** show the results of a Ramsey experiment with 2 MHz frequency detuning. The Ramsey fringes were fitted using Eq. (5.13). To reduce clutter, each point averages three adjacent wait time steps with 100 single-shot readouts each. Panels **e** and **f** present Hahn-Echo experiments of both qubits fitted with Eq. (5.14). Each point averages six adjacent time steps in panel **e** and three in panel **f** with 100 single-shot readouts each.

were performed at an intentional 2 MHz drive frequency detuning, to generate resolvable interference fringes. The resulting Ramsey oscillations and their decay, shown in Fig. 6.7**c** and **d**, yield dephasing times of $T_2^* = (942 \pm 128)$ ns for the left qubit and $T_2^* = (1194 \pm 243)$ ns for the right qubit. These values are typical for natural Si/SiGe devices and are indicative of dephasing primarily limited by low-frequency magnetic field noise, such as fluctuations in the Overhauser field [21, 29]. The larger statistical uncertainty in the right qubit reflects its reduced visibility and higher scatter in the spin-up readout signal, both of which degrade the precision of the fitted envelope.

The impact of noise of higher frequencies can be assessed using a Hahn-echo experiment. The results, shown in Fig. 6.7**e** and **f**, yield coherence times of $T_2^{\mathrm{HE}} = (40.74 \pm 1.65)$ µs for the left qubit and $T_2^{\mathrm{HE}} = (22.05 \pm 2.36)$ µs for the right qubit. As in previous measurements, the right qubit exhibits both reduced visibility and a shorter coherence time. Interestingly, the fitted decay exponent β of the right qubit yields a value closer to two, than in the single-qubit regime, indicating that the approach of the two-qubit working point might have moved the dot further away from the decoherence source (see Sec. 5.7.3).

Overall, the coherence times measured in the two-qubit regime are slightly lower but in well agreement with the values previously determined under single-qubit confinement. A comparison of the results with existing literature and an detailed discussion of the relevant decoherence channels are provided in Sec. 5.7.3.

Proof of concept

The main purpose of assessing the qubit coherence in the two-qubit regime was to validate the functionality of the newly developed sequential two-qubit pulse sequence. The shown data verify that the pulsed plunger manipulation scheme fulfills its intended purpose of initializing both qubits in the spin-down state and the accurate settling to the target detuning value before each microwave-driven manipulation. Proper initialization is most clearly demonstrated by the clean, high-contrast Rabi oscillations observed in Fig. 6.7**a** and **b**. Incomplete or faulty initialization would result in truncated oscillations due to non-deterministic preparation of the qubits in the ground state. In contrast, the observed sinusoidal behavior with good visibility confirms that both qubits are consistently prepared in their ground state prior to the control pulse. Furthermore, the detuning control is best verified through the Ramsey measurements presented in Fig. 6.7**c** and **d**, which display interference fringes with the periodicity of the intentionally applied frequency detuning. The resonance frequency of the qubits is strongly dependent on the detuning value (see Sec. 6.3) and would lead to unintentionally fast Ramsey fringes or even off-resonant drive if set incorrectly. Consequently, the observation of coherent and reproducible qubit dynamics under this pulse protocol serves as strong evidence for successful implementation of two-qubit control infrastructure.

6.3 Exchange coupling spectroscopy in a two-qubit system

A central prerequisite for implementing two-qubit gates in spin qubit systems is the ability to precisely control and characterize the exchange interaction J between adjacent electrons. In gate-defined semiconductor quantum dots, this coupling is mediated by the tunable tunnel barrier and is strongly dependent on the detuning parameter ε, which defines the energy asymmetry between the two dots. This section presents a detailed experimental characterization of the exchange coupling strength $J(\varepsilon)$ and its impact on the energy spectrum of both qubits. To this end, electric-dipole spin resonance (EDSR) spectroscopy is employed to extract the exchange-induced shifts in resonance frequency for both qubits over a range of detuning values. These results enable a quantitative mapping of the two-qubit Hamiltonian under detuned conditions and establish the operational boundaries for exchange-driven qubit interactions in the selected device. The extracted functional form of $J(\varepsilon)$ can be used for calibrated two-qubit gate design in future experiments.

6.3.1 Microwave control for state-selective EDSR drive

Before detuning-dependent behavior can be reliably characterized, it is critical to ensure precise and robust microwave control over both qubits. This guarantees that transitions can be selectively driven across the entire detuning range, regardless of the changing resonance conditions. Only with such control in place can the evolution of the exchange interaction can be meaningfully extracted from the measured spectroscopy. Figure 6.8 illustrates an exemplary waveform for this two-step manipulation, as generated by the arbitrary waveform generator (AWG). The carrier signal of the microwave generator is provided to the LO port and the two AWG channels are connected to the I and Q ports of an IQ mixer, enabling sideband generation with user-defined modulation (see Sec. 3.5). Due to the 280 MHz resonance frequency separation between the two qubits, direct single-sideband excitation is not feasible within the limited bandwidth of the AWG. Instead, the LO frequency is positioned midway between the two qubits' Larmor frequencies. In this configuration, the left and right sidebands of the IQ mixer are used to selectively switch between the control and target qubit drive in runtime. The two sidebands are sequentially addressed by the visible change in phase between the I and Q signals (AWG Ch1 and Ch2) across the dashed black line, which separates the two pulse segments: optional control qubit preparation (left) and target qubit manipulation (right).

The drive amplitudes are adjusted to match the effective Rabi frequencies of both qubits. Specifically, the AWG output for the left qubit is reduced to 0.4 V to match the Rabi frequency of the right qubit at 1 V, enabling a similar pulse duration for both π-pulses (see Sec. 3.5). Furthermore, the modulation frequency of the control qubit section is dynamically adapted to the changing LO frequency. This ensures the drive of the control qubit to be always on resonance, while the sideband addressing the target qubit is modulated with a fixed frequency of 150 MHz and consequently changes with the LO frequency. In the shown example, this corresponds to a total sideband spacing of 270 MHz, where the control qubit is driven on resonance but the target qubit is probed at a detuning of 10 MHz.

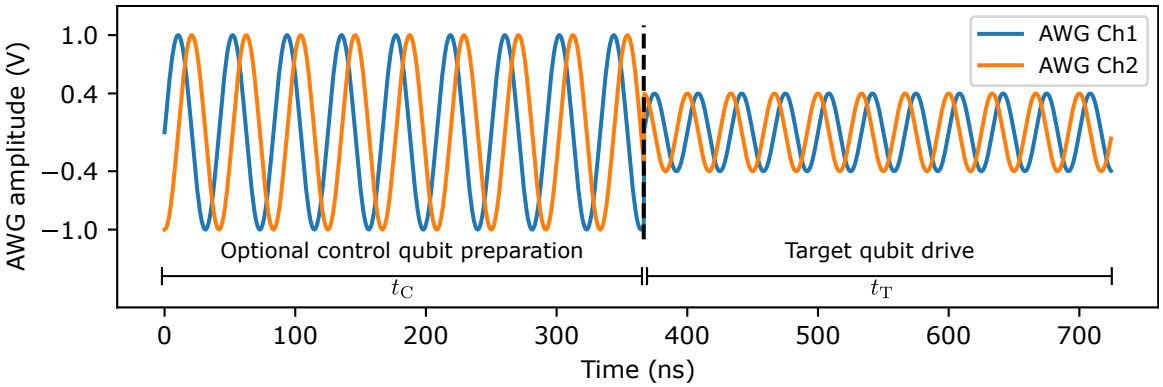

Figure 6.8: Two-step AWG modulation signal for EDSR spectroscopy. The first optional segment before the dashed black line is used for preparation of the control qubit state with a microwave burst of duration t_C and adaptive frequency modulation to stay resonant regardless of the LO frequency. The second segment addresses the target qubit with a constant modulation frequency of 150 MHz and a burst duration of t_T. The AWG Ch1 and Ch2 are connected to the I and Q port of an IQ mixer. Together with a microwave generator attached to the LO port, both qubits can be addressed in runtime by sideband switching. For visualization reasons, both modulation frequencies have been divided by a factor of five.

In summary, the presented way of microwave control allows to switch between sidebands, adjust the power and change the microwave frequency on a nanosecond scale. All these degrees of freedom are necessary to coherently control a two-qubit system and are not inherently available, as adjustments of power or frequency at the microwave source typically require milliseconds to be adapted. This flexible waveform structure allows fast and state-selective EDSR driving with full control over both spin states and builds the foundation for probing exchange interaction and conditional gate operations across the detuning axis.

6.3.2 Frequency spectroscopy over detuning

The exchange-induced energy shift of antiparallel spin states as a function of detuning can be visualized by resolving the resonance frequency of the target qubit conditioned on the spin state of the control qubit. This is achieved by preparing the control qubit in either the spin-down state $|\downarrow\rangle$, as initialized in the default $|\downarrow\downarrow\rangle$ configuration, or in the spin-up state $|\uparrow\rangle$ via a calibrated π-pulse at the control qubit's Larmor frequency. Either way, subsequent probing of the target qubit at different frequencies with a π-pulse will reveal its conditional resonance. The ability to perform these conditional excitations critically relies on two factors: a precise calibration of the Rabi frequencies to ensure the fidelity of both π-pulses, and the assumption that these Rabi frequencies remain constant over the detuning range. Prior to resolving conditional shifts, a full EDSR spectroscopy with the control qubit held in the $|\downarrow\rangle$ state is necessary to extract its resonance frequency over detuning and to enable accurate excitation into $|\uparrow\rangle$ at arbitrary detuning values. For this, EDSR spectroscopy over detuning is performed without altering the control qubit state. Therefore, the duration of the control qubit manipulation is $t_C = 0$ and the target qubit is

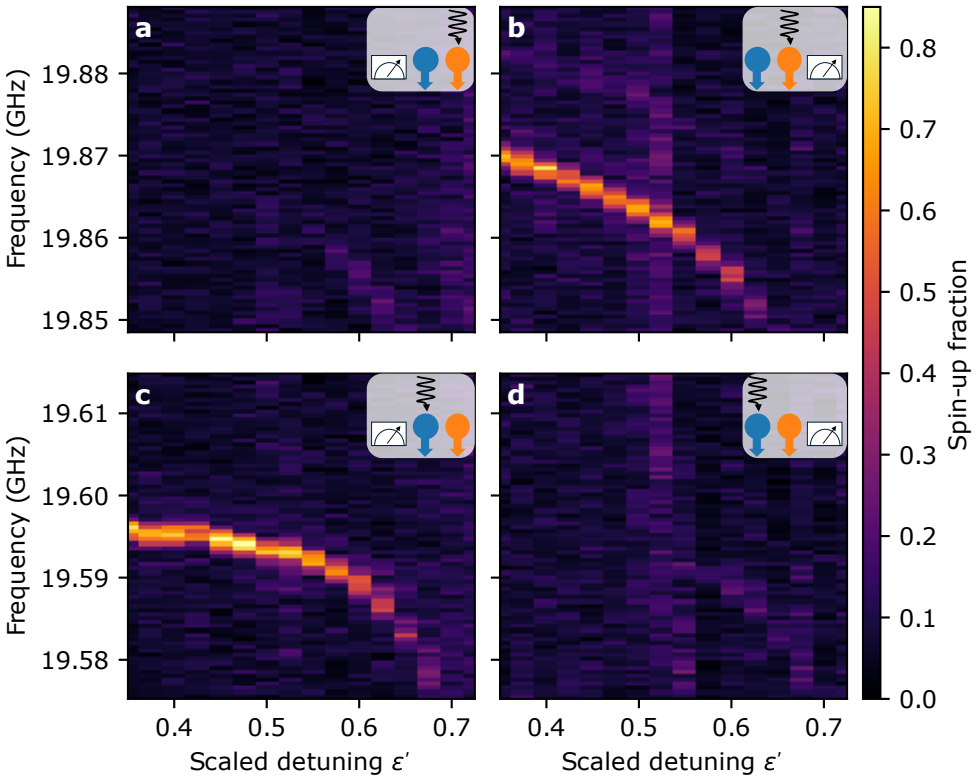

Figure 6.9: Conditional EDSR spectroscopy of the two-qubit system as a function of scaled detuning ε'. In all panels, the control qubit is initialized in the $|\downarrow\rangle$ state. Insets schematically indicate the initial spin states of the left (blue) and right (orange) qubit. The oscillating black arrow marks the driven qubit, and the position of the readout symbol identifies whether the data corresponds to the left or right qubit. Excitation pulses of π-pulse duration were used for the left ($t_{\pi,L} = 357$ ns) and right qubit ($t_{\pi,R} = 367$ ns). Panels **a** and **b** display the left and right qubit responses, respectively, to detuning spectroscopy of the right qubit. Panels **c** and **d** depict the complementary experiment, showing responses of the left (**c**) and right (**d**) qubit to detuning spectroscopy of the left qubit. Each pixel represents the averaged spin-up fraction obtained from 100 single-shot measurements.

driven for the duration of a π-pulse, which is known from zero detuning measurements (cf. Fig. 6.7).

The result of such a spectroscopy on both qubits is shown in Fig. 6.9. The figure is arranged such that both panels of the left and right column represent the readout of the left and right qubit, respectively. The rows are ordered by frequency, such that the top row only shows data around the (higher) Larmor frequency of the right qubit and the bottom row shows data around the (lower) Larmor frequency of the left qubit. The role of control and target qubit is determined by the frequency range of the shown data and consequently changes from row to row. Each pair of left and right panels within a given row stems from an identical microwave manipulation, but presents the response of both qubits to that same excitation. To facilitate interpretation, each panel includes a pictogram summarizing the experimental configuration. The blue and orange dots with arrows represent the left and right qubit and their initial spin state. The position of the readout symbol indicates

which qubit is read out to obtain the shown data and the black wavy arrow indicates the microwave manipulation and points at the target qubit.

The first two panels Fig. 6.9**a** and **b** show EDSR spectroscopy of the right qubit as the target qubit. As indicated in the insets, both qubits were initialized in $|\downarrow\downarrow\rangle$ prior to manipulation. Panel **a** shows the spin-up fraction of the left (control) qubit which remains mostly idle due to the far off-resonant frequency range. Instead, the spin-up fraction of the right (target) qubit in panel **b** reveals a pronounced resonance which is clearly detuning dependent. Additionally, a faint resonance can be observed at about 10 MHz higher frequency. This is consistent with the secondary resonance observed in Fig. 6.3 and can be attributed to a spin flip in the excited valley of the right qubit. The signal is faint, due to an only parasitic thermal population of the excited valley and the typically much weaker coupling to the microwave excitation [60]. The lower pair of panels in Fig. 6.9**c** and **d** show the outcome of EDSR spectroscopy close to the left qubit's Larmor frequency. This time, the left qubit shows a pronounced detuning dependent resonance frequency in panel **c**, while the right qubit (panel **d**) remains mostly unaffected.

The outcome that only panels **b** and **c** exhibit pronounced resonance features is not surprising, as it reaffirms that the left qubit is addressable in the lower frequency range and the right qubit in the higher one. More compelling, however, is the precise shape of the resonance frequency shift as a function of the scaled detuning parameter ε'. In both cases, the resonance frequency of the target qubit initially follows a linear decrease up to approximately $\varepsilon' = 0.5$, beyond which it transitions into a rather exponential dependence. This trend is consistent with the functional form described in Eq. (6.7) and is commonly interpreted as the combined effect of a linear Stark shift and an exponentially increasing exchange interaction with detuning [40]. Another interesting phenomenon is that the off-resonant qubits in panels **a** and **d** show a weak but gradually increasing signal following the, in turn, fading resonance of the target qubits for $\varepsilon' > 0.5$. This is the first indication for an exchange-coupling mediated decoherence mechanism that couples both qubits.

The observed resonance behavior as a function of detuning of each qubit can be accurately fitted using the function defined in Eq. (6.7). Once determined, the detuning-dependent resonance frequencies are integrated into the dynamic microwave control framework (cf. Sec. 6.3.1) to continuously adapt the modulation frequency and prepare the control qubit in the excited state $|\uparrow\rangle$ at any detuning value. Leveraging this capability, EDSR spectroscopy was repeated for both qubits with the control qubit prepared in the excited state, and the resulting resonance curves are shown in Fig. 6.10. The first row in Fig. 6.10 again shows a spectroscopy of the right qubit as the target qubit but this time the left control qubit is initialized in $|\uparrow\rangle$ prior to the target qubit manipulation. The successful initialization of the control qubit is validated by the consistently high spin-up fraction of the left qubit in panel **a**. Again, a pronounced resonance curve of the target qubit is obtained in panel **b**, but this time it bends upward for $\varepsilon' > 0.5$. A similar scenario is visible in the lower row, where the right control qubit exhibits a consistently high spin-up fraction in panel **d** and the resonance of the left target qubit shows an upward trend for high detuning values in panel **c**.

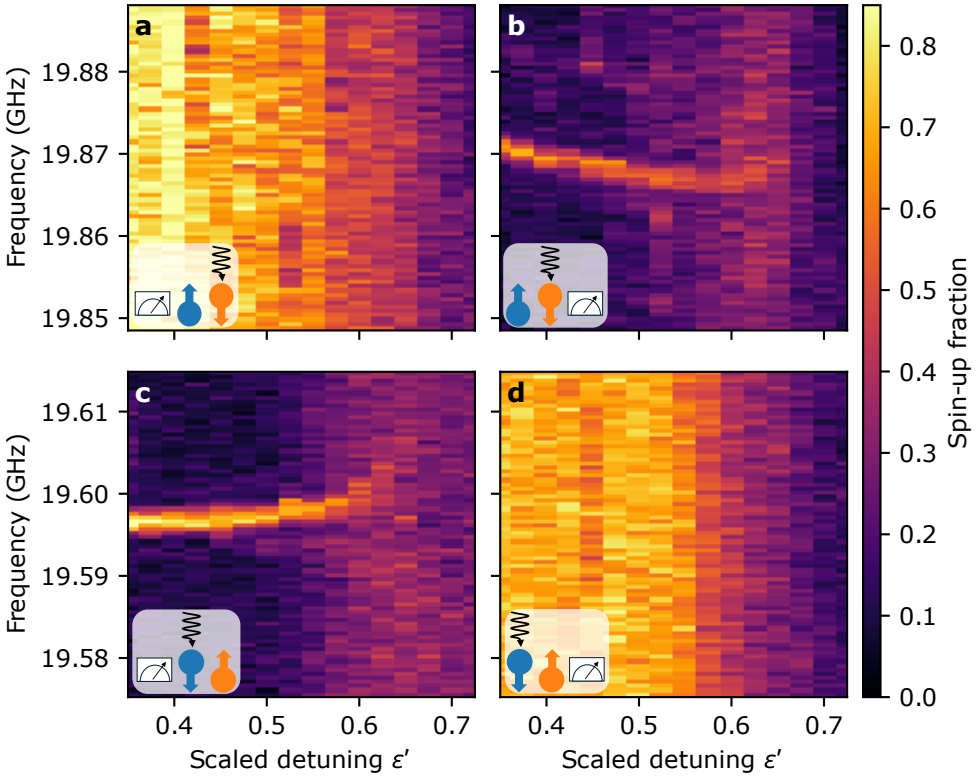

Figure 6.10: Conditional EDSR spectroscopy of the two-qubit system as a function of scaled detuning ε'. In all panels, the control qubit is initialized in the $|\uparrow\rangle$ state. Insets schematically indicate the initial spin states of the left (blue) and right (orange) qubit. The oscillating black arrow marks the driven qubit, and the position of the readout symbol identifies whether the data corresponds to the left or right qubit. Excitation pulses of π-pulse duration were used for the left ($t_{\pi,L} = 357\,\text{ns}$) and right qubit ($t_{\pi,R} = 367\,\text{ns}$). Panels **a** and **b** display the left and right qubit responses, respectively, to detuning spectroscopy of the right qubit. Panels **c** and **d** depict the complementary experiment, showing responses of the left (**c**) and right (**d**) qubit to detuning spectroscopy of the left qubit. Each pixel represents the averaged spin-up fraction obtained from 100 single-shot measurements.

The two-qubit dephasing appears more prominent in this second measurement as it causes a seemingly frequency independent rise of the background counts in panels **b** and **c** and a simultaneous decrease of the spin-up fraction in panels **a** and **d** for increasing detuning values. All seemingly frequency independent phenomena are an artifact of the frequency adaptive initialization of the control qubit and should be regarded as decoherence taking place during the control qubit preparation. The onset of decoherence shows in the fading of the resonance signal as well and is related to the same exchange-coupling mediated decoherence mechanism observed in Fig. 6.9. The origin will be elaborated in detail in Sec. 6.4 based on additional measurements over detuning. Most notably, the upward-bending resonance branches observed in panels **b** and **c** are direct, state-resolved evidence of a tunable exchange interaction. The shift in resonance frequency depending on the spin state of the control qubit precisely matches the predictions of the exchange Hamiltonian discussed in Sec. 6.1. This confirms not only the successful tuning of the device into the exchange regime, but also validates the functionality of all time-critical experimental

controls, being initialization, detuning sweeps, and microwave excitation, operating in unison.

Taken together, these spectroscopy results demonstrate full experimental access to the exchange-interaction in between the electrons of the double dot. With robust control established, the next section focuses on extracting and analyzing the exchange coupling strength from these measurements to quantify the detuning dependence of the interaction.

6.3.3 Exchange splitting

The preceding spectroscopy measurements detailed the transitions between the eigenstates $|\downarrow\downarrow\rangle$, $|\uparrow\downarrow\rangle$, $|\downarrow\uparrow\rangle$, and $|\uparrow\uparrow\rangle$ in the two-qubit system. To investigate the presence and properties of exchange coupling, a comprehensive spectral analysis as a function of the scaled detuning parameter ε' is shown in Fig. 6.11. Panels **a** and **b** depict the left qubit's conditional resonance branches, clearly demonstrating a dependency of its resonance frequency on the spin state of the right qubit. Correspondingly, panels **c** and **d** illustrate analogous conditional transitions for the right qubit, conditioned on the left qubit's spin state. This conditional frequency shift, the trademark of exchange interaction, becomes especially apparent when examining the summed spectra of each qubit's transitions in panels **e** and **f**. The observed frequency splitting conclusively demonstrates that the interaction is symmetric, validating the assumption of a mutual coupling rather than a unidirectional effect.

Each resonance branch exhibits Lorentzian-shaped peaks that are clearly resolved and allow precise extraction of the resonance frequencies. These four resonance branches are fitted simultaneously with the phenomenological model introduced in Eq. (6.7), using a common parameter set to ensure consistency across the fits. The resulting curves (black dashed lines in Fig. 6.11**e** and **f**) exhibit excellent agreement with the experimental data across the entire detuning range. Notably, the fit also captures the curvature of the resonance branches observed at high detuning values, suggesting the adequacy of the chosen exponential form for the description of the exchange coupling.

The fitted parameters are summarized in Tab. 6.2 and are discussed in detail below. The extracted qubit base frequencies ($f_{0,\mathrm{L}}$, $f_{0,\mathrm{R}}$) correspond to a detuning of $\varepsilon' = 0.35$ and reflect different Zeeman energies due to the combined effect of the external magnetic field and the micromagnet. These frequencies correspond to effective magnetic fields of 0.700 T and 0.709 T for the left and right qubit, respectively, highlighting the magnetic field gradient introduced by the micromagnet. Additionally, the Stark shift coefficients ($\lambda_{\mathrm{S,L}}$, $\lambda_{\mathrm{S,R}}$) quantify the sensitivity of each qubit's resonance frequency to detuning, reflecting the influence of gate voltage-induced electric fields on the qubit energy levels. Notably, the left qubit experiences a modest frequency shift of roughly −6.7 MHz across the entire measurement detuning range, while the right qubit exhibits a pronounced shift of approximately −36.7 MHz. The significant asymmetry in Stark shifts likely originates from the more sensitive positioning of the right qubit relative to the interdot barrier and/or the micromagnet. Such a proximity enhances susceptibility to both electric field fluctuations

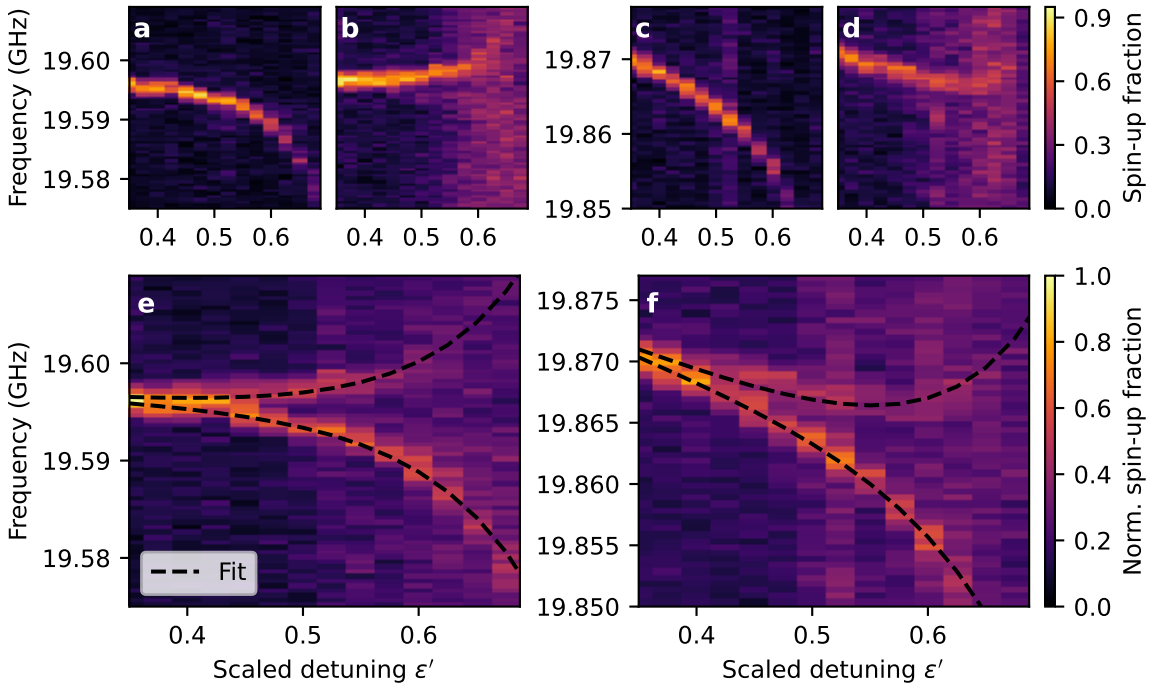

Figure 6.11: EDSR spectra of both qubits as a function of detuning. Excitation pulses of π-pulse duration were used for the left ($t_{\pi,L}$ = 357 ns) and right qubit ($t_{\pi,R}$ = 367 ns). **a** Response of the left qubit with the right qubit initialized in $|\downarrow\rangle$, showing the $f_1 : |\downarrow\downarrow\rangle \rightarrow |\downarrow\uparrow\rangle$ transition. **b** Same qubit probed after preparing the right qubit in $|\uparrow\rangle$, revealing the exchange-split transition $f_3 : |\downarrow\uparrow\rangle \rightarrow |\uparrow\uparrow\rangle$. **c, d** Right qubit response **c** without and **d** with prior preparation of the left qubit in $|\uparrow\rangle$, corresponding to the $f_2 : |\downarrow\downarrow\rangle \rightarrow |\downarrow\uparrow\rangle$ and $f_4 : |\uparrow\downarrow\rangle \rightarrow |\uparrow\uparrow\rangle$ transitions, respectively. The color bar next to panel **d** applies to panels **a-d** and indicates the measured spin-up fraction. **e** Sum of both left-qubit transitions from panels **a** and **b**, highlighting the increasing exchange-mediated frequency splitting with detuning. **f** Sum of right-qubit transitions from **c** and **d**. Data in panels **e** and **f** are normalized to one, as shown by the shared color bar.

Parameter	Fitted Value	Unit
$f_{0,\mathrm{L}}$	19.592 ± 0.000	GHz
$f_{0,\mathrm{R}}$	19.846 ± 0.000	GHz
$\lambda_{\mathrm{S,L}}$	−1.034 ± 0.138	MHz/meV
$\lambda_{\mathrm{S,R}}$	−5.672 ± 0.138	MHz/meV
J_0	1.083 ± 0.176	GHz
ε_0	0.576 ± 0.020	meV

Table 6.2: Fitted parameters for qubit resonance frequencies as a function of detuning using Eq. (6.7). All parameters are extracted from a simultaneous fit to all four resonance frequency branches in Fig. 6.11**a-d** as a function of detuning ε.

and spatial variations of the magnetic field gradient, leading to a stronger dependence of its resonance frequency with detuning. Such asymmetries are not rare in Si-based quantum dot arrays with integrated micromagnets and strong magnetic field gradients [61].
The exchange interaction is well described by the exponential model in Eq. (6.5), with a fitted coupling constant of J_0 = 1.08 GHz and a characteristic detuning scale ε_0 = 0.534 meV,

which is significantly smaller than the on-site Coulomb energy $U = 6.57\,\text{meV}$. This indicates that the exchange coupling increases by a factor of e for every 4.6 mV change in gate voltage, assuming an effective combined lever arm of $0.115\,\text{eV}\,\text{V}^{-1}$, and reaches J_0 at $\varepsilon = U$. Although the extracted exchange parameters in this work are presented in a universal and comparable form, direct quantifications of exchange coupling or full exchange spectra with calibrated lever arms are rarely reported explicitly in the literature. One exception is the work by Veldhorst et al. [40], which provides sufficient information to estimate a lower exchange coupling constant of $J_{0,\text{lit}} = 0.05\,\text{GHz}$ and a larger characteristic detuning scale $\varepsilon_{0,\text{lit}} = 1.2\,\text{meV}$. Compared to those values, the exchange profile observed in this study indicates operation in a significantly stronger tunnel coupling regime. This suggests that lowering the tunnel coupling between the dots might be feasible and beneficial in future experiments, particularly by improving the readout fidelity of the right qubit, which is highly sensitive to the interdot barrier voltage.

As a result of the fitted electric-dipole spin resonance (EDSR) spectra, the exchange energy $J(\varepsilon)$ can be extracted directly from the frequency difference between the resonance branches of each qubit. Fig. 6.12 illustrates the extracted exchange coupling J as a function of the detuning parameter ε. The measured frequency splittings $f_3 - f_1$ (left qubit) and $f_4 - f_2$ (right qubit) match closely, underscoring the robustness and mutual nature of the exchange coupling. These splittings are plotted as a function of both the absolute detuning ε and the scaled detuning ε', enabling direct conversion between the two representations. The solid black line corresponds to a fit using the exponential model introduced in Eq. (6.5) which captures the functional dependence of the exchange energy on detuning with excellent accuracy over the entire measured range. The resulting fit parameters match exactly with the values stated in Tab. 6.2. The logarithmic representation in panel **b** further highlights the exponential character of the extracted values, as evidenced by the linear trend. Importantly, the measured exchange coupling remains consistently smaller than the Zeeman energy gradient δE_z, thus confirming the weak interaction regime $J \ll |f_1 - f_2|$. This regime allows the implementation of conditional gates such as conditional rotations (CROT) or conditional phase (CPHASE) operations based on exchange-induced state-dependent resonance shifts [142].

In conclusion, the successful demonstration and accurate modeling of exchange splitting affirm the controllability and predictability of exchange interactions in our two-qubit device. The consistency between both qubit datasets and the fit underscores the robustness of the exponential description and supports its use for two-qubit gate calibration.

6.4 Qubit properties over detuning

A notable feature observed in the EDSR spectra in Fig. 6.11 is the fading visibility of the resonance branches with increasing detuning. Several mechanisms may contribute to this degradation. First, the efficiency of EDSR driving can vary with detuning, leading to changes in the Rabi frequency and potentially compromising the effectiveness of π-pulse calibration. Second, larger detuning values enhance the qubit's sensitivity to charge noise

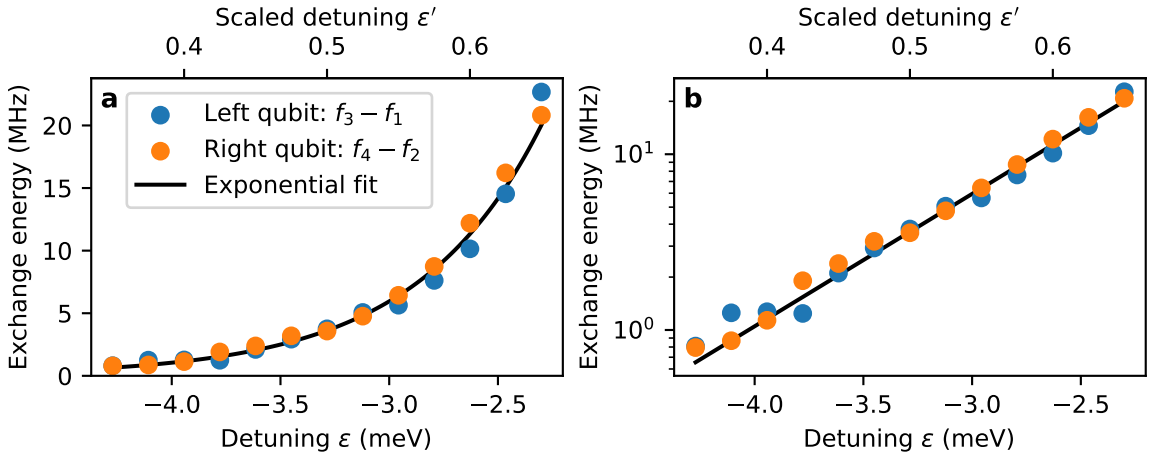

Figure 6.12: Extraction of the exchange interaction $J(\varepsilon)$ from the EDSR spectra. The plots show the resonance splitting for the left qubit $(f_3 - f_1)$ and the right qubit $(f_4 - f_2)$, as a function of detuning ε (bottom axis) and scaled detuning $\varepsilon' = \varepsilon/U$ (top axis). Panel **a** presents the data on a linear scale, while panel **b** shows the same data on a logarithmic scale to emphasize the exponential behavior. A global fit using the exponential model from Eq. (6.5) (solid black line) accurately captures the functional form of $J(\varepsilon)$ across the full detuning range.

through the exchange interaction $J(\varepsilon)$, thereby increasing decoherence. Additionally, other decoherence channels, such as energy relaxation processes characterized by the T_1 time, or magnetic field fluctuations arising from nuclear spins, may also contribute to the reduced spectral contrast.

These considerations naturally raise the question of how spin coherence and control fidelities evolve with detuning. In the following section, this topic is addressed through measurements of energy relaxation time T_1, Rabi oscillations, and Ramsey dephasing time T_2^* across a range of detuning values. These complementary time-domain experiments offer insight into the interplay between exchange interaction strength, spin coherence, and control robustness, and are crucial for identifying optimal operating points for high-fidelity quantum gate execution.

Rabi oscillations and control robustness

A straight-forward approach to assess qubit control robustness over detuning is by performing Rabi experiments. Fig. 6.13**a** shows coherent Rabi oscillations of the left qubit at scaled detuning $\varepsilon' = 0.5$, corresponding to an exchange coupling of $J = 3.6\,\text{MHz}$. At this working point, Rabi oscillations with a high visibility and a decay time $T_{2,\text{Rabi}} = 3375\,\text{ns}$ are observed, supporting reliable qubit control. The right qubit remains idle, confirming the expected outcome. In contrast, at $\varepsilon' = 0.625$ (Fig. 6.13**b**), where the exchange interaction increases to approximately $J = 15\,\text{MHz}$, the left qubit's Rabi oscillations become rapidly damped, with $T_{2,\text{Rabi}}$ dropping below the π-pulse duration of $t_{\pi,L} = 357\,\text{ns}$. Interestingly, the initial oscillation amplitude suggests that the drive strength remains unchanged, but decoherence prevents multiple rotations from being resolved. Simultaneously, the right (idle) qubit exhibits an exponential increase in spin-up probability on the same timescale

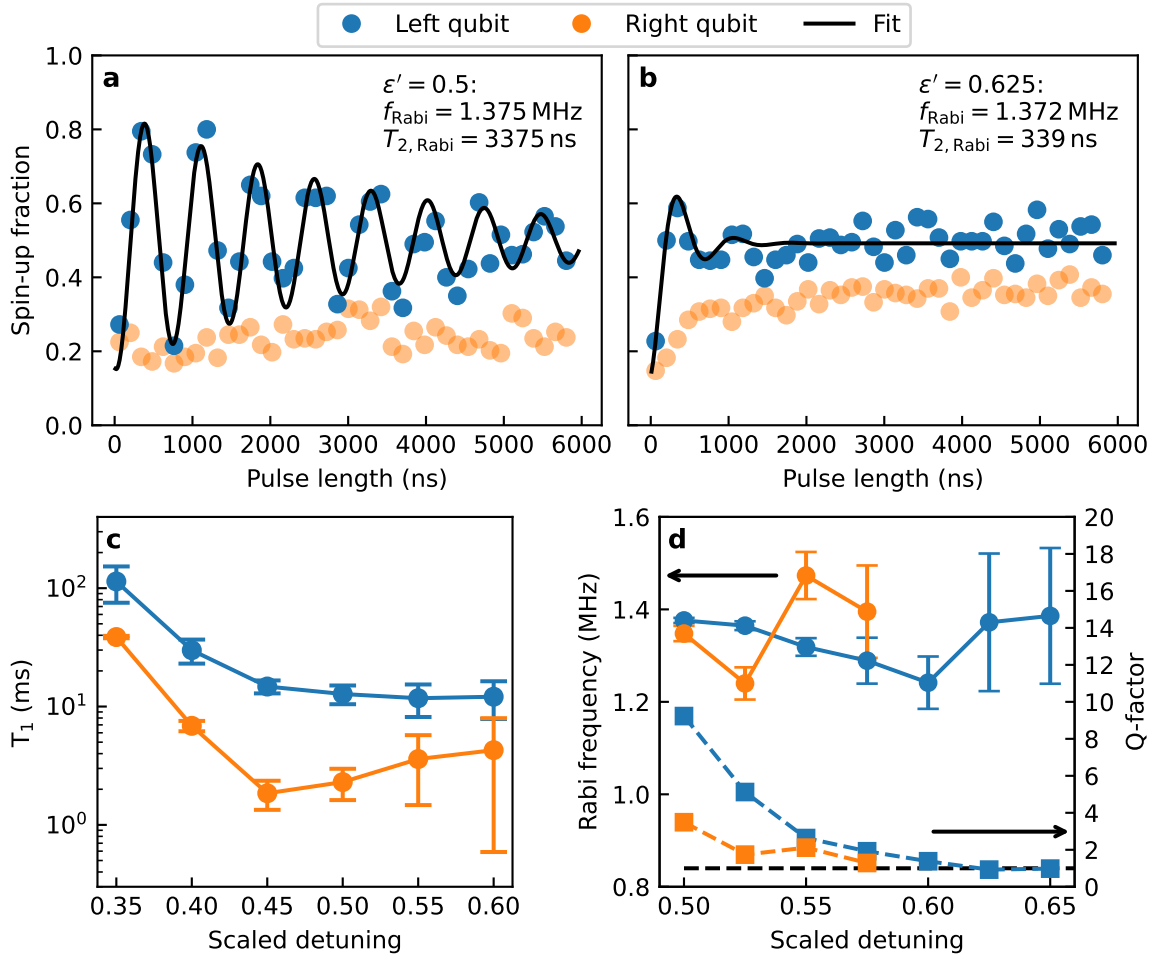

Figure 6.13: Coherence times in the two-qubit regime with exchange coupling as a function of scaled detuning. Solid and opaque point represent readings of the target and control qubit, respectively. **a** Rabi oscillations of the left qubit at $\varepsilon' = 0.5$, fitted with Eq. (5.12). The extracted $T_{2,\mathrm{Rabi}}$ indicates coherence suitable for two-qubit operations. Each point averages 400 single-shot readouts. **b** Same measurement at $\varepsilon' = 0.625$, where increased exchange coupling leads to strong decoherence and rapid damping of the Rabi oscillations. The observed $T_{2,\mathrm{Rabi}}$ time approaches the π-pulse duration. The idle (right) qubit shows exponential growth with a comparable timescale. Each displayed point averages four neighboring data points with 100 single-shot readouts each. **c** Results of pumped T_1 measurements of both qubits across detuning. Increased decoherence reduces spin-inversion fidelity, leading to larger fit uncertainties at higher detuning. Each data point represents the result of a fit to Eq. (5.11), based on 50 distinct wait times with 100 single-shot readouts acquired per wait time. **d** Extracted Rabi frequencies (circles) and Q-factors (squares) of both qubits versus detuning. While Rabi frequencies remain nearly constant, Q-factors drop rapidly toward unity (black dashed line), limiting coherent gate operations. Panels **a** and **b** correspond to individual points in this dataset.

as $T_{2,\mathrm{Rabi}}$, indicating population mixing between antiparallel spin states. This behavior likely originates from exchange-induced oscillations at the frequency of the exchange coupling. Decoherence of such oscillations between $|\uparrow\downarrow\rangle$ and $|\downarrow\uparrow\rangle$ is further amplified by charge noise coupling via $J(\varepsilon)$, which becomes increasingly sensitive at large detuning due to $\partial J/\partial\varepsilon \gg 0$ (see Fig. 6.11). The full detuning dependence of Rabi performance is

summarized in Fig. 6.13**d**, where Rabi frequencies (circles) and quality factors $Q = T_{2,\mathrm{Rabi}}/t_\pi$ (squares) are plotted. While Rabi frequencies remain nearly constant, the Q-factors rapidly decrease toward unity, indicating the limit where coherence time equals the pulse duration. This marks the threshold beyond which qubit control becomes impractical and helps explain the fading of EDSR branches at large detuning. Notably, upper EDSR branches require two coherent pulses to initialize and probe the system, resulting in a longer time to integrate noise, which explains their earlier disappearance in the spectrum.

Energy relaxation T_1

To examine whether energy relaxation contributes to the fading resonance signal, pumped T_1 measurements were performed across detuning and are shown in Fig. 6.13**c**. The increasingly large uncertainties for the highest detuning values are a consequence of impaired spin-up initialization fidelity due to the strong $T_{2,\mathrm{Rabi}}$ decoherence. While both qubits show a reduction in T_1 with increasing detuning by nearly an order of magnitude, the values saturate at approximately 12 ms (left) and 2 ms (right). These timescales are significantly longer than gate operations and therefore do not limit control fidelity. A side effect of shorter T_1 is reduced readout fidelity, since the readout window (20 ms) is comparable to the decay times. However, the reservoir tunneling rate of a few kHz allows for the most spin-up events to be detected in below 5 ms and Fig. 6.13**a** and **b** confirm that fully dephased spin-up fractions remain close to 50%, indicating that readout fidelity is still adequate in the investigated detuning range. Hence, energy relaxation can be excluded as the primary cause for fading coherence at large detuning.

Ramsey dephasing and nuclear spin noise

Ramsey experiments were conducted at various detuning values, to probe the contribution of quasi-static noise originating from nuclear spins in the natural Si substrate. The resulting free-induction decay times T_2^* are shown in Fig. 6.14. All measurements have been performed with a frequency detuning of 2 MHz and the data points for each qubit have been slightly offset from the probed detuning value for clarity. The displayed data points with error bars represent the fitted T_2^* with statistical uncertainties. The average value across all points is $T_2^* = 810$ ns, which is typical for natural Si [21] and consistent with dephasing dominated by the Overhauser field. To obtain a robust estimate of the mean value of T_2^* per detuning and its uncertainty, a weighted averaging method has been applied. The weights are chosen to be the inverse of the variance of each measurement, so that measurements with smaller uncertainty contribute more to the average. The standard error of the mean (SEM) represents the uncertainty in the weighted average and is typically smaller than the individual measurement uncertainties if many measurements are combined. This method is advantageous because it gives greater weight to measurements with lower uncertainty, resulting in a more reliable estimate of T_2^* at each detuning. The mean value and the corresponding SEM are displayed as confidence bands in opaque colors in the graph to provide a guide for the eye and a quantitative measure of the confidence in

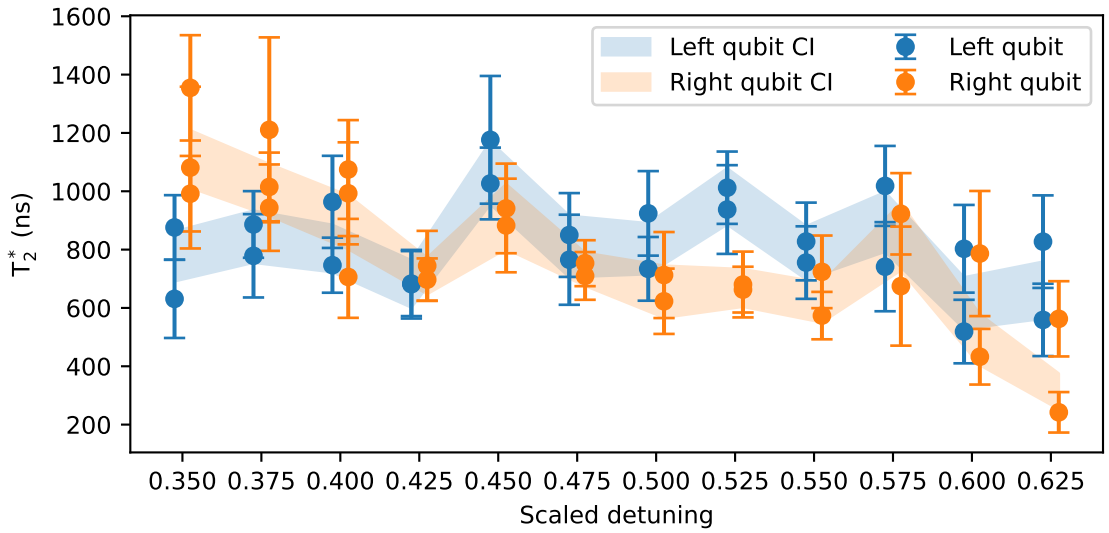

Figure 6.14: Ramsey decay times T_2^* as a function of scaled detuning ε' for both qubits. Each data point represents a fitted T_2^* value from an individual Ramsey measurement using Eq. (5.13). The data was recorded at a frequency detuning of 2 MHz. Error bars indicate fit uncertainties. Shaded confidence intervals (CI) represent the standard error of the mean, computed via weighted averaging using the inverse variance of each measurement. The extracted values show no strong dependence on detuning across most of the range, consistent with dephasing dominated by quasi-static nuclear spin noise in natural Si. A slight decrease at high detuning suggests the onset of additional dephasing mechanisms, likely due to increased charge noise sensitivity from the exchange interaction $J(\varepsilon)$.

the averaged value. No clear trend in T_2^* is observed across the detuning range, supporting the conclusion that nuclear spin noise is largely independent of detuning. A possible downward trend at the highest detuning values may signal the onset of charge-noise-induced dephasing. In comparison, Petit et al. [79] observed a strong detuning dependence of T_2^* in an isotopically purified ^{28}Si device, attributed to charge noise coupling via $J(\varepsilon)$. In the present device, the persistence of T_2^* confirms that hyperfine-induced decoherence remains dominant across most of the detuning range, further excluding it as the source of the fading EDSR visibility.

Conclusion

By systematically analyzing the decoherence channels, the dominant limitation to high-exchange operation is identified as charge noise coupling through the detuning-sensitive exchange interaction. Fluctuations in ε lead to fluctuations in $J(\varepsilon)$, which causes dephasing of the antiparallel spin states and suppresses coherent control [129, 135, 136, 143]. This mechanism explains both the loss of Rabi visibility and the fading of EDSR spectra in Fig. 6.11 at $J \gtrsim 20$ MHz. For the demonstration of two-qubit gates, an optimal working point at $\varepsilon' = 0.5$ was chosen. At this detuning, an exchange coupling of approximately $J = 3.6$ MHz is achieved, which allows spectrally resolved conditional operations, while maintaining sufficient coherence for gate execution.

7 Two–Qubit Gates

Two-qubit gates represent a pivotal step toward universal quantum computation, as they enable the creation of entangled states that form the foundation of non-classical information processing. Importantly, the combination of single-qubit rotations with any entangling two-qubit operation is sufficient to realize universal quantum logic [130]. As established in earlier sections, the system operates in the weak-coupling regime $J \ll \Delta E_Z$, where the exchange interaction is smaller than the Zeeman energy difference. Under these conditions, the class of natively accessible two-qubit operations includes conditional rotations (CROT) and conditional phase (CPHASE) gates [142]. However, in the current control setup, ns-scale detuning pulses required for CPHASE gates are not supported due to low-pass filtering on the plunger gate lines (cf. Sec. 3.3). Therefore, CROT gates were the primary choice for implementing conditional two-qubit operations. With robust control sequences, reliable spin readout, and a tunable exchange interaction experimentally verified, all essential prerequisites for executing two-qubit gate operations are in place. Building on this groundwork, the focus now shifts toward putting these mechanisms into practice by demonstrating conditional two-qubit operations.

7.1 Operation at constant detuning

Following the systematic detuning-dependent coherence characterization presented in Sec. 6.4, a working point at $\varepsilon' = 0.5$ was identified as the most favorable compromise between interaction strength and coherence. Frequency spectroscopies starting from the ground state ($|\downarrow\downarrow\rangle$) or with prior initialization of the control qubit in the excited state ($|\uparrow\downarrow\rangle$ or $|\downarrow\uparrow\rangle$) are shown in Fig. 7.1. The dataset reveals four conditional resonance frequencies corresponding to the transitions: $f_1 : |\downarrow\downarrow\rangle - |\uparrow\downarrow\rangle$, $f_2 : |\downarrow\downarrow\rangle - |\downarrow\uparrow\rangle$, $f_3 : |\downarrow\uparrow\rangle - |\uparrow\uparrow\rangle$ and $f_4 : |\uparrow\downarrow\rangle - |\uparrow\uparrow\rangle$ (cf. Fig. 6.1). This conditional resonance behavior is clearly illustrated in Fig. 7.1, where overlapping measurement windows display only one visible transition at a time, depending on the control qubit configuration. The resonance frequencies yield an exchange energy of $J(\varepsilon' = 0.5) = (3.58 \pm 0.31)$ MHz, calculated as the mean frequency difference between the conditional transitions of each qubit. The Zeeman energy difference is extracted as $\Delta B_z = f_4 - f_3 - J = 267.1$ MHz. By inserting these values into the analytic form of the exchange energy (cf. Eq. (6.4)), the tunnel coupling between the two electrons is determined to be $t_0 = 1.46$ GHz. This value is a factor of 1.5 higher than reported values at similar operating points, such as 0.9 GHz in Ref. [40] and 0.8 GHz in Ref. [79]. In retrospect, this suggests that the interdot barrier voltage could have been lowered further

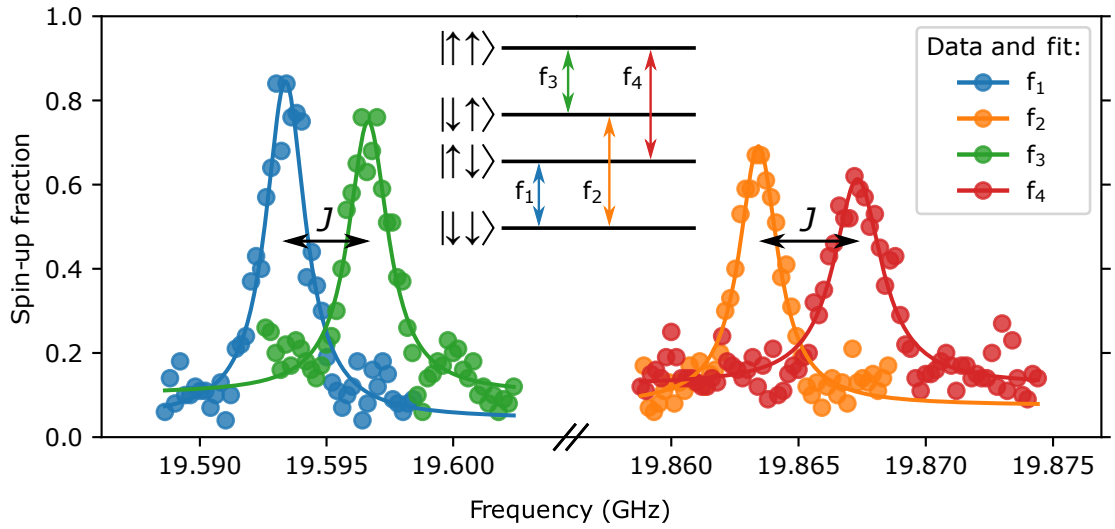

Figure 7.1: All four resonance frequencies of the two-qubit system measured at scaled detuning $\varepsilon' = 0.5$. The left qubit shows resonances at f_1 and f_3, corresponding to the control (right) qubit being in $|\downarrow\rangle$ and $|\uparrow\rangle$, respectively. Similarly, the right qubit resonances f_2 and f_4 appear when the left (control) qubit is in $|\downarrow\rangle$ and $|\uparrow\rangle$, respectively. The overlapping measurement regions highlight the mutual exclusivity of each frequency pair, as only one resonance appears depending on the spin state of the control qubit. The inset illustrates the observed transitions in the energy diagram for a constant detuning value. Each point represents an average of 100 single-shot readouts.

to improve the readout and initialization fidelity of the right qubit, which was sensitive to the barrier tuning.

All four resonance lines are well separated and display high visibility under π-pulse excitation, with spin-up fractions reaching up to 80% for the left qubit and 70% for the right qubit. These results confirm high readout contrast and establish a robust foundation for implementing the CROT gate.

7.2 Conditional rotations (CROT) with a static condition

Building on the identification of all four conditional resonance frequencies, the next essential step is to confirm the coherent controllability of each transition. This is accomplished by demonstrating Rabi oscillations on all four conditional transitions, each of which represents a possible CROT gate. The CROT gate, as a core entangling operation, applies a spin rotation on a target qubit conditioned on the spin state of a control qubit. Its implementation enables quantum logic such as the controlled-NOT (CNOT) gate when combined with suitable single-qubit rotations [62].

Figure 7.2 presents Rabi oscillations at the previously identified frequencies f_1 through f_4, validating conditional control over both qubits. Panels **a** and **b** show the left and right qubits being driven at f_1 and f_2, respectively, starting from the joint ground state $|\downarrow\downarrow\rangle$. Panels **c** and **d** depict oscillations at f_3 and f_4, after initializing the control qubit in the

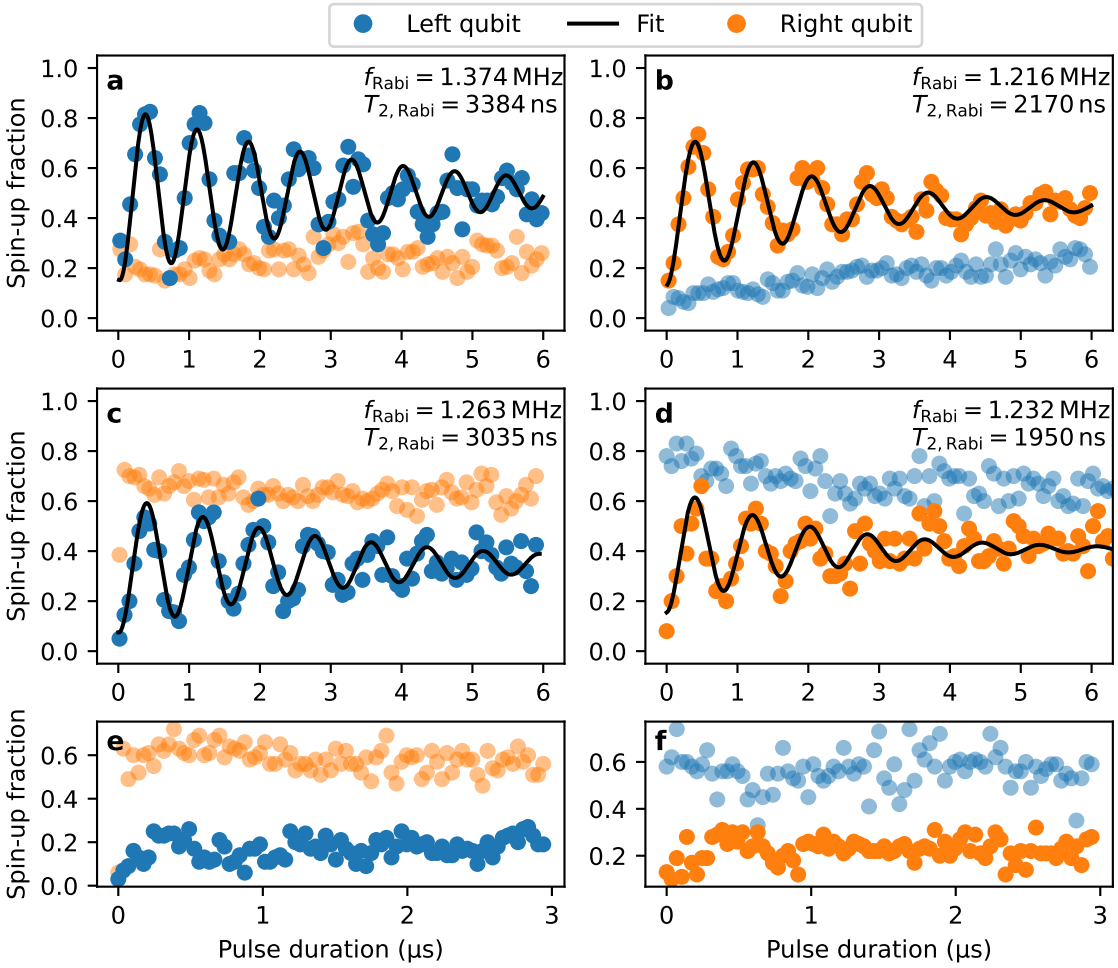

Figure 7.2: Conditional rotations in a two-qubit system demonstrated by Rabi oscillations for all four initial two-qubit states. **a** Left qubit driven at f_1 with initial state $|\downarrow\downarrow\rangle$. **b** Right qubit driven at f_2 with initial state $|\downarrow\downarrow\rangle$. **c** Left qubit driven at f_3 with initial state $|\downarrow\uparrow\rangle$. **d** Right qubit driven at f_4 with initial state $|\uparrow\downarrow\rangle$. **e** Control measurement showing suppressed rotation when driving the left qubit at f_1 with initial state $|\downarrow\uparrow\rangle$. **f** Control measurement showing suppressed rotation when driving the right qubit at f_2 with initial state $|\uparrow\downarrow\rangle$. To avoid clutter, each displayed point in panels a,b,c (d,e,f) is the mean of two (one) measurements of neighboring pulse lengths with 100 readouts each.

spin-up state. Each trace confirms coherent qubit rotation that depends strictly on the spin state of the control qubit. The selectivity of the operation is demonstrated by the idle qubit (in faint color) remaining mostly unaffected. The weak drift observed in the spin-up fraction of the idle qubit across all measurements in Fig. 7.2 is consistent with the effect of detuning noise on the exchange interaction, as discussed in Sec. 6.4. Charge-induced fluctuations in ε lead to variations in $J(\varepsilon)$, causing residual mixing between the antiparallel spin states and thereby a gradual population change in the idle qubit.

The extracted Rabi frequencies and coherence times ($T_{2,\mathrm{Rabi}}$) reveal good gate performance with coherent control over multiple oscillations. Panels **e** and **f** serve as control experiments, confirming the absence of Rabi oscillations when the qubit is driven at the incorrect

conditional frequency, i.e. when the control qubit is in the wrong spin state. Together, these results mark a successful realization of conditional two-qubit operations and establish a strong foundation for implementing entangling gates. Apart from quantum computation, these results also build the foundation of quantum non-demolishing (QND) readout in semiconductor-based devices. For instance, an arbitrary spin state of the left qubit can be indirectly measured by applying a conditional π-pulse at f_2. Repeated readout of the right qubit then reveals the state of the left qubit without direct disturbance. This process can be continued until the left qubit's spin state relaxes due to a T_1 process. Such a QND readout protocol has been realized in Refs. [30, 61, 144].

In summary, CROT gates are essential components for spin-based quantum computation, enabling conditional logic between neighboring qubits. The demonstration of coherent, state-selective control at all conditional frequencies provides critical validation of two-qubit gate functionality.

7.3 Conditional rotations (CROT) with a dynamic condition

In static protocols, the control qubit is typically initialized in a fixed spin state prior to applying a microwave pulse to the target qubit. However, the full potential of CROT gates can be revealed by exploring scenarios where the control qubit's state dynamically evolves during the gate operation. This is particularly relevant for understanding real-time interactions in quantum circuits, where gate operations and qubit states are not strictly sequential but can overlap or interfere.

7.3.1 CROT with time-dependent condition

One way to realize such a dynamic condition is by gradually increasing the duration of the initialization pulse applied to the control qubit at frequency f_2 in the first step of the microwave manipulation sequence (cf. Sec. 6.3.1). This results in Rabi oscillations of the control qubit as it is evolved through superpositions of $|\downarrow\rangle$ and $|\uparrow\rangle$. Subsequently, the target qubit is addressed at frequency f_1 in the second step of the microwave pulse using a variable duration t_T, allowing its Rabi oscillations to be probed as a function of the dynamically evolving spin state of the control qubit. This measurement, here referred to as a "Double-Rabi experiment", provides a time-resolved view of conditional spin control, revealing the action of a CROT gate under continuously changing input conditions.

A baseline for this experiment is established by performing it at zero detuning, $\varepsilon' = 0$, where the exchange interaction is negligible and conditional dynamics should be absent. The results, shown in Fig. 7.3, should be interpreted row-wise, with each pair of panels **a** and **b** showing the readings of the left and right qubit, respectively, after an identical two-step microwave pulse sequence. In this case, the right qubit is driven first as the control qubit, and the left qubit is addressed second as the target. Each panel displays the measured spin-up fraction as a function of microwave pulse duration on the right

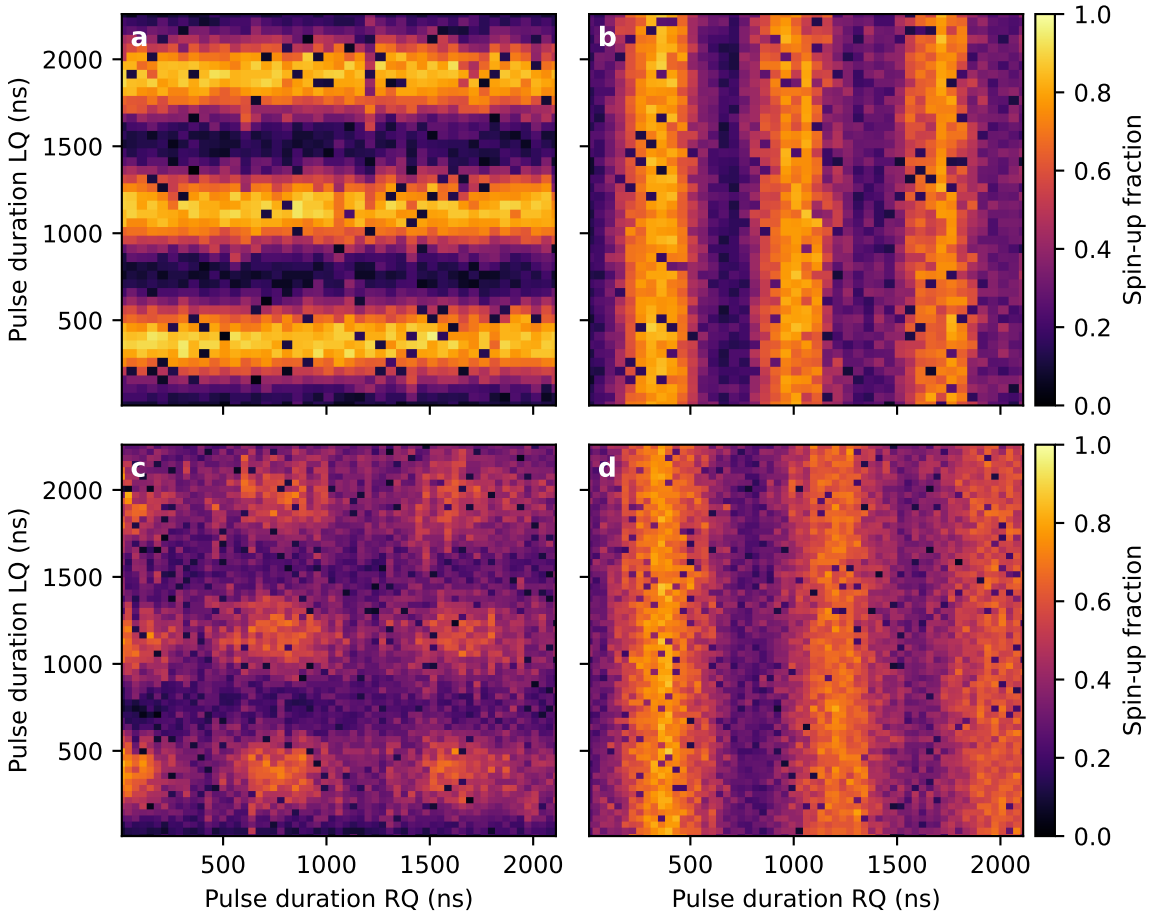

Figure 7.3: Double-Rabi experiment performed on both qubits under two different detuning conditions. In all panels, the x-axis indicates the pulse duration applied to the right qubit (RQ) at frequency $f_2(\varepsilon)$, and the y-axis shows the pulse duration applied to the left qubit (LQ) at frequency $f_1(\varepsilon)$. The right qubit is driven first (control), followed by the left qubit (target), using a sequential microwave pulse sequence. Each pixel represents the spin-up fraction averaged over 100 single-shot readouts. **a,b** At zero detuning ($\varepsilon' = 0$), where the exchange interaction is negligible, both qubits undergo independent, unconditional Rabi oscillations. This is reflected in the horizontal and vertical stripe patterns seen in the left qubit (**a**) and right qubit (**b**), respectively. **c,d** At finite detuning ($\varepsilon' = 0.5$), corresponding to an exchange interaction of $J = 3.6\,\mathrm{MHz}$, conditional dynamics emerge. The right qubit (**d**) displays vertical Rabi oscillation stripes, defining the dynamic control condition. In contrast, the left qubit (**c**) exhibits modulated Rabi oscillations in the y-direction. The amplitude of the oscillations depends on the instantaneous spin state of the right qubit and demonstrates the conditional behavior characteristic of a CROT gate.

qubit (x-axis) and the left qubit (y-axis). In this uncoupled regime, both qubits exhibit independent Rabi oscillations. As a result, vertical and horizontal stripe patterns emerge, corresponding to coherent oscillations of each qubit that are unaffected by the drive applied to the other. This independence confirms the absence of conditional behavior and serves as a reference for identifying true two-qubit interactions in the coupled case.

At finite exchange coupling, the outcome changes significantly. Fig. 7.3**c** and **d** show the same Double-Rabi experiment repeated at a scaled detuning of $\varepsilon' = 0.5$, where the exchange interaction is $J = 3.6\,\mathrm{MHz}$. The right qubit is again addressed first at frequency f_2 and

serves as the control, followed by the left qubit targeted at frequency f_1. Exactly as before, panel **d** shows a vertical stripe pattern that represents the Rabi oscillations of the right control qubit and governs the "condition" for the CROT operation. In contrast, the spin-up fraction of the left qubit in panel **c** shows an interrupted horizontal stripe pattern this time. This new appearance can be interpreted as modulated Rabi oscillations in y-direction whose amplitude clearly depends on the state of the control qubit in x-direction. When the control qubit is near $|\downarrow\rangle$ (low spin-up fraction), the left qubit exhibits pronounced Rabi oscillations, consistent with the conditional rotations at frequency f_1 shown in Fig. 7.2**a**. When the control qubit is near $|\uparrow\rangle$ (high spin-up fraction), however, the Rabi oscillations of the left qubit are strongly suppressed, indicating that the resonance condition has changed to f_3 due to the exchange interaction.

The randomly distributed dark pixels across all panels are row-wise correlated and mark measurements at which the upload of the microwave manipulation failed for yet unknown software reasons. The difference in visibility and the Rabi frequency of the right qubit can be attributed to the increased susceptibility to charge noise at elevated detuning energy and subtle working point differences in between both measurements. The fundamentally different outcome of the zero-detuning and finite-detuning measurements underscores the central role of exchange coupling in enabling state-dependent control. In the exchange-coupling regime, the target qubit manipulation is gated by the spin state of the control qubit, demonstrating the essence of the CROT operation. Together, these results provide a direct visualization of conditional spin control in real time.

7.3.2 Frequency-resolved CROT with time-dependent condition

Another demonstration of dynamically conditioned controlled rotations in the two-qubit system is achieved by coherently driving the control qubit for varying durations t_C, while probing the resonance frequency of the target qubit using a calibrated π-pulse. For this experiment, the system is operated at a scaled detuning of $\varepsilon' = 0.5$, where the exchange interaction is $J = 3.6\,\mathrm{MHz}$. The left qubit is driven as the control at its resonance frequency f_1, and the right qubit is probed across a frequency window centered at the average of its two conditional resonances, $(f_2 + f_4)/2$. This dynamic measurement scheme enables a time-resolved spectroscopy of the target qubit's resonance, conditioned on the evolving quantum state of the control qubit.

The resulting time-resolved EDSR spectroscopy of the right (target) qubit as a function of the pulse length applied to the left (control) qubit is displayed in Fig. 7.4. The frequency axis is plotted relative to the right qubit's resonance at $f_2 = 19.863\,\mathrm{GHz}$. Panel **a** shows the spin-up fraction of the left control qubit as a function of its own drive time and the swept frequency used to probe the target. The signal remains uniform along the frequency axis, since it is always driven at its exact resonance frequency f_1 using a dynamically updated feedback (cf. Sec. 6.3.1). Pronounced Rabi oscillations along the pulse duration axis demonstrate the dynamic evolution of the control qubit's state.
The spin-up fraction of the right target qubit is displayed in panel **b**. As the control qubit is driven through coherent Rabi oscillations, the resonance condition of the target qubit

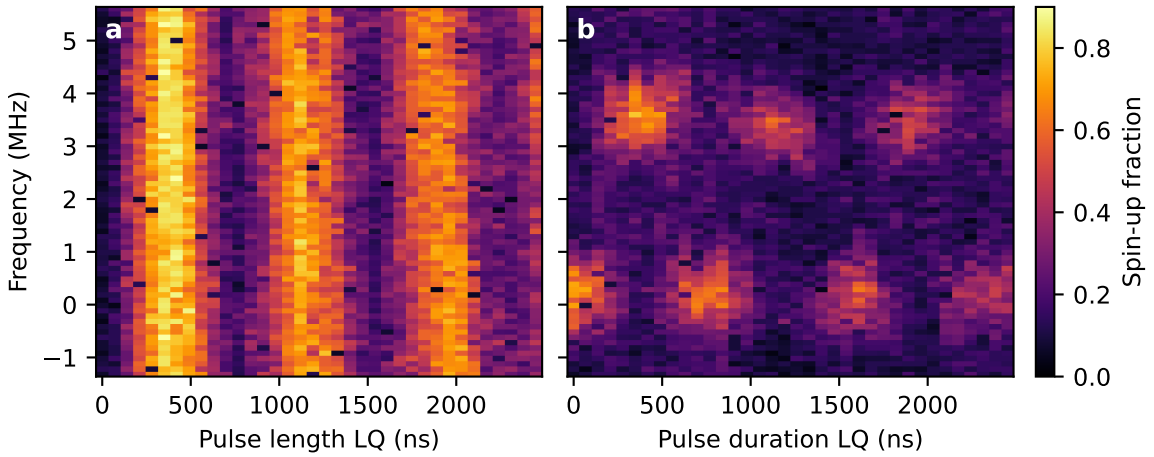

Figure 7.4: Exchange spectroscopy of the right (target) qubit as a function of frequency and (left) qubit pulse length at $\varepsilon' = 0.5$. The measurement was performed at 18 dBm external microwave power and AWG modulation amplitudes of 0.4 V for the left qubit and 0.6 V for the right qubit. The frequency axis is offset by the right qubit's resonance of $f_2 = 19.863$ GHz. **a** Control (left) qubit readout showing Rabi oscillations as a function of pulse length. The signal remains frequency-independent due to dynamic feedback that drives the control qubit at its resonance frequency f_1 during each iteration. **b** Target (right) qubit readout after applying a π-pulse ($t_\mathrm{T} = 676$ ns) to the right qubit. The alternating bright spots reflect a conditional shift in the right qubit's resonance frequency, depending on the control qubit's spin state. The observed frequency splitting of $J = 3.6$ MHz is consistent with the exchange interaction strength at $\varepsilon' = 0.5$. Each pixel represents an average of 100 single-shot readouts.

oscillates between two values, separated by $J = 3.6$ MHz, which is consistent with the exchange coupling strength the given detuning. This leads to the conclusion that the alternating bright spots resemble the switching of the resonance frequency between f_2 and f_4 conditional to the current state of the control qubit.

A particularly striking feature of this result is the direct visualization of the quantized nature of spin. When the control qubit is driven for a $\pi/2$ time, corresponding to a superposition state on the equator of the Bloch sphere, the target qubit shows an equal response at both conditional resonance frequencies f_2 and f_4. Rather than forming a single, shifted peak, the response is split, revealing the probabilistic projection of a quantum superposition into spin-up or spin-down eigenstates. This underscores the discrete nature of spin quanta and demonstrates a real-time, frequency-domain visualization of quantum state evolution.

Furthermore, this experiment presents a method for quantum nondemolition (QND) readout [145]. Specifically, the quantum state of the left (information) qubit is mapped onto the spectral response of the right (ancilla) qubit. By measuring the spin-up fraction of the ancilla qubit at either f_2 or f_4, and comparing the result to the maximum expected signal contrast, one can directly infer the exact composition of the other qubit's superposition state. This approach allows to reconstruct the spin state of the information qubit without disturbing it through direct measurement.

In conclusion, this dynamic exchange spectroscopy experiment offers a compelling real-time view of conditional qubit control, revealing both the quantized nature of spin and

the spin-state-dependent resonance splitting induced by exchange interaction. Beyond demonstrating the essential mechanism of the CROT gate, it highlights a powerful indirect readout technique that enables quantum nondemolition measurement of one qubit via the spectroscopic response of another. Together, these results provide deep insight into the coherent dynamics of coupled spin qubits and establish a robust platform for quantum computing in multi-qubit architectures.

8 Conclusion

The realization of a universal quantum computer requires the operation of many thousands to millions of coherently coupled qubits. The prospect of using existing industrial semiconductor fabrication techniques and infrastructure for up-scaling and reproducibility makes silicon-based spin qubits one of the most promising platforms to achieve this goal. However, the operational requirements for silicon spin qubits significantly exceed those of conventional complementary metal-oxide-semiconductor (CMOS) logic, particularly by imposing new challenges in form of qubit coherence, coherent control, and quantum connectivity. The central objective of this work was to demonstrate that Si-based spin qubit devices fabricated in an industrial environment can meet these challenges and enable multi-qubit operation with tunable inter-qubit coupling.

This thesis focuses on Si/SiGe two-qubit devices provided by the Interuniversity Microelectronics Centre (imec) in Leuven, Belgium [35]. These devices represent the first spin qubit systems fully realized in a 300 mm industrial semiconductor process, including all fabrication steps from heterostructure growth to the monolithic integration of cobalt micromagnets (CoMM) for spin control. This differentiates the investigated samples from other reported industrially fabricated spin qubit devices, that use post-CMOS processing to integrate CoMMs [26, 29, 36]. Addressing the central objective of this work required overcoming two fundamental challenges: to achieve high-fidelity, universal control of individual qubits and to realize a tunable interaction regime that enables coherent two-qubit logic. Together, these milestones lie at the forefront of current research efforts toward scalable quantum computation, which demands both the industrial reproducibility of high-performance qubits and their controllable quantum interconnection to harness quantum parallelism for solving classically intractable problems [11].

At the outset of any experimental research in quantum information science lies the essential yet often underrated task of establishing a platform capable of probing the fragile and elusive nature of quantum systems. In this work, a custom-built dilution refrigerator, operating at mK temperatures within a carefully engineered low-noise environment, served as the primary platform for high-fidelity quantum measurements. To further advance experimental capability and increase sample throughput, a second cryogenic system was developed in parallel, expanding the infrastructure for quantum device testing in our research group. Both platforms underwent extensive noise characterization and suppression, ensuring the stability and sensitivity required to resolve quantum mechanical dynamics with high temporal precision.

The identification of a suitable working point forms a first foundational step toward achieving single-qubit control in spin-based quantum devices. This process involves the

definition of two singly occupied quantum dots and spin-selective readout via a proximal charge sensor. A systematic tuning protocol was devised to coordinate voltages across 15 metal gates, enabling dot formation in the silicon quantum well and spin-resolved detection using the Elzerman protocol. Rapid adiabatic passage (RAP) plays a critical role in bridging the gap between electrostatic quantum dot characterization and coherent qubit control, as it provides an efficient and noise-resilient method for identifying qubit resonance frequencies with high visibility in spin qubit systems. A complementary, dedicated study was carried out on the ^{28}SiMOS D06 Die07 device to explore the applications and limitations of RAP in detail. This study emphasized that RAP enables spin inversion fidelities exceeding 90% even in the presence of resonance frequency fluctuations. Its near-ideal performance is only limited by state preparation and readout errors, which were conclusively identified and optimized using the reliable feedback provided by RAP.

Building on these foundational steps, controlled single-qubit manipulation of both qubits in the $^{\text{nat}}$Si/SiGe D09 Die02 device was demonstrated through coherent Rabi oscillations in the MHz range, accomplishing the first objective of this thesis. A dominant source of decoherence in silicon-based spin qubit systems is low-frequency magnetic noise originating from nuclear spin fluctuations of naturally abundant ^{29}Si isotopes. This is reflected in the characteristic difference between Ramsey and Hahn-echo coherence times, where the Ramsey sequence is sensitive to low-frequency dephasing, while the Hahn-echo protocol mitigates such effects using a refocusing π-pulse. Specifically, the left and right qubit showed Ramsey coherence times of $T_{2,\text{L}}^{*} = (1.13 \pm 0.11)\,\mu\text{s}$ and $T_{2,\text{R}}^{*} = (1.04 \pm 0.10)\,\mu\text{s}$, and Hahn-echo times of $T_{2,\text{L}}^{\text{HE}} = (79.00 \pm 1.54)\,\mu\text{s}$ and $T_{2,\text{R}}^{\text{HE}} = (31.85 \pm 2.03)\,\mu\text{s}$, respectively. Reduced coherence of the right qubit was attributed to its closer proximity to the asymmetrically placed, current-carrying charge sensor. This highlights the sensor as a local decoherence source and points to a layout optimization strategy. Positioning the sensor farther from the qubit is expected to enhance coherence, offering a favorable trade-off against slightly reduced readout sensitivity. Nevertheless, the obtained coherence times are competitive with typical academic results for natural silicon [21] and confirm a well-isolated spin environment suitable for high-fidelity quantum operations. Compared to performance benchmarks of other industrially fabricated devices ($T_2^{*} \sim 1.3\,\mu\text{s}$, $T_2^{\text{HE}} > 100\,\mu\text{s}$) [26, 29], the observed performance is slightly below optimal values. This deviation is attributed to residual 1/f charge noise in the qubit platform, typically originating from defects in oxide layers [129], and suggests that further improvements may be achievable through optimizations in fabrication. Furthermore, a complementary study demonstrated that the Rabi frequency of the left qubit in the nominally identical $^{\text{nat}}$Si/SiGe D09 Die05 device could be increased to 12 MHz by tuning confinement gate voltages that modulate the dot's position relative to the electron dipole spin resonance (EDSR) drive line. This highlights the strong sensitivity of microwave drive efficiency to dot localization and identifies gate-defined positioning as a key lever for optimizing coherent control. The achieved drive strength exceeds values reported in other industrial Si/SiGe devices [26, 29] and is competitive with leading academic implementations [21]. Together, these results establish a solid performance baseline for single-qubit operation in industrially fabricated devices and point to EDSR drive optimization as a promising strategy for further improving control fidelity.

The transition from independent to coupled qubit control was enabled by pulsed readout and manipulation schemes realized in this work, allowing simultaneous operation of both qubits of the ^{nat}Si/SiGe D09 Die02 device. After forming a double quantum dot with one electron per site, the interdot barrier was gradually lowered to induce wavefunction overlap and give rise to exchange coupling between the qubits. In this regime, the resonance frequency of one qubit depends on the spin state of the other, leading to a conditional response that identifies active spin-spin interaction. By pulsing the energy detuning between the two dots, the overlap and the strength of the exchange interaction could be precisely modulated. Spectroscopic measurements along the detuning axis demonstrated a mutual and tunable exchange coupling J, reaching values up to $J = 20\,\mathrm{MHz}$ and placing the system in the strong coupling regime [40, 141].

In the exchange-coupled two-qubit regime, coherence is primarily limited by charge noise, as revealed by a combined analysis of detuning-dependent energy relaxation, Rabi and Ramsey measurements. These experiments identify fluctuations in the electrostatic confinement potential of the double quantum dot as the dominant source of decoherence. A promising route to suppress this effect involves operating in the symmetric regime, where the exchange coupling is controlled via pulsed interdot barrier modulation at zero detuning. This approach would significantly reduce sensitivity to charge noise but requires synchronized compensation on the plunger gates. While implementation is currently constrained by the availability of only two RF control lines, expanding the setup to include a third line would enable access to the symmetric regime and allow to improve two-qubit control fidelity.

In a final application, the central goal of this thesis was achieved with the successful implementation of spin-selective two-qubit operations on the ^{nat}Si/SiGe D09 Die02 device. Pronounced Rabi oscillations at all four spin-state-dependent resonance conditions at finite exchange-coupling confirmed the reliable operation of the conditional rotation (CROT) gate and marked the achievement of functional two-qubit logic on the studied device. Beyond static control qubit initialization, real-time control was validated by dynamically evolving the control qubit state during operation and monitoring the conditional response of the target qubit in both time and frequency domains. These experiments conclusively verify coherent two-qubit interactions and showcase a powerful indirect readout technique that enables quantum nondemolition measurement through the spectroscopic response of the coupled qubit. Together, these results provide deep insight into the coherent dynamics of coupled spin qubits and underscore the feasibility of quantum computing in multi-qubit architectures.

Universal two-qubit control requires an entangling two-qubit gate combined with high-fidelity single-qubit operations [130]. In this thesis, both single-qubit operations and the two-qubit CROT gate have been independently realized, marking key achievements in the operation of industrially manufactured Si/SiGe spin qubit devices. However, universal control requires nanosecond-scale tunability of the exchange interaction to switch between isolated and coupled qubit regimes. Building on the developed two-qubit control infrastructure, future work may integrate bias-tees into the currently low-pass-filtered plunger gate control to enable fast detuning pulses. This would complete the requirements

for universal two-qubit gates and enable studies of fidelity benchmarks and quantum algorithms.

All qubit metrics in this work were intentionally compared with natural silicon devices to provide a consistent baseline for performance assessment. However, it is well established that isotopically purified ^{28}Si devices exhibit substantially enhanced coherence times in both academic and industrial settings [21, 26]. A promising next step is therefore to apply the optimization strategies proposed in this thesis to ^{28}Si-based spin qubit devices, where the reduced noise environment offers an ideal platform for single- and two-qubit benchmarking.

The results of this thesis demonstrate successful single- and two-qubit control of a state-of-the-art Si/SiGe spin qubit device fabricated using advanced industrial 300 mm wafer process technologies. These achievements confirm that the stringent requirements of quantum computing, such as low-noise environments for coherent multi-qubit control and tunable inter-qubit connectivity, can be met within an industrial framework. By bridging the gap between academic prototyping and scalable hardware, this work highlights the maturity of industrial semiconductor fabrication for next-generation quantum technologies and brings the vision of a universal quantum computer a step closer to reality.

A Appendix

A.1 List of measured samples

Process number	Sample type	Wafer/Subdie	Layout	Qubit drive	Details
AL210563	natSiMOS	D06 Die01	SD5	ESR	
AL102977	^{28}SiMOS	D03 Die07	SD5	ESR	Device 2-2
AL102977	^{28}SiMOS	D06 Die07	SD5	ESR	Device 6-1
AL102977	^{28}SiMOS	D06 Die07	SD5	ESR	Device 6-5
AL110437	natSi/SiGe	D09 Die05	SD15B	EDSR	300 nm CoMM
AL110437	natSi/SiGe	D09 Die02	SD15A	EDSR	300 nm CoMM
AL110437	natSi/SiGe	D09 Die07	SD15B	EDSR	300 nm CoMM
AL110437	natSi/SiGe	D09 Die02	SD15B	EDSR	300 nm CoMM

Table A.1: Device ID of all successfully operated imec devices

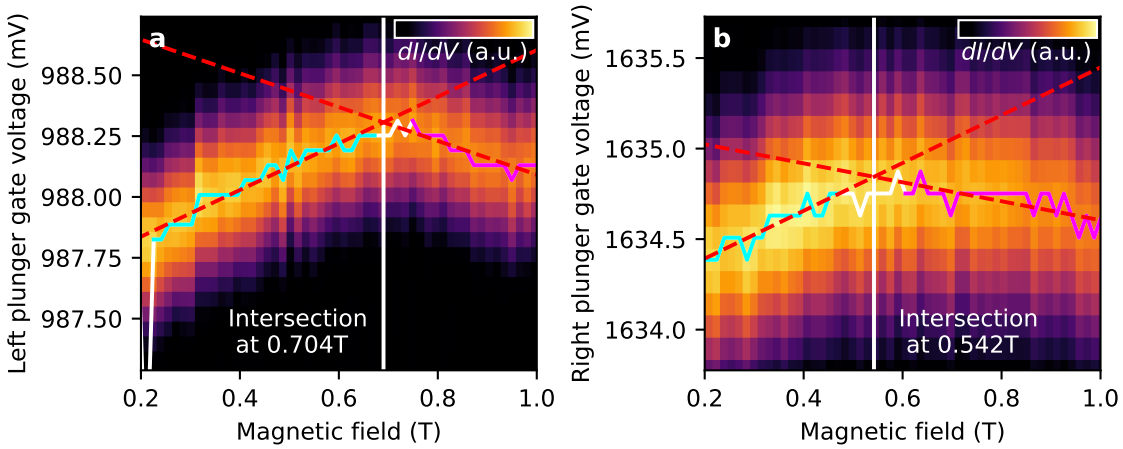

Figure A.1: a Valley splitting determination for the left quantum dot. The smoothed differential SET current is shown as a function of left plunger gate voltage and magnetic field while tracking the $(1) - (2)$ charge transition. The charge transition of each vertical sweep is extracted as the point of maximal derivative (white line), and linear fits (dashed red lines) are applied to segments before (pink) and after the slope inversion (light blue). Their intersection at $B_{\mathrm{ST,L}} = 0.074\,\mathrm{T}$ yields a valley splitting of $E_{\mathrm{V,L}} = 82\,\mu\mathrm{eV}$. **b** Analogous measurement for the right dot using the right plunger gate. The transition exhibits a kink at $B_{\mathrm{ST,R}} = 0.542\,\mathrm{T}$, corresponding to a valley splitting of $E_{\mathrm{V,R}} = 63\,\mu\mathrm{eV}$. Both valley splittings are significantly larger than obtained in Fig. 5.13 for a different working point.

A.2 Magnetospectroscopy at early device tuning stages

Complementary magnetospectroscopy measurement of both quantum dots at a single-qubit working point at early stages of device tuning. The measurement was performed by sweeping the magnetic field from high to low, to ensure a consistent CoMM magnetization, and by sweeping the respective plunger date of the left and right dot over the $(1) - (2)$ charge transition. The intersection of linear fits to pink and light blue regions of the $(1) - (2)$ charge transition of both dots reveals significantly larger magnetic field values at which the sign of the slope changes, being $B_{\mathrm{ST,L}} = 0.704\,\mathrm{T}$ and $B_{\mathrm{ST,R}} = 0.542\,\mathrm{T}$ and correspond to valley splitting energies of $E_{\mathrm{V,L}} = 82\,\mu\mathrm{eV}$ and $E_{\mathrm{V,R}} = 63\,\mu\mathrm{eV}$ for the left and right quantum dot, respectively. These results emphasize the susceptibility of the valley splitting energies on the exact qubit site and working point voltages.

A.3 Eigenenergies of the two-spin Hamiltonian

We can show that the Hamiltonian

$$H = hf_1\, S_z^1 + hf_2\, S_z^2 + hJ\left(\vec{S}^1 \cdot \vec{S}^2 - \tfrac{1}{4}\right)$$

has eigenstates and eigenenergies depending on the strength of the exchange energy hJ. Here $f_{1,2}$ are the Larmor frequencies for the two spins, $h = 2\pi\hbar$ is the Planck constant and the exchange term is written so that for a pair of spin-half particles the triplet states (with

$\vec{S}^1 \cdot \vec{S}^2 = \frac{1}{4}$) are not shifted while the singlet (with $\vec{S}^1 \cdot \vec{S}^2 = -\frac{3}{4}$) acquires an energy shift of $-hJ$.)

Strong–exchange limit
When

$$J \gg \left| f_1 - f_2 \right|,$$

the exchange term dominates and the eigenstates are the usual singlet/triplet states:

$$\begin{aligned} |T_+\rangle &= |\uparrow\uparrow\rangle\,, \\ |T_0\rangle &= (|\uparrow\downarrow\rangle + |\downarrow\uparrow\rangle)/\sqrt{2}\,, \\ |S\rangle &= (|\uparrow\downarrow\rangle - |\downarrow\uparrow\rangle)/\sqrt{2}\,, \\ |T_-\rangle &= |\downarrow\downarrow\rangle\,. \end{aligned}$$

The eigenenergies can be determined by treating singlet and triplet states separately. For any triplet state (S=1) the exchange term vanishes since

$$\vec{S}^1 \cdot \vec{S}^2 - \tfrac{1}{4} = 0.$$

- For $|T_+\rangle = |\uparrow\uparrow\rangle$, each spin has $S_z = +\frac{1}{2}$ so the Zeeman energy is

$$E_{T_+} = \frac{h}{2}(f_1 + f_2).$$

- For $|T_-\rangle = |\downarrow\downarrow\rangle$, both spins have $S_z = -\frac{1}{2}$ giving

$$E_{T_-} = -\frac{h}{2}(f_1 + f_2).$$

- For $|T_0\rangle = \frac{1}{\sqrt{2}}(|\uparrow\downarrow\rangle + |\downarrow\uparrow\rangle)$, the two product components have Zeeman energies that cancel, since one spin is up and the other down, resulting in

$$E_{T_0} = 0.$$

For the singlet state $|S\rangle = \frac{1}{\sqrt{2}}(|\uparrow\downarrow\rangle - |\downarrow\uparrow\rangle)$ (S = 0) the Zeeman contributions cancel by the same argument as for $|T_0\rangle$, but the exchange term gives

$$\vec{S}^1 \cdot \vec{S}^2 - \tfrac{1}{4} = -1,$$

so

$$E_S = -hJ.$$

Thus, in the strong-exchange limit the eigenenergies are:

$$\begin{aligned} E\left(|T_+\rangle\right) &= \tfrac{h}{2}(f_1 + f_2), \\ E\left(|T_0\rangle\right) &= 0\,, \\ E\left(|T_-\rangle\right) &= -\tfrac{h}{2}(f_1 + f_2), \\ E\left(|S\rangle\right) &= -hJ\,. \end{aligned}$$

Weak–exchange limit
When

$$J \ll \left|f_1 - f_2\right|,$$

the Zeeman energies (which are diagonal in the product basis) dominate. In this limit it is more natural to work in the product basis:

$$|\uparrow\uparrow\rangle\,, \quad |\uparrow\downarrow\rangle\,, \quad |\downarrow\uparrow\rangle\,, \quad |\downarrow\downarrow\rangle\,.$$

Their Zeeman energies (without the exchange term of the Hamiltonian) are:

$$\begin{aligned} E_{\uparrow\uparrow} &= \frac{h}{2}(f_1 + f_2)\,, \\ E_{\uparrow\downarrow} &= \frac{h}{2}(f_1 - f_2)\,, \\ E_{\downarrow\uparrow} &= \frac{h}{2}(f_2 - f_1)\,, \\ E_{\downarrow\downarrow} &= -\frac{h}{2}(f_1 + f_2)\,. \end{aligned}$$

Considering the exchange term, the antiparallel product states yield

$$\langle\uparrow\downarrow|\,\vec{S}^1\cdot\vec{S}^2\,|\uparrow\downarrow\rangle = \langle\downarrow\uparrow|\,\vec{S}^1\cdot\vec{S}^2\,|\downarrow\uparrow\rangle = -\frac{1}{4},$$

so the expectation value of the exchange term for these states is

$$hJ\left(-\frac{1}{4} - \frac{1}{4}\right) = -\frac{h}{2}J\,.$$

For the fully polarized states $|\uparrow\uparrow\rangle$ and $|\downarrow\downarrow\rangle$ one has

$$\langle\vec{S}^1\cdot\vec{S}^2\rangle = \frac{1}{4},$$

so the exchange contribution is zero.

Therefore, in the weak-exchange limit the eigenenergies are:

$$\begin{aligned} E\left(|\uparrow\uparrow\rangle\right) &= \tfrac{h}{2}(f_1 + f_2)\,, \\ E\left(|\uparrow\downarrow\rangle\right) &= \tfrac{h}{2}(f_1 - f_2) - \tfrac{h}{2}J\,, \\ E\left(|\downarrow\uparrow\rangle\right) &= \tfrac{h}{2}(f_2 - f_1) - \tfrac{h}{2}J\,, \\ E\left(|\downarrow\downarrow\rangle\right) &= -\tfrac{h}{2}(f_1 + f_2)\,. \end{aligned}$$

It is common to express the two middle states in the product basis in terms of singlet and triplet combinations. In the limit $J \ll |f_1 - f_2|$ the proper eigenstates become

$$\begin{aligned} |\downarrow\uparrow\rangle &= (|T_0\rangle - |S\rangle)/\sqrt{2}\,, \\ |\uparrow\downarrow\rangle &= (|T_0\rangle + |S\rangle)/\sqrt{2}\,, \end{aligned}$$

with the energies given above.

These results show how the exchange interaction splits the degeneracy in the two-spin system and how the eigenenergies depend on whether the Zeeman or exchange term is dominant.

Bibliography

[1] G. E. Moore. "Cramming more components onto integrated circuits (1965)". In: *IEEE Solid-State Circuits Society Newsletter* 11.3 (Sept. 2006), pp. 33–35. DOI: 10.1109/n-ssc.2006.4785860.

[2] Y. Kundu et al. "A Comparison of the Cerebras Wafer-Scale Integration Technology with Nvidia GPU-based Systems for Artificial Intelligence". In: (Mar. 2025). DOI: 10.48550/ARXIV.2503.11698.

[3] D. J. Paul. "Si/SiGe heterostructures: from material and physics to devices and circuits". In: *Semiconductor Science and Technology* 19.10 (Sept. 2004), R75–R108. DOI: 10.1088/0268-1242/19/10/r02.

[4] M. M. Waldrop. "The chips are down for Moore's law". In: *Nature* 530.7589 (Feb. 2016), pp. 144–147. DOI: 10.1038/530144a.

[5] D. Deutsch and R. Josza. "Rapid solution of problems by quantum computation". In: *Proceedings of the Royal Society of London. Series A: Mathematical and Physical Sciences* 439.1907 (Dec. 1992), pp. 553–558. DOI: 10.1098/rspa.1992.0167.

[6] S. P. Jordan. *Quantum Algorithm Zoo*. https://quantumalgorithmzoo.org.

[7] R. P. Feynman. "Simulating physics with computers". In: *International Journal of Theoretical Physics* 21.6–7 (June 1982), pp. 467–488. DOI: 10.1007/bf02650179.

[8] I. B. Djordjevic. "Quantum Algorithms and Methods". In: *Quantum Information Processing, Quantum Computing, and Quantum Error Correction*. Elsevier, 2021, pp. 159–192. DOI: 10.1016/b978-0-12-821982-9.00006-x.

[9] P. Shor. "Algorithms for quantum computation: discrete logarithms and factoring". In: *Proceedings 35th Annual Symposium on Foundations of Computer Science*. SFCS-94. IEEE Comput. Soc. Press, Nov. 1994, pp. 124–134. DOI: 10.1109/sfcs.1994.365700.

[10] B. Fauseweh. "Quantum many-body simulations on digital quantum computers: State-of-the-art and future challenges". In: *Nature Communications* 15.1 (Mar. 2024). DOI: 10.1038/s41467-024-46402-9.

[11] I. Georgescu, S. Ashhab, and F. Nori. "Quantum simulation". In: *Reviews of Modern Physics* 86.1 (Mar. 2014), pp. 153–185. DOI: 10.1103/revmodphys.86.153.

[12] R. Van Meter and D. Horsman. "A blueprint for building a quantum computer". In: *Communications of the ACM* 56.10 (Oct. 2013), pp. 84–93. DOI: 10.1145/2494568.

[13] D. Wecker et al. "Gate-count estimates for performing quantum chemistry on small quantum computers". In: *Physical Review A* 90.2 (Aug. 2014), p. 022305. DOI: 10.1103/physreva.90.022305.

[14] M. Kjaergaard et al. “Superconducting Qubits: Current State of Play”. In: *Annual Review of Condensed Matter Physics* 11.1 (Mar. 2020), pp. 369–395. DOI: 10.1146/annurev-conmatphys-031119-050605.

[15] P. Hrmo et al. “Native qudit entanglement in a trapped ion quantum processor”. In: *Nature Communications* 14.1 (Apr. 2023). DOI: 10.1038/s41467-023-37375-2.

[16] K. Wintersperger et al. “Neutral atom quantum computing hardware: performance and end-user perspective”. In: *EPJ Quantum Technology* 10.1 (Aug. 2023). DOI: 10.1140/epjqt/s40507-023-00190-1.

[17] D. Y. Fedyanin. “Optoelectronics of Color Centers in Diamond and Silicon Carbide: From Single-Photon Luminescence to Electrically Controlled Spin Qubits”. In: *Advanced Quantum Technologies* 4.10 (Aug. 2021). DOI: 10.1002/qute.202100048.

[18] A. Gaita-Ariño et al. “Molecular spins for quantum computation”. In: *Nature Chemistry* 11.4 (Mar. 2019), pp. 301–309. DOI: 10.1038/s41557-019-0232-y.

[19] G. Burkard et al. “Semiconductor spin qubits”. In: *Reviews of Modern Physics* 95.2 (June 2023), p. 025003. DOI: 10.1103/revmodphys.95.025003.

[20] D. Loss and D. P. DiVincenzo. “Quantum computation with quantum dots”. In: *Physical Review A* 57.1 (Jan. 1998), pp. 120–126. DOI: 10.1103/physreva.57.120.

[21] P. Stano and D. Loss. “Review of performance metrics of spin qubits in gated semiconducting nanostructures”. In: *Nature Reviews Physics* 4.10 (Aug. 2022), pp. 672–688. DOI: 10.1038/s42254-022-00484-w.

[22] M. Veldhorst et al. “An addressable quantum dot qubit with fault-tolerant control-fidelity”. In: *Nature Nanotechnology* 9.12 (Oct. 2014), pp. 981–985. DOI: 10.1038/nnano.2014.216.

[23] F. Borjans et al. “Single-Spin Relaxation in a Synthetic Spin-Orbit Field”. In: *Physical Review Applied* 11.4 (Apr. 2019), p. 044063. DOI: 10.1103/physrevapplied.11.044063.

[24] T. Koch. “Fidelity Benchmarking of Industrial Silicon/Silicon-Germanium Qubits”. PhD thesis. Karlsruhe Institute of Technology, 2024.

[25] J. Yoneda et al. “A quantum-dot spin qubit with coherence limited by charge noise and fidelity higher than 99.9%”. In: *Nature Nanotechnology* 13.2 (Dec. 2017), pp. 102–106. DOI: 10.1038/s41565-017-0014-x.

[26] S. Neyens et al. “Probing single electrons across 300-mm spin qubit wafers”. In: *Nature* 629.8010 (May 2024), pp. 80–85. DOI: 10.1038/s41586-024-07275-6.

[27] M. F. Gonzalez-Zalba et al. “Scaling silicon-based quantum computing using CMOS technology”. In: *Nature Electronics* 4.12 (Dec. 2021), pp. 872–884. DOI: 10.1038/s41928-021-00681-y.

[28] R. Li et al. “A crossbar network for silicon quantum dot qubits”. In: *Science Advances* 4.7 (July 2018). DOI: 10.1126/sciadv.aar3960.

[29] H. C. George et al. “12-spin-qubit arrays fabricated on a 300 mm semiconductor manufacturing line”. In: (Oct. 2024). DOI: 10.48550/ARXIV.2410.16583.

[30] S. G. J. Philips et al. “Universal control of a six-qubit quantum processor in silicon”. In: *Nature* 609.7929 (Sept. 2022), pp. 919–924. DOI: 10.1038/s41586-022-05117-x.

[31] N. W. Hendrickx et al. “A four-qubit germanium quantum processor”. In: *Nature* 591.7851 (Mar. 2021), pp. 580–585. DOI: 10.1038/s41586-021-03332-6.

[32] R. Xue et al. “Si/SiGe QuBus for single electron information-processing devices with memory and micron-scale connectivity function”. In: *Nature Communications* 15.1 (Mar. 2024). DOI: 10.1038/s41467-024-46519-x.

[33] J. Dijkema et al. “Cavity-mediated iSWAP oscillations between distant spins”. In: *Nature Physics* 21.1 (Dec. 2024), pp. 168–174. DOI: 10.1038/s41567-024-02694-8.

[34] L. M. K. Vandersypen et al. “Interfacing spin qubits in quantum dots and donors—hot, dense, and coherent”. In: *npj Quantum Information* 3.1 (Sept. 2017). DOI: 10.1038/s41534-017-0038-y.

[35] imec. *Infrastructure: semiconductor cleanrooms and state-of-the-art labs*. https://www.imec-int.com/en/infrastructure. Accessed: 2025-01-30.

[36] B. Klemt et al. “Electrical manipulation of a single electron spin in CMOS using a micromagnet and spin-valley coupling”. In: *npj Quantum Information* 9.1 (Oct. 2023). DOI: 10.1038/s41534-023-00776-8.

[37] W. Pauli. “Über den Zusammenhang des Abschlusses der Elektronengruppen im Atom mit der Komplexstruktur der Spektren”. In: *Zeitschrift für Physik* 31.1 (Feb. 1925), pp. 765–783. DOI: 10.1007/bf02980631.

[38] R. Shankar. *Principles of Quantum Mechanics*. Springer US, 1994. DOI: 10.1007/978-1-4757-0576-8.

[39] J. R. Petta et al. “Coherent Manipulation of Coupled Electron Spins in Semiconductor Quantum Dots”. In: *Science* 309.5744 (Sept. 2005), pp. 2180–2184. DOI: 10.1126/science.1116955.

[40] M. Veldhorst et al. “A two-qubit logic gate in silicon”. In: *Nature* 526.7573 (Oct. 2015), pp. 410–414. DOI: 10.1038/nature15263.

[41] C. K. Maiti, L. K. Bera, and S. Chattopadhyay. “Strained-Si heterostructure field effect transistors”. In: *Semiconductor Science and Technology* 13.11 (Nov. 1998), pp. 1225–1246. DOI: 10.1088/0268-1242/13/11/002.

[42] M. A. Green. “Intrinsic concentration, effective densities of states, and effective mass in silicon”. In: *Journal of Applied Physics* 67.6 (Mar. 1990), pp. 2944–2954. DOI: 10.1063/1.345414.

[43] F. A. Zwanenburg et al. “Silicon quantum electronics”. In: *Reviews of Modern Physics* 85.3 (July 2013), pp. 961–1019. DOI: 10.1103/revmodphys.85.961.

[44] F. Schäffler. “High-mobility Si and Ge structures”. In: *Semiconductor Science and Technology* 12.12 (Dec. 1997), pp. 1515–1549. DOI: 10.1088/0268-1242/12/12/001.

[45] F. Schaffler et al. “High-electron-mobility Si/SiGe heterostructures: influence of the relaxed SiGe buffer layer”. In: *Semiconductor Science and Technology* 7.2 (Feb. 1992), pp. 260–266. DOI: 10.1088/0268-1242/7/2/014.

[46] M. Friesen et al. “Valley splitting theory of SiGe/Si/SiGe quantum wells”. In: *Physical Review B* 75.11 (Mar. 2007), p. 115318. DOI: 10.1103/physrevb.75.115318.

[47] S. Goswami et al. “Controllable valley splitting in silicon quantum devices”. In: *Nature Physics* 3.1 (Dec. 2006), pp. 41–45. DOI: 10.1038/nphys475.

[48] A. Hollmann et al. “Large, Tunable Valley Splitting and Single-Spin Relaxation Mechanisms in a $Si/Si_xGe_{(1-x)}$ Quantum Dot”. In: *Physical Review Applied* 13.3 (Mar. 2020), p. 034068. DOI: 10.1103/physrevapplied.13.034068.

[49] J. R. F. Lima and G. Burkard. “Valley splitting depending on the size and location of a silicon quantum dot”. In: *Physical Review Materials* 8.3 (Mar. 2024), p. 036202. DOI: 10.1103/physrevmaterials.8.036202.

[50] M. Volmer et al. “Mapping of valley splitting by conveyor-mode spin-coherent electron shuttling”. In: *npj Quantum Information* 10.1 (June 2024). DOI: 10.1038/s41534-024-00852-7.

[51] P. Huang and X. Hu. “Spin relaxation in a Si quantum dot due to spin-valley mixing”. In: *Physical Review B* 90.23 (Dec. 2014), p. 235315. DOI: 10.1103/physrevb.90.235315.

[52] G. Scappucci et al. “Crystalline materials for quantum computing: Semiconductor heterostructures and topological insulators exemplars”. In: *MRS Bulletin* 46 (7 July 2021), pp. 596–606. DOI: 10.1557/S43577-021-00147-8.

[53] R. Hanson et al. “Spins in few-electron quantum dots”. In: *Reviews of Modern Physics* 79.4 (Oct. 2007), pp. 1217–1265. DOI: 10.1103/revmodphys.79.1217.

[54] F. H. L. Koppens et al. “Driven coherent oscillations of a single electron spin in a quantum dot”. In: *Nature* 442.7104 (Aug. 2006), pp. 766–771. DOI: 10.1038/nature05065.

[55] C. H. Yang et al. “Spin-valley lifetimes in a silicon quantum dot with tunable valley splitting”. In: *Nature Communications* 4.1 (June 2013). DOI: 10.1038/ncomms3069.

[56] D. M. Fleetwood et al. “Effects of oxide traps, interface traps, and ‘border traps’ on metal-oxide-semiconductor devices”. In: *Journal of Applied Physics* 73.10 (May 1993), pp. 5058–5074. DOI: 10.1063/1.353777.

[57] T. McJunkin et al. “SiGe quantum wells with oscillating Ge concentrations for quantum dot qubits”. In: *Nature Communications* 13.1 (Dec. 2022). DOI: 10.1038/s41467-022-35510-z.

[58] B. Paquelet Wuetz et al. “Atomic fluctuations lifting the energy degeneracy in Si/SiGe quantum dots”. In: *Nature Communications* 13.1 (Dec. 2022). DOI: 10.1038/s41467-022-35458-0.

[59] M. P. Losert et al. “Practical strategies for enhancing the valley splitting in Si/SiGe quantum wells”. In: *Physical Review B* 108.12 (Sept. 2023), p. 125405. DOI: 10.1103/physrevb.108.125405.

[60] E. Kawakami et al. “Electrical control of a long-lived spin qubit in a Si/SiGe quantum dot”. In: *Nature Nanotechnology* 9.9 (Aug. 2014), pp. 666–670. DOI: 10.1038/nnano.2014.153.

[61] T. F. Watson et al. “A programmable two-qubit quantum processor in silicon”. In: *Nature* 555.7698 (Feb. 2018), pp. 633–637. DOI: 10.1038/nature25766.

[62] D. M. Zajac et al. “Resonantly driven CNOT gate for electron spins”. In: *Science* 359.6374 (Jan. 2018), pp. 439–442. DOI: 10.1126/science.aao5965.

[63] N. Hendrickx et al. “Fast two-qubit logic with holes in germanium”. In: *Nature* 577.7791 (Jan. 2020), pp. 487–491. DOI: 10.1038/s41586-019-1919-3.

[64] T. Koch et al. “Industrial 300 mm wafer processed spin qubits in natural silicon/silicon-germanium”. In: *npj Quantum Information* 11.1 (Apr. 2025). DOI: 10.1038/s41534-025-01016-x.

[65] A. Tosato et al. *QARPET: A Crossbar Chip for Benchmarking Semiconductor Spin Qubits*. 2025. DOI: 10.48550/ARXIV.2504.05460.

[66] A. R. Mills et al. “Two-qubit silicon quantum processor with operation fidelity exceeding 99%”. In: *Science Advances* 8.14 (Apr. 2022). DOI: 10.1126/sciadv.abn5130.

[67] A. J. Weinstein et al. “Universal logic with encoded spin qubits in silicon”. In: *Nature* 615.7954 (Feb. 2023), pp. 817–822. DOI: 10.1038/s41586-023-05777-3.

[68] A. Noiri et al. “Fast universal quantum gate above the fault-tolerance threshold in silicon”. In: *Nature* 601.7893 (Jan. 2022), pp. 338–342. DOI: 10.1038/s41586-021-04182-y.

[69] N. D. Stuyck. “Design and Characterization of Quantum Silicon-Based Devices for Semiconducting Qubit Implementation”. PhD thesis. KU Leuven, 2021.

[70] N. I. Dumoulin Stuyck et al. “Low dephasing and robust micromagnet designs for silicon spin qubits”. In: *Applied Physics Letters* 119.9 (Aug. 2021), p. 094001. DOI: 10.1063/5.0059939.

[71] H. Grabert, M. H. Devoret, and M. Kastner. “Single Charge Tunneling: Coulomb Blockade Phenomena in Nanostructures”. In: *Physics Today* 46.4 (Apr. 1993), pp. 62–63. DOI: 10.1063/1.2808874.

[72] L. J. Geerligs et al. “Influence of Dissipation on the Coulomb Blockade in Small Tunnel Junctions”. In: *Europhysics Letters (EPL)* 10.1 (Sept. 1989), pp. 79–85. DOI: 10.1209/0295-5075/10/1/014.

[73] J. Park et al. “Passive and active suppression of transduced noise in silicon spin qubits”. In: *Nature Communications* 16.1 (Jan. 2025). DOI: 10.1038/s41467-024-55338-z.

[74] A. A. Konakov et al. “Lande factor of the conduction electrons in silicon: temperature dependence”. In: *Journal of Physics: Conference Series* 324 (Oct. 2011), p. 012027. DOI: 10.1088/1742-6596/324/1/012027.

[75] H. Bluhm et al. *Electrons in Solids: Mesoscopics, Photonics, Quantum Computing, Correlations, Topology*. De Gruyter, Mar. 2019. DOI: 10.1515/9783110438321.

[76] M. Le Bellac. *A Short Introduction to Quantum Information and Quantum Computation*. Cambridge University Press, June 2006. DOI: 10.1017/cbo9780511755361.

[77] R. Shankar. *Fundamentals of Physics II: Electromagnetism, Optics, and Quantum Mechanics*. Yale University Press, May 2020. DOI: 10.12987/9780300252446.

[78] R. B. Keller. "Skin Effect". In: *Design for Electromagnetic Compatibility–In a Nutshell*. Springer International Publishing, Aug. 2022, pp. 135–143. DOI: 10.1007/978-3-031-14186-7_10.

[79] L. Petit et al. "Universal quantum logic in hot silicon qubits". In: *Nature* 580.7803 (Apr. 2020), pp. 355–359. DOI: 10.1038/s41586-020-2170-7.

[80] P. Steinacker et al. "A 300 mm foundry silicon spin qubit". In: (Oct. 2024). DOI: 10.48550/ARXIV.2410.15590.

[81] J. J. Pla et al. "A single-atom electron spin qubit in silicon". In: *Nature* 489.7417 (Sept. 2012), pp. 541–545. DOI: 10.1038/nature11449.

[82] V. N. Golovach, M. Borhani, and D. Loss. "Electric-dipole-induced spin resonance in quantum dots". In: *Physical Review B* 74.16 (Oct. 2006), p. 165319. DOI: 10.1103/physrevb.74.165319.

[83] Y. Tokura et al. "Coherent Single Electron Spin Control in a Slanting Zeeman Field". In: *Physical Review Letters* 96.4 (Jan. 2006), p. 047202. DOI: 10.1103/physrevlett.96.047202.

[84] K. C. Nowack et al. "Coherent Control of a Single Electron Spin with Electric Fields". In: *Science* 318.5855 (Nov. 2007), pp. 1430–1433. DOI: 10.1126/science.1148092.

[85] J. Yoneda et al. "Fast Electrical Control of Single Electron Spins in Quantum Dots with Vanishing Influence from Nuclear Spins". In: *Physical Review Letters* 113.26 (Dec. 2014), p. 267601. DOI: 10.1103/physrevlett.113.267601.

[86] R. Neumann and L. R. Schreiber. "Simulation of micro-magnet stray-field dynamics for spin qubit manipulation". In: *Journal of Applied Physics* 117.19 (May 2015). DOI: 10.1063/1.4921291.

[87] K. Takeda et al. "A fault-tolerant addressable spin qubit in a natural silicon quantum dot". In: *Science Advances* 2.8 (Aug. 2016). DOI: 10.1126/sciadv.1600694.

[88] A. Sigillito et al. "Site-Selective Quantum Control in an Isotopically Enriched Si28/Si0.7Ge0.3 Quadruple Quantum Dot". In: *Physical Review Applied* 11.6 (June 2019), p. 061006. DOI: 10.1103/physrevapplied.11.061006.

[89] F. Pobell. *Matter and Methods at Low Temperatures*. 3rd, rev. and exp. ed. 2007. Berlin, Heidelberg: Springer Berlin Heidelberg, 2007. 1461 pp.

[90] Qinu. *Version XL*. https://qinu.de/version-xl/. Accessed: 2025-04-25.

[91] A. Zilz. "Investigation of the Rarefied Gas Flow in the Pumping Tube of a 3He/4He Dilution Refrigerator". Master's thesis. Karlsruhe Institute of Technology, 2022.

[92] J. Ferrero. "Development of a cryogenic platform with fast turnaround in-situ characterization of semiconductor circuits for qubit applications". PhD thesis. Karlsruhe Institute of Technology, 2024.

[93] M. Microwave. *How to think about IQ mixers*. https://markimicrowave.com/technical-resources/application-notes/how-to-think-about-iq-mixers/. Accessed: 2024-10-23. 2015.

[94] J. Ferrero et al. "Noise reduction by bias cooling in gated Si/Si_xGe_{1-x} quantum dots". In: *Applied Physics Letters* 124.20 (May 2024). DOI: 10.1063/5.0206632.

[95] W. G. van der Wiel et al. "Electron transport through double quantum dots". In: *Reviews of Modern Physics* 75.1 (Dec. 2002), pp. 1–22. DOI: 10.1103/revmodphys.75.1.

[96] D. Maradan et al. "GaAs Quantum Dot Thermometry Using Direct Transport and Charge Sensing". In: *Journal of Low Temperature Physics* 175.5–6 (Apr. 2014), pp. 784–798. DOI: 10.1007/s10909-014-1169-6.

[97] J. M. Elzerman et al. "Single-shot read-out of an individual electron spin in a quantum dot". In: *Nature* 430.6998 (July 2004), pp. 431–435. DOI: 10.1038/nature02693.

[98] A. Morello et al. "Single-shot readout of an electron spin in silicon". In: *Nature* 467.7316 (Sept. 2010), pp. 687–691. DOI: 10.1038/nature09392.

[99] N. Gläser. "Enhancement of Molecular Spin Sensitivity and Blip Detection Efficiency in Silicon Spin Qubits". Master's thesis. Karlsruhe Institute of Technology, 2024.

[100] F. Bloch. "Nuclear Induction". In: *Physical Review* 70.7–8 (Oct. 1946), pp. 460–474. DOI: 10.1103/physrev.70.460.

[101] M. Shafiei et al. "Resolving Spin-Orbit- and Hyperfine-Mediated Electric Dipole Spin Resonance in a Quantum Dot". In: *Physical Review Letters* 110.10 (Mar. 2013), p. 107601. DOI: 10.1103/physrevlett.110.107601.

[102] K. Li, D. C. Spierings, and A. M. Steinberg. "Efficient adiabatic rapid passage in the presence of noise". In: *Physical Review A* 108.1 (July 2023), p. 012615. DOI: 10.1103/physreva.108.012615.

[103] N. Chanda, P. Patnaik, and R. Bhattacharyya. "Optimal population transfer using adiabatic rapid passage in the presence of drive-induced dissipation". In: *Physical Review A* 107.6 (June 2023), p. 063708. DOI: 10.1103/physreva.107.063708.

[104] X.-F. Liu et al. "Accelerated Adiabatic Passage of a Single Electron Spin Qubit in Quantum Dots". In: *Physical Review Letters* 132.2 (Jan. 2024), p. 027002. DOI: 10.1103/physrevlett.132.027002.

[105] S. Shevchenko, S. Ashhab, and F. Nori. "Landau–Zener–Stückelberg interferometry". In: *Physics Reports* 492.1 (July 2010), pp. 1–30. DOI: 10.1016/j.physrep.2010.03.002.

[106] C. Zener. "Non-Adiabatic Crossing of Energy Levels". In: *Proceedings of the Royal Society of London. Series A, Containing Papers of a Mathematical and Physical Character* 137.833 (Sept. 1932), pp. 696–702. DOI: 10.1098/rspa.1932.0165.

[107] S. Haroche and J.-M. Raimond. *Exploring the Quantum*. Oxford University Press, Aug. 2006. DOI: 10.1093/acprof:oso/9780198509141.001.0001.

[108] A. W. Overhauser. "Polarization of Nuclei in Metals". In: *Physical Review* 92.2 (Oct. 1953), pp. 411–415. DOI: 10.1103/physrev.92.411.

[109] H. Bluhm et al. "Dephasing time of GaAs electron-spin qubits coupled to a nuclear bath exceeding 200 μs". In: *Nature Physics* 7.2 (Dec. 2010), pp. 109–113. DOI: 10.1038/nphys1856.

[110] J. Bylander et al. "Noise spectroscopy through dynamical decoupling with a superconducting flux qubit". In: *Nature Physics* 7.7 (May 2011), pp. 565–570. DOI: 10.1038/nphys1994.

[111] L. M. K. Vandersypen and I. L. Chuang. "NMR techniques for quantum control and computation". In: *Reviews of Modern Physics* 76.4 (Jan. 2005), pp. 1037–1069. DOI: 10.1103/revmodphys.76.1037.

[112] E. Paladino et al. "1/f noise: Implications for solid-state quantum information". In: *Reviews of Modern Physics* 86.2 (Apr. 2014), pp. 361–418. DOI: 10.1103/revmodphys.86.361.

[113] F. H. L. Koppens et al. "Universal Phase Shift and Nonexponential Decay of Driven Single-Spin Oscillations". In: *Physical Review Letters* 99.10 (Sept. 2007), p. 106803. DOI: 10.1103/physrevlett.99.106803.

[114] D. Keith et al. "Ramped measurement technique for robust high-fidelity spin qubit readout". In: *Science Advances* 8.36 (Sept. 2022). DOI: 10.1126/sciadv.abq0455.

[115] T. A. Gomez et al. "Introduction to spectral line shape theory". In: *Journal of Physics B: Atomic, Molecular and Optical Physics* 55.3 (Feb. 2022), p. 034002. DOI: 10.1088/1361-6455/ac4f31.

[116] D. Sitter. "Magnetometry of Single-Molecule Magnets Using a Silicon-Based Spin Qubit". Master's thesis. Karlsruhe Institute of Technology, 2025.

[117] J. Lin et al. "Independent state and measurement characterization for quantum computers". In: *Physical Review Research* 3.3 (Sept. 2021), p. 033285. DOI: 10.1103/physrevresearch.3.033285.

[118] H. E. Ercan, S. N. Coppersmith, and M. Friesen. "Strong electron-electron interactions in Si/SiGe quantum dots". In: *Physical Review B* 104.23 (Dec. 2021), p. 235302. DOI: 10.1103/physrevb.104.235302.

[119] J. Dodson et al. "How Valley-Orbit States in Silicon Quantum Dots Probe Quantum Well Interfaces". In: *Physical Review Letters* 128.14 (Apr. 2022), p. 146802. DOI: 10.1103/physrevlett.128.146802.

[120] P. Scarlino et al. "Second-Harmonic Coherent Driving of a Spin Qubit in a Si/SiGe Quantum Dot". In: *Physical Review Letters* 115.10 (Sept. 2015), p. 106802. DOI: 10.1103/physrevlett.115.106802.

[121] B. Undseth et al. "Nonlinear Response and Crosstalk of Electrically Driven Silicon Spin Qubits". In: *Physical Review Applied* 19.4 (Apr. 2023), p. 044078. DOI: 10.1103/physrevapplied.19.044078.

[122] N. F. Ramsey. “A Molecular Beam Resonance Method with Separated Oscillating Fields”. In: *Physical Review* 78.6 (June 1950), pp. 695–699. DOI: 10.1103/physrev.78.695.

[123] O. E. Dial et al. “Charge Noise Spectroscopy Using Coherent Exchange Oscillations in a Singlet-Triplet Qubit”. In: *Physical Review Letters* 110.14 (Apr. 2013), p. 146804. DOI: 10.1103/physrevlett.110.146804.

[124] R.-B. Liu, W. Yao, and L. J. Sham. “Control of electron spin decoherence caused by electron–nuclear spin dynamics in a quantum dot”. In: *New Journal of Physics* 9.7 (July 2007), pp. 226–226. DOI: 10.1088/1367-2630/9/7/226.

[125] E. L. Hahn. “Spin Echoes”. In: *Physical Review* 80.4 (Nov. 1950), pp. 580–594. DOI: 10.1103/physrev.80.580.

[126] E. Kawakami et al. “Gate fidelity and coherence of an electron spin in an Si/SiGe quantum dot with micromagnet”. In: *Proceedings of the National Academy of Sciences* 113.42 (Oct. 2016), pp. 11738–11743. DOI: 10.1073/pnas.1603251113.

[127] A. Faribault and D. Schuricht. “Spin decoherence due to a randomly fluctuating spin bath”. In: *Physical Review B* 88.8 (Aug. 2013), p. 085323. DOI: 10.1103/physrevb.88.085323.

[128] Y. M. Galperin et al. “Non-Gaussian Low-Frequency Noise as a Source of Qubit Decoherence”. In: *Physical Review Letters* 96.9 (Mar. 2006), p. 097009. DOI: 10.1103/physrevlett.96.097009.

[129] M. M. E. K. Shehata et al. “Modeling semiconductor spin qubits and their charge noise environment for quantum gate fidelity estimation”. In: *Physical Review B* 108.4 (July 2023), p. 045305. DOI: 10.1103/physrevb.108.045305.

[130] A. Barenco et al. “Elementary gates for quantum computation”. In: *Physical Review A* 52.5 (Nov. 1995), pp. 3457–3467. DOI: 10.1103/physreva.52.3457.

[131] S. M. Girvin. *Modern condensed matter physics*. Ed. by K. Yang. Cambridge: Cambridge University Press, 2019. 697 pp.

[132] G. Burkard et al. “Physical optimization of quantum error correction circuits”. In: *Physical Review B* 60.16 (Oct. 1999), pp. 11404–11416. DOI: 10.1103/physrevb.60.11404.

[133] T. Meunier, V. E. Calado, and L. M. K. Vandersypen. “Efficient controlled-phase gate for single-spin qubits in quantum dots”. In: *Physical Review B* 83.12 (Mar. 2011), p. 121403. DOI: 10.1103/physrevb.83.121403.

[134] X. Hu and S. Das Sarma. “Charge-Fluctuation-Induced Dephasing of Exchange-Coupled Spin Qubits”. In: *Physical Review Letters* 96.10 (Mar. 2006), p. 100501. DOI: 10.1103/physrevlett.96.100501.

[135] Y.-P. Shim and C. Tahan. “Barrier versus tilt exchange gate operations in spin-based quantum computing”. In: *Physical Review B* 97.15 (Apr. 2018), p. 155402. DOI: 10.1103/physrevb.97.155402.

[136] M. A. Fogarty et al. “Integrated silicon qubit platform with single-spin addressability, exchange control and single-shot singlet-triplet readout”. In: *Nature Communications* 9.1 (Oct. 2018). DOI: 10.1038/s41467-018-06039-x.

[137] J. C. C. Hwang et al. “Impact of g -factors and valleys on spin qubits in a silicon double quantum dot”. In: *Physical Review B* 96.4 (July 2017), p. 045302. DOI: 10.1103/physrevb.96.045302.

[138] M. Veldhorst et al. “Spin-orbit coupling and operation of multivalley spin qubits”. In: *Physical Review B* 92.20 (Nov. 2015), p. 201401. DOI: 10.1103/physrevb.92.201401.

[139] T. Fujisawa, T. Hayashi, and S. Sasaki. “Time-dependent single-electron transport through quantum dots”. In: *Reports on Progress in Physics* 69.3 (Feb. 2006), pp. 759–796. DOI: 10.1088/0034-4885/69/3/r05.

[140] V. Srinivasa et al. “Simultaneous Spin-Charge Relaxation in Double Quantum Dots”. In: *Physical Review Letters* 110.19 (May 2013), p. 196803. DOI: 10.1103/physrevlett.110.196803.

[141] W. Huang et al. “Fidelity benchmarks for two-qubit gates in silicon”. In: *Nature* 569.7757 (May 2019), pp. 532–536. DOI: 10.1038/s41586-019-1197-0.

[142] L. Petit et al. “Design and integration of single-qubit rotations and two-qubit gates in silicon above one Kelvin”. In: *Communications Materials* 3.1 (Nov. 2022). DOI: 10.1038/s43246-022-00304-9.

[143] D. Culcer, X. Hu, and S. Das Sarma. “Dephasing of Si spin qubits due to charge noise”. In: *Applied Physics Letters* 95.7 (Aug. 2009). DOI: 10.1063/1.3194778.

[144] T. Nakajima et al. “Quantum non-demolition measurement of an electron spin qubit”. In: *Nature Nanotechnology* 14.6 (Apr. 2019), pp. 555–560. DOI: 10.1038/s41565-019-0426-x.

[145] X. Xue et al. “Repetitive Quantum Nondemolition Measurement and Soft Decoding of a Silicon Spin Qubit”. In: *Physical Review X* 10.2 (Apr. 2020), p. 021006. DOI: 10.1103/physrevx.10.021006.

Acknowledgments

Nach vielen Jahren des Physikstudiums bin ich stolz, nun an dem Punkt angekommen zu sein, an dem ich meine Doktorarbeit zu Papier bringe. Wie so oft im Leben lassen sich die kleinen und großen Herausforderungen am besten mit guten Weggefährten meistern. Deshalb möchte ich diese Seite nutzen, um all jenen meinen aufrichtigen Dank auszusprechen, die mir den Weg geebnet oder mich ein Stück begleitet und die Reise so viel schöner gemacht haben.

An erster Stelle danke ich meinem Doktorvater Wolfgang, der mich in seine Gruppe aufgenommen hat, obwohl ich von Quantenphysik ungefähr so viel wusste wie ein Elektron vom Wetter. Du warst immer unermüdlich, wenn es darum ging, plötzlich auftretende Notfälle zu beheben oder mir neue Möglichkeiten zur Verbesserung aufzuzeigen. Unsere persönlichen Gespräche waren für mich immer eine Freude, und ich bin dankbar für die Zeit und all das, was ich von dir lernen durfte.

Ein großes Dankeschön geht auch an Clément, der uns eigenhändig mit Projekten für mindestens drei Doktorarbeiten versorgt hat. Unvergesslich bleiben die legendären Messmarathons, in denen wir innerhalb einer Woche zahllose Hall- und Qubitproben durchgemessen haben – idealerweise abgerundet mit einer Runde Volleyball. Danke für die hervorragende Zusammenarbeit, die unzähligen Meetings und den freundschaftlichen Umgang jenseits der Arbeit.

Besonders danke ich meinen Weggefährten und Leidensgenossen im Team Halbleiter: Thomas, Daniel (und Julian). Danke, dass ihr mich nicht nur in die Gruppe, sondern auch in eure Herzen aufgenommen habt. Es war mir ein Vergnügen, mit euch die eine oder andere Quantennuss zu knacken, und ich wünsche mir, dass wir unsere Freundschaft auch nach der Promotion lebendig halten und uns nicht aus den Augen verlieren. Mein Dank gilt ebenso den „Neuen“, Daniel und Lucas, die die Flamme der Begeisterung weitertragen, den Gruppenalltag bereichern und unsere Forschung weiterführen.

Natürlich darf auch der Rest der Gruppe nicht unerwähnt bleiben – allen voran Dennis, Luca, Ioannis und Christoph. Ihr wart der Grund, warum ich mich damals für diese Gruppe entschieden habe, und ihr habt maßgeblich dazu beigetragen, dass ich mich während der Promotion so wohlgefühlt habe. Danke für eure Unterstützung in der Endphase – sei es beim Korrigieren von Texten und Vorträgen oder beim Abnehmen von Last, wenn ich es mir mal wieder unnötig schwer gemacht habe. Danke für die meeega Zeit in den letzten vier Jahren und all die Erinnerungen, die wir gemeinsam geschaffen haben.

Ein besonderer Dank gilt auch meinen Freunden Thomas, Clemens und Peter, die mich seit dem ersten Tag im Physikstudium begleiten. Auch wenn uns nach dem Master die Wege in verschiedene Richtungen geführt haben, weiß ich, dass ihr immer für mich da seid – denn verschränkte Teilchen trennt man nicht so einfach.

Zu guter Letzt – und eigentlich an allererster Stelle – danke ich meiner wundervollen Frau Fabienne. Danke, dass du mich durch den gesamten PhD unermüdlich unterstützt, mir den Rücken freigehalten und für meine endlosen Überstunden und Messmarathons Verständnis gezeigt hast. Vor allem in der finalen Phase warst du eine unschätzbare Hilfe. Ich freue mich auf viele weitere Jahre mit dir und unserer wunderbaren Tochter Leonie, die diesen neuen Lebensabschnitt zweifellos prägen und bereichern wird.